Theoretical Considerations of Biological Systems in the Presence of High Frequency Electric Fields: Microfluidic and Tissue Level Implications

Michael Benjamin Sano

Dissertation submitted to the faculty of the Virginia Polytechnic Institute and State University in partial fulfillment of the requirements for the degree of

Doctor of Philosophy
In
Biomedical Engineering and Sciences

Rafael V. Davalos, Committee Chair

Chang Lu

John Robertson

John Rossmeisl

Gary Brown

Shay Soker

June 14, 2012
Blacksburg, VA
Keywords: Irreversible Electroporation, Contactless Dielectrophoresis

Theoretical Considerations of Biological Systems in the Presence of High Frequency Electric Fields: Microfluidic and Tissue Level Implications

Michael Benjamin Sano

ABSTRACT

The research presented in this dissertation is the result of our laboratory's effort to develop a microfluidic platform to interrogate, manipulate, isolate, and enrich rare mammalian cells dispersed within heterogeneous populations. Relevant examples of these target cells are stem cells within a differentiated population, circulating tumor cells (CTCs) in the blood stream, and tumor initiating cells (TICs) in a population of benign cancer cells. The ability to isolate any of these rare cells types with high efficiency will directly lead to advances in tissue engineering, cancer detection, and individualized medicine.

This work lead directly to the development of a new cell manipulation technique, termed contactless dielectrophoresis (cDEP). In this technique, cells are isolated from direct contact with metal electrodes by employing fluid electrode channels filled with a highly conductive media. Thin insulating barriers, approximately 20 μm, serve to isolate the fluid electrode channels from the low conductivity sample buffer. The insulating barriers in a fluid-electrical system create a number of unique and interesting challenges from an electrical engineering standpoint. Primarily, they block the flow of DC currents and create a non-constant frequency response which can confound experimental results attempting to characterize the electrical characteristics of cells. Due to these, and other, considerations, the use of high-voltage high-frequency signals are necessary to successfully manipulate cells.

The effect of these high frequency fields on cells are studied and applied to microfluidic and tissue level applications. In later chapters, theoretical and experimental results show how high frequency and pulsed electric fields can ablate cells and tissue. Understanding the parameters

necessary to electroporate cells aids in the development of cDEP devices where this phenomenon is undesirable and gives insight towards the development of new cancer ablation therapies where targeted cell death is sought after. This work shows that there exists a finite frequency spectrum over which cDEP devices can operate in which cells are minimally affected by the induced electric fields.

Finally, lessons learned in the course of the development of cDEP were adapted and applied towards cancer ablation therapies where electroporation are favorable. It was found that bursts of high frequency pulsed electric fields can successfully kill cells and ablate tissue volumes through a process termed High Frequency Irreversible Electroporation (H-FIRE). This technique is advantageous as these waveforms mitigate or eliminate muscle contractions associated with traditional IRE technologies. Similarly, the use of fluid electrodes in cDEP inspired the use of an organs vascular system as the conductive pathway to deliver pulses. This novel approach allows for the ablation of large volumes of tissue without the use of puncturing electrodes. These techniques are currently undergoing evaluation in tissue engineering applications and pre-clinical evaluation in veterinary patients.

Acknowledgements

I would like to thank all of the colleagues, students, and professors who have helped bring this work to fruition. I would like to thank my advisor Dr. Davalos for his continued enthusiasm, encouragement, and support. Without his leadership and insight this work would not have been possible. I would like to thank Dr. Roberson, Dr. Rossmeisl, and the rest of my committee for their continued passion, effort and help. I am deeply appreciative of all the members of the Bio-Electro-Mechanical Systems (BEMS) laboratory whose insight and intuition aided in the steady progression of this project. I would especially like to thank John Caldwell, Chris Arena, Paulo Garcia, and Ganesh Balasubramanian who have been great friends and collaborators throughout the course of my graduate career.

My passion for research and academic pursuits has been continuously fueled and refreshed by a strong group of friends who share similar research and social interests. Chris Szot, Bill Vogt, Lyle Hood, Kate Colacino, Andrea Rojas, and the rest of the SBES crew, thanks for the countless great times we have had, listening to me complain, and for contributing to my awesome record on the table. John Keegan, Nick Lattanzio, Katrina Butner, Liz Dennis, Chris Buchannon, Casey Parker, Rob Sikorski, and the rest of the architecture crew; thanks for the countless hours of relaxation, insanity, and hypothetical conversation that your friendships have provided.

Finally, I would like to thank my family, and loved ones for their continuous support and encouragement. Without them, I surely would not be where I am today. To my parents, thank you for your support of my wildly diverse academic pursuits. I am truly fortunate to have amazing role models with unparalleled work ethic who instilled in me a deep passion and enthusiasm for learning. Marisa and Chris thank you for all of your love and support, but most importantly thank you for setting the bar high; I am continuously motivated and inspired by your drive and passion. To my niece and nephews, Mila, Jack, and Liam, thank you for the instantaneous change in perspective. Most importantly, I would like to thank the love of my life, Lauren Faidley, for her continued love, support, and encouragement. I cannot thank you enough for your patience and the serenity that your presence invokes.

Ut Prosm

Contents

List of Figures

Chapter 1: Introduction

The research presented in this dissertation is the result of our laboratory's effort to develop a microfluidic platform to interrogate, manipulate, isolate, and enrich rare mammalian cells dispersed within heterogeneous populations. Relevant examples of these target cells are stem cells within a differentiated population, circulating tumor cells (CTCs) in the blood stream, and tumor initiating cells (TICs) in a population of benign cancer cells. The ability to isolate any of these rare cells types with high efficiency will directly lead to advances in tissue engineering, cancer detection, and individualized medicine.

Isolation of rare mammalian cells typically relies on two mechanisms: mechanical filtration or antibody labeling. Mechanical filtration techniques result in high specificity and enrichment ratios in cases where the target cells have significant geometrical or mechanical differences. Similarly, when the surface proteins of a target population are well defined and understood, antibody labeling techniques are highly successful. Numerous scientifically interesting target cells fail to meet these criteria, providing the motivation and need for the development of advanced sorting techniques.

Dielectrophoresis (DEP), a force which induces the motion cells in a *non*-uniform electric field, provides an extra dimension of properties to aid in the interrogation and manipulation of cells. The motion of cells experiencing this force is dependent on their size, shape, and electrical properties. The electric fields employed in this technique can be either static or dynamic, and swept over a large frequency spectrum. This allows for the isolation of cells based on specific characteristics in their cytoplasm, cytoskeleton, nucleus, and cell membrane including the presence of surface proteins and morphological differences.

As dielectrophoresis employs electric fields in conductive media, the effects of these fields on interrogated cell populations must be considered. In the absence of an external field, the voltage drop across a cell membrane, or transmembrane potential (TMP), is typically on the order of -70

mV and is due to active ion and molecular transport necessary for homeostasis. In this resting state, the 5 nm membrane experiences an electric field of approximately 14 MV/m (140 kV/cm) and is negligibly affected by the resulting electro-thermal processes. In a static electric field, redistribution and reorientation of ions causes an increase in the voltage drop across a cell's membrane. The increase in TMP is highly dependent on the magnitude and frequency of the applied field, as well as the radius of cell. As the TMP is elevated, thermal mechanism increase the mean intermolecular distance and transport of molecules across the membrane increases. Experimental and theoretical analysis suggest that in an attempt to minimize this mean free energy, hydrophilic and hydrophobic pores form within the cell membrane in a process generally referred to as electroporation (EP).

Typically, the electroporation effect is temporary and after the external field is removed, cells return to their resting state. However, if the TMP is elevated above a certain threshold (approximately 1 V), the cell membrane is permanently destabilized resulting in cell death. Due to the capacitive nature of the cell membrane there is a delay between the onset of the electric field and the TMP reaching its maximum value. If the electric field is pulsed or oscillated with switching times shorter than the charging time of the cell membrane (approximately 10 microseconds for mammalian cells), then the electroporation effects are mitigated.

Irreversible electroporation (IRE) is of strong interest in tissue ablation fields, but is undesirable in searching and sorting applications where culture and analysis of cells is desired post processing. The presence of these effects in devices which employ dielectrophoresis is a significant challenge and is the basis for the hypothesis driving this work: ***There exists an optimal frequency range in which rare cells of interest can be sorted using dielectrophoresis while being negligibly impacted by the effects of electroporation.***

Chapter 2: Rare Cell Isolation

Rare cells, those found in low proportion in a fluid or heterogeneous mixture, often have a large impact on biological systems. A few spores of toxic bacteria in a drinking supply can endanger a large population. Scarce circulating tumor cells in a blood sample can indicate a patient's development of metastatic cancer. Methods of finding these and other rare cells are essential for the development of clinical diagnostic tests and new therapeutic techniques as well as providing pure populations for cell for comprehensive cell biology [7]. In addition the ability to isolate and enrich rare cells plays an important role in homeland security and water purity applications [8].

Magnetic-activated cell sorting (MACS) and Fluorescence-activated cell sorting (FACS) are the state of the art in cell isolation and enrichment. These techniques use antibody-conjugated magnetic beads and fluorophore-conjugated antibodies to label and process target cells. Systems employing MACS and FACS provide high throughput screening; however, they have large initial and operational costs, require specialized training, may affect cell fate and function due to sheer stress [9]. There are a myriad of other cellular properties which can be targeted and exploited using microfluidics to isolate and enrich cells without the need for specific cell markers. This chapter will describe in detail the use of surface, volumetric, mechanical, and electrical properties of cells which can be manipulated to detect rare cells.

2.1. Sized Based Isolation

An obvious and easily characterized property of cells is their physical size. Human cell sizes span three orders of magnitude, from 6-8 micron for red blood cells to over 130 micron for the ovum and some nerve cells. Additionally, the size distribution of a specific cell type may vary based their on state or health and a number of interesting and useful methods for isolating cells based on size have been developed. This section will focus on three different types of sized based techniques, namely, mechanical exclusion, hydrodynamic separation, and inertial separation.

2.1.1. Mechanical Exclusion

The simplest microfluidic sorting methods aim to improve macro-scale exclusion filtration in which samples are driven through a porous filter. Microfabrication techniques improve the selectivity of exclusion filtration by capitalizing on the resolution of photolithography to produce pillars or gratings with precisely controlled distances. Excluding membrane filtration, three main types of microfluidic exclusion filtration will be discussed in this section, pillar-type, weir-type, and cross flow-type filtration.

Pillar-type filtration

Pillar-type filtration devices are the simplest form of exclusion filtration. Typically, pillars are fabricated in parallel rows such that the edge to edge spacing of the pillars decreases in subsequent columns. As cells are passed through the device, large cells become physically trapped allowing smaller cells to pass freely. Once the desired sample has been passed through the device, it is flushed with clean buffer in the opposite direction to retrieve the trapped cells. This technique is exceedingly simple and effective when the target cell is much larger than the background cells and their population is small. Mohamed and colleagues used this technique to show that using this technique, breast, colon, and kidney cancer cells could be isolated from whole blood in samples containing approximately 13,000:1 red blood to cancer cells [10]. The advantages of this technique are abundant; Fabrication is simple and can be accomplished using mass fabrication techniques, operation is achieved using simple pumping mechanisms and can be automated, flow rates can be increased by adjusting the channel width, and sample recovery is trivial. This type of device, however, has a critical drawback in that flow rate diminishes as the number of cells trapped increases and the channel becomes clogged. The remaining mechanical exclusion techniques aim to overcome this challenge.

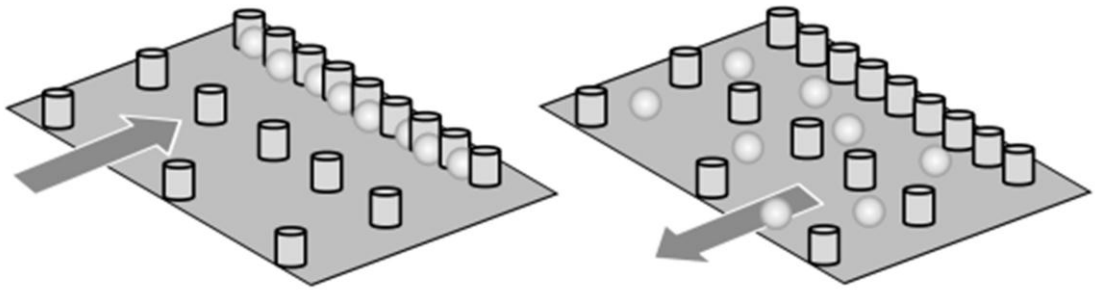

Figure 2-1: Pillar-type filtration devices reversibly trap cells based on size. Recovery of cells is achieved by the device with flushing clean buffer in the opposite direction.

Cross-flow filtration

Cross-flow filtration devices consist of a central sample channel with a filtration mechanism separating adjacent filtrate channels. The first microfluidic incarnation of this technique was proposed by Brody and colleagues in 1996 [11]. In this device, triangular pores were etched into silicon between two microfluidic channels. Brody demonstrated the ability to remove 16 μm spheres from a sample, and theoretically, this technique could filter particles as small as 0.1 μm. This method has been adapted to polymeric microdevices by using rows of pillars with a narrow edge-to-edge spacing or shallow side channels. In both cases, the gap between features is larger than the background particles and smaller than the target cells. Using a pillar type cross-flow filtration device, Chen and colleagues were able to remove 82.3% of red blood cells from whole blood [12]. VanDelinder and Groisman demonstrated a polymeric device with shallow side channels recover 10% of the total plasma volume from whole blood at 0.65 μL/hour [13]. In a more recent work by the same authors, shallow side perfusion channels were used to simultaneously remove red blood cells from whole blood and exchange the hematocrit with a new buffer resulting in an approximate 4000 fold increase in the white blood cell fraction [14].

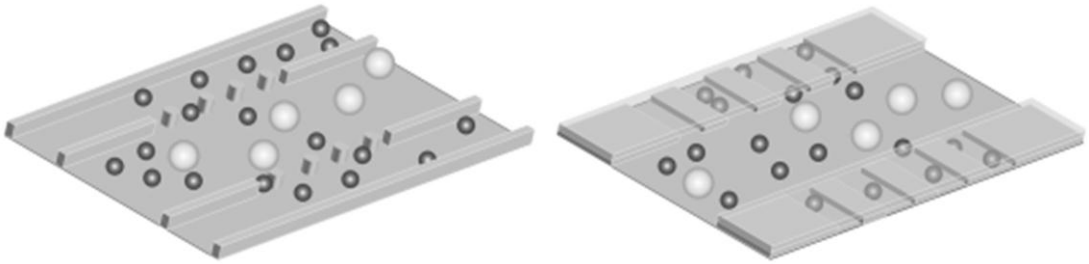

Figure 2-2: Cross-flow filtration devices use side channels which are inaccessible to larger particles to filter background cells or media from the sample.

Weir-type filtration

Weir-type filtration devices get their name from a simple dam which allows water to flow over its crest. The microfluidic adaption of these devices uses parallel channels which are separated by continuous barriers which extend to from the channel floor and produce a small gap between the barriers and the channel's ceiling. When fluid is driven through the main channel, some fluid and any particles smaller than the gap are allowed to flow into the side channels. These devices have achieved a high degree of success in the isolation of red blood cells from plasma and

plasma from whole blood suspensions. Chen and colleagues were able to remove 91.2% of red blood cells from plasma and separate 27.4% of white blood cells from whole blood with a throughput of 10 μL/min [12].

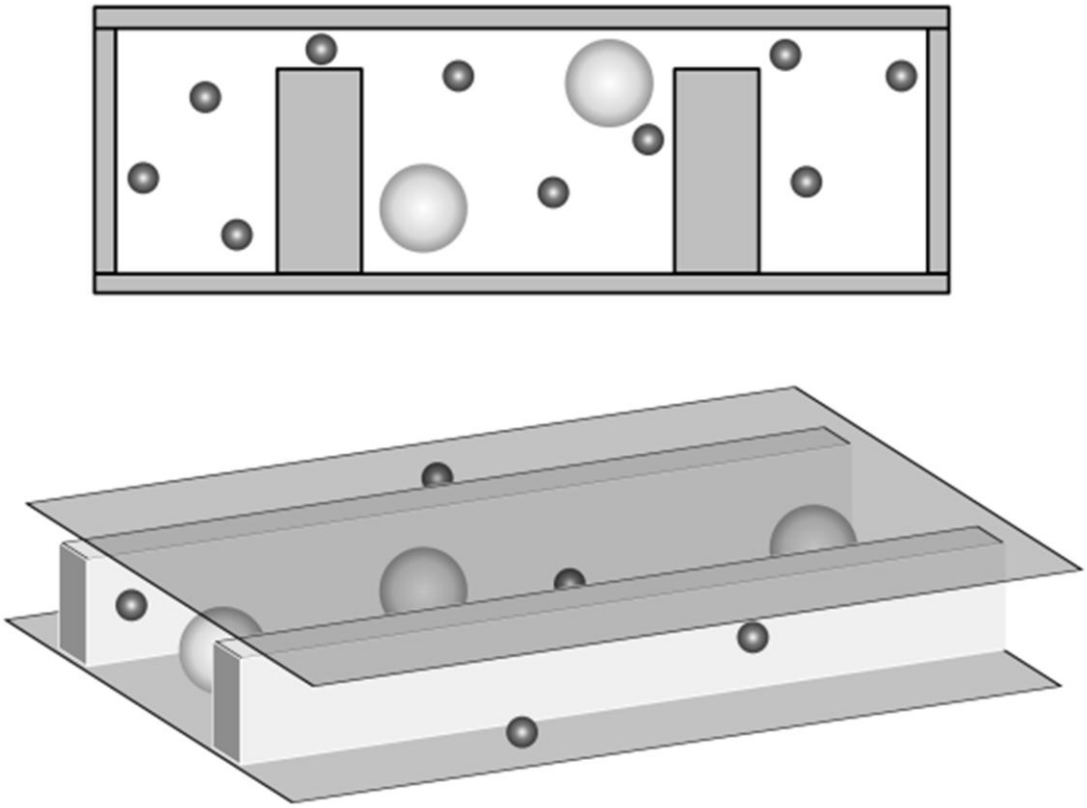

Figure 2-3: Weir type filtration device allows fluid to flow between a main channel and side isolation channels while excluding cells larger than the gap between the channel ceiling and the barriers.

2.1.2. Hydrodynamic Filtration

Hydrodynamic filtration methods operate on the principal that at low Reynolds number, the center of a particle will follow the fluid streamline on which it is situated. These devices aim to manipulate the streamlines of the fluid to alter the path that cells of a specific size will follow.

Deterministic Lateral Displacement

Deterministic lateral displacement is a method in which migration paths for particles is precisely determined by manipulating the laminar flow around an array of obstacles [15]. In each row, the obstacles are separated by a center-to-center distance, d. Each subsequent row of obstacles is shifted horizontally by a distance, Δd. As the flow exits the gap between two obstacles, it

bifurcates into d/Δd lanes around the obstacles in the next row. Due to the laminar nature of the flow, a consequence of the low Reynolds number in the microfluidic context, the lanes do not cross or mix. As these lanes go through subsequent rows of obstacles, their order shifts by one (e.g. Lane 1 becomes lane 2, lane 2 becomes lane 3, and lane d/Δd becomes lane 1). The lanes regain their original position after passing through d/Δd rows. Neglecting diffusion, particles with a radius smaller than Δd will follow the fluid streamlines and shift one lane as it passes through each set of obstacles, returning to its original position every d/Δd rows. These smaller particles follow a zigzag path with no net movement in the lateral direction.

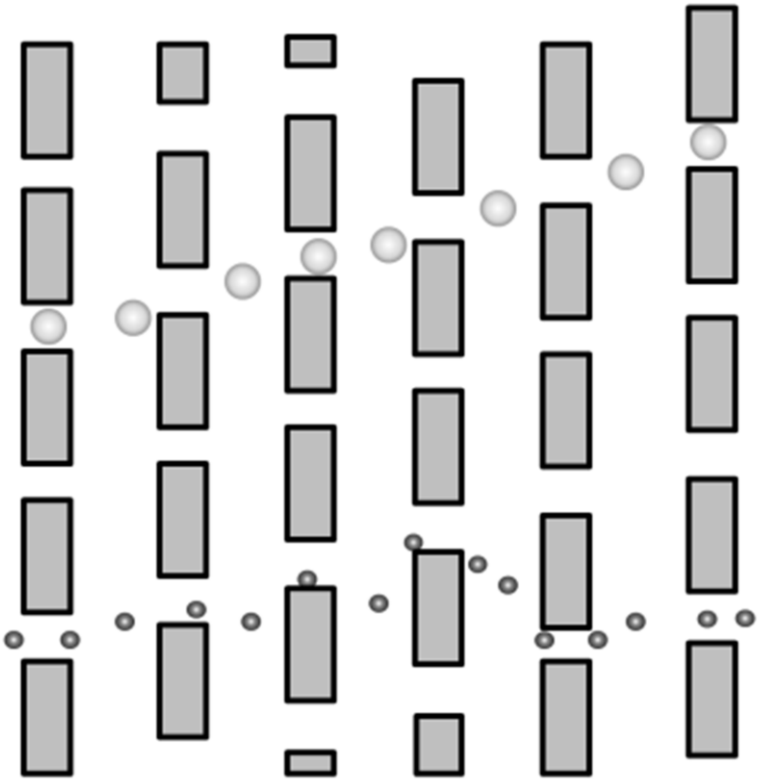

Figure 2-4: Schematic of a deterministic lateral displacement device. Particles with radii less than the width of the lanes remain on their original streamlines and have zero net displacement. Larger particles

In laminar flow, particles the center of a particle tends to travel along the same continuous streamline. When the radius of the particle exceeds Δd, the net effect is different. Take for example, a large particle which has its centerline in the middle of the first lane. If the particles radius is larger than the width of the first lane, then part of the particle occupies the two adjacent lanes. As the approaches an obstacle, it is bumped from the first lane, into the second, shifting its centerline onto an adjacent streamline. This process repeated every time the particles lane is

directly adjacent to an obstacle. The result is a net displacement of the particle. Huang et al. originally demonstrated this techniques ability to isolate particles based on their size with a resolution of 10 nanometers[15]. Davis et al. demonstrated the ability to separate white blood cells from red blood cells and platelets as well as the ability to produce purified, cell free, plasma using this technique [16]. In addition, Inglis, Lord, and Nordon achieved a tenfold enrichment of leukocytes at flow rates of greater than 1 mL per minute in a parallel lateral displacement device[17].

Hydrophoretic Separation

Hydrophoresis is the motion of a cell due to changes in the local pressure field. Devices to manipulate particles using this force typically employ structures on the top and bottom of a channel which are slanted perpendicularly to the fluid flow [18,19]. The geometry of these structures creates an anisotropic fluidic resistance which generates a secondary transverse flow perpendicular to the direction of the bulk flow. These convective vortices force cells to follow size dependent streamlines along the length of the grooves.

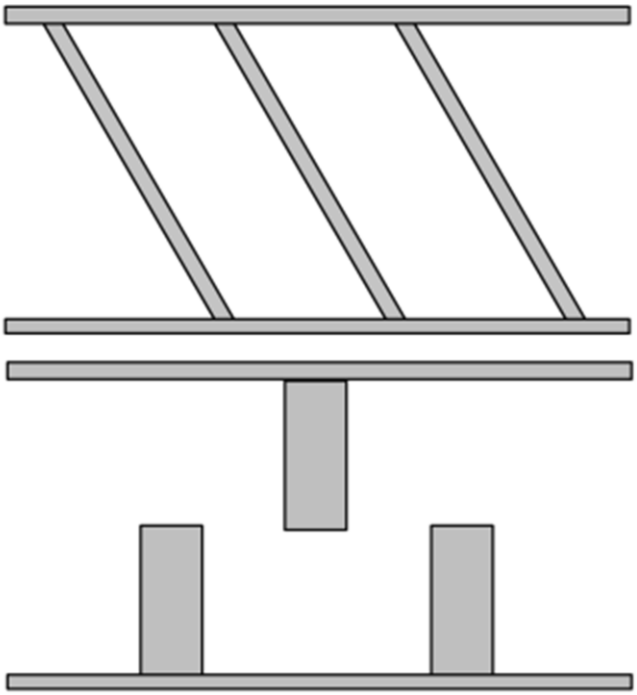

Figure 2-5: Hydrophotetic devices use specifically designed geometric features to manipulate particle streamlines. (Top) From the top, structures are slanted perpendicular to the flow. (Bottom) From the side, structures alternate between top and bottom of the device.

Choi and Park originally demonstrated this technique to separate microparticles based on their size and showed that pressure gradients can be intrinsically created by the geometry of a device to manipulate particles [18]. This technique was later used to enrich white blood cells 210-fold [20]. Whole blood was passed through a device which first focused both types of cells along a single edge of the channel. The cells then passed through a region containing slanted structures which allowed the red blood cells to pass unobstructed, but forced the white blood cells to the opposite side of the channel before they could continue downstream.

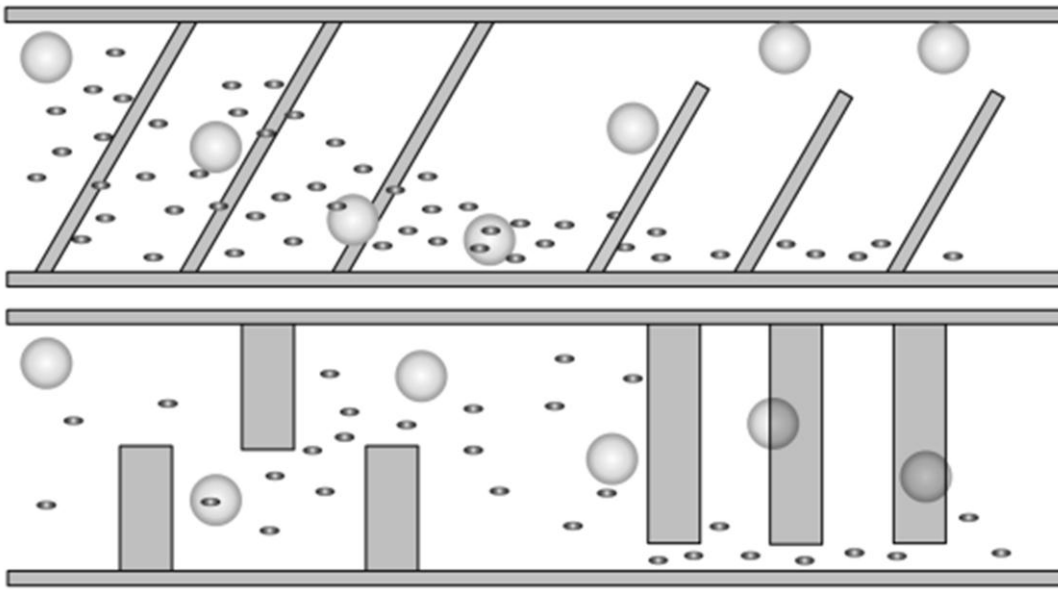

Figure 2-6: Schematic of a hydrophotetic and sized based exclusion device to continuously sort cells (Adapted from Choi et al 2007).

This technique exhibits a high degree of sensitivity towards the size of target cells. Choi et al. later demonstrated this with U937 human leukemia monocytes by isolating cells based on their cell cycle. The differences in cell radii between the G_0/G_1 and G_2/M phases were significant enough to sort a heterogeneous population into these phase sets [21]. This technique has also recently been demonstrated to isolate platelets from dilute whole blood with 76.8% purity using ten channels in parallel to achieve a flow rate of 12 mL/hour[22].

2.2. Mass Based Isolation

2.2.1.Inertia

Typically, microfluidic devices operate in a regime where viscous forces dominate the inertial forces acting on particles. This ratio of these forces is often represented by a dimensionless term, the Reynolds number (Re).

$$Re = \frac{\rho VL}{\mu} = \frac{VL}{\upsilon} \quad [4.1]$$

$$\frac{\rho\, V^2 L^2}{\mu VL} = \frac{inertial\ forces}{viscous\ forces} \quad [4.2]$$

V is the mean velocity of the object relative to the fluid [m/s], L is a characteristic linear dimension [m] μ is the dynamic viscosity of the fluid [kg/(m·s)], υ is the kinematic viscosity [m²/s] and ρ is the density of the fluid [kg/m³]. However, with careful manipulation of device geometries and fluid velocities, inertial forces can be used to manipulate cells. It can be seen that for microfluidic channels with dimensions on the order of 100 μm and flow velocities near or below 0.01 m/s, the Reynolds number approaches 1, implying that inertial and viscous forces can play significant roles in the behavior of the fluid and particles[23]. This assumes a sample fluid with density and viscosity similar to water (μ≅0.001 Pa s, ρ≅1000kg/m^3). It should be noted that in this regime laminar, not turbulent flow, expected except in the most extreme cases.

The first of two main inertial effects in microfluidic devices is the inertial migration of particles within a confined channel. Particles traveling in a microfluidic flow experience drag forces parallel to the direction of the flow, a result of normal and sheer stresses, and a lift force perpendicular to the flow. For geometries with Reynolds number close to 1, the lift forces acting on the particles scale differently depending on the location of the particle within the channel [24]. This gives rise to a wall effect lift which acts away from the wall towards the center line and a shear gradient lift that acts from the center line towards the wall in Poiseuille flow. These two components give rise to inertial lift equilibrium locations [25].

The second effect is seen in the inertial migration of particles in curved channels. Migration occurs because of a combination of inertial effects on the particle and the influence of Dean flow, or recirculating fluid flow caused by a radial pressure gradient, within the curved channel [26]. These two components act in superposition resulting in unique equilibrium positions which

are dependent on particle size [27]. The Dean number, D_n, characterizes the effects of the recirculating flow

$$D_n = Re \left[\frac{d}{R}\right]^{\frac{1}{2}} \quad [4.3]$$

where R is the channel radius of curvature, and d is the hydraulic diameter of the channel. Assuming properly designed channel dimensions, low flow rates, and low Dean numbers ($D_n \approx 1$), result in centrifugal effects which are too small to influence the flow [28]. At higher flow rates, ($D_n \approx 10$), the recirculating flows begin to alter the behavior of the bulk flow. Lee et al. demonstrated that Dean flows can be induced in straight channels in which the cross-sectional area of the channel is rapidly increased and decreased [29] and implemented this technique to isolate blood plasma with a purity of 62.2% at 1.2 mL/hour. Hur et al. showed that cells can be sorted based on size and deformability in their recent work isolating metastatic cells from normal and benign cells from the same origin [30].

2.2.2.Gravity / Sedimentation

Typically, microfluidic devices contain shallow channels in which the location of particles in the z-plane is constrained or considered irrelevant to device performance. However, in some microfluidic systems the effect of gravity, buoyancy, and sedimentation can be beneficial in isolating particles. In the absence of any other force fields, a fully submerged spherical cell is subject to gravitational, buoyant, and drag forces.

$$m\ddot{z} = \left(m - \frac{1}{6}\pi d^3 \rho\right)\vec{g} - 6\pi\mu d\dot{z} \quad [4.4]$$

where m and d are the mass and diameter of the cell, ρ and μ are the density and viscosity of the suspending fluid, $\vec{g}$ and z are the acceleration due to gravity and the spatial coordinate in the z direction, respectively [31]. By carefully tuning the fluid velocity within a microfluidic channel, the sedimentation time of certain particles can be tuned for separation. Huh et al. showed that the sedimentation velocity, $U_{SED} = d^2 g\Delta\rho/18\mu$, can be used to predict the sedimentation profile for beads and perfluorocarbon droplets [32] [Δρ is the difference in viscosity between the particles and the suspending fluid]. Experimentally, they used a planar microfluidic channel turned on its side

to isolate 1 and 20 μm beads with purity greater than 99%. Warrick et al. modified this principal to create a micro-cell concentrator capable of increasing the concentration of target cells 50-fold [33].

Gravity based microfluidics are relatively new, however, these and other mass based sorting techniques are ideal platforms for cell searching as they rely on a single intrinsic force field. Relying on gravitational and inertial forces rather than electric or magnetic forces for sorting vastly simplifies the operation of these devices. A challenge remains in increasing the selectivity of these devices towards rare cells which may be similar in mass and size to their more populous counterparts, however, as presented earlier [30], the deformability of specific cell types may provide an additional exploitable property in these devices.

2.3. Electrical Based Isolation

2.3.1. DEP

The first experiments with dielectrophoresis were described by Hebert Pohl in his 1951 article "The Motion and Precipitation of Suspensoids in Divergent Electric Fields". In this work, a straight wire electrode was placed vertically in the center of a 10 cm Petri dish. A foil band, placed around the inner ring of the dish, was used as an outer electrode. When particles of carbon or polyvinyl chloridepolyvinyl acetate copolymers were suspended in a media and 10,000 volts (AC or DC) were applied, the particles rapidly accumulated near the center electrode. Subsequent experiments were conducted to determine with a high degree of certainty that this motion was not due to electrokinetics, the motion of a charged particle in a uniform electric field.

In the early 1990's many researches began to fabricate complex electrode arrays on silicon and quartz substrates. The new level of precision and scale allowed for the creation of complex geometries and new methods of inducing dielectrophoretic effects. Fuhr was the first to demonstrate linear motion of particles using a array of electrodes powered by a traveling square wave voltage [34]. The small scale of these devices and their increased surface to volume ratios reduce the effects of joule heating and electrolysis, which on the macro-scale were mitigated

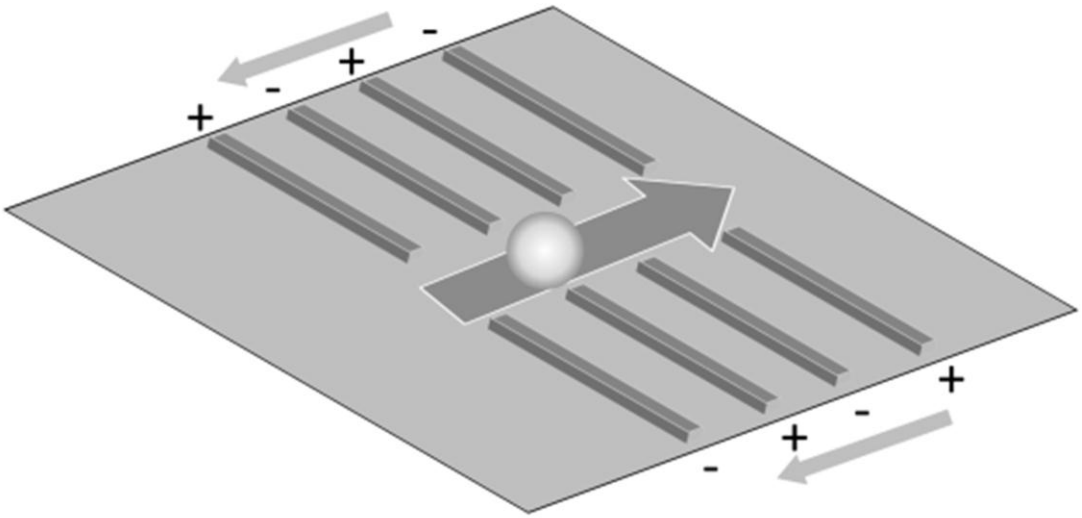

Figure 2-7: Traveling wave DEP device trap cells in an electric field which moves along the channel. The polarity of specific electrodes is alternated driving cells down the channel.

through the use of low conductivity solutions (on the order of 10^{-4} S/m). This allowed, for the first time, the use of physiologically relevant media (conductivity on the order of 1 S/m) and the dielectrophoretic study of mammalian cells in their natural state[35]. Since this development, many other planar electrode geometries have been developed to facilitate the isolation and enrichment of rare cells using dielectrophoresis.

Dielectrophoresis field flow fractionation (depFFF) devices exploit the balance between DEP levitation, hydrodynamic lift, sedimentation, and fluid drag to influence the elution times to isolate cells. Using this technique, Gascoyne and colleagues recently demonstrated a tumor cell isolation efficiency of 92% in a (depFFF) device using an electric field generated at 60 kHz [36]. Other groups have used interdigitated, castellated, and pin-plate geometry electrodes to trap DNA [37], viruses [38], and cells [39-41]. In these devices, the electrodes are patterned onto the bottom of the sample channels. This results in a high DEP forces near the surface of the electrodes which diminishes as particles move further from the channel surface, however, some groups are developing three-dimensional electrode structures to provide uniform electric fields throughout the channel depth [42].

2.3.2. Insulator Based Dielectrophoresis

Insulator based dielectrophoresis (iDEP) devices employ insulating structures within a microfluidic channel to produce non-uniformities when electrodes are inserted into the ends of the channel [43,44].

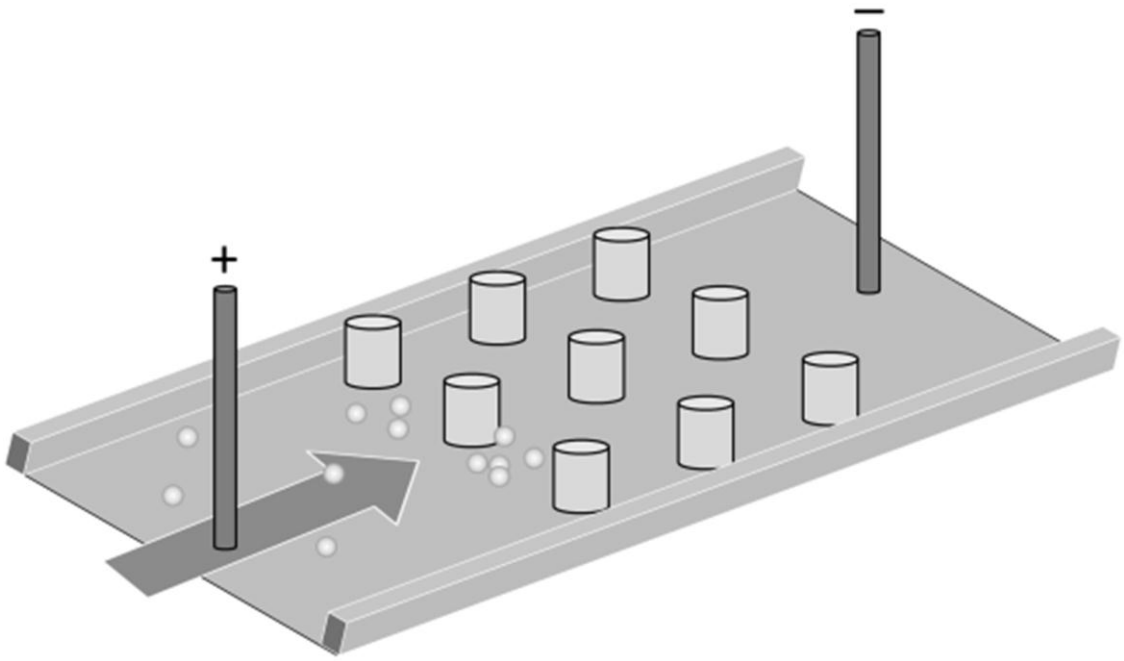

Figure 2-8: iDEP is facilitated using electrokinetic flow to drive particles into regions of highly non-uniform electric field produced by insulating structures within the channel.

The concept of trapping cells using dielectrophoresis without the use of embedded electrodes was first presented by Cummings and Singh in 2000 [45]. Lapizco-Encinas and colleagues demonstrated the ability of this technique to trap live and dead E. coli cells using a DC electric field of 400 V/cm in a glass channel containing an array of insulating pillars [8] . The difference in Clausius-Mossotti factor between the live and dead cells resulted in a banding effect between pillars in which dead cells occupied an inner region close to the insulating pillars and live cells occupied a separate region further from the pillars. This group later demonstrated the ability of this technique to enrich spores and viruses and the potentiality of this technique to isolate bacteria, cells, and inert particles from each other [44].

In a device with 40 μm edge to edge pillar spacing, Lapizco-Encinas et al. further demonstrated the ability of iDEP to enrich proteins[46] and Gallo-Villanueva later showed enrichment of DNA in a similar device [47]. More recently, Moncada-Hernandez and Lipizco-Encinas demonstrated the

ability of iDEP to simultaneously enrich and isolate bacteria from yeast cells with enrichment factors of 50 and 37, respectively [48]. This was accomplished by applying a 1500 V/cm field for 60 seconds, then decreasing the field to 500V/cm to release the bacterial cells, and finally reducing the field to 200 V/cm to release the yeast cells and flush them downstream. Davalos and colleagues showed that polymer based iDEP devices performed as well as those fabricated in glass and that the addition of surfactants to the media greatly reduces the electric field necessary to trap particles [49]. The evaluation of cell populations after enrichment was later demonstrated through the inclusion of a downstream impedance sensor [50].

Pysher and Hayes demonstrated the versatility of iDEP geometries using a channel containing saw-tooth features which were places sequentially closer together [51]. In this device, bacterial cells were driven, by electrokinetic force, through regions with progressively increasing field gradients and it was found that live and dead cells trapped in distinct regions.

2.3.3. Contactless Dielectrophoresis

Contactless dielectrophoresis (cDEP) is a method of cell manipulation first demonstrated by Shafiee and colleagues [52]. The devices consist of fluid electrode channels filled with a highly conductive media, typically phosphate buffer solution, and a sample channel. A thin insulating membrane between the fluid electrode channels and the sample channel serves to isolate the sample from direct contact with metal electrodes. Capacitive coupling between the electrode channels and the sample channel occurs when an AC voltage is applied across the fluid electrode channels and a non-uniform electric field is produced within the sample channel. Shafiee et al. demonstrated a method to enrich live human leukemia cells form a mixed population of live and dead cells in a cDEP device containing insulating pillars within the sample channel [53]. A mixed sample of live and dead cells was driven through a sample channel using pressure driven flow at a rate of 0.02 mL/hr. Fluid electrodes separated from the sample channel by a 20 μm barrier created a non-uniform electric field in a trapping region containing insulating pillars. When a 50 V_{RMS} signal was applied at frequencies between 200 and 500 kHz, greater than 90% of the live cells became trapped near the insulating pillars while all dead cells passed freely through the device.

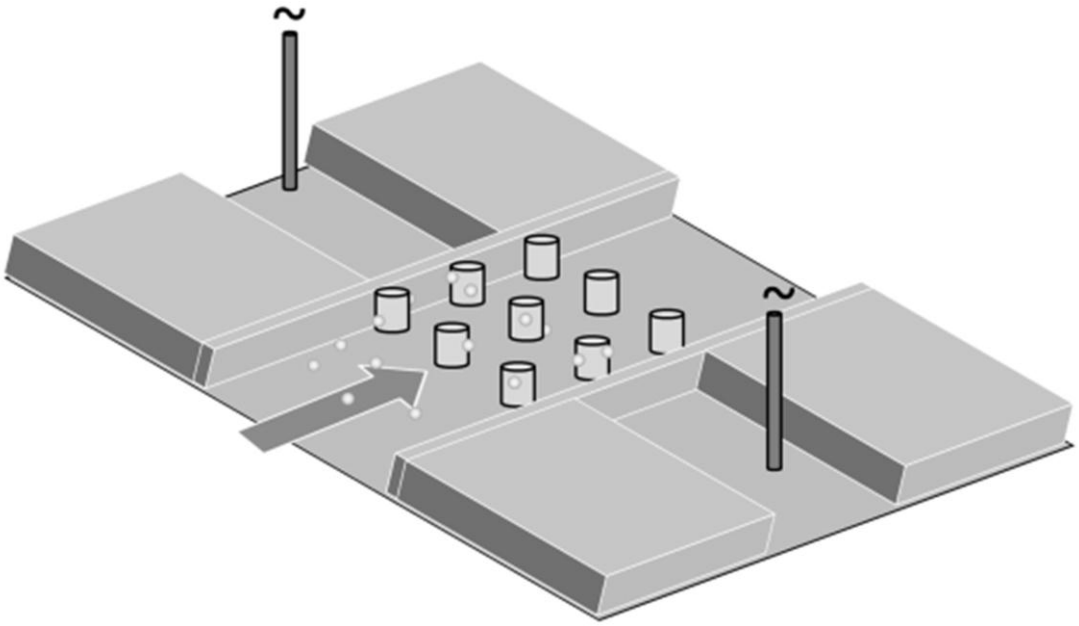

Figure 2-9: cDEP is facilitated by pressure driven flow which drives cells into regions of highly non-uniform electric field produced by fluid electrode channels which are isolated from the sample by a thin membrane. The addition of pillars within the sample channel increases the non-uniformity of the field.

Later, Shafiee et al. demonstrated the ability of cDEP to isolate live THP-1 cells from a mixed population containing similarly sized 10 μm beads using positive DEP when 70 V_{RMS} at 300 kHz was applied [54]. They also demonstrated the ability to enrich 2 μm beads using negative DEP at 190 V_{RMS} and 300 kHz.

Typically, the impedance of the insulating barriers will dominate the system at frequencies below 100 kHz causing a large proportion of the applied voltage to drop across the barriers. Above 100 kHz, the capacitive nature of the barriers causes their total impedance to roll off, allowing a voltage to drop across the sample channel resulting in the formation of a strongly non-uniform electric field. Numerical and experimental evaluation of these devices indicate that the value for $\nabla(\vec{E} \cdot \vec{E})$ in the sample channel must be approximately $1x10^{12}$ V^2m^{-3} to successfully manipulate cells [55].

Improvements of the frequency response of cDEP devices focus on two main factors, namely increasing the capacitance of the insulating barriers and increasing the resistance of the sample channel between the fluid electrodes. An increase in barrier capacitance causes the impedance of

the barriers to roll off sooner resulting in a larger proportion of the voltage drop across the sample channel at lower frequencies. Similarly, because an equal current must flow through the barriers and the sample channel, increasing the resistance of the sample channel increases the proportion of the voltage drop which occurs across the sample. The physical geometry and the material properties of the materials present in this system influence the resistance ($R = \rho L/A$) and capacitance ($C = \epsilon_0 \epsilon_r A/d$) of each element where ρ and ϵ_r are the resistivity and relative static permittivity of the material respectively, *A* is the cross-sectional area, *L* is the length of the resistor and d is the separation distance between two conductive components.

Increasing the resistance of the sample channel between the fluid electrodes can be achieved by increasing the length of sample channel between the fluid electrodes, reducing the depth or width of the sample channel, or by decreasing the conductivity of the sample buffer. Reductions in the depth and width of the sample channel have the undesirable consequence of reducing the total throughput of the device for a constant volumetric flow rate. Mammalian cells are typically sensitive to conditions in sample media, such as its osmolality. Currently, the sample buffer used in a cDEP device with living cells has a conductivity of approximately 100 μS/cm. Identification and use of a lower conductivity physiologically relevant media has the potential to greatly improve device frequency responses.

Increasing the capacitance of the insulating barriers can be achieved by increasing their height or width, decreasing their thickness, or by selecting substrate materials with higher relative permittivities. Currently, most cDEP devices employ insulating barriers which are 20 μm thick which is approaching the limit of what can be reliably fabricated using traditional soft lithography stamping techniques.

Sano et al. recently demonstrated a contactless dielectrophoresis device capable of operating over a wide frequency spectrum between 1 kHz and 10 MHz [55]. This allowed for the manipulation of mammalian cells using cDEP at frequencies at which the Clausius-Mossotti factor can be either positive or negative. This device has been used to examine the cross-over frequency and calculate the area specific membrane capacitance of breast cancer, leukemia, white, and red blood cells [56].

The dielectrophoretic phenomenon was first discovered over 60 years ago. However, recent advances in MEMS fabrication technologies have reduced the dimensions over which these forces are applied. Precision fabrication is dramatically increasing the sensitivity of this technique and mass fabrication methods such as injection molding and hot embossing are essential in bringing this technology closer to clinical application. This chapter introduced the use of surface, volumetric, mechanical, and electrical properties to detect rare cells. Each of these techniques has advantages and drawbacks; however, in conjunction they have to potential to isolate rare cells with unprecedented specificity. Furthermore, the combination of these techniques with electrochemical and impedance sensors, micro pumps and transducers, and picoliter analysis holds great promise in bringing BioMEMS to a clinical reality.

Chapter 3: Concept and Development of Contactless Dielectrophoresis

The original concept for contactless dielectrophoresis (cDEP) came from an attempt to develop a microfluidic system which used DC electric fields to drive samples through a sample channel and perpendicular AC electric field to deflect cells into different paths. This concept was an attempt to improve the selectivity of iDEP technologies by interrogating cells based on their frequency dependent, rather than DC, Clausius-Mossotti factor. The original design consisted of a T-shaped microfluidic channel shown in Figure 3-1. The entire device would be primed with a low conductivity isotonic solution suitable for mammalian cells. A DC electric field would be used to drive cells from left to right through the device. At the center of the device, the sample channel would widen abruptly and at a specific angle. At this location a vertical channel intersects the main channel and an array of closely spaced pillars form a 'wall' such that fluid and current can flow freely, but cells could not enter the vertical channel. Theoretically, An AC signal applied across this vertical channel, combined with the rapid

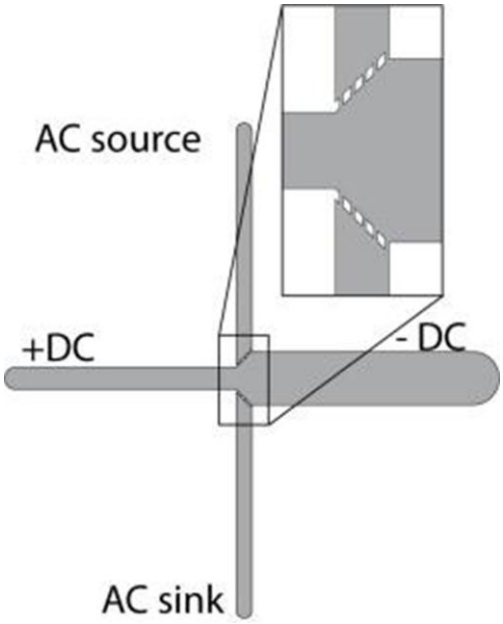

Figure 3-1: Original concept for perpendicular AC and DC electric fields. Insulating pillars separate the vertical and horizontal channels

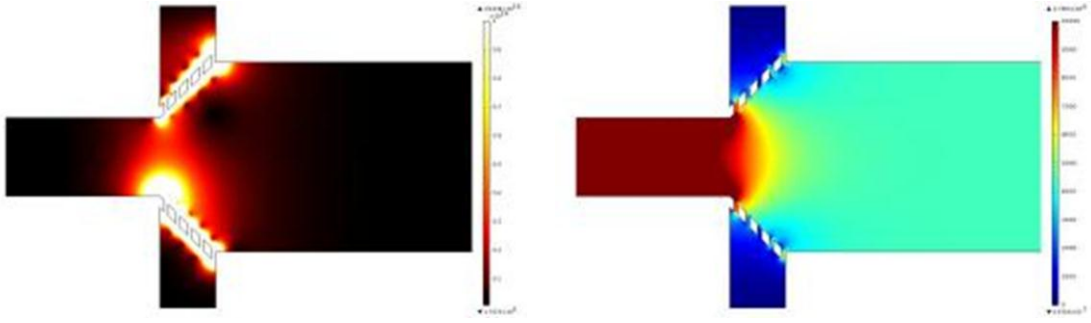

Figure 3-2: Numerical simulations for original perpendicular fields concept. [Left] The DEP field [V/m^3] within the device is not 'uniform' or symmetric over the width of the channel. The pillars create regions of very high gradient in the electric field which could impact experimental results. [Right] Electrokinetic fluid velocity [μm/s] simulations show that the fluid velocity decreases substantially when the channel widens. This could be advantageous as cells would experience DEP forces for longer.

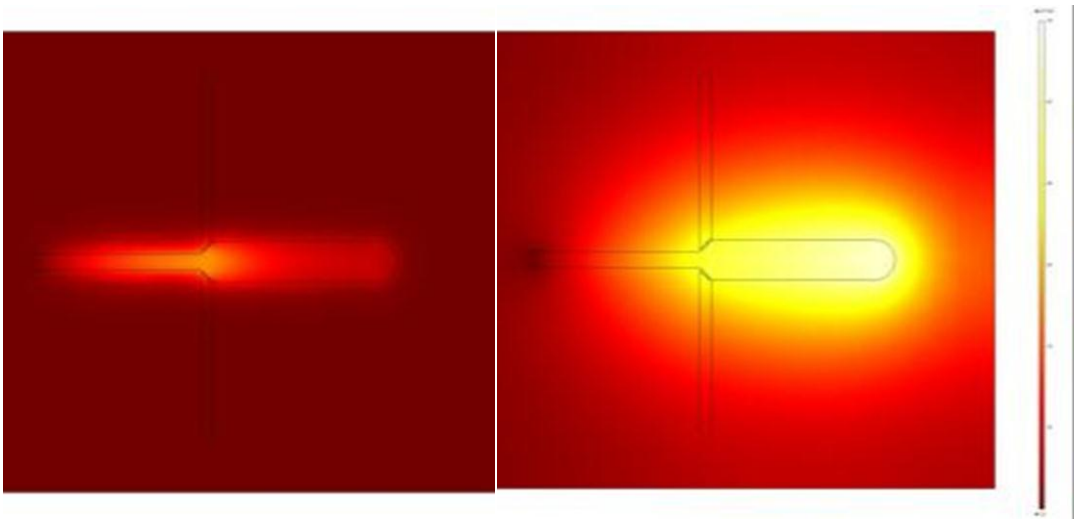

Figure 3-3: Thermal model of the perpendicular field concept device incorporating fluid heat transfer and electrokinetic flow. 1000 V_{DC} is applied across the 1 cm long horizontal channel with 0.01 S/m conductivity buffer. [Left] The temperature within the device begins to increase within 1 second of applying the field. [Right] After 1 minute, the temperature within the sample channel has increased by 27 °C.

widening of the horizontal channel will induce a frequency dependent DEP force that will deflect cells in the y-direction. By sweeping the frequency of the applied voltage and monitoring the deflection of the cells, the electrical characteristics of the cells can be determined. This design paradigm is advantageous as it allows for the use of perpendicular voltages from DC to very high frequency AC with minimal electrical considerations. However, the low conductivity buffer in the vertical channel would present a significant resistance and there would be a voltage drop across that channel which must be accounted for when determining appropriate experimental parameters.

Cells typically cannot survive in deionized water, and the low conductivity, isotonic solution typically used experimentally has a conductivity of approximately 100 μS/cm. The electric field in these devices is applied across the entire sample volume and the fluid temperature would increase due to Joule heating. As the DC potential used in this configuration is responsible for fluid pumping only, this effect might be mitigated if fluid velocities are kept low. The AC potential used would likely be quite substantial, on the order of 1000 V_{RMS}. This would likely result quantifiable Joule heating at the very center of the device.

In this initial concept geometry, the pillars which separate the vertical and horizontal channels introduce anomalies in the electric field. As current pathways are distorted around these pillars, regions of very high gradient of electric field are formed. Figure 3-2 shows the distortions in the

DEP field. Ideally, designs would be optimized such that the DEP field is uniform in the transition zone so that the vertical location of cells does not drastically influence how they behave in this region. The presence of the pillars creates regions of high and low DEP forces in the transition region. This effect can be mitigated by reducing the distance between the pillars and the total number of pillars along the length of the transition zone. This strategy, taken to its extreme, is the origin of the contactless dielectrophoresis platform.

In contactless dielectrophoresis (cDEP) a solid barrier, rather than pillars, isolates the perpendicular fluid channels as shown in Figure 3-4. This eliminates most of the non-uniformities in the DEP field within the transition region, but introduces a number of challenges that must be overcome. The primary consideration, and the focus of much of this document, is that a solid barrier acts as a capacitor, blocking direct currents. This limits the effective operating region of this device to medium and high frequencies, though as will be shown in Chapter 11:, with careful consideration, DC fields can be employed in specific cDEP geometries.

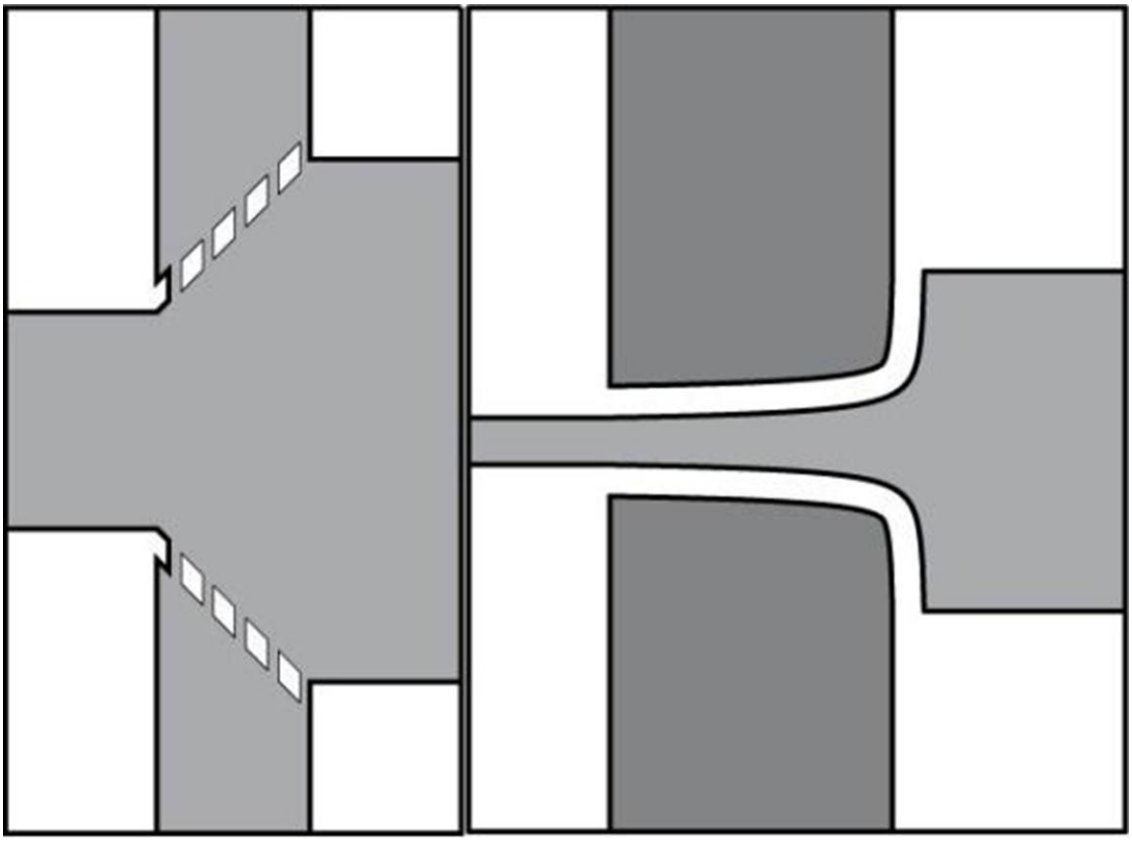

Figure 3-4: Comparison of perpendicular fields approaches. [Left] The original concept uses a continuous sample channel with pillars which block cells from entering certain regions. The angle and spacing between pillars creates the DEP force used to manipulate cells. [Right] The contactless dielectrophresis concept device physically isolates the sample and electrode channels with a solid barrier. The geometry of the barrier and sample channel influence the DEP force. Light grey regions contain a low conductivity isotonic buffer while dark grey regions contain a high conductivity buffer.

Preliminary models of the cDEP platform were conducted using the conductive media module in COMSOL 3.5 using a time dependent simulation, shown in Figure 3-5. The design consists of two fluid electrode channels with a conductivity of 1.4 S/m, a sample channel with conductivity of 0.001 S/m and two insulating barriers with conductivity of 0.83×10^{-12}. A potential of 500*sin(100*t) was applied to the distal boundary of the top fluid electrode channel. It should be noted that 500 V_{peak} is 353.5 $V_{RMS.}$ The resulting simulation, shown in Figure 3-5, shows four regions of high electric field form within the sample channel. These regions correspond to the corners of the fluid electrode channels and are the regions where particles experiencing positive DEP will trap. There is also a region of relatively low electric field at the center of the sample channel where particles experiencing negative DEP will tend to trap. Figure 3-5 shows experimental results from a cDEP device with a 50 micron wide sample channel and 50 micron

thick barriers. When 150 V_{RMS} is applied at 600 kHz, 4 micron beads experience a positive DEP force and are trapped along the edges of the sample channel.

These preliminary modeling and experimental results show the feasibility of the cDEP platform. Modeling these systems in the time domain provides some important insight into temporal changes occurring as the field oscillates and the charging time of capacitive membrane between the sample channel and the fluid electrodes. The following chapters will outline methods for determining the frequency response of these devices.

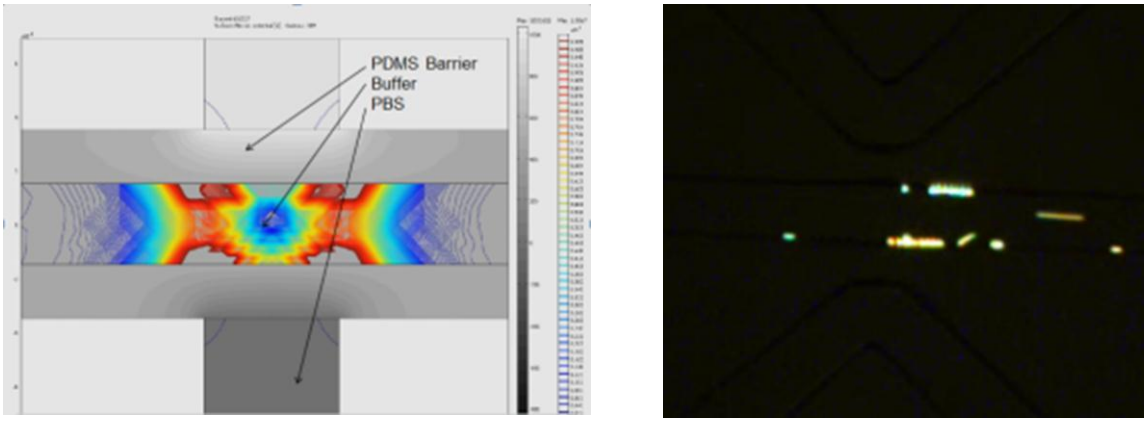

Figure 3-5: Numerical analysis and experimental validation of a simplified cDEP geometry. [Left] A sinusoidal 500 V_{peak} potential is applied to the fluid electrodes. [Right] 4 micron beads trapping in regions of high electric field gradient when 150 V_{RMS} is applied at 600 kHz.

Chapter 4: Theory

The application of a voltage across conductive and dielectric materials will induce an electric field

$$\vec{E} = -\nabla\phi \quad [4.1]$$

where ϕ is the applied voltage. Under the influence of this electric field, dielectric particles immersed in a conductive fluid will become polarized. If the electric field is non-uniform, particles are driven towards the regions of field gradient maxima by a translational dielectrophoretic force ($\vec{F}_{DEP}$) [57]

$$\vec{F}_{DEP} = \gamma_{DEP}\,\nabla\left|\vec{\mathrm{E}}\cdot\vec{\mathrm{E}}\right| \quad [4.2]$$

where γ_{DEP} is half the induced dipole moment, of the particle. For a spherical particle, this quantity can be represented as:

$$\gamma_{DEP} = 2\,\pi\epsilon_m r^3 Re[K(\omega)] \quad [4.3]$$

where r is the radius of the cell, ϵ_m is the relative permitivity of the suspending medium, and $Re[K(\omega)]$ is the real part of the Clausius-Mossotti (C-M) factor.

$$K(\omega) = \frac{\epsilon_c^* - \epsilon_m^*}{\epsilon_c^* + 2\epsilon_m^*} \quad [4.4]$$

$$\epsilon^* = \epsilon + \frac{\sigma}{i\omega} \quad [4.5]$$

where ϵ_c^* and ϵ_m^* are the permittivity of the cell and suspending medium respectively, σ is the conductivity, ω is the frequency of the applied field, and $i = \sqrt{-1}$.

A particle independent DEP vector can be defined as

[4.6]

$$\vec{\Gamma} = \frac{\vec{F}_{DEP}}{\gamma_{DEP}} = \nabla\left|\vec{\mathrm{E}} \cdot \vec{\mathrm{E}}\right|$$

$$\vec{\Gamma} = \nabla|(-\nabla\phi) \cdot (-\nabla\phi)| \quad [4.7]$$

$$\vec{\Gamma} = \nabla\left|\left(\frac{d\phi}{dx}\right)^2 + \left(\frac{d\phi}{dy}\right)^2 + \left(\frac{d\phi}{dz}\right)^2\right| \quad [4.8]$$

$$\vec{\Gamma} = \begin{bmatrix} \left(\frac{d^3}{dx^3} + \frac{d^3}{dxdy^2} + \frac{d^3}{dxdz^2}\right)\hat{e}_x \\ \left(\frac{d^3}{dx^2dy} + \frac{d^3}{dy^3} + \frac{d^3}{dydz^2}\right)\hat{e}_y \\ \left(\frac{d^3}{dx^2dz} + \frac{d^3}{dy^2dz} + \frac{d^3}{dz^3}\right)\hat{e}_z \end{bmatrix} \phi^2 \quad [4.9]$$

where $\hat{e}_j$ is a unit vector in the *j* direction. From this, we can see that the motion of a particle due to DEP is highly influenced by the magnitude of the applied voltage as well as the spatial non-uniformity, in all three dimensions, of the electric field created.

The application of a uniform electric field to an ionic liquid in a microfluidic field gives rise to electrical double layer (EDL) formation along the channel wall. The ions closest to the channel walls are subject to strong electrostatic forces which cannot be overcome by thermal diffusion. As result, these ions are statically bound to the surface of the channel forming a fixed Stern layer. The electrostatic force within the EDL deteriorates further from the channel surface and mobile ions begin to move parallel to the EDL. The net effect of ionic drag caused by the mobile ions on the bulk fluid induces a phenomenon known as *electro-osmotic(EO) flow* [58]. The velocity of an ionic fluid under EO flow (v_{eo}) is calculated by

$$v_{eo} = \mu_{eo}\vec{E} \quad [4.5]$$

where $\mu_{eo}$is the elctro-osmotic mobility of the ionic fluid and $\vec{E}$ is the magnitude of the applied electric field. The electro-osmotic mobility

$$\mu_{eo} = -\frac{\epsilon\zeta}{\eta} \quad [4.6]$$

is a function of the surface potential between the solid and liquid phase (ζ) and the viscosity (η) of the fluid [59].

An EDL will additionally form around a charged particle (or cell) placed in an infinite ionic liquid under a uniform field. In the case of a positively charged cell, a double layer consisting of an excess of positive ions will form. The cell will then be driven towards the region of highest positive potential by a Coulombic force ($\vec{F_c}$) which is proportional to the net charge of the cell (q) and equal to

$$\vec{F_c} = q\vec{E} \quad [4.7]$$

[60]. This force is also known as *electrophoresis* and the resulting electrophoretic velocity ($\vec{V}_{ep}$) of a spherical cell can be calculated using the Hückel equation [59]

$$\vec{V}_{ep} = \mu_{ep}\vec{E} \quad [4.8]$$

This velocity is a function of the electrophoretic mobility (μ_{ep}) of the cell and the applied field. The electrophoretic mobility

$$\mu_{ep} = \frac{V_{ep}}{E} = \frac{q}{f} \quad [4.9]$$

where $f = 6\pi\mu a$ is the stokes frictional factor for a spherical particle in creeping flow. The electrophoretic mobility is also defined as

$$\mu_{ep} = -\frac{3}{2}\frac{\epsilon_m \zeta_p}{\mu} \quad [4.10]$$

is a function of the surface potential between the cell and the surrounding medium (ζ_p) and the permittivity of the surrounding media (ϵ_m). The net velocity of the cell as result of these two forces is referred to as the *electrokinetic velocity* ($\vec{V}_{ek}$)

$$\vec{V}_{ek} = (\mu_{eo} + \mu_{ep})\vec{E} \quad [4.11]$$

where $\mu_{eo}$and $\mu_{ek}$are the electro-osmotic and electrophoretic mobilities respectively. These two terms summed are often referred to as the electrokinetic mobility of a particle (μ_{ek}).

$$\vec{V}_{ek} = \mu_{ek}\vec{E} \quad [4.12]$$

The velocity of a particle due to dielectrophoresis can be calculated as follows; In the case of cells, which exist in a micron scaled regime, these forces are opposed by a Stokes drag force.

$$F_{Drag} = 6\pi\eta r v \quad [4.13]$$

where η is the mass density of the fluid, v is the velocity of the cell relative to the fluid. The velocity of the particle can then be calculated by evaluating the balance of forces.

$$F_{DEP} - F_{Drag} = m * a \quad [4.14]$$

Rearranging these terms:

$$m \cdot a - \vec{F}_{Drag} = \vec{F}_{DEP} \quad [4.15]$$

$$m \cdot \ddot{x} - 6\pi\eta r \cdot \dot{x} = \vec{F}_{DEP} \quad [4.16]$$

$$x = \alpha(1 - exp\left[\left(-\frac{6\pi\eta r}{m}\right)t\right]) \quad [4.17]$$

The term $-\frac{6\pi\eta r}{m}$ is known as the characteristic time and for cells in a microfluidic environment, is on the order of 10^{-6}. The acceleration term in this equation can be assumed to be zero since the characteristic time for small particles is orders of magnitude smaller than the time scale of external forces. Therefore,

$$v = \mu_{DEP}\nabla\left(\vec{E}\cdot\vec{E}\right) \quad [4.18]$$

where μ_{DEP} is the dielectrophoretic mobility defined as

$$\mu_{DEP} = \frac{\epsilon_m r^2 Re\{K(\omega)\}}{3\eta} \quad [4.19]$$

When cells encounter a region in which electrokinetic forces and dielectrophoretic forces critically oppose each other, the cells net velocity is reduced. Cells will become trapped when the following inequality is satisfied

$$\nabla\left(\vec{E}\cdot\vec{E}\right) \geq \frac{\mu_{ek}\vec{E}}{\mu_{DEP}} \quad [4.20]$$

Theoretical Analysis of Acceleration

Using a very simple calculation, we can prove that for most cases, acceleration due to electrokinetic phenomena is negligible.

$$characteristic\ time = \frac{mass}{6\pi\mu r} \quad [4.1]$$

$$mass = density * volume = \rho v \quad [4.2]$$

$$mass = \rho * \frac{4}{3}\pi r^3 \qquad [4.3]$$

$$characteristic\ time = \frac{2\rho\pi r^3}{9\pi\mu r} = \frac{2\rho r^2}{9\mu} \qquad [4.4]$$

Assume that the density of a cell is equal to the density of water ~$1000\frac{kg}{m^3}$ and that the dynamic viscosity of water (μ) is $1.0\mathrm{E}^{-3}\ \left[\frac{Ns}{m^2}\right]$

$$\frac{2 * 1000 * (10E^{-6})^2}{9 * 1.0E^{-3}} \left[\frac{\frac{kg}{m^3} * m^2}{N * \frac{s}{m^2}}\right]$$

$$= 2.2E^{-5}\left[\frac{\frac{kg}{m}}{kg * \frac{m}{s^2} * \frac{s}{m^2}}\right] \qquad [4.5]$$

$$= 2.2E^{-5}\left[\frac{\frac{kg}{m}}{\frac{kg}{m * s}}\right]$$

$$= 2.2E^{-5}[s]$$

Note that this corresponds to a frequency of approximately 45 kHz.

Clausius-Mossitti Factor Conversions

$$Prove\ that\ \frac{\sigma_p^* - \sigma_e^*}{\sigma_p^* + 2\sigma_e^*} = \frac{\varepsilon_p^* - \varepsilon_e^*}{\varepsilon_p^* + 2\varepsilon_e^*}$$

$$\sigma^* = \sigma + i\omega\varepsilon$$

$$\varepsilon^* = \varepsilon - i\frac{\sigma}{\omega}$$

$$\frac{\sigma_p + i\omega\varepsilon_p - \sigma_e + i\omega\varepsilon_e}{\sigma_p + i\omega\varepsilon_p + 2\sigma_e + 2i\omega\varepsilon_e} * \frac{i}{i}$$

$$\frac{i\sigma_p + ii\omega\varepsilon_p - i\sigma_e + ii\omega\varepsilon_e}{i\sigma_p + ii\omega\varepsilon_p + i\,2\sigma_e + i2i\omega\varepsilon_e}$$

$$\frac{i\sigma_p - \omega\varepsilon_p - i\sigma_e - \omega\varepsilon_e}{i\sigma_p - \omega\varepsilon_p + 2i\sigma_e - 2\omega\varepsilon_e} * \frac{\frac{1}{\omega}}{\frac{1}{\omega}}$$

$$\frac{\left(i\frac{\sigma_p}{\omega} - \varepsilon_p\right) - \left(i\frac{\sigma_e}{\omega} - \varepsilon_e\right)}{\left(i\frac{\sigma_p}{\omega} - \varepsilon_p\right) + \left(2i\frac{\sigma_e}{\omega} - 2\varepsilon_e\right)}$$

$$\frac{-\left(\varepsilon_p - i\frac{\sigma_p}{\omega}\right) + \left(\varepsilon_e - i\frac{\sigma_e}{\omega}\right)}{-\left(\varepsilon_p - i\frac{\sigma_p}{\omega}\right) - 2\left(\varepsilon_e - i\frac{\sigma_e}{\omega}\right)}$$

$$\frac{-\varepsilon_p^* + \varepsilon_e^*}{-\varepsilon_p^* - 2\varepsilon_e^*} * \frac{-1}{-1}$$

$$\frac{\varepsilon_p^* - \varepsilon_e^*}{\varepsilon_p^* + 2\varepsilon_e^*}$$

Alternatively,

$$\frac{\varepsilon_p^* - \varepsilon_e^*}{\varepsilon_p^* + 2\varepsilon_e^*}$$

$$\frac{(\varepsilon_p - i\frac{\sigma_p}{\omega}) - \left(\varepsilon_e - i\frac{\sigma_e}{\omega}\right)}{\left(\varepsilon_p - i\frac{\sigma_p}{\omega}\right) + 2\left(\varepsilon_e - i\frac{\sigma_e}{\omega}\right)}$$

$$\frac{(\varepsilon_p - i\frac{\sigma_p}{\omega}) - \left(\varepsilon_e - i\frac{\sigma_e}{\omega}\right)}{\left(\varepsilon_p - i\frac{\sigma_p}{\omega}\right) + 2\left(\varepsilon_e - i\frac{\sigma_e}{\omega}\right)} * \frac{\omega}{\omega}$$

$$\frac{(\omega\varepsilon_p - i\,\sigma_p) - (\omega\varepsilon_e - i\sigma_e)}{(\omega\varepsilon_p - i\,\sigma_p) + 2(\omega\varepsilon_e - i\sigma_e)} * \frac{i}{i}$$

$$\frac{(i\omega\varepsilon_p - i^2\sigma_p) - (i\omega\varepsilon_e - i^2\sigma_e)}{(i\omega\varepsilon_p - i^2\,\sigma_p) + 2(i\omega\varepsilon_e - i^2\sigma_e)}$$

$$\frac{(i\omega\varepsilon_p + \sigma_p) - (i\omega\varepsilon_e + \sigma_e)}{(i\omega\varepsilon_p + \sigma_p) + 2(i\omega\varepsilon_e + \sigma_e)}$$

$$\frac{(\sigma_p + i\omega\varepsilon_p) - (\sigma_e + i\omega\varepsilon_e)}{(\sigma_p + i\omega\varepsilon_p) + 2(\sigma_e + i\omega\varepsilon_e)}$$

$$\frac{\sigma_p^* - \sigma_e^*}{\sigma_p^* + 2\sigma_e^*}$$

Analysis of the Transmembrane Potential and DEP Forces Acting on Cells in AC Electric Fields

Spherical and single shell model analysis adapted form Turku and Lucaciu [61]

Consider a dielectric sphere in a conductive media subject to a uniform alternating electric field

$$\vec{E} = Eexp(i\omega t) \qquad [4.21]$$

where ω is the angular frequency of the field. The complex permittivity of the media is defined as

$$\vec{\varepsilon} = \varepsilon - \frac{i\sigma}{\omega} \qquad [4.22]$$

Similarly, the complex conductivity of the media is defined as

$$\vec{\sigma} = \sigma + i\omega\varepsilon \qquad [4.23]$$

The electric field is related to the local charge density by

$$\nabla \cdot \vec{E} = \frac{\rho}{\varepsilon_0} \qquad [4.24]$$

where ρ is the charge density and ε_0 is the permittivity of free space. The electric field is related to the local voltage by

$$\vec{E} = -\nabla V \qquad [4.25]$$

From this we can calculate relate the potential in a system to the local charge density by

$$\nabla \cdot \nabla V = \frac{\rho}{\varepsilon_0} \qquad [4.26]$$

by noting that $\nabla \cdot \nabla = \nabla^2$ is the Laplace operator Δ we arrive at

$$\Delta V = \frac{\rho}{\varepsilon_0} \qquad [4.27]$$

In a charge free region of space this reduces to the Laplace equation

$$\Delta V = 0 \qquad [4.28]$$

In spherical coordinates

$$\Delta V = \frac{\partial^2 V}{\partial r^2} + \frac{1}{r^2}\frac{\partial^2 V}{\partial \theta^2} + \frac{1}{r^2 sin^2(\theta)}\frac{\partial^2 V}{\partial \phi^2} + \frac{2}{r}\frac{\partial V}{\partial r} + \frac{\cot(\theta)}{r^2}\frac{\partial V}{\partial \theta} \qquad [4.29]$$

However, due to the full spherical symmetry, θ and ϕ derivatives are zero

$$\Delta V = \frac{\partial^2 V}{\partial r^2} + \frac{2}{r}\frac{\partial V}{\partial r} \qquad [4.30]$$

The solutions for the Laplace equation for a sphere are well known

$$V_{external} = -\left(\vec{E}_r - \frac{\vec{P}R^3}{3\varepsilon_{ext} r^2}\right)\cos(\theta) \;\; for\, r \geq R \qquad [4.31]$$

$$V_{internal} = \; -\vec{E}_{internal} r\cos(\theta) \;\; for\, r < R \qquad [4.32]$$

where the internal electric field ($\vec{E}_{internal}$) and the polarization density ($\vec{P}$) are defined as

$$\vec{E}_{internal} = 3\left(\frac{\varepsilon_{external}}{\varepsilon_{internal} + 2\varepsilon_{external}}\right)\vec{E} \qquad [4.33]$$

$$\vec{P} = 3\,\varepsilon_{external}\left(\frac{\varepsilon_{internal} - \varepsilon_{external}}{\varepsilon_{internal} + 2\varepsilon_{external}}\right)\vec{E} \qquad [4.34]$$

Similarly, the solutions for the Laplace equation for a spherical shell are well known

$$V_e = \; -\left(\vec{E}\, r - \frac{\vec{P}R^3}{3\varepsilon_e r^2}\right)\cos(\theta) \quad for\, r \geq R \qquad [4.35]$$

$$V_m = -\left(\vec{E}_m r - \frac{\vec{P}_m R_i}{3\varepsilon_m r^2}\right)\cos(\theta) \quad for\ R_i < r < R \qquad [4.36]$$

$$V_i = -\vec{E}_i r cos(\theta) \quad for\ r \leq R_i \qquad [4.37]$$

where the subscripts e, m , and i refer to the external, membrane, and internal components, respectively. The electric field and polarization density coefficients for a spherical shell are

$$\vec{E}_m = \frac{\vec{\varepsilon}_e(\vec{\varepsilon}_i + 2\vec{\varepsilon}_m)}{\vec{\varepsilon}_m(\vec{\varepsilon}_i + 2\vec{\varepsilon}_i) + 2\alpha(\vec{\varepsilon}_e - \vec{\varepsilon}_m)(\vec{\varepsilon}_i - \vec{\varepsilon}_m)}\vec{E} \qquad [4.38]$$

$$\vec{E}_i = 3\frac{\vec{\varepsilon}_e + 2\vec{\varepsilon}_m}{\vec{\varepsilon}_m(\vec{\varepsilon}_i + 2\vec{\varepsilon}_e) + 2\alpha(\vec{\varepsilon}_e - \vec{\varepsilon}_m)(\vec{\varepsilon}_i - \vec{\varepsilon}_m)}\vec{E} \qquad [4.39]$$

$$\vec{P}_m = 3\varepsilon_m\frac{\vec{\varepsilon}_e(\vec{\varepsilon}_i - \vec{\varepsilon}_m)}{\vec{\varepsilon}_m(\vec{\varepsilon}_i + 2\vec{\varepsilon}_e) + 2\alpha(\vec{\varepsilon}_e - \vec{\varepsilon}_m)(\vec{\varepsilon}_i - \vec{\varepsilon}_m)}\vec{E} \qquad [4.40]$$

$$\vec{P} = 3\varepsilon_e\frac{\vec{\varepsilon}_m(\vec{\varepsilon}_i - \vec{\varepsilon}_e) - \alpha(\vec{\varepsilon}_e - \vec{\varepsilon}_m)(\vec{\varepsilon}_i - \vec{\varepsilon}_m)}{\vec{\varepsilon}_m(\vec{\varepsilon}_i + 2\vec{\varepsilon}_e) + 2\alpha(\vec{\varepsilon}_e - \vec{\varepsilon}_m)(\vec{\varepsilon}_i - \vec{\varepsilon}_m)}\vec{E} \qquad [4.41]$$

where

$$\alpha = \frac{1}{3}(1 - (1 - \delta)^3) \qquad [4.42]$$

$$\delta = d/R \qquad [4.43]$$

where d and R and the thickness of the membrane and the radius of the cell, respectively. The potential difference (transmembrane potential) can be defined as

$$\Delta\vec{v} = v_i(R_i) - v_e(R) \qquad [4.44]$$

$$v_i(R_i) = -\vec{E}_i R_i cos(\theta) \qquad [4.45]$$

$$\boldsymbol{v_i(R_i) = -3\frac{\vec{\varepsilon}_e + 2\vec{\varepsilon}_m}{\vec{\varepsilon}_m(\vec{\varepsilon}_i + 2\vec{\varepsilon}_e) + 2\alpha(\vec{\varepsilon}_e - \vec{\varepsilon}_m)(\vec{\varepsilon}_i - \vec{\varepsilon}_m)}\vec{E}(R - d)\cos(\theta)} \qquad [4.46]$$

$$v_e(R) = -\left(\vec{E}R - \frac{\vec{P}R^3}{3\varepsilon_e R^2}\right)\cos(\theta) \quad [4.47]$$

$$= -\left(\vec{E}\,R - \frac{\vec{P}R}{3\varepsilon_e}\right)\cos(\theta) \quad [4.48]$$

$$= -\left(\vec{E}R - \frac{R}{3\varepsilon_e}\,3\varepsilon_e \frac{\vec{\varepsilon}_m(\vec{\varepsilon}_i - \vec{\varepsilon}_e) - \alpha(\vec{\varepsilon}_e - \vec{\varepsilon}_m)(\vec{\varepsilon}_i - \vec{\varepsilon}_m)}{\vec{\varepsilon}_m(\vec{\varepsilon}_i + 2\vec{\varepsilon}_e) + 2\alpha(\vec{\varepsilon}_e - \vec{\varepsilon}_m)(\vec{\varepsilon}_i - \vec{\varepsilon}_m)}\vec{E}\right)\cos(\theta) \quad [4.49]$$

$$-\left(1 - \frac{\vec{\varepsilon}_m(\vec{\varepsilon}_i - \vec{\varepsilon}_e) - \alpha(\vec{\varepsilon}_e - \vec{\varepsilon}_m)(\vec{\varepsilon}_i - \vec{\varepsilon}_m)}{\vec{\varepsilon}_m(\vec{\varepsilon}_i + 2\vec{\varepsilon}_e) + 2\alpha(\vec{\varepsilon}_e - \vec{\varepsilon}_m)(\vec{\varepsilon}_i - \vec{\varepsilon}_m)}\vec{E}\right)\vec{E}R\cos(\theta) \quad [4.50]$$

$$\boldsymbol{v_e(R) = \frac{3\vec{\varepsilon}_m\vec{\varepsilon}_e + \alpha(\vec{\varepsilon}_e - \vec{\varepsilon}_m)(\vec{\varepsilon}_i - \vec{\varepsilon}_m)}{\vec{\varepsilon}_m(\vec{\varepsilon}_i + 2\vec{\varepsilon}_e) + 2\alpha(\vec{\varepsilon}_e - \vec{\varepsilon}_m)(\vec{\varepsilon}_i - \vec{\varepsilon}_m)}\,\vec{E}Rcos(\theta)} \quad [4.51]$$

This reduces to (cite)

$$\Delta\vec{\mathrm{v}} = 3\vec{\varepsilon}_e \frac{\delta\vec{\varepsilon}_m + \alpha(\vec{\varepsilon}_i - \vec{\varepsilon}_m)}{\vec{\varepsilon}_m(\vec{\varepsilon}_i + 2\vec{\varepsilon}_e) + 2\alpha(\vec{\varepsilon}_e - \vec{\varepsilon}_m)(\vec{\varepsilon}_i - \vec{\varepsilon}_m)}\,\vec{E}Rcos(\theta) \quad [4.52]$$

By assuming that

$$\varepsilon_{rm} = \frac{\varepsilon_m}{\varepsilon_e} \quad [4.53]$$

$$\sigma_{rm} = \frac{\sigma_m}{\sigma_i} \ll 1 \quad [4.54]$$

$$\delta \ll 1 \quad [4.55]$$

as is the case for mammalian cells and adopting a new format for the TMP of

$$\Delta\vec{v} = (Q + \frac{M_1}{1 + i\omega\tau_1} + \frac{M_2}{1 + i\omega\tau_2}) \quad [4.56]$$

we find the following coefficients

$$Q = 3\frac{\delta\varepsilon_r}{\varepsilon_{rm}(\varepsilon_r + 2)} \quad [4.57]$$

$$M_1 = \frac{3}{2}\left(1 + \frac{\sigma_{rm(\sigma_r+2)}}{2\delta\sigma_r}\right)^{-1} \qquad [4.58]$$

$$M_2 = 6\frac{\delta(\varepsilon_r - \sigma_r)}{\varepsilon_{rm}(\varepsilon_r + 2)(\sigma_r + 2)^2} \qquad [4.59]$$

Expanding and considering only the real components of the TMP we get

[4.60]

Where in general

$$\tau = \frac{\varepsilon_2 + 2\varepsilon_1}{\sigma_2 + 2\sigma_1} \qquad [4.61]$$

Recognizing that Q and M_2 are much smaller than M_1 this can be reduced to

$$\Delta v = \frac{M_1 ERcos(\theta)}{(1 + \omega^2\tau_1^2)^{\frac{1}{2}}}\cos(\omega t - \tan^{-1}(\omega\tau_1)) \qquad [4.62]$$

This generalized equation for TMP is often simplified (Zimmerman 1982) and presented as

$$\Delta v = \frac{3}{2}ER(1 + \omega^2\tau_1^2)^{-\frac{1}{2}}cos(\theta) \qquad [4.63]$$

For a square pulse with length T, the maximum TMP can be approximated as

$$\Delta v = \frac{3}{2}ERcos(\theta)\left[1 - \exp\left(-\frac{T}{\tau_1}\right)\right] \qquad [4.64]$$

Correlation of terms to DEP

The dielectrophoretic force acting on a neutral sphere in a non-uniform electric field is

$$\vec{F}_{DEP} = \left(\vec{P}_{eff}\nabla\right)E \qquad [4.65]$$

where

$$\vec{P}_{eff} = \varepsilon_e\vec{\chi}\vec{\mathrm{E}} \qquad [4.66]$$

where $\vec{\chi}$ is the dimensionless susceptibility. The DEP force for a spherical (non-shell) particle then becomes [62]

$$\vec{F}_{DEP} = \frac{2}{3}\pi r^3 \varepsilon_e [Re\ \vec{\chi}\cos(\omega t) - Im\vec{\chi}\sin(\omega t)]\cos(\omega t)\,\nabla\vec{E}^2 \quad [4.67]$$

$$\vec{\chi} = K + \frac{N}{1 + i\omega\tau} \quad [4.68]$$

$$K = \frac{3(\varepsilon_r - 1)}{\varepsilon_r + 2} \quad [4.69]$$

$$N = -\frac{9(\varepsilon_r - \sigma_r)}{(\varepsilon_r + 2)(\sigma_r + 2)} \quad [4.70]$$

In the case of a spherical (non-shell) model

$$\tau = \frac{\varepsilon_i + 2\varepsilon_e}{\sigma_i + 2\sigma_e} \quad [4.71]$$

The real and imaginary parts of the susceptibility become

$$Re\ \vec{\chi} = K + \frac{N}{1 + \omega^2\tau^2} \quad [4.72]$$

$$Im\ \vec{\chi} = -\frac{N\omega\tau}{1 + \omega^2\tau^2} \quad [4.73]$$

The time average DEP force then becomes

$$\langle\vec{F}_{DEP}\rangle = \frac{1}{3}\pi r^3 Re\vec{\chi}\nabla\vec{E}^2 \quad [4.74]$$

This time averaged calculation based on a spherical model poorly predicts experimental behavior of biological cells. It is therefore useful to look the spherical shell model. Notice that the electric field and polarization density (E and P) in equations **18 -21** all share a common denominator which can be forced into the form

$$\Gamma\left(1 - i\frac{\Omega_1}{\omega}\right)\left(1 - i\frac{\Omega_2}{\omega}\right) \quad [4.75]$$

Taking only first order terms of δ we get

$$\Gamma = \varepsilon_m(\varepsilon_i + 2\varepsilon_e) + 2\delta(\varepsilon_e - \varepsilon_m)(\varepsilon_i - \varepsilon_m) \quad [4.76]$$

$$\Omega_1 = \frac{\sigma_m}{\varepsilon_m} + 2\delta \frac{[(\sigma_i - \sigma_m)\varepsilon_m - (\varepsilon_i - \varepsilon_m)\sigma_m]\,[(\sigma_e - \sigma_m)\varepsilon_m - (\varepsilon_e - \varepsilon_m)\sigma_m]}{\varepsilon_m^2[(\sigma_i + 2\sigma_e)\varepsilon_m - (\varepsilon_i + 2\varepsilon_e)\sigma_m]} \quad [4.77]$$

$$\Omega_2 = \frac{\sigma_i + 2\sigma_e}{\varepsilon_i + 2\varepsilon_e} - 2\delta \frac{[(\sigma_i - \sigma_m)(\varepsilon_i + 2\varepsilon_e) - (\varepsilon_i - \varepsilon_m)(\sigma_i + \sigma_e)][(\sigma_e - \sigma_m)(\varepsilon_i + 2\varepsilon_e) - (\varepsilon_e - \varepsilon_m)(\sigma_i + 2\sigma_e)]}{(\varepsilon_i - 2\varepsilon_e)^2[(\sigma_i + 2\sigma_E)\varepsilon_m - (\varepsilon_i + 2\varepsilon_e)\sigma_m]} \quad [4.78]$$

Expanding again in terms of $\sigma_{rm} = \frac{\sigma_m}{\sigma_e}$ and taking only first order terms

$$\Omega_1 = \frac{\sigma_m}{\varepsilon_m} + \frac{2\delta\sigma_i}{\varepsilon_m(\sigma_r + 2)} \quad [4.79]$$

$$\Omega_2 = \frac{\sigma_i + 2\sigma_e}{\varepsilon_i + 2\varepsilon_e}\left[1 + \frac{2\delta}{\varepsilon_r}\left(\frac{2(\varepsilon_r - \sigma_r)^2}{\varepsilon_{rm}(\sigma_r + 2)} + \frac{\varepsilon_r - \sigma_r}{\sigma_r + 2} - \varepsilon_{rm}\right)\right] \quad [4.80]$$

Using these two characteristic frequencies and expanding the effective polarization and susceptibility in terms σ_{rm} and δ, we can calculate the DEP force

$$\vec{\chi} = \left(K + \frac{N_1}{1 + i\omega\tau_1} + \frac{N_2}{1 + i\omega\tau_2}\right) \quad [4.81]$$

where the time constants $\tau_1 = 1/\Omega_1$ and $\tau_2 = 1/\Omega_2$.

$$K = 3\frac{\varepsilon_r - 1}{\varepsilon_r + 2} \quad [4.82]$$

$$N_1 = -\frac{9}{2}\frac{\sigma_r}{\sigma_r + 2}\left(1 + \frac{\sigma_{rm}(\sigma_r + 2)}{2\delta\sigma_r}\right)^{-1} \quad [4.83]$$

$$N_2 = -9\frac{\varepsilon_r - \sigma_r}{(\varepsilon_r + 2)(\sigma_r + 2)} \quad [4.84]$$

The DEP force can then be rewritten as

$$\vec{F}_{DEP} = \frac{1}{4}V\varepsilon_e\left(k + \frac{N_1}{1 + i\omega\tau_1} + \frac{N_2}{1 + i\omega\tau_2}\right)\nabla\vec{E}^2 \quad [4.85]$$

Notice that the first and third terms in the parenthesis are the same terms derived in the spherical model. The middle term, describes the relative contribution of the cell membrane. The term $\tau_1$describes the time constant associated with the cell membrane and is an indicator of the first

crossover frequency. This term shows up again in the exponential term for the transmembrane potential providing a correlation between negative DEP and electroporation.

Important Equations	
Single Spherical Shell Model	
$\vec{F}_{DEP} = \frac{1}{4} V \varepsilon_e \left(k + \frac{\boldsymbol{N_1}}{\boldsymbol{1 + i\omega\tau_1}} + \frac{N_2}{1 + i\omega\tau_2} \right) \nabla \vec{E}^2$	DEP force acting on a spherical shell V = volume
$\Delta v = \frac{3}{2} ER \left(1 + \boldsymbol{\omega^2 \tau_1^2}\right)^{-\frac{1}{2}} cos(\theta)$	Transmembrane potential of a cell in an AC field
$\Delta v = \frac{3}{2} ERcos(\theta) \left[1 - \mathbf{exp}\left(-\frac{\boldsymbol{T}}{\boldsymbol{\tau_1}} \right) \right]$	Transmembrane potential of a cell in a pulsed field T = pulse width
$\Omega_1 = \frac{1}{\tau_1} = \frac{\sigma_m}{\varepsilon_m} + 2\delta \frac{[(\sigma_i - \sigma_m)\varepsilon_m - (\varepsilon_i - \varepsilon_m)\sigma_m]\,[(\sigma_e - \sigma_m)\varepsilon_m - (\varepsilon_e - \varepsilon_m)\sigma_m]}{\varepsilon_m^2 [(\sigma_i + 2\sigma_e)\varepsilon_m - (\varepsilon_i + 2\varepsilon_e)\sigma_m]}$	Inverse of the characteristic time associated with the cell membrane
Generalized Dielectrophoresis Equation	
$\vec{F}_{DEP} = 2\,\pi \epsilon_m r^3 Re \left[\frac{\epsilon_c^* - \epsilon_m^*}{\epsilon_c^* + 2\epsilon_m^*} \right] \nabla \left| \vec{\mathrm{E}} \cdot \vec{\mathrm{E}} \right|$	DEP force of a spherical particle suspended in conductive media
Generalized Transmembrane Potential Equation	
$\Delta v = \frac{3}{2} ERcos(\theta)$	Maximum transmembrane potential of a cell in an electric field - Period or Pulse Width much larger than membrane charging time
Joule Heating	
$Q = \sigma \lvert \nabla v \rvert^2$	Heating due to the application of an electric field across a conductive media

Chapter 5: Electronics

Contactless Dielectrophoresis Electronics

Contactless dielectrophoresis devices require high frequency, high voltage signals. This section outlines work made in fabricating electronics capable of generating a 200 V_{RMS} or greater signal at frequencies between 10 and 100 kHz. Two iterations of a basic design were completed and a third robust design has been used successfully for experimentation with continuous usage times greater than 8 hours. The designs follow a simple scheme which first amplifies a small signal using an operational amplifier or similar topology as a voltage and current amplification stage. The signal is then fed through a transformer which steps up the voltage to an appropriate level. This simple topology becomes increasingly expensive as the target voltages and frequencies are increased. Therefore, an additional goal of this project was to create a basic system which minimizes cost while meeting the other performance goals.

Version 1

The first iteration of this design used a high voltage precision operational amplifier (OPA445) capable of operating on +/- 45 V_{DC} rails. The output current rating on the OPA445 is too low (15 mA) to drive an output transformer so four unity gain current buffers (BUF634) were placed in the output path to provide extra current sourcing capability. Each BUF634 has a maximum output current of 250 mA. The amplified signal was then passed through a Coilcraft FL2015 cold cathode fluorescent lamp (CCFL) transformer with a 1:100 turns ratio. This transformer has a maximum voltage output rating of 1600V_{RMS}.

This system performed well with a reasonably flat output near 200 V_{RMS} between 30 and 100 kHz. These electronics failed during stress testing and the source of the failure could not be determined. One possible source of the failure could have been related to the maximum secondary output current of the FL2015-9L transformer (0.011 A) which would require a total of 1.1 A from the input. This would exceed the output current capabilities of the amplification stage. However, it is unlikely that this current limit was reached during stress testing. This topology is worth rebuilding if experimental target frequencies fall within this range. The total cost of components for this system was below $10, with all of the components except the input and feedback resistors provided through free sample programs at Texas Instruments and Coilcraft.

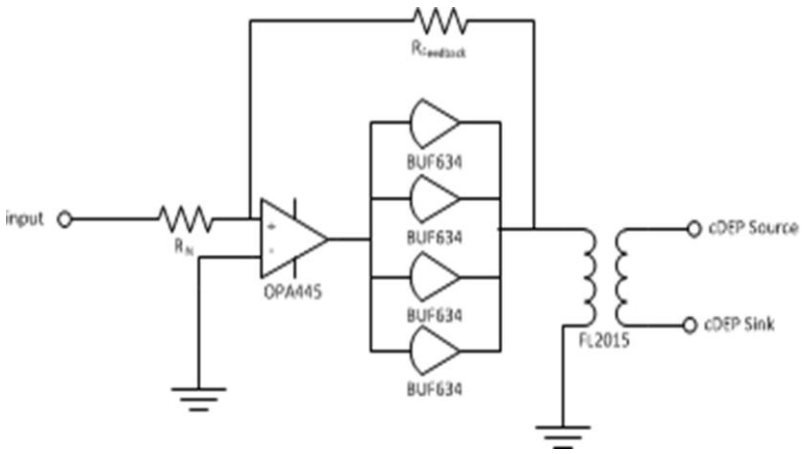

Figure 5-1: Schematic of the first generation cDEP electronics.

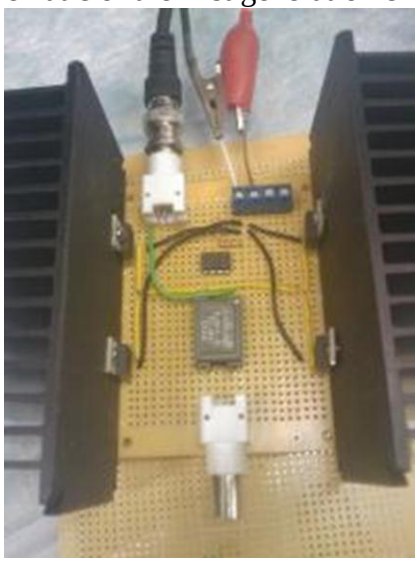

Figure 5-2: Version 1 electronics: S2P109 – OPA445 amplifier with 4 BUF634 output buffers boosted through a 1:100 FL2015-9L transformer.

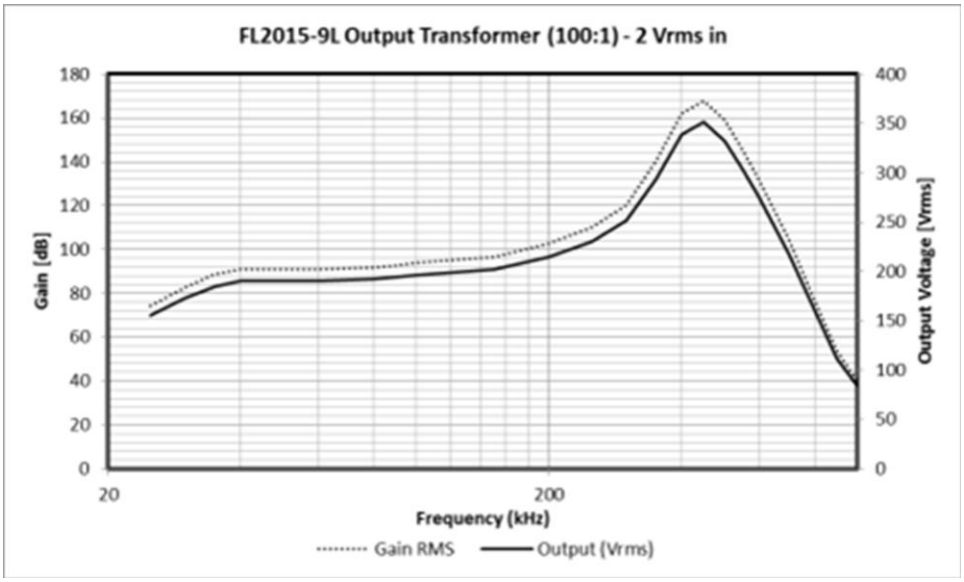

Figure 5-3: Version 1 electronics output through an FL2015-9L output transformer

An alternate amplification stage using the LT1210 in a bridged 9 watt wide band driver configuration was attempted before abandoning the FL2015-9L as the output transformer stage.

Version 2

The second iteration of this design aimed to boost the voltage output of the amplification stage such that a lower turns ratio, higher output current transformer could be used. A bridged LM3886 high power audio amplifier topology was selected for its simplicity and the availability of a dual amplifier (LM4780) package.

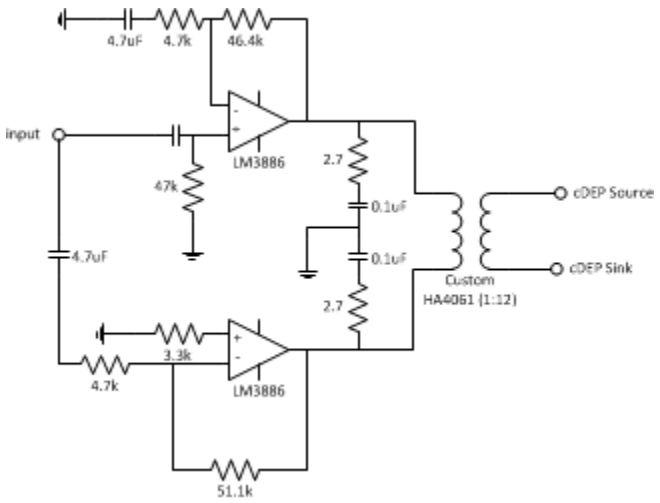

Figure 5-4: LM3886 amplification topology used in the version 2 cDEP electronics.

Two HA4061 (1:3) transformers were modified such that their primary sides were connected in parallel and secondary sides connected in series to yield a 1:12 turns ratio. These transformers are rated at 5 amps max when both primary and secondary coils are connected in parallel. This rating should be reduced to at most 2.5 amps due to the series wiring of the secondary coils.

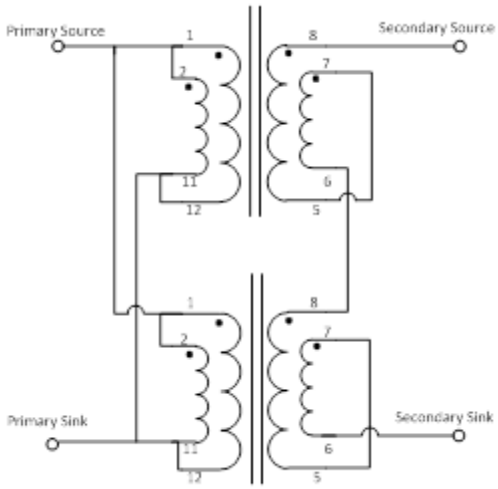

Figure 5-5: Modified two HA4061-AL transformer yeilds a 1:12 ratio capable of delivering up to 200 Vrms

The output of the modified transformer had a near-linear region between 10 and 100 kHz at $100V_{p\text{-}p}$ output. At 600 $V_{p\text{-}p}$ (approximately 200 V_{RMS}), this region was limited to 30 – 100 kHz before leakages in the system caused instability or distortion in the output waveform.

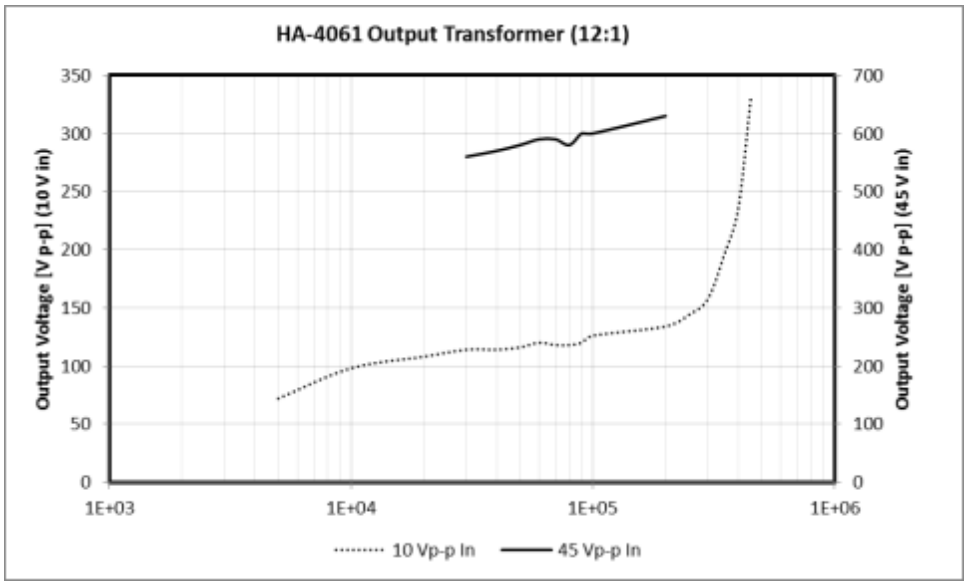

Figure 5-6: Version 2 Electronics output

The amplification and transformation stages were integrated with an unregulated DC power supply, a +9 and +/- 12 V regulated power stage, and a monolithic function generator to create a standalone cDEP electronics system. The function generation stage was later removed to protect the electronics from excessive knob turning by unsupervised users.

These electronics were validated by trapping 1 and 4 micron beads in a cDEP device. The beads were suspended in DI water and driven through the device with a syringe pump at a flow rate of 0.02 mL/hour. The electronics were turned on and the frequency was set to 40 kHz. The voltage was then increased until bead trapping was observed. At 140 V_{RMS}, both 1 and 4 micron beads began to trap around the insulating pillars. After approximately one minute, the voltage was turned off and the beads were released downstream. These results show that cDEP electronics can be fabricated from off the shelf, low cost components. If a single target frequency range is known, for example the crossover frequency of a target cell type, then component selection becomes less challenging.

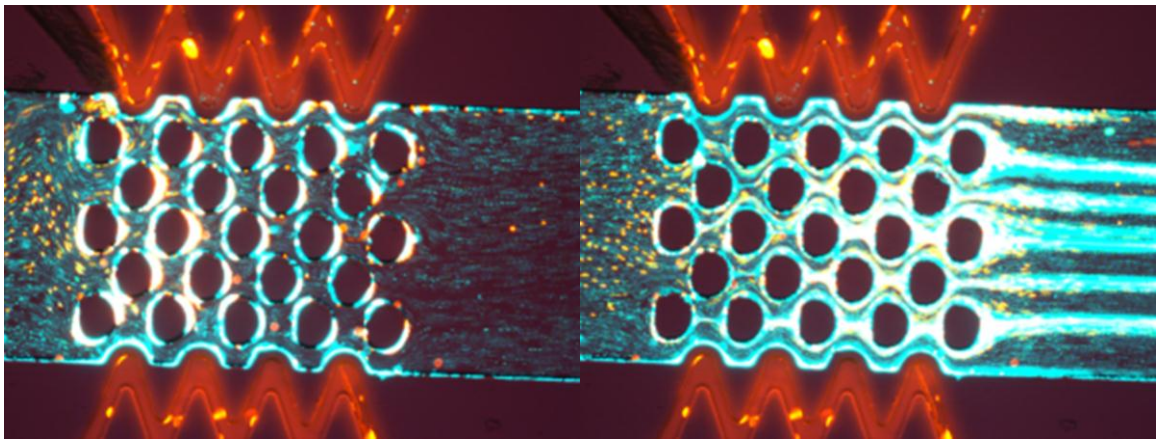

Figure 5-7: [Left] Positive DEP acting on 1 and 4 micron beads when 140 V_{RMS} at 40 kHz is applied. [Right] Release of beads after the electric field is turned off.

Difficulty in fabricating electronics appropriate for experimentation comes from the need for a transformer with a flat frequency response over a large frequency range. For example, in many of the experiments presented in subsequent chapters, a linear response is needed between 1 and 100 kHz or 100 kHz and 800 kHz. Typical off the shelf components are designed to operate at a single frequency or over a much narrower band. In the wide band cases, a custom wound transformer from Amp-Line was used. The amplification stage shown in Figure 5-4 had an effective band width of approximately 120 kHz. For wide band, low frequency experiments this was used to drive a custom transformer with a linear operating region between 10 and 100 kHz.

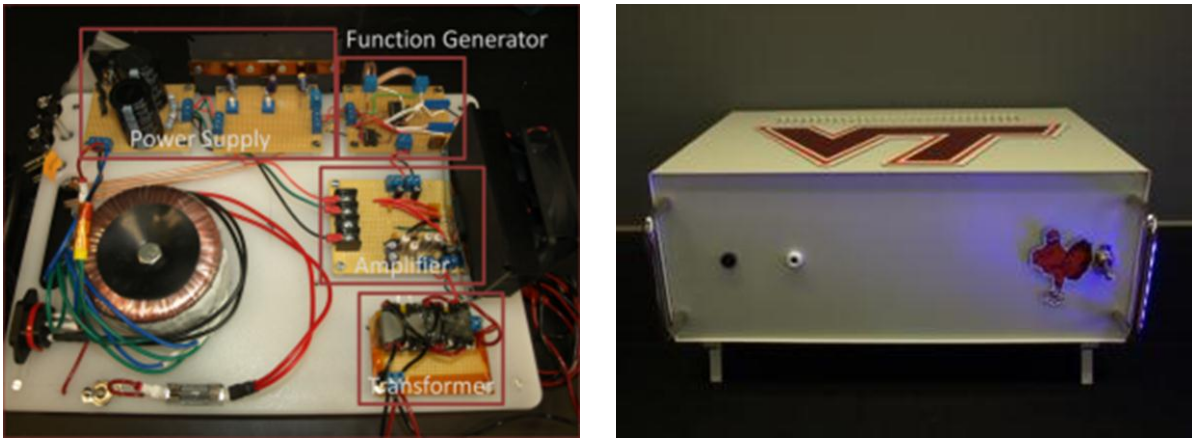

Figure 5-8: Internal components (left) and completed (right) cDEP electronics system.

Nano-second Electroporation Electronics

The generation of 1000 volt peak, high frequency bipolar square waves with pulse durations shorter than 5 microseconds is a technical challenge. These parameters far exceed the capabilities of monolithic amplifiers and push the limits of silicon components. There are a few commercial solutions which are capable of reaching the voltage and switching speed performance goals, however the current demands of *in-vivo* IRE treatments can reach 20 Amps or higher. Currently, there is not a commercial solution which can reach this level of performance and as such, a preliminary was developed to test the HFIRE hypothesis.

The HV1000P and HV1000N are commercially available **monopolar** pulse generators which can produce 950V peak pulses in positive or negative polarities, respectively. These pulse generators can produce pulses with widths between 55 nanoseconds and 10 microseconds and deliver a maximum current of 17 amps without additional thermal management.

The HV1000s were modified by removing the output shunting diodes. These protection diodes were intended to dump any opposite polarity voltages, presented at the output, directly to ground. The outputs of the pulsers were then terminated into a single 50Ω load. This load was necessary to protect the pulsers from firing into an open circuit and for the generation of well-formed square waves. At 450 volts, this load sinks 9 amps. The effective maximum power deliverable to our tissue is 3600 watts (450 volts, 8 amps).

A high voltage power supply was fabricated to produce a variable voltage with maximum rails at +/- 450 V. The output voltage from a variable transformer was stepped up using a center tapped toroidal transformer. This voltage was then passed through a full bridge rectifier and filtered through a capacitor bank. The capacitor bank also served as a charge storage reservoir and the required values were calculated as follows.

The HV1000s can source up to 17 amps. A safe approximation of the charge required for a single pulse can be assumed the same as a monopolar 100 μs IRE 20 amp pulse.

$$Q = \int_0^{100\ \mu s} 20A\ dt = 0.002\ C$$

The capacitor bank will have to be capable of storing 0.002 Coulombs of charge. The charge stored in a capacitor is dependent on the voltage to which it is charged. Assuming minimum and maximum treatment voltages of 50 and 850 V:

$$C = \frac{Q}{V}$$

$$C = \frac{0.002C}{50V} = 40\mu F$$

$$C = \frac{0.002C}{850V} = 2.35\mu F$$

A 40 μF capacitor bank rated at 850V would be sufficient to deliver high voltage monopolar pulses. The charging time of this capacitor bank, even with a modest high voltage supply (Labsmith @ 4.8mA) is on the order of 0.5 seconds. The Antek toroidal power transformer used in this power supply is capable 4A yielding a minimum charging time of

$$\int_0^t 4\, dt = 4t = 0.002C = 0.0005\, s = 500\mu s$$

The power supply in Figure 5-9 is capable of delivering IRE equivalent pulses at a repetition rate 1 pulse ever 500μs.

Negative thermal coefficient thermistors were used to prevent over currents when the power supply is switched on. Bleeder resistors (approximately 100kΩ) were placed between the power rails and ground to safely discharge the capacitor bank when the supply was turned off.

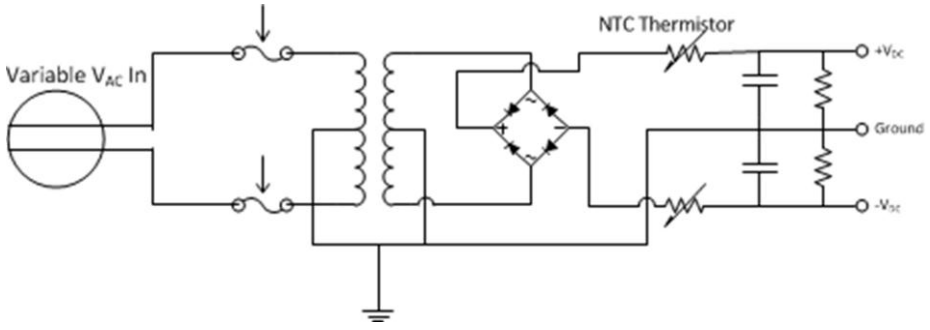

Figure 5-9: Generalized schematic used to build the +/- 450 V HFIRE power supply

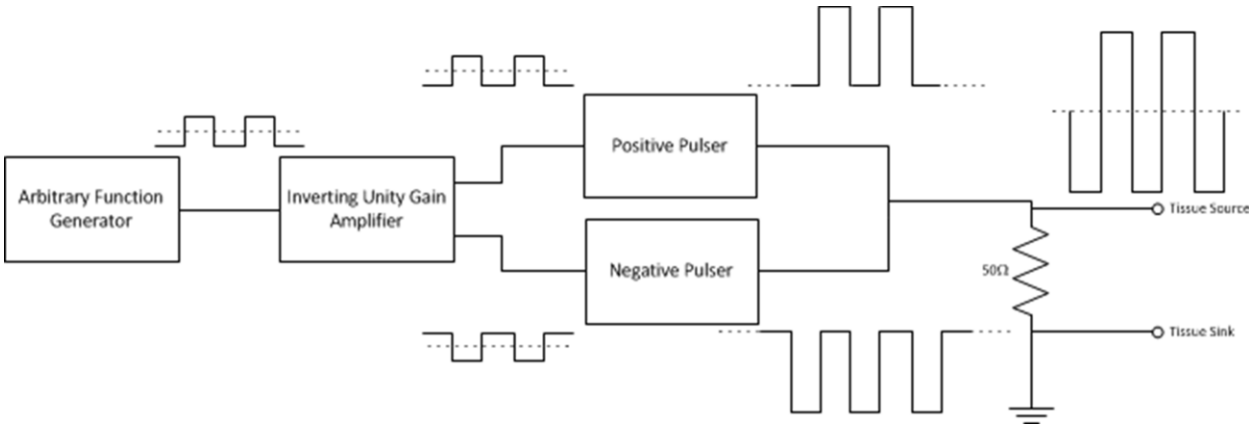

Figure 5-10: Block diagram of HFIRE electronics used for experimentation.

Both the positive and negative pulse generators are triggered with a *positive* 5V input signal. An arbitrary wave form generator was used to create the desired pulse train. The signal was then split and passed through a unity gain inverting amplifier to produce the necessary waveform to trigger the negative pulse generator. The high voltage outputs of the two generators were then combined and delivered to output jacks in parallel with a 50Ω load.

Figure 5-11: Experimental HFIRE electronics setup

Figure 5-12: 200V peak (400V peak to peak) output waveform of the HFIRE electronics.

Chapter 6: Microfluidics Fabrication Methods

A number of fabrication methods have been employed to create contactless dielectrophoresis microfluidic devices. In most devices, cleanroom facilities were utilized to create silicon master stamps which were then used to replicate devices using soft lithography. Additionally, we have developed a process for creating microfluidic devices and metal electrodes on glass without the need for a clean room facility. This section will outline these two methods.

Cleanroom Fabrication

The cleanroom fabrication process is outlined in Figure 6-1. A silicon master stamp was fabricated on a <100> silicon substrate. AZ 9260 (AZ Electronic Materials) photoresist was spun onto a clean silicon wafer and soft baked at 114C for 45 seconds. The wafer was then exposed to UV light for 45 seconds with an intensity of 12 W/m through a chrome plated glass mask. The exposed photoresist was then removed using Potassium based buffered developer AZ400K followed by another hard baking at 115°C for 45 seconds Deep Reactive Ion Etching (DRIE) was used to etch the silicon master stamp to a depth of 50 μm. Silicon oxide was grown on the silicon master using thermal oxidation for four hours at 1000^{o}C and removed with HF solvent to reduce surface scalloping.

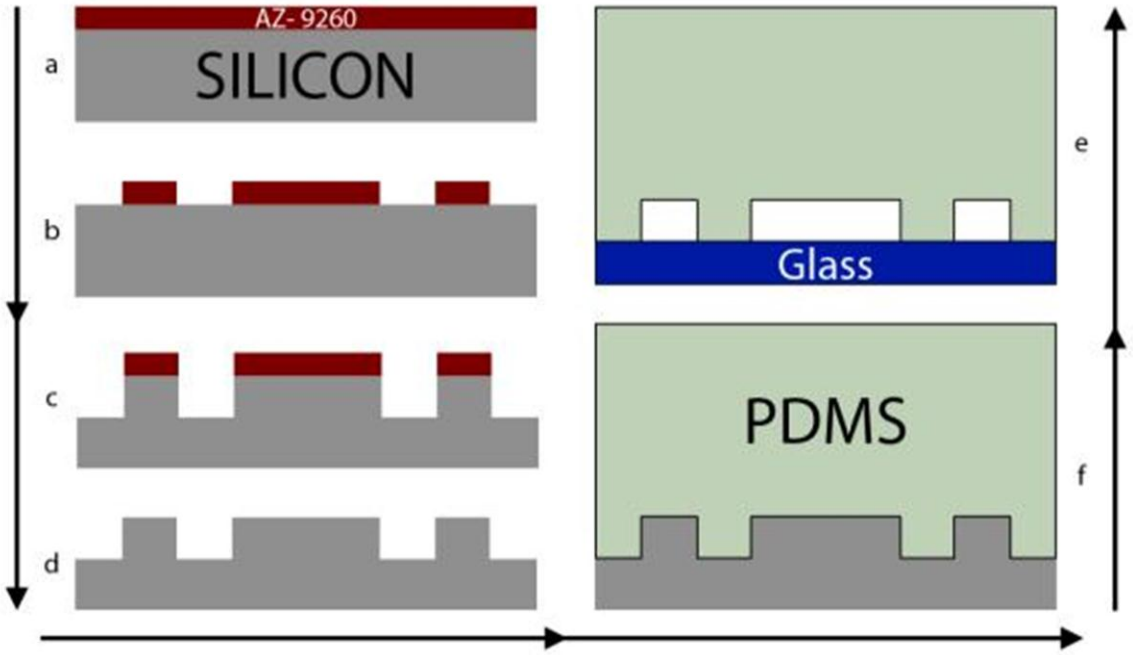

Figure 6-1: Cleanroom fabrication process. (a) Photoresist is spun onto a clean silicon wafer. The photoresist is then exposed to ultraviolet light through a transparency mask and (b) removed using lithography techniques. (c) Deep reactive ion etching is used to etch the silicon wafer to the desired depth (typically 50 microns) (d) then the photoresist is removed. After smoothing the silicon surface (f) PDMS is cured on the wafer. (e) Finally, the PDMS device is bonded to glass using air plasma.

Liquid phase polydimethylsiloxane (PDMS) was made by mixing the PDMS monomers and the curing agent in a 10:1 ratio (Sylgrad 184, Dow Corning, USA). The degassed PDMS liquid was poured onto the silicon master, cured for 45 min at 100°C, and then removed from the mold. Fluidic connections to the channels were punched using hole punchers (Harris Uni-Core, Ted Pella Inc., Redding, CA); 1.5mm for the side channels and 2.0mm for the main channel inlet and outlet. Glass microscope slides (75mm x 75mm x 1.2mm, Alexis Scientific) were cleaned with soap and water, rinsed with distilled water, ethanol, isopropyl alcohol, and then dried with compressed air. The PDMS mold was bonded to clean glass after treating with air plasma for 2 minutes.

Non-Cleanroom Microfabrication

Glass microscope slides were polished with a cerium oxide polishing compound (Angel Gilding Stained Glass Ltd, Oak Park, IL), rinsed with deionized water, and dried using compressed air. The slides were then sensitized using 3 mL of a tinning solution (Angel Gilding Stained Glass Ltd, Oak Park, IL) for 30 seconds. After this time had passed the solution was poured off the

slide and it was rinsed with deionized water.

A commercially available mirroring kit was used to deposit pure silver onto the microscope slides. 3mL each of silver reducer, silver activator, and silver solution (Angel Gilding Stained Glass Ltd, Oak Park, IL) were combined and immediately poured onto the sensitized slide. Silver was allowed to precipitate onto the slide for 5 minutes. This process was repeated, without tinning, one additional time resulting in a layer of silver approximately 100nm thick. It should be noted that a similar commercially available kit exists for the deposition of gold on glass.

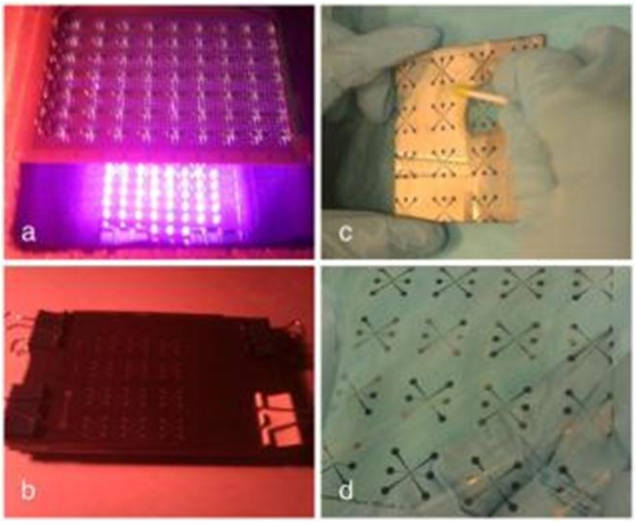

Figure 6-2: (a) Ultraviolet LED array exposing a laminated slide through a photo mask which is held in place by a (b) custom exposure frame. (c) Photoresist features cover silver which will be left after processing to create (d) silver electrodes on glass.

A negative thin film photoresist (#146DFR-4, MG Chemicals, Surrey, British Colombia, Canada) was cut into an 80 x 100 mm rectangle and the inner protective film was removed. A silvered slide was sprayed lightly with deionized water and the photoresist was laid on top of the slide such that approximately 20 mm of film extends over one edge. Any existing bubbles were pushed to the edges resulting in a smooth surface. The film extending over one edge was then bent around to the bottom of the slide to form a leading edge for lamination. The slides were then passed through an office laminator (#4, HeatSeal H212, General Binding Corporation, Lincolnshire, IL) twice at low heat, cleaning the laminator between each pass.

A 7x9 array of low cost 400 nm 20 mW light emitting diodes (LEDs) was fabricated to produce the ultraviolet light necessary for exposure. An exposure case was fabricated by

lining the top, bottom and sides of a styrofoam container with black felt in order to reduce internal reflections. A 4 by 6 inch piece of sheet glass from a photo frame and a piece of 4 by 6 inch piece of fiberboard covered by black felt formed the front and back of the exposure frame. A laminated side was placed with photoresist up onto the back plate of the exposure frame. A photomask printed at 20k DPI on a transparent film (Output City, Cad / Art Services Inc, Bandon, OR) was placed ink side down onto the photoresist. The top plate was then placed on top and the entire assembly was held in place using large binder clips.

The exposure frame was placed inside the exposure case and the LED array placed 12 cm above the exposure frame. Slides then were exposed to UV light for 45 seconds. After exposure, the outer protective film was removed from the photoresist. The slides were then placed in a 200 mL bath containing a 10:1 DI water to negative photo developer (#4170-500ML, MG Chemicals, Surrey, British Colombia, Canada) solution for approximately 4 minutes. A foam brush was used to gently brush the surface of the slide in order to expedite the development process. Cotton swabs soaked in developer were used gently wipe areas with small features to ensure complete development. The slides were placed in a beaker containing DI water to halt the development process and gently dried using pressurized air.

Electrode structures on the microscope slides were fabricated by removing all silver not covered by the patterned photoresist. A two part silver remover was included in the mirroring kit used to deposit the silver. 1 mL of each part of the silver remover was combined in a 5 mL beaker. A cotton swab was used to apply the silver remover to the glass slide until only the silver covered by photoresist remained on the slide. The photoresist was then removed by placing the slide in a bath of acetone.

Microfluidic channels were created through polymer replication on stamps which had not undergone the final acetone wash, leaving the patterned photoresist intact. Liquid phase polydimethylsiloxane (PDMS) in a 10:1 ratio of monomers to curing agent (Sylgrad 184, Dow Corning, USA) was degassed under vacuum prior to being poured onto the photoresist master and cured for 1 hour at 100°C. After removing the cured PDMS from the stamp, fluidic connections to the channels were punched in the devices using 1.5 mm core borers

(Harris Uni-Core, Ted Pella Inc., Redding, CA). Glass microscope slides (75 mm x 75 mm x 1.2 mm, Alexis Scientific) were cleaned with soap and water, rinsed with distilled water, ethanol, isopropyl alcohol, and then dried with compressed air. The PDMS replica was bonded to the glass slides after treating with air plasma for 2 minutes in a PDC-001 plasma cleaner (Harrick Plasma, Ithaca, New York).

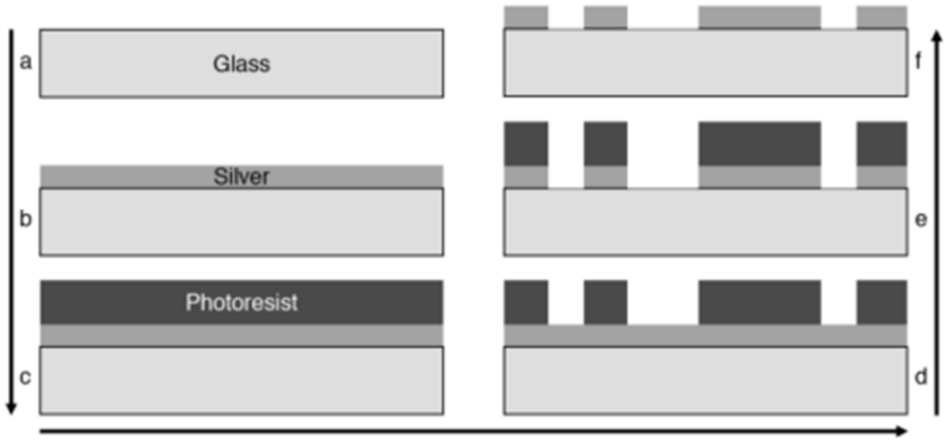

Figure 6-3: Schematic representation of the fabrication process. (a) A glass slide is cleaned and polished. (b) Silver is deposited onto the glass using a commercial mirroring kit. (c) Thin film photoresist is laminated on top of the silver. (d) The photoresist is exposed and developed. (e) The exposed silver is chemically removed and (f) the photoresist is dissolved.

Electrical connections to the embedded electrodes were formed by securing high voltage electrical wires to contact pads using high purity silver paint (Structure Probe Inc., West Chester, PA). This was allowed to dry for one hour creating a solid connection. A drop of 5 minute epoxy (Devcon Inc., Danvers, MA), used to secure the electrical connections, was placed on top of each electrode pad and allowed to cure for 24 hours.

Polystyrene microspheres were used to prove the functionality of these devices through the demonstration of dielectrophoresis. 1 μL of 1 μm and 4 μL of 4 μm beads (FluoSpheres sulfate, Invitrogen, Eugene, Oregon) were suspended in 5 mL of DI water with a final conductivity of 6.2 μS/cm. 40 uL of this sample solution was pipetted into the devices. A syringe pump was used to drive samples at a rate of 0.02 mL/hour (PHD Ultra, Harvard Apparatus, Holliston, Massachusetts).

An AC electric field was created by amplifying (AL-50HF-A, Amp-Line Corp., Oakland Gardens, NY) the output signal of a function generator (GFG-3015, GW Instek, Taipei, Taiwan). A step up transformer was used when voltages greater than 30 V_{RMS} were required. Voltage and frequency were measured using an oscilloscope (TDS-1002B, Tektronics Inc. Beaverton, OR) connected to the output stage of the amplifier.

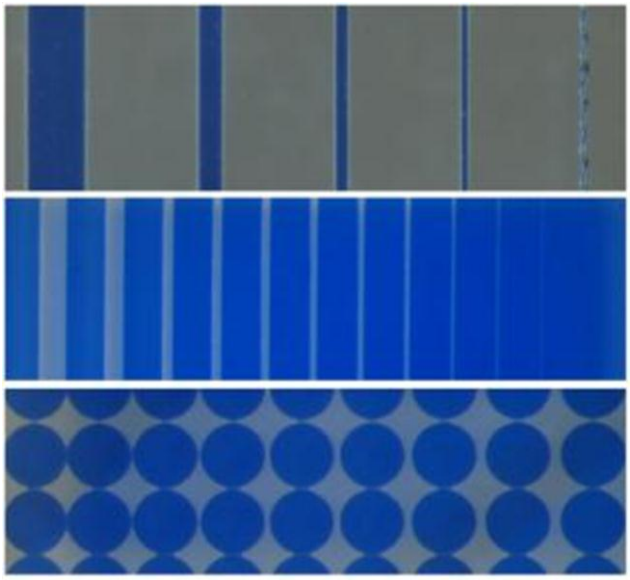

Figure 6-4: [Top] 500, 250, 100, 50, and 25µm (left to right) thick structures. A 10µm test structure existed on the mask, but did not develop. [Center] 500µm structures separated by 300, 200, 100, 90, 80, 70, 60, 50, 40, 30, 20, and 10µm left to right. [Bottom] 250µm diameter pillars separated by 10, 20, 30, 40, 50, 60, 70, and 80µm from left to right.

In the absence of the silver substrate, test structures 50 µm wide and greater could be reliably fabricated using this process. Structures 25 µm thick formed successfully after exposure, however, they did not have enough surface area to adhere completely onto plain glass slides during the development process. The resulting photoresist structures did not form perfectly straight lines as seen in Figure 6-4 [Top]. 10 µm test structures on the mask did not develop. 500 µm wide test structures consistently developed when separated by 40 µm or more as seen in Figure 6-4 [Center].

Some photoresist could not be removed between features separated by distances of 20 and 30 µm resulting in poor PDMS replication. A 10 µm gap could not be developed between structures. Similarly, 250 µm pillars were easily developed and replicated when separated by 40 µm or more as seen in Figure 6-4 [Bottom].

A single photoresist layer produced channels with a minimum width of 50 µm and a nominal depth of 50 µm. 100 µm deep channels were produced by removing the outer protective sheet after lamination, laminating another sheet on top of the previous layer, and exposing for 105 seconds.

The silver substrate improved photoresist adhesion. As a result, photoresist features with widths down to 25 µm could be fabricated. The photoresist effectively protected features from silver the removal process resulting in the successful formation of electrodes with line widths down to 25 µm.

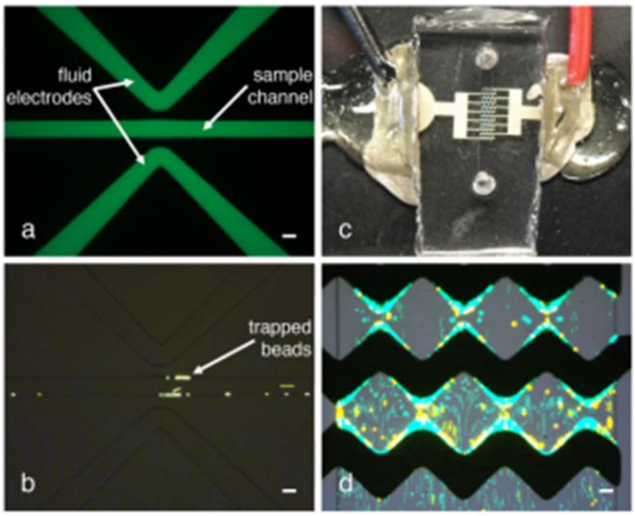

Figure 6-5: (a) Examples of cDEP devices with 50 µm minimum feature sizes which can be produced using this process. (b) 4 µm beads driven by pressure are trapped in the region between the two electrodes when a 150 V_{RMS} 600 kHz signal is applied. (c) Silver electrodes deposited on glass encapsulated in a 1mm wide microfluidic channel. Conductive silver paint is used to ensure an electrical connection between the wires and the deposited silver. Epoxy holds the wires permanently in place. (d) 1 and 4 µm beads driven by pressure are entrapped by dielectrophoretic forces when a 7.3 V_{RMS} 60 Hz signal is applied to the electrodes. The scale bar is 50 µm.

The fluid electrode channels in the cDEP device (Figure 6-5a) are filled with a highly conductive fluid, typically phosphate buffered saline. The 50 µm insulating membrane which isolates the fluid electrode channels from the sample channel acts as a large resistor in parallel with a capacitor. When a high frequency signal is applied across the fluid electrode channels, the impedance of the barriers is over come and a voltage drop occurs across the sample channel. The electric field generated within the sample channel is non-uniform due to the shape of the insulating barriers. When a 600 kHz signal is across the sample channel, 4

μm beads suspended in deionized water feel a positive dielectrophoretic force which acts to push them into regions of highest electric field non-uniformity. When the applied voltage is increased to 150 V_{RMS}, the dielectrophoretic force overcomes the fluid drag force and the beads are trapped along the channel wall, as shown in Figure 6-5b. This action is reversible and when the voltage is turned off, the particles are released downstream.

Traditional DEP devices employ metal electrodes patterned on glass. The device in Figure 6-5c has an array of interdigitated saw tooth electrodes, separated by 50 and 350 μm at their minimum and maximum respectively. This device was encapsulated by a 1 mm wide, 50 μm deep channel which allowed pressure driven flow to drive particles over the electrodes. The geometry of the metal electrodes creates a non-uniform electric field when an AC signal is applied. At 60 Hz, the 1 and 4 μm beads experience a negative DEP force that acts away from the electrodes and opposes the fluid drag force. When the applied voltage is increased to 7.3 V_{RMS} the DEP force and drag force become balanced and the particles are trapped, as shown in Figure 6-5d.

Chapter 7: Isolation of Live / Dead Cells

Introduction

The utilization of DEP to manipulate live and dead cells has previously been demonstrated through several approaches. To start, Suehiro *et al.* were able to utilize dielectrophoretic impedance measurements to selectively detect viable bacteria [63]. Conventional interdigitated electrode DEP micro devices have also been used to separate live and heat-treated Listeria cells[64]. Huang *et al.* investigated the difference in the AC electrodynamics of viable and non-viable yeast cells through DEP and electrorotation experiments[65] and a DEP-based microfluidic device for the selective retention of viable cells in culture media with high conductivity was proposed by Docoslis et al. [66].

Insulator-based dielectrophoresis (iDEP) has also been employed to concentrate and separate live and dead bacteria for water analysis[67]. In this method, electrodes inserted into a microfluidic channel create an electric field which is distorted by the presence of insulating structures. The devices can be manufactured using simple fabrication techniques and can be mass-produced inexpensively through injection molding or hot embossing[68,69].

Contactless dielectrophoresis (cDEP) provides non-uniform electric fields in microfluidic channels required for DEP cell manipulation without direct contact between the electrodes and the sample [70]. In this method, an electric field is created in the sample microchannel using electrodes inserted into two conductive microchambers, which are separated from the sample channel by thin insulating barriers. These insulating barriers exhibit a capacitive behavior and therefore an electric field can be produced in the main channel by applying an AC field across the barriers[70]. Furthermore, the absence of contact between the electrodes and the sample fluid prevents problems associated with more conventional approaches to DEP including contamination, bubble formation, and the detrimental effects of joule heating.

In this study, the abilities of cDEP to selectively isolate and enrich a cell population was investigated. This was demonstrated through the separation of viable cells from a

heterogeneous population also containing dead cells. Two cDEP microfluidic devices were designed and fabricated out of polydemethilsiloxane (PDMS) and glass using standard photolitography. The DEP response of the cells was investigated under various electrical experimental conditions in the range of our power supply limitations. Human leukemia THP-1 viable cells were successfully isolated from dead (heat treated) cells without lysing.

The separation of viable and nonviable cells is a critical starting point for this new technology to move towards more advanced applications. Optimization of these devices would allow for selective separation of cells from biological fluids for purposes such as: the diagnosis of early stages of diseases, drug screening, sample preparation for downstream analysis, enrichment of tumor cells to evaluate tumor lineage via PCR, as well as treatment planning. By using viable/nonviable separation as a model for these applications, a new generation of cDEP devices can be tailored around the results reported in this study[71-76].

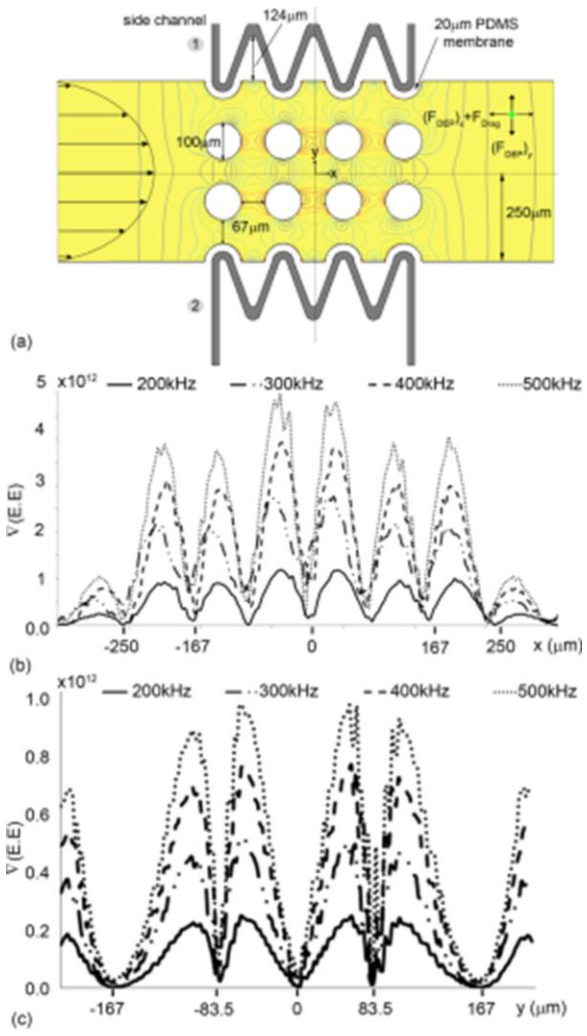

Figure 7-1: 2D top view schematic of device 2, showing the dominated acting forces on the particle. The contours represent the electric fields modelled in Comsol multiphysics. (b) Line plot of the gradient of the electric field squared ($kg^2mC^{-2}S^{-4}$) for four different electrical boundary conditions with efficient numerical cell trapping (V_1=30V_{rms} at 200kHz, 300kHz, 400kHz, and 500kHzV_2= Ground) along the x axis (y=0). (c) Line plot of the gradient of the electric field squared ($kg^2mC^{-2}S^{-4}$) for four different electrical boundary conditions with efficient numerical cell trapping (V_1=30V_{rms} at 200kHz, 300kHz, 400kHz, and 500kHz, and V_2= Ground) along the y axis (x=0).

Cell Preparation

The live samples of THP-1 human leukemia monocytes were washed twice and resuspended

in a buffer used for DEP experiments (8.5%sucrose [wt/vol], 0.3% glucose [wt/vol], and 0.725% [wt/vol] RPMI [77]) to 10^6 cells/mL. The cell samples to be killed were first pipetted into a conical tube and heated in a 60^{o}C water bath for twelve minutes; an adequate time determined to kill a majority of the cell sample. These dead cells were then washed twice and resuspended in the DEP buffer.

To enable simultaneous observation under fluorescent microscope, cells were stained using a LIVE/DEAD® Viability/Cytotoxicity Kit for mammalian cells (Molecular Probes Inc.). Calcein AM, which is enzymatically converted to green fluorescent calcein, was added to the live cell sample at 2μL per ml of cell suspension. Ethidium homodimer-1 (EthD-1) was added to the dead cell sample at 6μL per ml of cell suspension. This can only pass through damaged cell membranes and upon nucleic acid-binding produces a red fluorescence.

The two samples were then vortexed for 5 minutes, washed once and resuspended in DEP buffer. The live and dead suspensions were then mixed together in one conical tube and the final conductivity of 110-115μS/cm was measured with a SevenGo Pro conductivity meter (Mettler-Toledo, Inc., Columbus, OH). Live and dead cells were indistingushable under bright field evaulation.

Experimental Set-Up

The microfluidic devices were placed in a vacuum jar for 30 minutes prior to experiments to reduce problems associated with priming. Pipette tips were used to fill the side channels with Phosphate Buffered Saline (PBS) and acted as reservoirs. Aluminum electrodes were placed in the side channel reservoirs. The electrodes inserted in side channel 1 of the device (Figure 7-1a) were used for excitation while the electrodes inserted in side channel 2 were grounded. Thin walled Teflon tubing (Cole-Parmer Instrument Co., Vernon Hills, IL) was inserted into the inlet and outlet of the main channel. A 1 mL syringe containing the cell suspension was fastened to a micro-syringe pump (Cole Parmer, Vernon Hills, IL) and connected to the inlet tubing. Once the main channel was primed with the cell suspension the syringe pump was set to 0.02mL/hr; equivalent to a velocity of 222 μm/second. This flow rate was maintained for 5

minutes prior to experiments.

Trapping efficiency for this device was determined for voltages of 20 V_{RMS}, 30 V_{RMS}, 40 V_{RMS}, 50 V_{RMS} and frequencies of 200 kHz, 300 kHz, 400 kHz, 500 kHz at a constant flow rate of 0.02mL/hr. Experimental parameters were tested at random to mitigate any variation in cell concentration, flow rate, device functionality and other experimental variables. Additionally, trapping efficiency was calculated at 0.02 mL/hr, 0.04 mL/hr, 0.06 mL/hr, 0.08 mL/hr, and 0.10 mL/hr with electrical parameters held constant at 500 kHz and $30V_{RMS}$. Electrical parameters were selected randomly for each experiment for a total of five trials at each combination. The electric field was maintained for 30 seconds during each experiment. During the 30 second interval, all cells entering the trapping region of the device (the region containing pillars in the main channel) were counted, representing the total number of cells. Cells that were not trapped were counted as they left the device trapping region. Trapping efficiency was recorded as the percentage of cells trapped of the total cells entering the trapping regoin. Cells that were trapped but later lysed while under the AC field were included in the percentage of trapped cells, but it was noted that cell viability was decreased due to the electric field.

Electrical Equipment

AC electric fields were applied to the microfluidic devices using a combination of waveform generation and amplification equipment. Waveform generation was performed by a function generator (GFG-3015, GW Instek, Taipei, Taiwan) whose output was then fed to a wideband power amplifier (AL-50HF-A, Amp-Line Corp., Oakland Gardens, NY). The wideband power amplifier performed the initial voltage amplification of the signal and provided the necessary output current to drive a custom-wound high-voltage transformer (Amp-Line Corp., Oakland Gardens, NY). This transformer was placed inside a grounded cage and attached to the devices using high-voltage wiring. Frequency and voltage measurements were accomplished using an oscilloscope (TDS-1002B, Tektronics Inc. Beaverton, OR) connected to a 100:1 voltage divider at the output of the transformer.

Results and Discussion

The gradient of the electric field along the x-axis (y=0) of the main channel of device 2 is plotted in Figure 7-1b. For these electrical boundary conditions (V_1= $30V_{rms}$ at 200kHz, 300kHz, 400kHz, and 500kHz and V_2=Ground) cell trapping was observed. Local maximums in the gradient of the electric field occurred in line with the edges of the insulating pillars while the minimum gradient was experienced as cells passed through the region between two pillars. The highest electric field gradient was observed to occur at the two insulating pillars which had edges in the center of the device. The electric field gradients in the center of the device along the y-axis (x=0) are shown in Figure 7-1c and the highest gradient was observed in line with the edges of the insulating pillars. It should be noted that the maximum gradient is observed at y=+/- 83.5µm and cells traveling through the exact center of the device (along the x-axis) experience a lower DEP force than those just off-center. The electric field gradient within the channel increased with applied signal frequency from 200kHz to 500kHz. This increase in gradient is not linear and these parameters represent the limitations of our current electrical setup. Theoretically, the device has a maximum gradient of electric field within the channel occuring between 600kHz and 700kHz as seen in Figure 7-2d. Above this frequency, leakages in the system begin to dominate the response and the electric field within the channel drops off.

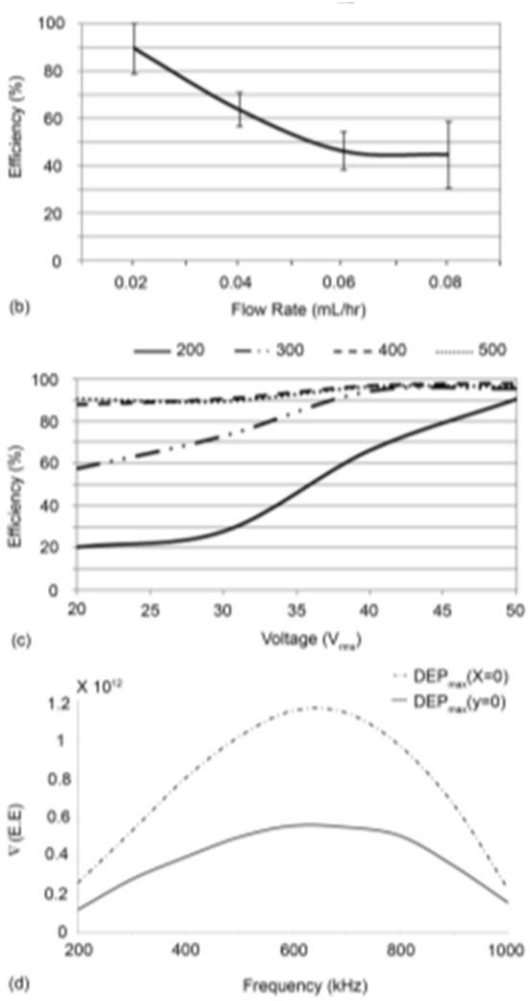

Figure 7-2: (b) Trapping efficiency of device 2 at 500kHz and 30Vrms for flow rates of 0.02, 0.04, 0.06, and 0.08mL/hr. (c) Trapping efficiency at 0.02mL/hr of device 2 at 200, 300, 400, and 500kHz as voltages increase from 20Vrms to 50Vrms. (d) Maximum gradient of the electric field along the x (y=0) and y (x=0) axis of frequencies between 200kHz and 1000kHz.

Live THP-1 cells were observed to experience positive DEP force at the reported frequencies and the DEP force applied on dead cells appeared to be negligible. The majority of cell

trapping was observed in the region between the first two columns of insulating barriers at 0.02mL/hour. However, the distribution of trapped cells became more uniform at higher flow rates. At 0.02 mL/hour, we observed trapping efficiencies greater than 90% at all tested frequencies (200 kHz, 300 kHz, 400 kHz, and 500 kHz). However, lysing was common at all frequencies when a voltage of 50 V_{RMS} was applied. At the highest two frequencies, lysing was common at 40 V_{RMS} and over 10% of the cells lysed at 50 V_{RMS} (Figure 7-2c).

Trapping efficiency experiments for higher flow rates were conducted at 500 kHz and 30 V_{RMS} because these parameters yielded a high trapping efficicncy of 89.6% at 0.02 mL/hour. Trapping efficiency was reduced by an increase in flow rate and reached a minimum of 44.8% (+/- 14.2) at 0.8 mL/hour (Figure 7-2b). Flow rates greater than 0.1 mL/hour were not reported due to limitations of our recording software that resulted in the inability to accurately count the number of cells entering and exiting the trapping region of the device.

Due to the capacitance effect of the PDMS barriers in cDEP devices, the corresponding gradient of the electric field for voltage-frequency pairs are different for each design. These devices were designed to provide a sufficient gradient of the electric field for DEP cell manipulation within the limitations of our power supply and the PDMS breakdown voltage. The high trapping efficiency makes the device presented an optimal design for selective entrapment and enrichment of cell samples. This process is depicted in Figure 7-3; initially live cells (green) and dead cells (red) passed through the trapping region due to pressure driven flow (Figure 7-3a). Live cells were selectively concentrated in the trapping region under the application of a 500 kHz, 40 V_{RMS} signal (Figure 7-3b). Under these parameters, the DEP force on the dead cells was not sufficient to influence their motion and they passed through the trapping region. The enriched sample of live cells can be controllably released for later analysis once the electric field is turned off (Figure 7-3c).

Conclusion

This work has demonstrated the ability of cDEP to selectively concentrate specific cells from diverse populations through the separation of viable cells from a sample containing both viable and non-viable human leukemia cells. Repeatability, high efficiency, sterility, and an inexpensive fabrication process are benefits inherent to cDEP over more conventional methods of cell separation. This method is also unique in that direct evaluation is possible with little or no sample preparation. The resulting time and material savings are invaluable in homeland security and biomedical applications. Given cDEP's numerous advantages, the technique has tremendous potential for sample isolation and enrichment for drug screening, disease detection and treatment, and other lab-on-a-chip applications.

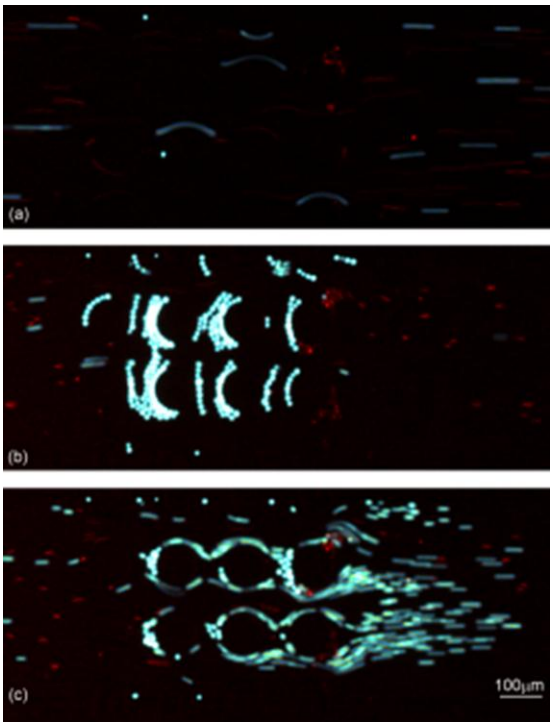

Figure 7-3: Experimental results for device 2: (a) Dead (red and live (green) THP-1 cells are moving left to right due to pressure driven flow. (b) 30 seconds after applying the electric field (V1=40V_{rms} at 500 kHz and V2=Ground) live cells were trapped due to positive DEP but dead cells pass by. (c) Releasing the trapped live cells by turning off the power supply.

Chapter 8: Development of Low Frequency Contactless Dielectrophoresis

Introduction

Clinical diagnosis, therapeutics, and comprehensive cell biology benefit from the ability to isolate and enrich rare cells derived from a heterogeneous population [7]. Fluorescence-activated cell sorting (FACS) and magnetic-activated cell sorting (MACS) are the most commonly utilized sorting methodologies. These techniques use fluorophore-conjugated antibodies and antibody-conjugated magnetic beads to label and process target cells. Systems employing FACS and MACS provide high throughput screening; however, they have large initial and operational costs, require specialized training, may affect cell fate and function due to shear stress, the use of antibodies, and fluorophores, and requires prior knowledge about cell surface markers [9]. Because of this, there is a growing need for a marker-independent isolation and purification method.

A number of marker-independent methods have been developed which sort cells by exploiting unique physical phenomena which can be manipulated on the microscale including streamline manipulation [78], microstructure flow perturbation [21], gravity [33], and inertial forces [23]. Other methods sort cells based on their intrinsic properties including their volumetric [79], mechanical [10], magnetic [80], and electrical [36] properties. Recently, Mach et al. demonstrated a massively parallel filtration capable device capable of isolating bacteria from blood with a flow rate of 8mL/min using inertial forces [81]. Choi et al. were able to isolate cells based on their phase in the cell life cycle in a grooved microfluidic device [21]. Mohamed et al. demonstrated the ability to isolate circulating cancer cells from whole blood based on size and deformability in a device containing pillars in stages of decreasing pillar-to-pillar spacing [10]. These devices have obvious advantages due to their simplicity and dependence on singular physical phenomenon (i.e., hydrodynamics).

Other methods have recently been reported which improve selectivity to sort sells of similar size, but different genotype by employing electromagnetic forces. Gascoyne et al. demonstrated a tumor cell isolation efficiency of 92% in a dielectrophoresis (DEP) field flow fractionation device using an electric field generated at 60 kHz [36]. DEP is a phenomenon which occurs at the

micro-scale when a dielectric particle is placed in a non-uniform electric field. A net force is generated due to charge distributions within the particle. This has been successfully used to examine, manipulate, isolate, or enrich particles [82], DNA [37,83], viruses [38], and cells [39-41]. DEP devices typically consist of metal electrodes deposited onto a glass substrate [84]. The geometry of these electrodes generates the non-uniform electric field required for DEP. Alternatively, insulator based dielectrophoresis (iDEP) devices employ insulating structures within a microfluidic channel to produce non-uniformities when electrodes are inserted into the ends of the channel [43,44]. These devices can employ both DC and AC electric fields [85] and many geometric configurations including sawtooth channels [86,87].

Contactless dielectrophoresis (cDEP) devices are a new adaptation of this technique in which fluid electrodes, isolated from the main microfluidic channel by a thin membrane, provide the necessary electric field in the sample channel [52-54]. This helps mitigate some challenges with traditional dielectrophoresis devices including fouling, bubble formation, and electrode delamination [88]. cDEP devices can be fabricated by replication from a single etch master stamp and can be translated to mass fabrication techniques, similar to methods used for iDEP [50], while eliminating direct sample-electrode contact. The insulating barriers capacitively couple the fluid electrodes to the sample channel resulting in a complex frequency dependent electric field gradient within the sample channel. The magnitude of the electric field gradient at any frequency is dependent on the geometric and material properties of the device. This work presents a continuous sorting device which is the first cDEP design capable of exploiting the Clausius-Mossotti factor at frequencies where it is either positive or negative for different mammalian cell types. Experimental devices were fabricated using a cost effective fabrication technique which does not require the use of a cleanroom or specialized equipment. An analytical model was developed to evaluate cDEP devices as a network of parallel resistor-capacitor pairs. Two theoretical devices are presented and evaluated using finite element methods to demonstrate the effect of geometry on the development of electric field gradients across a wide frequency spectrum. Finally, we present a third experimental device capable of continuously sorting human leukemia cells from dilute blood samples.

Theory

The application of a voltage across conductive and dielectric materials will induce an electric field

$$\vec{E} = -\nabla\phi \qquad [8.1]$$

where ϕ is the applied voltage. Under the influence of this electric field, dielectric particles immersed in a conductive fluid will become polarized. If the electric field is non-uniform, particles are driven towards the regions of field gradient maxima by a translational dielectrophoretic force ($\vec{F}_{DEP}$) [57]

$$\vec{F}_{DEP} = \gamma_{DEP}\,\nabla\left|\vec{\mathrm{E}}\cdot\vec{\mathrm{E}}\right| \qquad [8.2]$$

where γ_{DEP} is half the induced dipole moment, of the particle. For a spherical particle, this quantity can be represented as:

$$\gamma_{DEP} = 2\,\pi\epsilon_m r^3 Re[K(\omega)] \qquad [8.3]$$

where r is the radius of the cell, ϵ_m is the relative permitivity of the suspending medium, and $Re[K(\omega)]$ is the real part of the Clausius-Mossotti (C-M) factor.

$$K(\omega) = \frac{\epsilon_c^* - \epsilon_m^*}{\epsilon_c^* + 2\epsilon_m^*} \qquad [8.4]$$

$$\epsilon^* = \epsilon + \frac{\sigma}{i\omega} \qquad [8.5]$$

where ϵ_c^* and ϵ_m^* are the permittivity of the cell and suspending medium respectively, σ is the conductivity, ω is the frequency of the applied field, and $i = \sqrt{-1}$.

A particle independent DEP vector can be defined as

$$\vec{\Gamma} = \frac{\vec{F}_{DEP}}{\gamma_{DEP}} = \nabla\left|\vec{\mathrm{E}}\cdot\vec{\mathrm{E}}\right| \qquad [8.6]$$

$$\vec{\Gamma} = \nabla|(-\nabla\phi)\cdot(-\nabla\phi)| \qquad [8.7]$$

$$\vec{\Gamma} = \nabla \left| \left(\frac{d\phi}{dx}\right)^2 + \left(\frac{d\phi}{dy}\right)^2 + \left(\frac{d\phi}{dz}\right)^2 \right| \qquad [8.8]$$

$$\vec{\Gamma} = \begin{bmatrix} \left(\frac{d^3}{dx^3} + \frac{d^3}{dxdy^2} + \frac{d^3}{dxdz^2}\right)\hat{e}_x \\ \left(\frac{d^3}{dx^2dy} + \frac{d^3}{dy^3} + \frac{d^3}{dydz^2}\right)\hat{e}_y \\ \left(\frac{d^3}{dx^2dz} + \frac{d^3}{dy^2dz} + \frac{d^3}{dz^3}\right)\hat{e}_z \end{bmatrix} \phi^2 \qquad [8.9]$$

where $\hat{e}_j$ is a unit vector in the *j* direction.

Contactless dielectrophoresis devices can be modeled analytically as five resistor-capacitor (R-C) pairs in series. R-C pairs represent the source and sink electrode channels, the two insulating barriers, and the sample channel. The current entering and leaving each of these pairs must be the same and the total impedance of each pair can be calculated using Kirchhoff's current law and Ohm's Law.

$$Z = \frac{X_c^2 R - iX_c R^2}{R^2 + X_c^2} \qquad [8.10]$$

$$X_c = \frac{-1}{\omega C} \qquad [8.11]$$

Z is the total impedance of the resistor-capacitor pair, X_c is the capacitive reactance, C is the capacitance, and R is the resistance.

The physical geometry and the material properties of the materials present in this system influence the resistance ($R = \rho L/A$) and capacitance ($C = \epsilon_0 \epsilon_r A/d$) of each element where ρ and ϵ_r are the resistivity and relative static permittivity of the material respectively, A is the cross-sectional area, L is the length of the resistor and d is the separation distance between two conductive components. It should be noted that for the insulating membranes in a traditional cDEP device, $L=d$.

Methods

Clausius-Mossotti Factor Analytical Model

The Clausius-Mossotti factor for THP-1 human leukemia monocytes and red blood cells (RBC) was modeled over a logarithmic distribution between 100 Hz and 100 MHz using MATLAB (Version R2010a, MathWorks Inc., Natick, MA, USA). Dispersing cytoplasmic properties which effect high frequency behavior was modeled for RBCs as presented by Gimsa et al. (1996). In this method, the conductivity and permittivity of the cell were influenced by an additional dispersion term σ_c and ϵ_c respectively.

$$\sigma_c = \sigma_{c_0} + \Delta\sigma \cdot \frac{(\omega * \tau_c)^{2*(1-\alpha)}}{(1 + \omega \cdot \tau_c)^{2(1-\alpha)}} \quad [8.12]$$

$$\epsilon_c = \epsilon_{c_\infty} + \Delta\epsilon_r \cdot \frac{1}{(1 + \omega \cdot \tau_c)^{2(1-\alpha)}} \quad [8.13]$$

ϵ_{c_∞} and σ_{c_0} are the high frequency permittivity and initial conductivity of the cytoplasm, $\Delta\epsilon_r$ and $\Delta\sigma_r$ are frequency dependant ratios of change, α is the distribution range of dispersion frequencies**,** and τ_c is the cytoplasmic time constant.

$$\tau_c = \frac{\epsilon_c}{\sigma_c} \quad [8.14]$$

Table 8-1 summarizes the dielectric properties used to calculate the C-M factor for THP-1 and RBCs.

	THP-1	**RBC**	**Units**
ϵ_m	$80\varepsilon_0$[^]	$80\varepsilon_0$[^]	
ϵ_c	154.4[+]	212[‡]	
σ_m	0.01[#]	0.01[#]	$[S/m]$
σ_c	0.65[+]	0.4[‡]	$[S/m]$
c_m	0.0177[*]	0.00997[‡]	$[F/m^2]$
$\Delta\epsilon_r$	-	162[‡]	

$\Delta\sigma_r$	-	$0.135^{\ddagger}$	$[S/m]$
α	-	$0^{\dagger}$	
ϵ_{c_∞}	-	$50\varepsilon_0{}^{\ddagger}$	

Table 8-1: Dielectric properties used to calculate the C-M factor for THP-1 and RBCs. Values derived from ‡ [2], † [3], * [89], + [4], ^ assumption based on water content, and # measured values.

Device Design

Three cDEP devices were devised to numerically evaluate the $\vec{\Gamma}$ frequency response and the impedance of the fluid electrodes, sample channel, and insulating barriers between 10 Hz and 100 MHz. The third device was further used to validate the numerical model experimentally. Design 1, Figure 8-1a-b, has geometric features similar to previously reported devices [53]. These previous designs typically have a limited bandwidth in which cells can be manipulated and Device 1 served as a baseline for comparison with traditional cDEP devices. Specifically, the device is designed with fluid electrodes that are separated from each side of the sample channel by 20 μm. The fluid electrodes are 4.2 cm long, 300 μm wide, and 50 μm deep. The sample channel has maximum and minimum widths of 500 and 100 μm, respectively, which makes the channel appear to have rounded 'saw tooth' features that protrude into the channel. The insulating barriers, which separate the fluid electrodes from the sample channel, are 20 μm wide and travel along the top and bottom of the sample channel for 600 μm for a total barrier length of 0.12 cm.

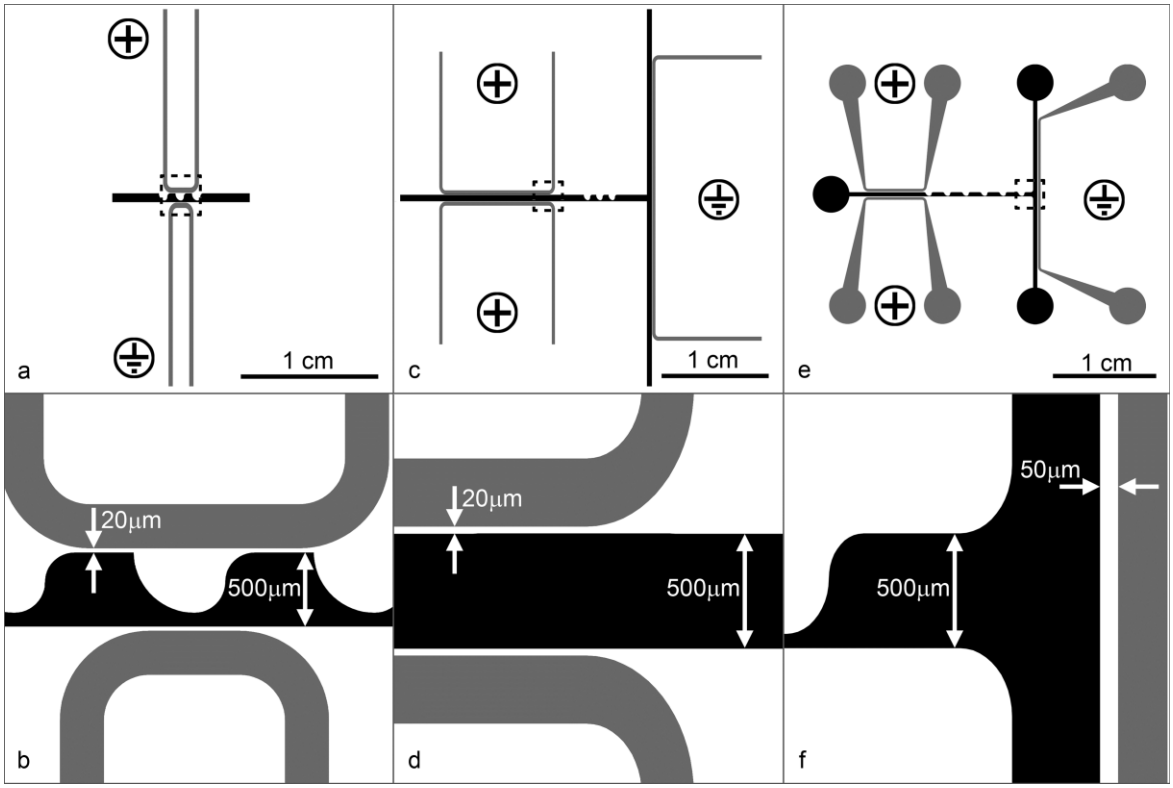

Figure 8-1: Schematics for (a-b) Device 1, (c-d) Device 2, and (e-f) Device 3. Device 1 has geometrical feature sizes similar to traditional cDEP devices reported in the literature. The total barrier length and distance between source and sink electrodes is increased in Devices 2 and 3. Fluid electrode channels (gray) had boundary conditions of 100 V and ground applied at their inlets as shown above.

Design 2, Figure 8-1c-d, incorporates physical features to expand the $\vec{\Gamma}$ frequency response. The fluid electrodes are 10 cm long, 300 μm wide, and 50 μm deep. The sample channel retains the same geometric 'saw tooth' features as Design 1, however, the source and sink electrode channels are positioned such that there is a 1cm distance between them. The sample channel then forms a 'T' junction along the right side. The insulating barriers which separate the fluid electrodes from the sample channel are 20 μm wide. The total length in which the barriers are 20 μm wide is 1cm on the left top and bottom (source) and 2 cm along the right side (sink) for a total barrier length of 4 cm.

Design 3, Figure 8-1d-e, was created for experimental validation of the numerical and analytical results presented below. This design contains the same 'saw-tooth' features as the previous designs, with three additional teeth to increase the total duration in which cell are exposed to electric field gradients. The overall device geometry is similar to Device 2, but has been modified to conform to the minimum feature size of 40 μm possible with the fabrication process

presented in sections 3.4 and A.1. The sample channel has a nominal width of 500 μm with constrictions from the 'saw-teeth' reducing the width to 100 μm. The sample channel forms a 'T' junction along the right side with approximately 1.2 cm between the source and sink electrodes. There are two source electrode channels which are each approximately 3 cm long with a minimum width of 300 μm. The barriers separating the source electrodes from the sample channel are 50 μm thick for approximately 5.8 mm on top and bottom. The sink electrode channel is approximately 3.7 cm long with a minimum width of 300 μm. The barrier separating the sink electrode channel from the sample channel is 50 μm thick for approximately 1.6 cm. The total barrier length for Design 3 is approximately 2.78 cm.

Analytical and Numerical Device Modeling

The geometric features of Devices 1 and 2 were used to create lumped element representations for the electrode channels, insulating barriers, and the sample channel by calculating their associated resistances and capacitances. Three dimensional geometries were created using Autocad (Autocad Mechanical 2010, Autodesk Inc, San Rafael, CA, USA). The geometries were imported into COMSOL Multiphysics (Version 4.0, Comsol Inc., Burlington, MA, USA) and the AC/DC module was used to solve for the potential distribution, ϕ, using the governing equation $\nabla \cdot (\sigma^* \nabla \phi) = 0$ where σ^* is the complex conductivity ($\sigma^* = \sigma + i\omega\epsilon$). Edges of the electrode channels were modeled as a uniform potential of 100V and ground as depicted in **Error! Reference source not found.**. The frequency of the applied signal was incrementally increased from 100 Hz to 10^9 Hz using the MATLAB to create a logarithmically distributed frequency distribution. Physical regions within the model were set to represent poly(dimethylsiloxane) (PDMS) (Sylgard 184, Dow Corning, USA), phosphate buffer solution (PBS), or sample media. ϕ was used to calculate the magnitude of the particle independent DEP force vector ($|\vec{F}|$).

PDMS was defined as having a conductivity (σ) of 0.83×10^{-12} S/m and a relative permittivity (ε_r) of 2.65 as provided by the manufacturer. PBS was modeled as having a conductivity of 1.4 S/m and a relative permittivity of 80 as measured and assumed based on water composition respectively. The conductivity of the sample was 100 μS/cm and the permittivity was also assumed to be 80.

Device Fabrication

Briefly, a thin film photoresist (#146DFR-4, MG Chemicals, Surrey, British Colombia, Canada) was laminated onto glass microscope slides. The laminated slides were exposed to ultraviolet (UV) light through a film transparency mask (Output City, Cad / Art Services Inc., Bandon, OR) using an array of UV light emitting diodes and a custom exposure frame. The slides were then developed in negative photo developer (#4170-500ML, MG Chemicals, Surrey, British Columbia, Canada) and used as a master stamp for PDMS replication. The PDMS molds were bonded to the glass slides after treating with air plasma (Harrick Plasma, Ithaca, New York). For a full description of this process, see supplementary data in section A.1.

Cell Preparation

The live samples of THP-1 human leukemia monocytes (American Type Culture Collection, Manassas, VA, USA) were washed twice and resuspended in a buffer used for experiments (8.5%sucrose [wt/vol], 0.3% glucose [wt/vol], and 0.725% [wt/vol] RPMI [77]) to $1x10^6$cells/mL. THP-1 cells were stained using a LIVE/DEAD® Viability/Cytotoxicity Kit for mammalian cells (Molecular Probes Inc., Carlsbad, CA, USA). Calcein Red/Orange, which is enzymatically converted to fluorescent calcein, was added to the sample at 2 µL per mL of cell suspension. A drop of whole blood, obtained via a diabetic finger stick from willing volunteers, was added to 5 mL of buffer. The suspension was then diluted to achieve a red blood cell concentration of $1x10^7$cells.

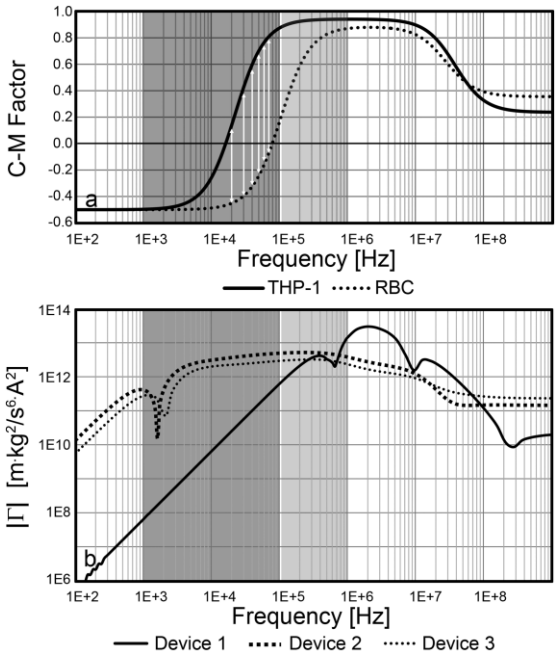

Figure 8-2: cDEP devices can be optimized to develop high $\left|\vec{F}\right|$ values at low frequencies. (a)THP-1 and RBCs have unique Clausius-Mossotti factor curves. The white arrows show regions where the C-M factor for THP-1 cells is positive while the C-M factor for RBCs is negative. (b) Device 2 and 3 generate significantly higher electric field gradients near the first C-M factor crossover frequency. The light and dark gray regions show the operating frequencies for traditional cDEP devices and the optimal cDEP operating frequencies respectively.

The two cell samples were then vortexed for 5 minutes, washed once and resuspended in buffer. The THP-1 and RBC suspensions were then mixed together in one conical tube with a final concentration of $1x10^6$ and $1x10^7$ cells/mL, respectively. The buffer had a final conductivity of 100-115 µS/cm measured with a SevenGo Pro conductivity meter (Mettler-Toledo, Inc., Columbus, OH, USA).

Experimental Setup

A syringe pump was used to drive samples at a rate of 0.01 mL/hour (PHD Ultra, Harvard Apparatus, Holliston, MA, USA). An AC electric field was created by amplifying (AL-50HF-A, Amp-Line Corp., Oakland Gardens, NY, USA) the output signal of a function

generator (GFG-3015, GW Instek, Taipei, Taiwan). A step up transformer was used to achieve output voltages up to 300 V_{RMS} between 50 and 100 kHz. Voltage and frequency were measured using an oscilloscope (TDS-1002B, Tektronics Inc. Beaverton, OR, USA) connected to the output stage of the transformer.

Results and Discussion

Analytical Method

Cells are repelled from regions of maximal electric field gradient at frequencies where C-M factor is negative. Conversely, when the C-M factor is positive, cells are driven towards regions of maximal electric field gradient. Mammalian cells exhibit a negative C-M factor at low frequencies. As frequency increases, the C-M factor begins to increase, crossing into the positive domain at frequencies on the order of 1 kHz. The lowest frequency at which the C-M factor is exactly zero is known as the *first crossover frequency*. The magnitude of the C-M factor changes drastically in proximity to the first crossover frequency and it is expected that in this region, cells of similar genotypes will be most easily discriminated.

Over a majority of the frequency spectrum, the C-M factor for THP-1 cells and RBCs is of similar magnitude and direction as seen in Figure 8-2a. In these regions, the resulting DEP force will tend to drive both cell types into similar regions. This action is intrinsic and is independent of device geometry. At frequencies between 20 kHz and 70 kHz the C-M factors for THP-1 and RBCs are opposite, as indicated by the white arrows. This indicates that a DEP force will move the cells in opposite directions. Between 70 kHz and 500 kHz the C-M factor is of similar direction, but of greater magnitude for THP-1 cells. It is important to note that if the conductivity of the buffer solution is increased, these regions will shift and occur at higher frequencies. The light gray region of Figure 8-2a depicts the typical frequencies over which cDEP devices are able to manipulate cells. The dark gray region represents the ideal operating range over which mammalian cells of different genotypes will likely have distinct C-M factors.

The particle independent DEP force vector ($\vec{\Gamma}$) is highly dependent on the voltage drop within the sample channel. The dielectric breakdown of PDMS limits the magnitude of experimental voltages; therefore, it is important that a large proportion of the total voltage drop across the device occurs across the sample channel. In a traditional cDEP device, represented by Device 1, the impedance of the insulating barriers dominates the sample and electrode channels. This results in a large voltage drop across the insulating barriers at low frequencies. As shown in Figure. 8-3a, the capacitive nature of the barrier causes its impedance to decrease with increasing frequency. These devices are able to manipulate cells and particles at frequencies above 100 kHz [53], when approximately 1% of the total voltage drop occurs across the sample channel.

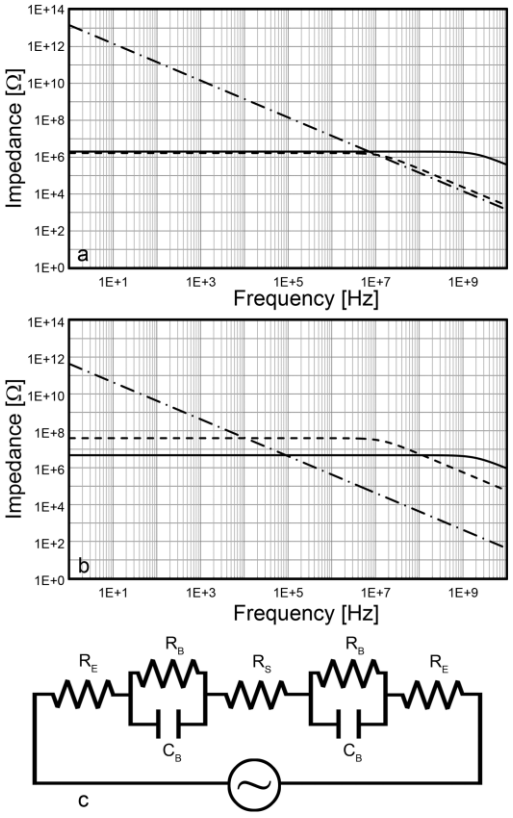

Figure. 8-3: The frequency response of cDEP devices can be improved by altering the geometry. (a) The impedance of the insulating barriers in a traditional cDEP device (Device 1) results in small voltage drops across the sample channel. (b) The geometry can be altered (Device 2) to increase the sample channel voltage drop at frequencies near the first C-M Factor cross over point. The solid, dashed, and dash-dotted lines represent the impedance of the electrode channels, sample channel, and insulating barriers, respectively. (c) Simplified cDEP resistor-capacitor analytical network.

Device 2 represents a cDEP device with geometric features that increase barrier capacitance and sample channel resistance. This causes the impedance of the barriers to roll off at lower frequencies and increase the proportion of voltage drop across the sample channel as shown in Figure. 8-3b. In this geometry, 1% of the total voltage drop occurs across the sample channel at approximately 100 Hz. At frequencies of 1, 10, 100, and 1000 kHz, the voltage drop across the sample channel is 0.01, 0.12, 1.16, and 9.40 percent, respectively, of the total voltage drop across Device 1. In contrast, at the same frequencies, the voltage drop across the sample channel of Device 2 is 8.54, 45.97, 81.67, and 88.50 percent respectively. This shows that the geometric properties of cDEP devices can be manipulated to reduce the impedance of the

insulating barriers and increase the total voltage drop across the sample channel. This is important due to the high dependence of Γ on the magnitude and spatial changes of the voltage.

The electrode and sample channels have relatively small capacitive components, which are omitted in Figure. 8-3c. This additional capacitance causes the impedance of these elements to roll off at frequencies above 10 MHz as shown in Figure. 8-3a and b. At frequencies above 10 MHz, the materials begin to appear homogeneous, and the ability of cDEP devices to produce useful electric field gradients may be diminished.

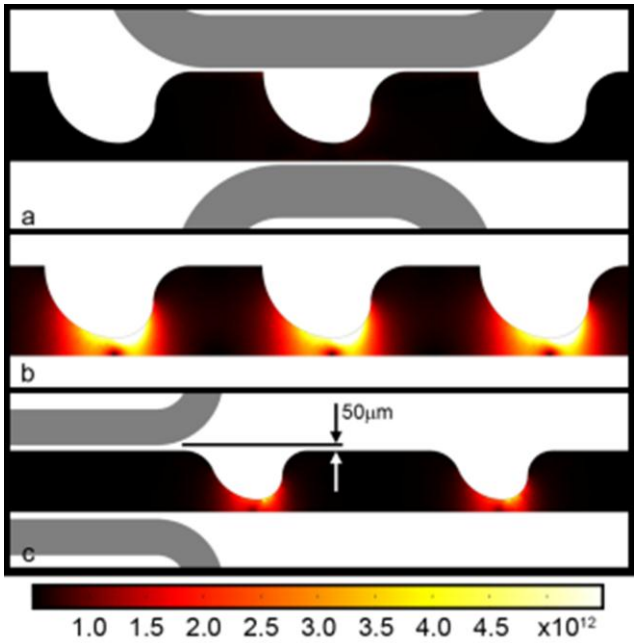

Figure 8-4: Geometric features impact device performance. At 100 V_{RMS} (a) Device 1 fails to generate a significant electric field gradient at 50 kHz as a result of small barrier capacitance and sample channel resistance. (b) Device 2 produces higher electric field gradients due to its longer barriers and increased distance between source and sink electrodes. (c) Device 3 produces significant electric field gradients at 50 kHz. The legend depicts the value of $|\vec{\Gamma}|$ in units of $[m \cdot kg^2 \cdot s^{-6} \cdot A^{-2}]$.

Numerical Method

Previously reported cDEP devices demonstrated the ability to manipulate cells and particles with numerically calculated Γ values of $1x10^{12}$ $[m \cdot kg^2 \cdot s^{-6} \cdot A^{-2}]$ or greater [52-54]. This value is used here as a minimum threshold representing the ability of a theoretical cDEP device to manipulate cells. As shown in Figure 8-2b, the electric field gradient of Device 1 reaches this magnitude, at approximately 100 kHz. This is consistent with results reported previously [53] for traditional cDEP devices. Between 1 and 10 MHz, the electric field gradient developed within the sample channel increases to above $1x10^{13}$ $[m \cdot kg^2 \cdot s^{-6} \cdot A^{-2}]$, however, in this range, the C-M factor is expected to drop towards zero reducing the total DEP force. Additionally, the generation of high voltage signals at these frequencies is difficult and requires specialized equipment. The light gray region of Figure 8-2b depicts the typical frequency range over which traditional cDEP devices achieve particle isolation and enrichment [52-54].

The electric field gradient within the sample channel of Device 2 is above $1x10^{12}$ $[m \cdot kg^2 \cdot s^{-6} \cdot A^{-2}]$ between 3 kHz and 10 MHz. Within this frequency range, the electric field gradient is similar to that reported for traditional cDEP devices capable of isolating live from dead cells [53]. The electric field gradient produced in Device 2 is of significant magnitude to manipulate cells while the C-M factor is close to the first crossover frequency for THP-1 cells**.** These results effectively demonstrate that the geometric features of a cDEP device can be modified so that cells can be manipulated using both positive and negative DEP.

At 50 kHz, the lower limit of our electronics' capabilities, Device 1 does not generate an electric field gradient above $1x10^{12}$ $[m \cdot kg^2 \cdot s^{-6} \cdot A^{-2}]$, as shown in Figure 8-4a. In contrast, Device 2 generates electric field gradients in excess of $5x10^{12}$ $[m \cdot kg^2 \cdot s^{-6} \cdot A^{-2}]$ in regions close to the 'saw-tooth' features. Figure 8-4b and c show the regions of high electric field gradient within Device 2. The asymmetrical features create regions of highest electric field gradient proximal to the top of the sample channel.

Numerical analysis of Device 3, Figure 8-4c, shows that the device is capable of generating an electric field gradient above $1x10^{12}$ $[m \cdot kg^2 \cdot s^{-6} \cdot A^{-2}]$ at 50 kHz. Figure 8-4c shows that Device 3 produces an asymmetrical electric field gradient of similar shape

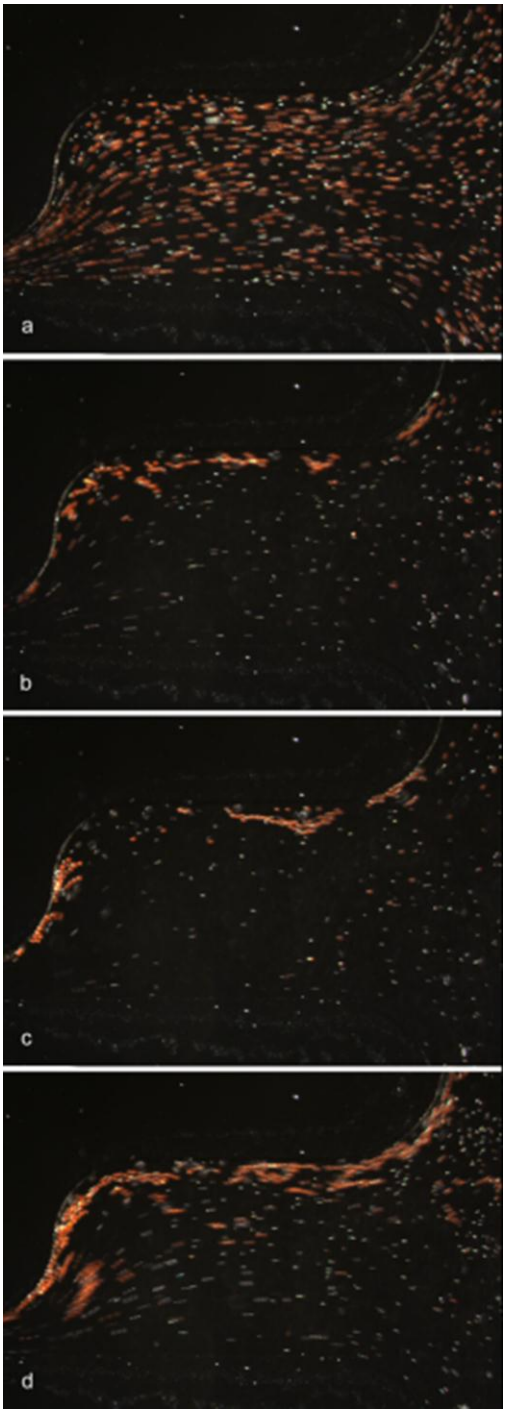

Figure 8-5: THP-1 cell can be sorted from a heterogeneous population. Cell pass through the device with a uniform distribution when (a) the electric field is turned off. (b) However, THP-1 cells are attracted towards regions at the top of the sample channel while RBCs pass through unaffected when $231V_{RMS}$ at 50 kHz, (c) $227V_{RMS}$ at 70 kHz, and (d) $234V_{RMS}$ 90 kHz is applied.

but lower magnitude compared to Device 2. The electric field gradient within the sample channel of Device 3 is above 1x10^{12} $[m \cdot kg^2 \cdot s^{-6} \cdot A^{-2}]$ between 4 kHz and 10 MHz as shown in Figure 8-2b.

Experimental Validation

Microfluidic channels 50 μm and greater in width can be repeatedly produced using the process described. This directly matches the photoresist manufacturer's specifications. Narrower features failed to develop smooth and well defined lines (results not shown). Channels separated by 40 μm or greater could be fully developed and PDMS replication resulted in water tight bonds between parallel channels. Higher resolution photoresist films could be used to reduce the minimum feature sizes; however, many of these films are only available in industrial quantities and were not evaluated.

In the absence of an applied electric field, THP-1 cells and RBCs passed freely through Device 3 without being affected as shown in Figure 8-5. When 231 V_{RMS} at 50 kHz was applied, 'pearl chain' formation of THP cells, indicative of DEP, was initially observed. Cells then began to slowly migrate from the bottom of the sample channel towards the top wall. THP-1 cells which were in the sample channel prior to the application of the electric field continued to exit the device through the top and bottom paths of the 'T-channel'. After approximately 1 minute, all of the initial cells had passed through the device and new cells were reaching the 'T-intersection'. These cells had experienced a DEP force the entire distance between the electrodes and most were exiting only through the top path of the 'T-channel'. At this voltage and frequency, shown in Figure 8-5b, THP-1 cells did not become trapped near the saw-tooth features and continued to travel along the upper channel wall while RBCs passed through the device unaffected. Similar results were observed at 60 kHz.

Between 70 and 100 kHz, THP-1 cells formed pearl chains and migrated towards the top wall of the sample channel when 250 V_{RMS} or greater was applied. Additionally, some chains began to trap near the saw-tooth features as shown in Figure 8-5c and d. At 80 to 100 kHz a small number of cells began to decrease in fluorescence, indicative of electroporation or cell damage [90]. The number of cells trapping increased with both increasing applied voltage and frequency.

The purpose of the devices presented above was to demonstrate the theoretical ability of cDEP to function at low frequencies. The experimental results presented validate the approach and establish that the contactless dielectrophoresis platform is capable of manipulating cells at frequencies below 100 kHz in physiologically suitable buffers. Operating at these low frequencies will allow for the manipulation of cells using negative dielectrophoresis, a task previously unachievable using cDEP. At frequencies between 50 and 90 kHz a large positive DEP force was observed acting on the human leukemia cells. At 50 kHz, theory predicts that the Clausius-Mossotti factor for RBCs is slightly negative. This in conjunction with their smaller size resulted in the observation of a negligible negative DEP force. It is expected that at lower frequencies a more dominant negative DEP force will act on the RBCs while a positive force continues to act on the THP-1 cells. The combination of these opposing forces may split the cells into separate streams for collection.

Alternatively, the geometry of the outlet channels could be modified such that the bifurcation at the end of the sample channel splits the flow into two non-equal branches. A small portion of the flow containing the cancer cells would be allowed to flow towards the upper outlet, and the remaining flow containing the majority of the RBCs would be directed towards the lower outlet. This change in geometry could alleviate the need for a strong negative DEP force acting on the RBCs as they would only need to be forced from the top portion of the channel. In this geometry, the Zweifach-Fung effect, in which particle fraction tends to increase in the high-flow-rate branch [91], could increase sorting purity since a small negative DEP force acting on the RBCs would cause a depletion region near the walls.

Conclusion

The fabrication technique presented here has been used to successfully demonstrate the first cDEP device with insulating barriers greater than 20 μm. The low cost of fabrication, simplicity, availability of supplies, and exclusion of toxic chemicals make this technique ideal for researchers that do not have access to a cleanroom. Furthermore, this process displays potential as a rapid, low cost solution for the fabrication of complex multi-phased devices capable of sorting, isolating, and enriching samples as well as performing downstream analysis, such as

impedance detection. In contrast to traditional cell sorting technologies such as FACS and MACS, the single stamp fabrication and associated electronics do not require specialized equipment and have a relatively low cost of entrance. Additionally, cDEP does not require the use of surface markers, dyes, or antibodies which require substantial prior knowledge of the cell's biology.

Traditional cDEP devices are capable of developing the electric field gradients necessary for dielectrophoretic manipulation between 100 kHz and 1 MHz. The frequency dependent behavior of cDEP devices creates a unique set of challenges in manipulating mammalian cells. The first crossover frequency for many cells anticipated to be below this frequency range for low conductivity sample buffers. Additionally, cells of similar genotypes may have crossover frequencies which occur within a narrow frequency range. Since the C-M factor for these cells may not differ significantly except in proximity to the crossover frequencies, it is paramount that future cDEP devices be capable of manipulating particles between 1 and 100 kHz.

Numerical results indicate that these devices will continue to develop useful DEP forces at frequencies as low as 1 kHz. This is advantageous because systems designed to operate above 100 kHz and 100 V_{RMS} require custom electronics and magnetics. Preliminary experiments with RBCs, macrophages, leukemia monocytes, prostate and breast cancer cells (results not shown) indicate that between 50 and 100 kHz RBCs and macrophages experience a negligible DEP response. Meanwhile, the leukemia, breast, and prostate cancer cells exhibit a strong positive DEP response which forces them into the top half of the channel. The ability of this device to separate low concentrations cancer cells from other common subpopulations found in blood will be the emphasis of future studies. Future work will focus on the development of complementary electronics, demonstration of a positive DEP response for THP-1 cells, a concurrent negative DEP response for RBCs resulting in continuous isolation of the two populations and quantification of selectivity, enrichment factor, and cell viability.

Chapter 9: Contactless Dielectrophoretic Spectroscopy

Introduction

The use of non-invasive methods to detect and enrich cancer cells independent of their genotype is critical for early diagnostic and treatment purposes. In addition, isolation of these cells could provide a workbench for clinicians to screen drug therapies prior to patient treatment. This would enable oncologists to tailor treatment on a patient-specific level and to ensure that the most effective treatment is being utilized [71-75]. Since many symptoms associated with cancers can be attributed to multiple diseases, diagnosis must be accomplished via medical analysis. There are a number of molecular, cytogenic, immunological, cytochemical, and morphological assays capable of making this diagnosis; however, low proportions of cancerous cells make these processes challenging [92].

During progression, tumor cells acquire the capacity to disseminate into blood circulation until they are detected and eliminated by the immune system or until they attach to the endothelial cells, extravasate, and grow as secondary tumors (metastasis) at distant sites. These circulating tumor cells (CTCs) could serve as early indicators of cancer [93]. The most reliable method currently available for CTC detection is automated digital microscopy (ADM), which uses image analysis to recognize immunochemically or immunomagnetically labeled tumor cells. A study using the CellSearch System™ (Veridex LLC, Warren, NJ), showed that the overall survival of patients with breast cancers harboring fewer than five CTCs in about 7 mL blood after 3-5 weeks of starting their therapy was a relatively long 18.5 months. Women who had five CTCs or more had much shorter median survival times, ranging from 1.3 to 3.6 months [94,95].

The majority of recent investigations have utilized qRT-PCR for the confirmation and genotyping of CTCs. This technique has been reported in scientific literature as a valid method to confirm various CTCs derived from bladder [96], breast [97], lung [98], prostate [99,100], and esophageal [101] cancers. Immunocytochemistry methods, using antibody-antigen identification are typically based on detection of specific tumor or epithelial cell markers present in CTCs. While these are reliable methods, the specificity of CTC separation and

their enrichment determines the quality of the results. The major drawback to this approach is that other cells, such as hematopoietic or fibroblasts cells, can express several epithelial markers such as keratins [102,103], causing incomplete separation. Typically, more sensitive techniques may require prior knowledge of cell-specific markers and antibodies to prepare target cells for analysis. As result, there is a growing need for a marker-independent isolation and purification method to increase yield, sensitivity, precision and reproducibility.

Dielectrophoresis (DEP), the motion of a particle in a non-uniform electric field, has become a robust method for analyzing nano-particles, cells, viruses, and DNA based on their physical and electrical properties [104]. Many devices exploit these dielectrophoretic forces by placing metal electrodes in a microfluidic channel containing spatial non-uniformities (iDEP) [43,44,86] or via electrodes patterned on the channel floor (traditional DEP) [105]. Traditional DEP has been employed to separate breast cancer cells from blood [106]. Post-concentration analysis of cells enriched in these devices can be challenging, since cells must come in direct contact with the electrode and may be contaminated.

A new technique, contactless dielectrophoresis (cDEP) [107], utilizes fluid electrode channels which are isolated from a sample channel by a thin insulating membrane. When an AC voltage is applied, capacitive coupling between the sample and electrode channels produces the non-uniform electric field necessary for DEP. This technique has recently demonstrated the ability to isolate THP-1 human leukemia monocytes from a heterogeneous mixture of live and dead cells [108]. The absence of contact between electrodes and the sample prevents bubble formation and avoids any contaminating effects the electrodes may have on the sample.

The key to using CTCs as predictive clinical biomarkers is their separation and enrichment. By first establishing the dielectrophoretic responses of normal and cancerous cells within this cDEP device, conditions to detect and enrich tumor cells from mixtures with non-transformed cells can be determined. This work is the first cDEP demonstration of both negative and positive DEP on mammalian cells. This is also the first demonstration of a cDEP device to investigate the electrical properties of cells. The frequency response of breast cancer, leukemia, macrophages, and red blood cells is investigated and their cell membrane capacitance is calculated. This

method provides a simple way to interrogate the electrical properties of cells which will enable future cDEP designs to be specifically fabricated towards CTC detection within biological fluids.

Theory

The single shell dielectric model introduced by Foster et al. [109] for the Clausius-Mossotti factor can be used to describe a cell as a membrane covered sphere with a membrane capacitance, C_m, suspended in a medium with conductivity, σ_M. The first frequency at which Re[K(ω)] = 0 is known as the first cross-over frequency (f_{xo1})

$$f_{xo1} = \frac{\sqrt{2}\sigma_M}{2\pi r C_m} \text{ [Hz]} \qquad [4.86]$$

At this frequency, the net DEP force acting on a cell will equal zero. Under the influence of an electric field at this frequency, the distribution of cells within the device will be identical to the case where no field is applied. Since this frequency can be determined experimentally and the cell radius and conductivity of the media are known, the capacitance of the cell membrane can be calculated. An expanded explanation of the Clausius-Mossotti factor and DEP theory can be seen in Chapter 4:.

Methods

Cell Preparation

Whole blood samples, obtained from healthy willing donors via diabetic finger stick, PC1 macrophages, MDA-MB231 breast cancer, PC3 prostate cancer, and THP-1 leukemia cells were independently suspended in a low conductivity isotonic solution (8.5% sucrose [wt/vol], 0.3% glucose [wt/vol], and 0.725% RPMI [wt/vol]) [77]. The cells were spun down a minimum of two times at 3100 RPM for five minutes to remove any residual hematocrit or culture media such that the conductivity of the samples was 115 +/- 15 μS-cm^{-1} as measured with a SevenGo Pro conductivity meter (Mettler-Toledo Inc., Columbus, OH). The radii for each cell type were measured using a Vi-CELL XR (Beckman Coulter, Inc, Miami, FL).

Device Fabrication

A silicon master stamp was fabricated on a <100> silicon substrate using photolithography. Deep Reactive Ion Etching (DRIE) was used to etch the silicon master stamp to a depth of 50 μm. Surface roughness was reduced by etching the wafer in tetramethylammonium hydroxide (TMAH) for 5 minutes. Finally, a thin layer of Teflon was deposited to facilitate stamp removal using typical DRIE passivation parameters. Liquid phase polydimethylsiloxane (PDMS) in a 10:1 ratio of monomers to curing agent was degassed under vacuum prior to being poured onto the silicon master and cured for 15 min at 150°C. Fluidic connections to the channels were punched into the PDMS using 1.5 mm core borers (Harris Uni-Core, Ted Pella Inc., Redding, CA). Glass microscope slides (75mm x 75mm x 1.2mm, Alexis Scientific) were cleaned with soap and water, rinsed with distilled water, ethanol, isopropyl alcohol, and then dried with compressed air. The PDMS replica was bonded to clean glass after treating with air plasma for 2 minutes in a PDC-001 plasma cleaner (Harrick Plasma, Ithaca, New York).

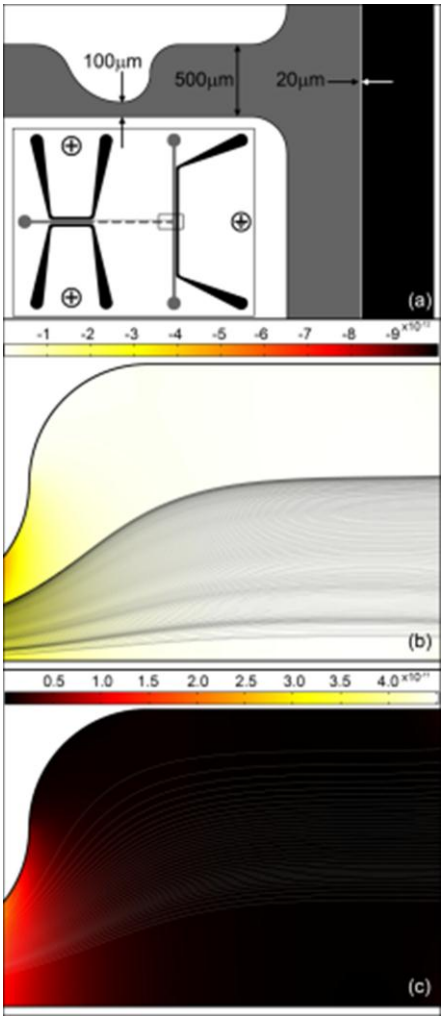

Figure 9-1: (a) Schematic of the low frequency contactless dielectrophoresis device. The fluid electrodes and sample channel are shown in black and grey, respectively. DEP force and particle trajectories for 200 MDA-MB231 cells at (b) 10 kHz and (c) 70 kHz. 84% of particles intersected the top of the channel in (c) indicating that a large number of cells will travel along the upper wall.

Device Geometry

The device, shown in Figure 9-1a, consists of a bifurcated sample channel, and three fluid electrode channels. The sample channel contains six saw-tooth features which reduce the total width of the channel from 500 to 100 μm. These features produce asymmetric electric field non-uniformities which act to push the cells towards the top or bottom of the channel. The source and sink electrodes are separated by 1.2 cm. There are two source electrode channels which are each approximately 3 cm long with a minimum width of 300 μm. The barriers separating the source electrodes from the sample

channel are 20 μm thick for approximately 5.8 mm on top and bottom. The sink electrode channel is approximately 3.7 cm long with a minimum width of 300 μm. The barrier separating the sink electrode channel from the sample channel is 20 μm thick for approximately 1.6 cm.

Simulations

Numerical simulations were conducted to determine the relative effects of DEP and drag forces acting on the cancer cells. The electric field distribution was modeled numerically in COMSOL Multiphysics 4.1 using the AC/DC module (COMSOL Inc., Burlington, MA, USA) by solving for the potential distribution. The boundary conditions were prescribed uniform potentials of 100 V at the inlets of the source electrode channels and as ground at the inlets of the sink electrode channels. The fluid dynamics were modeled using the laminar flow module. The inlet boundary condition was prescribed as a constant velocity of 50 μm/s as calculated based on the experimental flow rate and the cross-sectional area of the device. The outlet boundary conditions were prescribed as no pressure boundaries.

	MDA-MB231	**THP-1**	**PC1**	**RBC**	
Literature Values					
ε_M	$80\varepsilon_0$[^]	$80\varepsilon_0$[^]	$80\varepsilon_0$[^]	$80\varepsilon_0$[^]	
ε_c	$50\varepsilon_0$[‡]	$162.0\ \varepsilon_0$[+]	$91.6\ \varepsilon_0$[+]	$212\ \varepsilon_0$[‡]	
σ_M	0.01[#]	0.01[#]	0.01[#]	0.01[#]	S/m
σ_c	1.00[‡]	0.66[+]	0.46[+]	0.40[‡]	S/m
C_m	0.0163[«]	0.0196[+]	0.0110[+]	0.00997[Δ]	F/m^2
R	8.88 ± 0.818[#]	7.30 ± 0.966[#]	6.99 ± 1.17[#]	3.2[Δ]	μm
Measured and Calculated Values					
σ_M	0.0117	0.0104	0.0122	0.0180	[S/m]
f_{xo1}	19545	18651	30797	69774	[Hz]
C_m	0.01518 ± 0.0013	0.01719 ± 0.0020	0.01275 ± 0.0018	0.01089[*]	[F/m^2]

Table 9-1: Literature, Measured, and Calculated values of dielectric properties used to calculate the C-M factor and membrane capacitance for MDA-MB231, THP-1, PC1, and RBCs. Values derived from « [1], ‡ [2], † [3], + [4], ǂ [5], Δ [6], ^ an assumption based on water content, and # measurements.

The values for the electrical conductivity and permittivity of the PDMS, sample media, and PBS that were used in this numerical modeling were similar to those reported earlier [52,53]. The sample media and PBS had a permittivity of $80\varepsilon_0$ as assumed based on water content. The conductivity of the sample media and PBS were defined as 1.4 and 0.01 [S/m], respectively. The permittivity and conductivity of the PDMS were defined as $2.7\varepsilon_0$ and

$8.33x10^{-13}$ [S/m], respectively. Inside the sample channel Γ was investigated for frequencies between 100 Hz and 1 GHz. The Clausius-Mossotti factor for each cell type was calculated in MATLAB (Version R2010a, MathWorks Inc., Natick, MA, USA) using the single shell model and the parameters found in Table 9-1.

Experimental Parameters

The devices were placed into a vacuum jar for at least 30 minutes prior to experiments. The side channels were filled with PBS, and then aluminum electrodes were placed in each side channel inlet. Teflon tubing (22 gauge) was inserted into the inlet and outlets of the main channel. The inlet tubing was connected to a 1 mL syringe containing the cell suspension via a blunt needle.

Cell suspensions were driven through the sample channel at a rate of 0.005 mL/hour by a syringe pump (PHD Ultra, Harvard Apparatus, Holliston, MA). An inverted light microscope (Leica DMI 6000B, Leica Microsystems, Bannockburn, IL) was used to monitor the cells. For all cell types, 200 V_{RMS} was applied at frequencies between 10 and 70 kHz in increments of 10 kHz using a Trek Model 2205 high voltage amplifier (Trek Inc., Medina, New York). For RBCs, which did not exhibit a strong DEP response at 200 V_{RMS}, an additional set of experiments were recorded at 300 V_{RMS}.

For each data point the voltage was applied for five minutes to allow for any transient responses to pass, and then a two minute video was recorded. MATLAB was used to analyze the video from each experiment. Each frame was converted into a grey scale image and the location of each cell was recorded as it passed through a line from top to bottom of the channel. Data from each video was normalized to determine the distribution of cells within the channel. The location, from bottom to top, at which the cells were divided into equal populations was then determined as a function of frequency. The value of f_{xo1} for each cell type was determined by finding the frequency at which the centerline of the channel split the cells into equal populations.

Results and Discussion

Numerical Results

The single shell model of the C-M factor is a complex function involving the e lectrical properties of the suspending media, cell membrane and cytoplasm. Membrane capacitance, cytoplasmic conductivity, relative cytoplasmic permittivity, medium conductivity, relative medium permittivity, and cell radius impact the frequency response of the C-M factor. A sensitivity analysis of some of these parameters is shown in Supplemental Figure 1, and a full analysis can be seen in previous work by Docoslis et al. [110]. As presented in equation 9.1, variations in media conductivity, cell radius, and membrane capacitance alter the location of f_{xo1}. Experimentally, f_{xo1}, media conductivity, and cell radius can be measured providing the necessary parameters to calculate membrane capacitance.

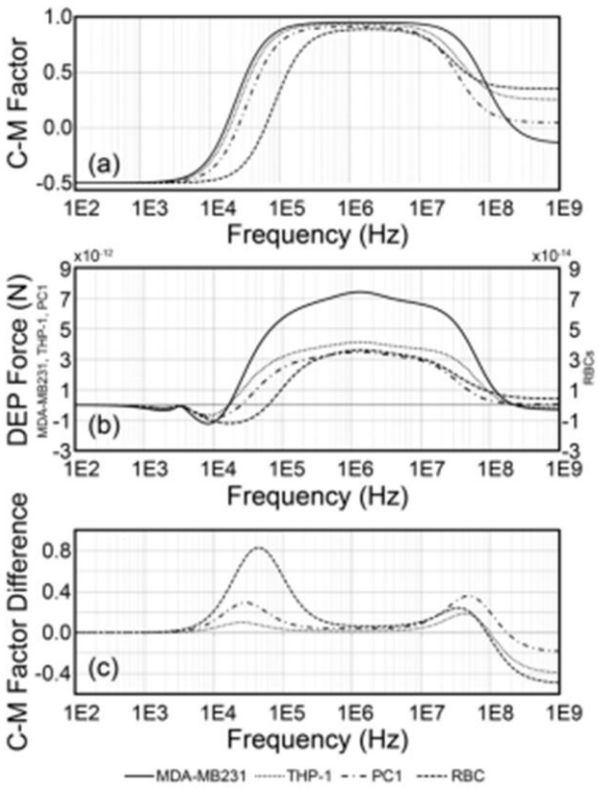

Figure 9-2: (a) Clausius-Mossotti factor (b) frequency dependent force and (c) difference in C-M factor between MDA-MB231 (solid) and THP-1 (dotted), PC1 (dash-dot), and RBCs (broken line).

As shown in Figure 9-2a, the C-M factor for MDA-MB231 and THP-1 cells are nearly identical between 100 Hz and 10 MHz while the PC1 and RBCs have distinct C-M factor curves. The total force acting on each cell type is shown in Figure 9-2b. These values were calculated using values from the C-M factors in Figure 9-2a, Table 9-1, and the values for Γ as described below. Although the C-M factor for MDA-MB231 and THP-1 cells are similar, the force acting on these cells is different, due to variances in their membrane capacitance and radius. The PC1 and RBCs are smaller than the cancerous cells and the total force acting on them is significantly lower. Numerically, the RBCs will experience a DEP force two orders of magnitude lower than the PC1 cells. This was manifested experimentally as the RBCs did not exhibit a significant DEP response until 300 V_{RMS} was applied.

Figure 9-2c shows the difference in C-M factor between the MDA-MB231 cell line and THP-1, PC1, and RBCs. There are two regions in the frequency spectrum where the C-M factor for these cells differs significantly. The first region occurs between 10 and 100 kHz and the second above 10 MHz. Typically, cDEP devices have a narrow operating region between 100 kHz and 1 MHz [53]. Below this range, the impedance of the insulating barriers dominates the system and cell manipulation is not possible. Above this range, the electronics necessary to produce voltages in excess of 100 V_{RMS} become impractical.

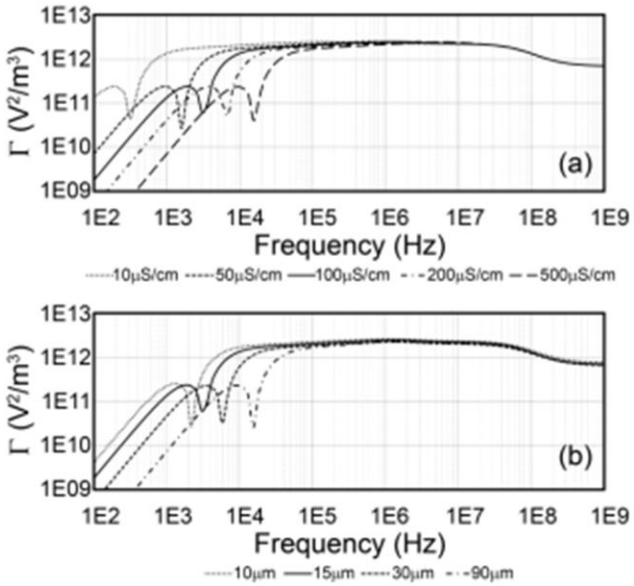

Figure 9-3: Parametric analysis of device performance varying (a) sample conductivity and (b) barrier thickness. Nominal values are: barrier thickness = 15 μm and sample conductivity = 100 μs/cm

The cDEP device geometry in Figure 9-1a was designed to operate at frequencies below 100 kHz while using a physiologically relevant sample media. As determined by our previous work in low frequency cDEP [55], a design goal of producing Γ above $1x10^{12}$ [V^2/m^3] was used to represent a significant value for cell manipulation. Briefly, this goal was achieved by increasing the total length of the insulating barriers and by increasing the distance between the source and sink fluid electrodes. Increasing the barrier length creates a larger capacitance which acts to decrease the total impedance of the barriers at lower frequencies. Increasing the distance between the fluid electrodes raises the resistance of the sample channel resulting in a larger proportion of the voltage drop to occur across the sample.

For this device, a constant trend was observed, independent of sample conductivity or barrier thickness. At low frequencies, the impedance of the insulating membrane between the sample channel and the fluid electrodes is very large resulting in a substantial portion of the applied voltage to drop across the barriers. As frequency increases, the capacitive nature of the barriers causes their net impedance to drop, allowing a higher proportion of the voltage drop

to occur over the length of the sample channel resulting in a relatively constant Γ value over a large frequency range.

cDEP devices are analogous to a series network of resistor-capacitor pairs and changes to the conductivity of the media and barrier thickness alter the frequency response of the devices. For sample media with low conductivities, similar to deionized water, the impedance of the sample channel is large, allowing a significant voltage drop to occur across the sample at lower frequencies. As sample conductivity is increased, shown in Figure 9-3a, the frequency at which significant Γ values are produced is shifted higher. Similarly, decreasing the thickness of the insulating membranes reduces their impedance and the proportion of the voltage drop that occurs across them. As shown in Figure 9-3b, this allows the barriers to be overcome at lower frequencies resulting in a rise to the maximum Γ value at a lower frequency. An optimized device will utilize the lowest conductivity, physiologically acceptable sample media and the thinnest insulating membrane practically fabricated. The experiments presented here used a physiological buffer with a conductivity of approximately 100 μS/cm and devices with barrier thickness of 20 μm resulting in significant Γ values at frequencies between 10 kHz and 100 MHz.

Computational modeling of the device (Figure 9-1b-c) indicates that the cells experience a negligible DEP force within the majority of the channel. The regions of highest DEP force occur in proximity to the constrictions. At 10 kHz, MDA-MB231 cells experience a maximum negative DEP force of approximately 1.0×10^{-12} [N]. At 70 kHz, the same cells will experience a maximum positive DEP force of approximately 5.0×10^{-12} [N]. The streamlines, representing MDA-MB231 cells, indicate that at low frequencies, when the C-M factor is negative, the distribution of cells is shifted towards the bottom of the channel. Although the largest non-uniformities in the electric field occur in proximity to the top wall, there is also a region of non-uniform electric field near the bottom of the channel. Numerically, this is manifested as a small depletion zone which forms near the bottom of the channel. At higher frequencies, where the C-M factor is positive, the distribution of cells is shifted towards the top of the channel. A total of 200 streamlines were simulated for an electric field of 200 V_{RMS} at 70 kHz. Eighty four percent

intersected the top wall indicating that for this frequency a large number of cells should be forced into a narrow region at the top of the channel.

Experimental Results

At 10 kHz, all cell types exhibited a negative DEP response. Figure 9-4a shows the distribution of all cell types at 10 kHz. The net effect was to force the distribution of cells towards the bottom of the channel with most of the cells passing below the center line. A large depletion region near the bottom wall exists for MDA-MB231, THP-1, and PC1 cells. Due to their smaller size, a more narrow depletion region was observed for the RBCs. At 10 kHz, lysing of some THP-1 and PC1 cells was also observed. Negative DEP, acting on THP-1 cells (200 V_{RMS} at 10 kHz), is shown in Figure 9-4c.

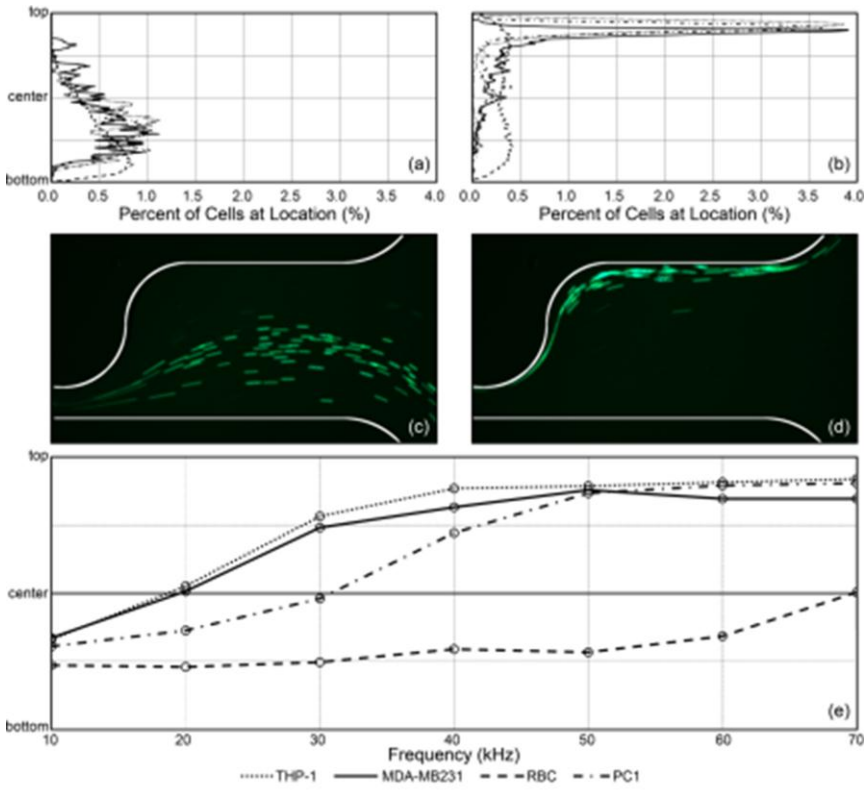

Figure 9-4: (a) The action of negative DEP forces the distribution of cells towards the bottom of the channel at 10 kHz. (b) At 70 kHz all cells experience positive DEP which distributes the cells towards the top of the channel. At this frequency, the distribution of RBCs is shifted only slightly above center. (c) Negative and (d) positive DEP are shown acting on THP-1 cells at 10 and 70 kHz (200 V_{RMS}), respectively. (e) Distribution of cells within the sample channel as a function of frequency. The lines indicate the location at which the cells are split into two equal populations. f_{xo1} for each cell type is the frequency at which the distribution crosses the center line.

At frequencies above 50 kHz, all cells except RBCs exhibited a positive DEP response. Theoretically, the magnitude of the C-M factor for positive DEP can be twice that for negative DEP. Experimentally, this resulted in cells occupying a much narrower region of the device when experiencing a strong positive DEP force. As the frequency was increased above f_{xo1} for each cell type, the cells occupied a narrowing region of the top half of the channel. At 70 kHz, the MDA-MB231, THP-1 and PC1 cells occupied a region approximately 50 μm wide adjacent to the wall at the top of the channel as shown in Figure 9-4b. Positive DEP, acting on THP-1 cells (200 V_{RMS} at 70 kHz), is shown in Figure 9-4d.

Figure 9-4e shows the location which splits the cells into equal populations as a function of frequency. MDA-MB231 and THP-1 cells exhibited a similar behavior. At 10 kHz, both cell types experienced a negative DEP force which progressed the cells into the bottom half of the channel. At 20 kHz, each exhibited a slight positive DEP response indicating that their respective f_{xo1} occurred between 10 and 20 kHz. As expected by numerical calculation of their C-M factors, the transition from negative to positive DEP occurred over a narrow frequency range. Between 40 and 70 kHz the MDA-MB231 and THP-1 cells exhibited a strong positive DEP response and generally occupied a narrow region at the top of the channel. The PC1 cells exhibited a negative DEP response between 10 and 30 kHz with a sharp transition to positive DEP at 40 kHz. At 300 V_{RMS}, the RBCs exhibited a negative DEP response between 10 and 60 kHz. Between 10 and 30 kHz, this acted to force the cells into the bottom 75% of the channel. Between 40 and 60 kHz, the negative DEP response began to diminish; however, the distribution remained shifted towards the bottom half of the channel. At 70 kHz, the RBCs exhibited a slight positive DEP response.

The membrane capacitance for MDA-MB231 cells determined by whole-cell impedance spectroscopy was previously reported by Han et al. to be 0.0163± 0.0017 [F/m^2] [1]. This value provides preliminary validation of our technique which calculates a capacitance value of 0.01518 ± 0.0013 for the MDA-MB231 cell line. The capacitance values for THP-1, PC1, and RBC lines were calculated to be 0.01719, 0.01275, and 0.01089 [F/m^2]. It should be noted RBCs were approximated as a spherical particle of radius 3.20 μm. The values used to for the calculations and the membrane capacitance for each cell type can be seen in Table 9-1.

Conclusion

This work presents the first successful use of cDEP to manipulate mammalian cells at frequencies where the C-M factor is both positive and negative. Numerical calculations of the C-M factor suggest that mammalian cells will experience similar DEP responses over a broad frequency spectrum with the exception of the regions in proximity to the first and second crossover frequencies. The electronics necessary to produce high voltage signals above 1 MHz are impractical, making the development of cDEP devices which operate near the first crossover frequency necessary if this technique is to gain acceptance in laboratory and clinical settings.

The procedure presented here provides a simple way to examine the specific membrane capacitance of mammalian cells which can easily be translated into an automated process. Changes in membrane capacitance have been previously reported as an indicator of the invasiveness of certain cancers [1] and a similar cDEP device could potentially be used as an indicator of patient health by examining cells taken from biopsy or found as CTCs. The ability to analyze cells of interest and develop predictive numerical models will enable the development of future dielectrophoresis devices and ultimately improve patient outcomes through the development of early cancer detection techniques.

Chapter 10: Multi-Layer Contactless Dielectrophoresis

Introduction

In Chapter 8: and Chapter 9: we cDEP demonstrated devices with the ability to manipulate cells employing applied potentials with frequencies as low as 1 kHz in a single layer device [56]. This was accomplished by increasing the capacitance associated with the barriers and increasing the resistance of the sample channel. Here we investigate for the first time, with detailed mathematical modeling, the properties of a multilayer device, in which the sample and fluid electrode channels occupy distinct layers, using finite element software.

Additionally, the resistance and capacitance of the fluid electrodes, sample channel, and insulating barriers are calculated numerically and evaluated as a simple low pass filter. This is used to predict the device performance characteristics and find an order of magnitude approximate for $\left|\nabla\left(\vec{E}\cdot\vec{E}\right)\right|$. These multilayer devices are electrically similar to single layer devices, maintain compatibility with mass fabrication techniques, and provide a potential method to significantly increase throughput compared to single layer cDEP devices. Finally, we validate the multilayer cDEP concept with a prototype device. Dielectrophoretic trapping of MDA-MB-231 breast cancer cells is demonstrated under a 250 V_{RMS} potential at 600 kHz and a flow rate of 1.0 mL/hour, a 100 fold increase in flow rate over the single layer version of the same design presented in previous chapters.

Theory

A cDEP device can be represented as the series combination of three resistors and two resistor–capacitor (RC) pairs in parallel. These represent the impedances of the two fluid electrodes, a single sample channel, and two insulating barriers. In this scenario, the capacitances associated with the sample channel and fluid electrodes are considered negligible. The total impedance (Z_{total}) of this network is easily calculated because all of these elements are in series; the current flowing through each individual RC pair must be the same.

$$Z(\omega)_{total} = 2\,R_{electrode} + 2\,R_{sample} + \frac{2\,X_{barrier}^2 R_{barrier} - iX_{barrier}R_{barrier}^2}{R_{barrier}^2 - X_{barrier}^2}\ [\Omega] \quad [10.1]$$

where R is the resistance and X is the capacitive reactance (X=-1/(ωC)). For simplicity, we can neglect the small capacitive elements associated with the fluid electrodes and sample channel as their capacitance is an order of magnitude lower than the barriers and their effect is negligible until frequencies above 10 MHz. Once this impedance is known, the current flowing through the system can be calculated for any given input voltage (V_{sample}). From this a transfer function describing the relative voltage drop across the sample channel can be derived

$$V_{sample} = I_{total} \cdot R_{sample} = \frac{V_{input}}{Z_{total}} \cdot Z_{sample}[V] \quad [10.2]$$

$$\frac{V_{sample}}{V_{input}} = \frac{Z_{sample}}{Z_{total}} \left[\frac{V}{V}\right] \quad [10.3]$$

This transfer function lends intuition towards to the optimal frequency range for operation of these devices as it has been previously shown that cDEP devices begin to perform well when about 1 percent of the total voltage drop occurs across the sample channel [55]. An approximation for $|\vec{\Gamma}|$ can be achieved by finding the change in resistance (∂R) of the sample channel per unit length (∂x)

$$R_{sample}(x) = \frac{L(x)}{\sigma \cdot h \cdot w(x)}\ [\Omega] \quad [10.4]$$

$$\frac{\partial R}{\partial x}(x) = \frac{w(x) - x \cdot w'(x)}{\sigma \cdot h \cdot w(x)^2} \left[\frac{\Omega}{m}\right] \quad [10.5]$$

where h is the depth of the channel, $L(x) = x$ is the length of the sample channel segment, and $w(x)$ is the width of the channel at location x. Assuming that the current passing through vertical sections of the channel remain constant, the change in voltage per unit length can be

found and a numerical approximation for $|\vec{\Gamma}|$ can be determined by

$$\left|\vec{\Gamma}\right| \approx \left|\frac{\partial(E(x)^2)}{\partial L}\right| \approx \left|\frac{E(x_1)^2 - E(x_2)^2}{x_1 - x_2}\right| \left[\frac{V^2}{m^3}\right] \qquad [10.6]$$

Methods

Numerical Modeling

Two-dimensional geometries were created using AutoCAD (AutoCAD Mechanical 2010, Autodesk Inc., San Rafael, CA, USA). The geometries were imported into COMSOL Multiphysics (Version 4.2, COMSOL Inc., Burlington, MA, USA) and extruded into a three dimensional geometry as shown in Figure 10-1a-c. The AC/DC module was used to solve for the potential distribution, ϕ. Edges of the electrode channels were modeled as a uniform potential of 100 V or ground. The frequency of the applied signal was incrementally increased from 10^2 to 10^9 Hz using MATLAB (Version R2010b, The MathWorks Inc., Natick, Massachusetts) to create a logarithmically dispersed frequency distribution. ϕ was used to calculate the magnitude of the particle independent DEP vector ($|\vec{\Gamma}|$). This was accomplished by evaluating the partial derivatives of ϕ in the *x*, *y* and *z* directions to determine the directional components of the electric field ($\vec{E}$). These values were then used to calculate $\vec{E}\cdot\vec{E}$. Finally, $|\vec{\Gamma}|$ was calculated by finding the magnitude of the partial derivatives of $|\vec{E}\cdot\vec{E}|$ in the *x*, *y*, and *z* directions. A representative surface plot of the $|\vec{\Gamma}|$ distribution is shown in Figure 10-1.

The numerical approximation of $|\vec{\Gamma}|$ in Equation 7 was calculated in MATLAB based on the electrical component model shown in Figure 10-1e. First, the resistance and capacitance of each element was calculated based on their geometrical properties. The total impedance of the system was then calculated and a frequency dependent transfer function was determined. This function was multiplied by 100 V to determine the voltage drop across the sample channel at frequencies between 10^2 and 10^9 Hz. The current flowing through the channel was then calculated based on the impedance of the sample channel at each frequency.

The geometry presented here has rounded saw tooth constrictions which compress the channel from 500 μm to 100 μm over a distance of 400 μm. These values were used as a linear approximation of the change in channel resistance per unit channel length near the constrictions. Finally, these values were used in Equation 7 to calculate the numerical approximation for $|\vec{\Gamma}|$.

The sample channel and fluid electrodes were prescribed conductivities of 0.01 and 1.4 S/m, respectively. Both were prescribed a relative permittivity of 80 as assumed based on their water composition. The remaining device was prescribed the material properties of either poly-dimethylsiloxane (PDMS), poly-methyl methacrylate (PMMA), polyimide (PI), or polyvinylidene fluoride (PVDF). These materials were selected due to their availability in thin films and suitable electrical properties.

A parametric study was conducted to examine the effect of device geometries on the particle independent DEP vector. Maximum and minimum values for the insulating barrier area, barrier thickness, sample channel depth, and electrode separation distance can be seen in Table 1. PDMS was used as the nominal device material except where stated otherwise.

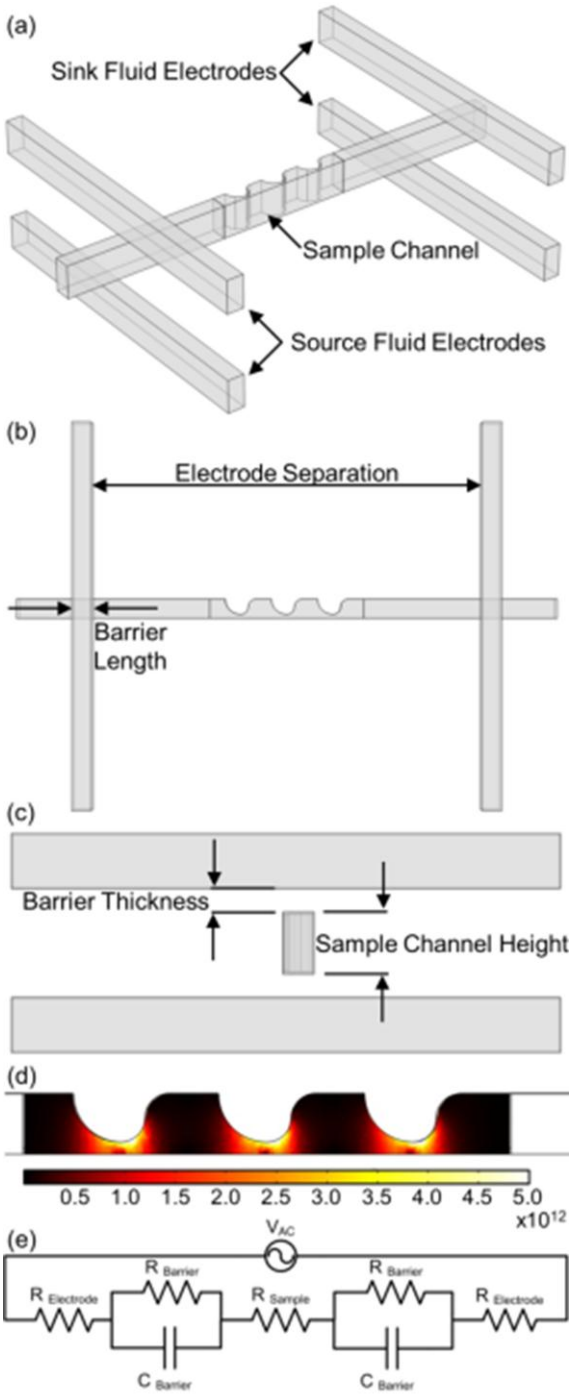

Figure 10-1: (a-c) Isometric, top, and side view schematics of the geometric configuration used in finite element analysis. (d) Surface plot of $|\vec{\Gamma}|$ calculated using the nominal values in Table 1 at 250 kHz. (e) Lumped element model used to calculate the numerical approximations of $|\vec{\Gamma}|$.

Cell Preparation

MDA-MB-231 human breast cancer cells were cultured in DMEM/F12 media. The medium was supplemented with 10% fetal bovine serum (FBS) and 1% of a penicillin/ streptomycin. Cultures were maintained in solution at 37 °C and 5% CO_2 in a humidified atmosphere. All cells were harvested by trypsinization at 80% confluence. The cells were suspended in a low conductivity buffer [77], stained with CellTrace calcein red/orange (Invitrogen, Eugene, OR, USA), washed twice, and suspended again in fresh buffer to achieve a solution conductivity of 100 μS/cm +/- 30 μS/cm and a cell concentration of $3x10^6$ cells/mL.

Experimental Parameters

Devices were fabricated courtesy of Protea Biosciences (Morgantown, WV, USA). Schematic representations of the device can be seen in Figure 10-1a-c. Two pairs of fluid electrode channels straddle a sample channel machined in 900 μm thick PMMA. The source and sink fluid electrode pairs were separated by 1.7 cm. 120 μm thick polycarbonate film layers separate the fluid electrodes from the sample channel. The nominal width of the sample channel was approximately 850 μm with 'saw tooth' features along one edge which constricted the channel to approximately 600 μm. The devices were placed into a vacuum jar for at least 30 minutes prior to experiments to minimize bubble formation within the device during priming. The fluid electrode channels were filled with Phosphate Buffered Saline (PBS) (Geno Technology, St. Louis, MO) and then wire

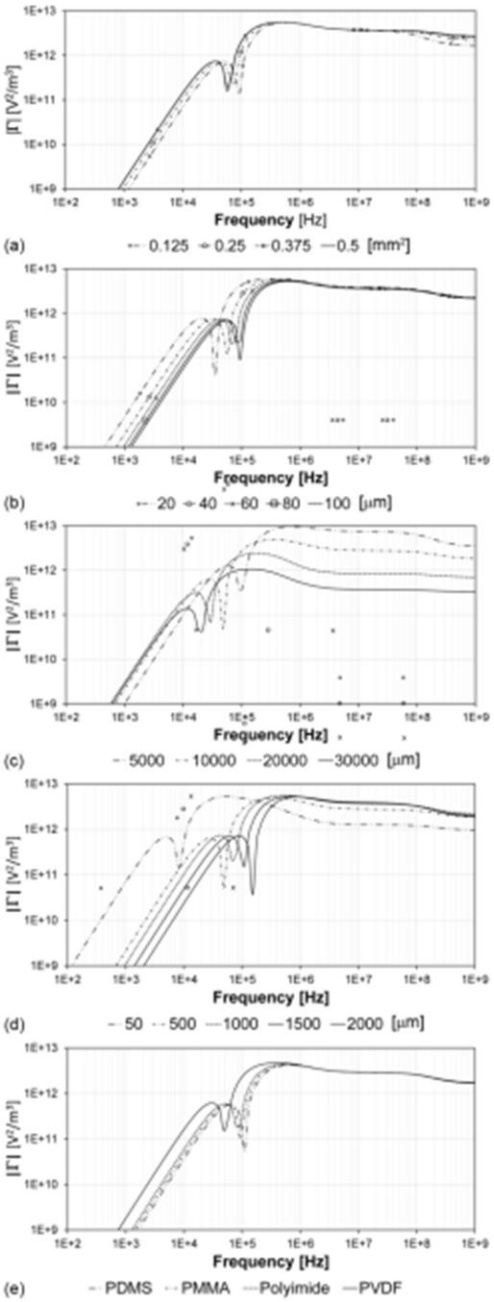

Figure 10-2: Finite element analysis of multilayer cDEP devices. The frequency responses of these devices change relative to (a) barrier cross sectional area, (b) barrier thickness, (c) electrode separation, (d) sample channel depth, and (e) barrier material.

electrodes were placed into the source and sink fluid electrode channels. The sample channel was primed with low conductivity buffer (100 μS/cm +/- 30 μS/cm), then tubing was press fit into the inlet of the channel. The inlet tubing was connected to a 1 mL syringe containing the cell suspension via a blunt needle.

Cell suspensions were driven through the sample channel at a rate of 1.0 mL/hour by a syringe pump (PHD Ultra, Harvard Apparatus, Holliston, MA). An inverted light microscope (Leica DMI 6000B, Leica Microsystems, Bannockburn, IL) was used to monitor the cells.

An AC electric field was created by amplifying (AL-50HF-A, Amp-Line Corp., Oakland Gardens, NY) the output signal of a function generator (GFG-3015, GW Instek, Taipei, Taiwan) to a maximum of 25 V_{RMS}. A step up transformer (AL-T340.4, Amp-Line Corp., Oakland Gardens, NY) was used to achieve output voltages up to 300 V_{RMS} at 600 kHz. Voltage and frequency were measured using an oscilloscope (TDS-1002B, Tektronics Inc. Beaverton, OR, USA) connected to the output stage of the transformer.

Results and Discussion

Numerical Modeling

A surface plot of $|\vec{\Gamma}|$ in the nominal configuration at 250 kHz is shown in Figure 10-1d. The two dimensional slice shown is at the center of the sample channel. In COMSOL, the barrier area was sequentially increased from 0.125 to 0.5 mm^2 by increasing the width of the fluid electrode channels. Because electrode channels are filled with a highly conductive solution (PBS), their dimensions have a negligible effect on the frequency response. Increasing the barrier area effectively reduces the barrier resistance ($R = \rho d/A$) and increases the barrier capacitance ($C = \varepsilon_0 \varepsilon_r A/d$) where d is the thickness, A is the area, ρ is the resistivity, ε_r is the permittivity of the barrier material and, ε_0 is the permittivity of free space. This causes the impedance of the barriers to roll off at a slightly lower frequency as barrier area increases. Figure 10-2a, shows that larger barrier cross sectional areas are preferred, however, there are diminishing returns. Larger unsupported barriers may collapse into the sample channel or break. Ultimately, supportive pillars or structures may be required resulting in a tradeoff between barrier area and mechanical

strength. The frequency response of the device will be negatively impacted by the addition of supportive pillars only to the extent at which they decrease the total barrier area. It is not anticipated that they will induce a strong DEP force as the electric field is relatively constant between fluid electrodes at the same potential.

Decreasing the thickness of the barrier increases the capacitance and decreases the resistance of the barrier. The impedance of thinner barriers falls off more quickly, improving the frequency response of the device as shown in Figure 10-2b. Similar mechanical considerations must be taken when decreasing the barrier thickness as when increasing the barrier cross sectional area. In addition, the voltage at which dielectric breakdown occurs is directly dependent on the thickness of the material. PDMS for example, has a dielectric strength of approximately 20 V/μm. A device with 100 μm barriers can withstand applied voltages in excess of 2000 V_{peak}; however, a thinner barrier of 20 μm can only withstand 400 V_{peak}. These limitations must be strongly considered in device design as simulations suggest that the maximum $|\vec{\Gamma}|$ does not increase significantly as the barrier becomes thinner. If very large voltages are necessary to achieve particle manipulation, for example in the case of organelles or viral particles where the effective particle radius is very small, then thicker membranes may be required at the expense of frequency response.

Increasing the separation distance between the source and sink electrodes has a net effect of increasing the resistance of the sample channel. This in turn causes a greater proportion of the voltage drop to occur across the sample channel. The consequence of this is that for large separation distances, the $|\vec{\Gamma}|$ increases more rapidly at lower frequencies, the response reaches its maximum more quickly, and becomes 'flat' over a larger frequency spectrum. For example, a $|\vec{\Gamma}| = 10^{11}$ is achieved at lower frequencies as the electrodes are pulled apart. At the same time, as shown in Figure 10-2c, the distance between the electrodes increases, causing a decrease in the change in voltage per unit length ($\partial V / \partial x$). This results in a lower maximum $|\vec{\Gamma}|$ value achieved in the sample channel. There is a tradeoff between the 'flatness' of the response needed and the maximum $|\vec{\Gamma}|$ achievable for a given device.

The depth of the sample channel may have the largest impact on the performance of cDEP devices from both an operational and electrical standpoint as shown in Figure 10-2d. The resistance of the sample channel increases linearly as the channel becomes shallower. This increases the total voltage drop across the sample channel, allowing for the generation of significant $|\vec{\Gamma}|$ values at lower frequencies. As the channel is made deeper, the resistance decreases and useful $|\vec{\Gamma}|$ values are pushed higher in frequency. As with barrier thickness and barrier area, the maximum achievable $|\vec{\Gamma}|$ value is independent of the depth of the sample channel. Only the frequency at which this maximum occurs is affected. As the sample channel depth increases beyond 500 μm, the effect on the frequency response becomes less significant and higher levels of throughput become accessible. For example, a multilayer device with a sample depth of 2000 μm (and all other values nominal) has similar electrical performance characteristics as some of the first cDEP devices reported [52], however, keeping bulk fluid velocities the same, the multilayer device will achieve approximately 40 times greater throughput (50 μm deep channels with a flow rate of 0.02 mL/hour verses 2000 μm deep and 0.8 mL/hour).

The membrane used to isolate individual layers of a multilayer device does not have to be the same material as the substrate in which the microfluidic features are patterned. This allows for the investigation of materials which may have better electrical properties than traditional stamping polymers such as PDMS. There are a wide range of biocompatible polymers which are readily available in thin films. Typically, these polymers have relative permittivities of approximately 3. This has to do with the similarity in density of these films and the Clausius-Mossotti relation (K) for an assembly of $–CH_2–$polymer units

$$\varepsilon = \frac{2K\upsilon + 1}{1 - K\upsilon} \qquad [10.7]$$

where $K = 0.327\text{x}10^{-3}$ and υ is the density of the polymer [111] .

Under the influence of a static field, the molecules of dielectric materials become polarized. In an AC field, the direction of the field oscillates. The direction of polarization of the molecules

changes to follow the direction of the applied field. Because this change is not instantaneous, the polarizations of the molecules lag behind the field with a characteristic time known as the relaxation time. This time is typically on the order of 10^{-11} seconds. For the frequencies studied here, the relaxation time for the barrier materials are considered negligible and the relative permittivity is held constant at all frequencies.

For membranes made of PDMS, PI, and PMMA there is no significant change in the frequency response of the devices when all of these materials are the same thickness, as shown in Figure 10-2e. The electrical properties of these materials, derived from manufactures data sheets, are presented in Table 2. The relative permittivity of PVDF, approximately 9.0, gives the material a higher capacitance per unit thickness. Devices using this material as the insulating barrier between layers reach their maximum $|\vec{\Gamma}|$ at lower frequencies. This increases the frequency range over which the devices exhibit a flat DEP response. The maximum $|\vec{\Gamma}|$ is nearly equivalent between each of these materials. This is advantageous as it allows for barrier materials selection to be made based on manufacturing and mechanical considerations.

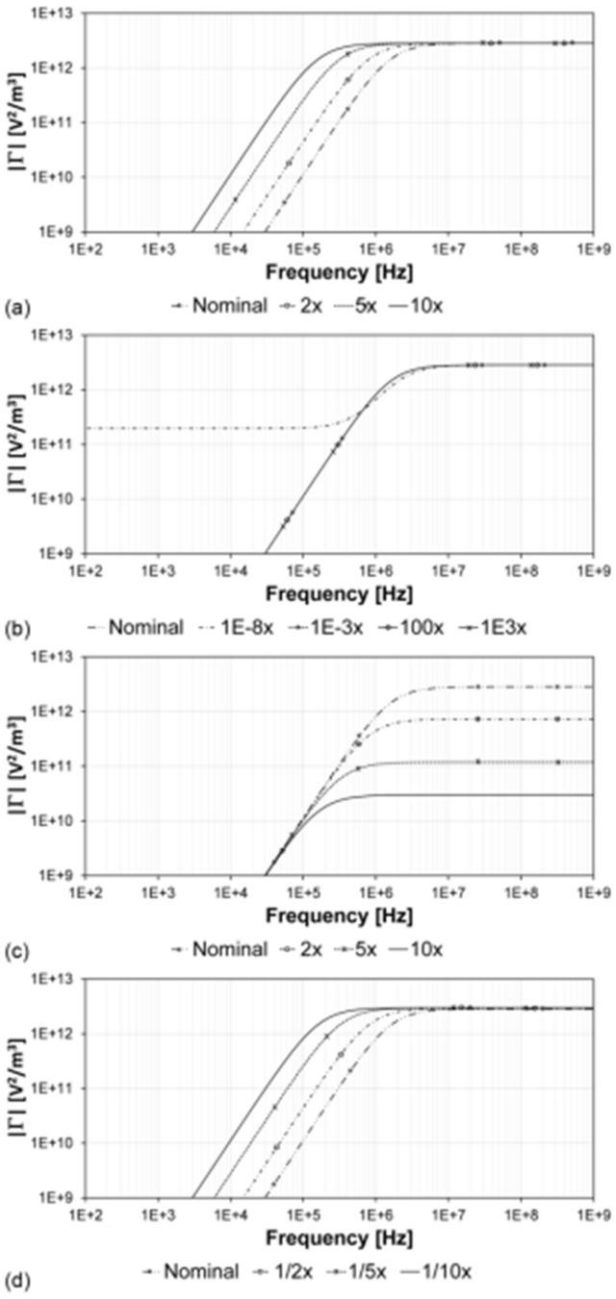

Figure 10-3: Numerical approximation of $|\vec{\Gamma}|$ in multilayer cDEP devices. The frequency responses of these devices change relative to (a) barrier capacitance, (b) barrier resistance, (c) electrode separation, (d) and sample channel depth.

PDMS films of predictable thickness can readily be fabricated by spin coating the polymer on a flat surface and procedures for PDMS-PDMS bonding are well documented in the literature [112]. Commercially available films are generally available in thicknesses of 25.3 μm (0.001 inches), however some specialty films, such as polyimide are available in thicknesses of 7.5 μm or less under brand names of Kapton and Corin XLS. These materials are advantageous over thicker films as they will have a lower net resistance and increased capacitance improving device performance, however, their breakdown voltages will be drastically reduced. In the case of a 7.5 μm polyimide film, operating voltages would be limited to those less than 90 V_{peak}. It should be noted that AC voltages are often applied and measured in terms of the root mean square (RMS) of the peak to peak voltage. The corresponding AC breakdown voltage of a 7.5μm polyimide film will be $\sqrt{2}$ times less than the DC voltage, or 64.6 V_{RMS}.

Equation 7 was used to conduct an additional parametric analysis for comparison with the results determined in COMSOL. This model used nominal values of $2x10^{6}$ [Ω], 2.86 $x10^{4}$ [Ω], 2.89 $x10^{14}$ [Ω], and 9.77 $x10^{-14}$ [F] for the sample resistance, fluid electrode resistance, barrier resistance, and barrier capacitance in Equation 1. These values represent the approximate values of the nominal multilayer device used in the multiphysics simulations. The effect of increasing barrier capacitance is shown in Figure 10-3a. A tenfold increase in barrier capacitance resulted in a frequency response which reaches the maximum $|\vec{\Gamma}|$ value an order of magnitude before the nominal case. This trend matches the results determined via finite element modeling of decreasing barrier thickness and increasing barrier cross sectional area and help validate the use of strictly numerical solutions to analyze cDEP devices.

The resistance of the barrier plays a minimal role in the performance of these devices as shown in Figure 3b. It is not until the resistance of the barrier (or resistivity of the material) is decreased eight orders of magnitude that this component makes a significant contribution. In that case, the resistances of the barrier and of the sample channel are of similar order of magnitude. This minimal effect of barrier resistance is due to the capacitive elements of the barriers which cause their impedance to start rolling off at very low frequencies.

Increasing only the resistance of the sample channel in Equation 1, similar to pulling the fluid electrodes further apart, decreases the maximum $|\vec{\Gamma}|$ value achieved. This trend, shown in Figure 10-3c, is due to the model representing the total voltage dropping over a longer distance, so the change in voltage per unit length becomes smaller. A tenfold increase in sample channel resistance resulted in a two order of magnitude drop in the maximum $|\vec{\Gamma}|$ value. However, the higher resistance sample channels have linear frequency responses over a larger frequency range. This method was also used to model the effect of reducing the sample channel depth. Here, the resistance of the sample channel was increased in Equation 1 and the height of the sample channel was changed proportionately in Equation 6. A tenfold decrease in sample height resulted in a $|\vec{\Gamma}|$ which reached its maximum at frequency an order of magnitude lower. These results, shown in Figure 10-3d, also exhibit the same trend found in the multiphysics simulations shown in Figure 10-2d.

These results show that approximating $|\vec{\Gamma}|$ numerically yield similar results and trends as compared to the more computationally demanding finite element methods. While this method cannot predict the spatial distribution of the electric field, it can be used to generate order of magnitude approximations and explore the implications of specific changes in device geometry. The numerical approximation of $|\vec{\Gamma}|$ (Figure **10-3**) predicts a smooth increase and plateau anticipated for a simple resistor-capacitor circuit. The finite element solutions (Figure 10-2) exhibit a sharp drop in $|\vec{\Gamma}|$ just prior to it reaching its maximum. This indicates the presence of losses, resonance, or inductance which are not accounted for in the numerical approximation. This behavior was not evident in our previous experimental work, though it may have been confounded by changes in the C-M factor, for the cells evaluated, at these transient frequencies.

Experimental Results

A top down view of the multilayer prototype device is shown in Figure 10-4a. In the absence of an electric field, cells flowed freely through the device as shown in Figure 10-4b. When a 250 V_{RMS} potential at 600 kHz was applied, individual cells were observed migrating towards each other forming ‘pearl chains’. This initial indication of the presence of a strong electric field continued at time progressed and successively longer chains of cells formed within the device. These chains, and individual cells, began to migrate towards the ‘saw

tooth' features along the bottom edge of the sample channel and become immobilized. After approximately one minute, a large number of cells had become trapped as shown in Figure 10-4c. Long chains of cells continued to slide along the bottom edge of the device, just above the trapped cells.

This is the first demonstration of dielectrophoresis in a device in which fluid electrodes are fabricated in separate substrates and physically isolated from the sample channel by a thin film. These preliminary results show that it is possible to generate an electric field within the sample channel of a multilayer cDEP device. The dielectrophoretic force generated was great enough to trap cells being driven at a flow rate of 1.0 mL/hour. This represents a 100 fold increase in flow rate compared to this geometry fabricated in a single layer of PDMS [55]. Future work will focus on producing devices with thinner membranes between the sample and fluid electrode layers, measuring the electrical characteristics of the devices, and evaluating the response of cells across a wide frequency spectrum.

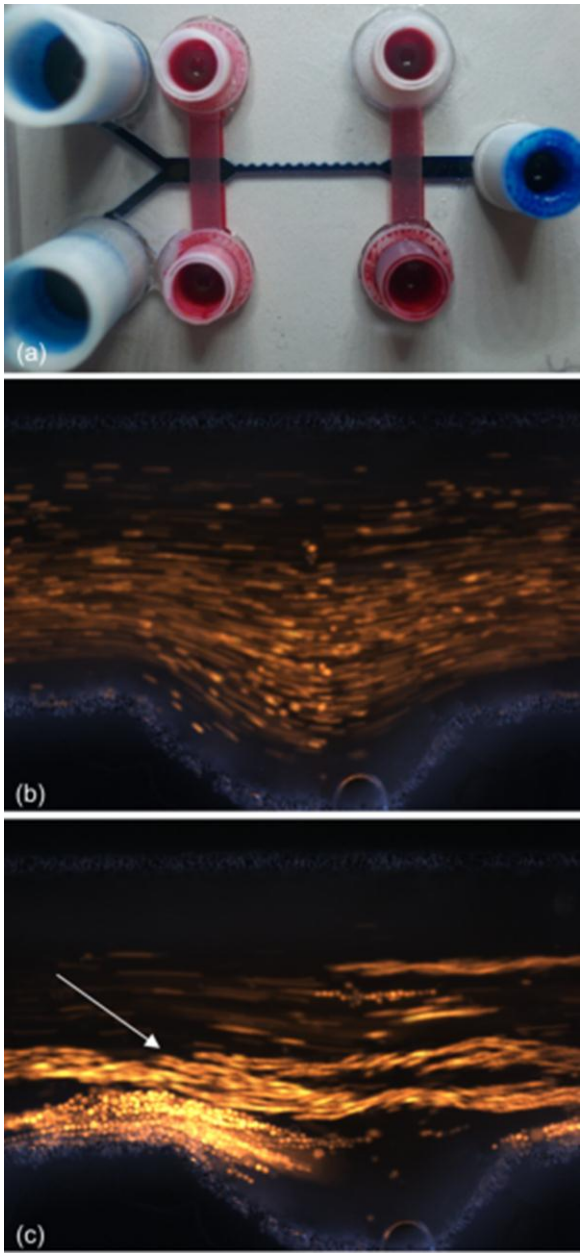

Figure 10-4: (a) A prototype multilayer cDEP device with fluid electrode channels (red) above and below the sample channel (blue). (b) Cells pass freely through the device when the electric field is turned off. (c) Under the influence of a 250 V_{RMS} electric field oscillating at 600 kHz, cells form 'pearl chains', indicated by the white arrow, and become immobilized near the saw tooth features at the edge of the sample channel.

Conclusion

Here we presented the geometrical considerations necessary to produce a multilayer cDEP device that achieves a high level of throughput while maintaining sufficient electric field non-uniformity to manipulate cells. These devices in their nature have a frequency response which must be understood when interpreting experimental results. For this reason the CM factor was decoupled from the ability of the device to produce highly non-uniform electric fields. From an experimental standpoint, production of high voltage, high frequency electrical signals becomes challenging above 1 MHz. Below 1 MHz, ionic and dipole relaxation are expected to influence cells with the former dominating over the later at lower frequencies. Ultimately, the electrical and physical properties of the cytoplasm, cellular and nuclear membranes will affect the dielectrophoretic response.

This work is the first description of a multilayer cDEP device. Analysis was completed using both finite element software and a more efficient numerical approximation. The non-uniform electric field generated within these multilayer devices is comparable to the single layer devices presented previously [108]. While the numerical approximation does not capture some of the intricate fluctuations in the frequency response, it provides an order of magnitude approximation. This approximation is significantly less computationally demanding than the 3D finite element solution taking seconds rather than hours to compute frequency responses for each parameter. This numerical approximation can be adapted for calculation using open source spreadsheet software, providing a less computationally demanding means to model complex cDEP devices. Additionally, this method should provide a reasonable approximation for other insulator based DEP devices.

We demonstrated trapping of MDA-MB231 breast cancer cells in a prototype device at a flow rate of 1.0 mL/hour. This represents a significant increase in throughput over previously reported cDEP devices. Future work will focus refining fabrication of these devices and demonstrating their ability to sort heterogeneous cell populations.

Of the parameters affecting device performance, electrode separation distance had the largest influence on the frequency response. This parameter was also the only one which significantly influenced the maximum value of $|\vec{\Gamma}|$. This has to do with losses associated with regions of the

sample channel between the electrodes not containing constricting features. Consequently, if higher $|\vec{\Gamma}|$ values are needed in conjunction with a low frequency response, a higher input voltage must be applied. The ultimate limiting factors in device performance then reside in breakdown voltage of the barrier material and the ability to generate high frequency signals at high voltages.

Chapter 11: Electrokinetic Flow in Contactless Dielectrophoresis

Introduction

Microfluidics is rapidly becoming the tool of choice for many complex biological applications. The small length scale allows for high control over convection and diffusion transport, reduced volumes decrease the quantity of sample and reagents consumed, and higher resolution and sensitivity are obtained. The low Reynolds number due to device dimensions ensures laminar flow in all but the most extreme circumstances. This produces predictable flow patterns that are ideal for separations and analysis, since low to negligible mixing is induced [113].

Electrokinetic techniques are one of the main pillars of microfluidics as analytical systems. These techniques have great potential for handling bioparticles, from macromolecules to cells. Isotacophoresis and isoelectric focusing have found important applications in protein separations [114]. One important characteristic of microanalytical electrokinetic methods is intact microorganisms can be analyzed. For example electrotaxis, the movement of adherent cells in response to an electric field, has been used to guide the migration of neural stem cells [115] and lung cancer cells in 3D scaffolds [116]. Electrorotation is another important electrokinetic method employed successfully for cell assessment that allows extracting dielectric properties [117] [57]. Electrical impedance has also been employed in microdevices for the detection and quantification of bacterial cells in suspensions, with great application in food safety analysis [118]. A number of excellent reviews which describe the assessment and manipulation of cells with electric fields in depth have been published recently [119-121].

Among the family of electrokinetic (EK) techniques, dielectrophoresis (DEP), the motion of a particle due to polarization effects in the presence of a non-uniform electric field, has proven to have an enormous potential for applications with cells [121]. Microfluidic applications exploiting DEP originally used electrodes patterned on the bottom of a channel which trapped cells as they were driven past by pressure flow [110]. Though design and fabrication of microdevices which apply this technique might be complex and expensive, its applications have been demonstrated as effective means to trap DNA [122], viruses [123], and bacterial [124] and mammalian cells [125]; as well as

for identification of antigen expression and blood typing [126]. Three-dimensional carbon electrodes, which require a less extensive fabrication process, have been used as an alternative to metal electrodes. Carbon-electrode dielectrophoresis (carbon-DEP) has been used to trap cells such as yeast and bacteria with the significant advantage of providing higher throughputs due to the 3-D configuration and allowing for centrifugal pumping in a CD-like platform [127-129]. However, electrode-based DEP can have some drawbacks such as loss of functionality due to fouling, which is common when working with bioparticles, such as cells. Additionally, direct contact between the electrodes and the sample can lead to cell damage [48,52].

As an alternative, a non-uniform electric field can also be produced by placing insulating structures within a channel and using two external electrodes placed at the inlet and outlet of a channel [43]. In this configuration usually DC fields are used and the electric field drives electroosmotic flow while the insulating structures distort the electric field distribution inducing a DEP force on any particles within the fluid. This technique, known as insulator-based dielectrophoresis (iDEP) is advantageous as the dielectrophoretic force produced extends to the entire height of the channel allowing for 3-D particle manipulation [130]. Recently, there has been an important progression of iDEP studies, demonstrating its application as an effective method to trap single cells [131], concentrate proteins [132] and DNA [47], separate and concentrate mixtures of particles [48,133], interrogate cell viability [134], and blood types [135]. These systems have also been used with low frequency AC potential, where the shape of the applied signal is an additional parameter to control particle manipulation [136]. Important progress on the mathematical modeling of iDEP systems has also been reported allowing for the prediction of particle selectivity, trapping and concentration within a microchannel [130,137]. The majority of iDEP studies have employed fairly high DC potentials to manipulate particles, from proteins [138] to cells [139]. The resulting Joule heating and electrothermal flow effects [140,141] are important challenges in iDEP that lead to electrochemical effects and bubble generation. These high DC potentials can also result in significant pH changes that can lead to bioparticle denaturation or cell death [142].

Despite these challenges, iDEP offers great potential and flexibility for successful cell manipulation. Due to that, other recent techniques related to iDEP have been developed. Insulator gradient dielectrophoresis (g-iDEP) employs tapered microchannels with insulating

saw-tooth structures along the wall, this method has been successfully employed for separating bacteria and assessing blood cells [51,143]. Contactless DEP (cDEP) is another successful technique where insulating structures distort the distribution of an electric field to generate DEP forces; however, this method has a significant advantage since the sample does not come in direct contact with the electrodes.

In cDEP, AC electric potentials are applied employing electrodes immersed in a highly conductive solution, which is isolated from the sample channel by thin insulating membranes. The capacitive nature of these membranes allows for the transmission of AC signals into a main sample channel. Electric fields are generated across the microchannel width, perpendicular to the particle flow, allowing for highly selective particle manipulation since positive and negative DEP can be employed [144]. Contactless DEP has found a special niche in biomedical and clinical applications. Recently, cDEP has been used to isolate live cancer cells from beads of similar size [54], dead cells of the same cell line [108], live cells from dissimilar cell lines [145], and dilute blood samples [146].

A significant challenge with current cDEP devices is the requirement of a syringe pump to accurately drive pressure driven flow of samples. This increases the peripheral equipment count and impacts the portability of the devices. In conjunction with the development of lab-on-a-chip technologies, there has been a surge in micro-scale pumping techniques aimed at eliminating the need for external pumps. These devices can be generalized into two main groups; mechanical displacement and electro-/magneto-kinetic pumps [147]. Mechanical displacement pumps apply a pressure force on a flexible diaphragm [148] or into peristaltic [149] and rotary pumping geometries [150]. In contrast, Electro-Magneto-kinetic pumps directly transfer electromagnetic energy into the fluid to achieve a steady state flow. Electro-hydrodynamic devices induce a fluid body force through the interaction of a dielectric fluid's space charge density and a non-uniform electric field [147]. These usually require a gradient in the conductivity or permittivity within the fluid, caused by unmixed fluid layers, suspended particles, or as a result of anisotropic heating [151]. Magnetohydrodynamic pumps use perpendicular electric and magnetic fields to induce a Lorentz force in the fluid which acts to drive the fluid in a direction perpendicular to both applied fields [152]. Alternatively, electro-osmotic pumping techniques rely on the surface charge that forms

when fluids come into contact with a channel wall [59]. This simple technique only requires the formation of an electric field along the direction of desired fluid motion.

This chapter shows the combination of cDEP and EK pumping for highly controlled microparticle manipulation in a microchannel with a set of six electrodes (Figure 11-1). AC potentials applied across the width of a microchannel were used to achieve dielectrophoretic trapping at the center of the main channel in an array of cylindrical insulating structures. EK pumping was created by generating a DC potential drop across side channels separated from the sample channel by thin membranes in a contactless manner. This established a DC potential drop across the length of the sample microchannel to achieve EK pumping. Driving the fluid electrokinetically was chosen due to its simple structure, ease of fabrication, fast response time, and the ease of integration with other micro-components and software controls. Application of an AC potential perpendicular to the electrokinetic flow, allowed for dynamic particle trapping and releasing by reduction or removal of the applied potential. This configuration eliminates the need of a micropump, simplifying the system and enhancing portability [153]. The performance of the system was simulated employing COMSOL *Multiphysics* to aid on the design of the microdevice. The results, from both experiments and simulations, demonstrate the important advantages for selective and highly controlled trapping, enriching and manipulation of microparticles at much lower applied potentials by employing the combination of AC-cDEP with EK pumping.

Theory

A hydrodynamic force, $\mathbf{F}_{\mathrm{DRAG}}$, is exerted on the particles as they translate through fluid.

$$\mathbf{F}_{DRAG} = 6\pi\eta r_p \mathbf{V} \qquad [11.1]$$

where **V** is the velocity of the particle relative to the suspending medium. The steady state velocity of the particles is determined by a balance between the dielectrophoretic forces and Stoke's drag in summation with the electrokinetic velocity. In this preliminary study, the effect of acceleration is considered negligible, and the relationship for particle translation is given by:

$$\mathbf{U} = \mathbf{V}_{ek} + \frac{\varepsilon_m r_p{}^2 \,\mathrm{Re}[K(\omega)]}{3\eta} \nabla(\mathbf{E}_{RMS} \cdot \mathbf{E}_{RMS}) \qquad [11.2]$$

3 Methods

3.1 Sample Preparation

Yellow-green fluorescent carboxylate-modified polystyrene microspheres with 1 μm in diameter (Invitrogen, Carlsbad, CA, USA), ex/em 505/515, were resuspended in distilled water to a concentration of 1 x 10^7 beads/ml. Final sample fluid had a conductivity of 0.001 S/cm and a pH of 5.7.

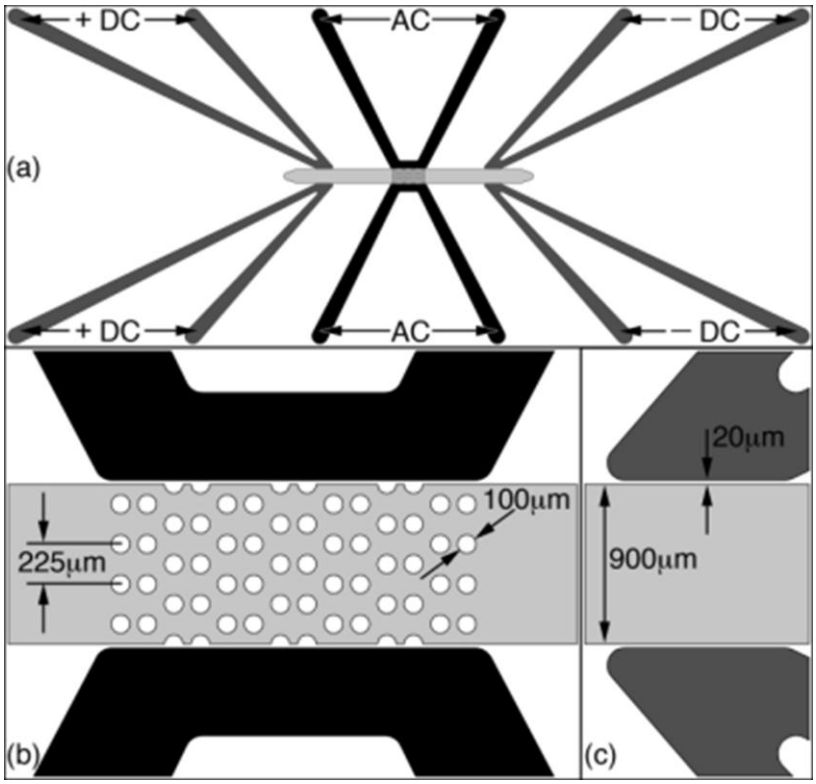

Figure 11-1: Schematic representations of the device used in this study. (a) The device consists of a single sample channel (light grey) and six fluid electrode channels. The DC fluid electrode channels (dark grey) were used to establish a DC field within the sample channel and set up EO fluid flow. The AC fluid electrode channels (black) were used to establish a strong DEP force around (b) insulating structures within the sample channel. (b-c) The barriers which isolate the fluid electrodes from the sample channel are 20 μm thick.

3.2 Device Fabrication

A silicon master stamp was fabricated on a <100> silicon substrate using photolithography. Deep Reactive Ion Etching (DRIE) was used to etch the silicon master stamp to a depth of 15 μm. Surface roughness was reduced by etching the wafer in tetramethylammonium hydroxide (TMAH) for 5 minutes. Finally, a thin layer of Teflon was deposited to facilitate stamp removal using typical DRIE passivation parameters. Liquid phase polydimethylsiloxane (PDMS) in a 10:1 ratio of monomers to curing agent (Sylgrad 184, Dow Corning, USA) was degassed under vacuum prior to being poured onto the silicon master and cured for 15 minutes at 150°C. Fluidic connections to the channels were punched into the PDMS using 1.5 mm core borers (Harris Uni-Core, Ted Pella Inc., Redding, CA). Glass microscope slides were cleaned with soap and water, rinsed with distilled water, ethanol, and then dried with compressed air. The PDMS replica was bonded to a clean glass after treating with air plasma for 2 minutes (Model PDC-001, Harrick Plasma, Ithaca, New York).

3.3 Device Geometry

The device, shown in Figure 11-1, consists of a straight sample channel (light grey) and six fluid electrode channels. The sample channel is 900 μm wide and contains 14 columns of pillars with 100 μm in diameter. Groups of two columns are offset from the neighboring sets by 225 μm in the y-direction center-to-center and all columns are arranged 150 μm from center-to-center in the x-direction. This geometry was chosen to minimize the effects of DC DEP in the x-direction and maximize the effect of AC DEP.

The fluid electrode channels are divided into two groups. Four DC fluid electrodes (dark grey) are located near the inlet and outlet of the sample channel. These are designed to establish a static DC voltage drop across the sample channel and induce EO flow. The two remaining fluid electrode channels (black) straddle the sample channel near the pillars. These are designed to establish an AC field and induce DEP trapping of particles at the pillars. The barriers separating the sample channel from the six fluid electrodes are 20 μm thick.

3.4 Mathematical model and simulations

Two-dimensional geometries were created using Autocad (Autocad Mechanical 2010, Autodesk Inc, San Rafael, CA, USA). The geometries were imported into COMSOL Multiphysics (Version 4.2, COMSOL Inc., Burlington, MA, USA) where the Electrostatics and AC/DC modules were used to solve for the potential distribution, ϕ, using the governing equation $\nabla\cdot(\sigma^* \nabla\phi)=0$ where σ^* is the complex conductivity, that is defined in terms of the real conductivity and permittivity as: $\sigma^*=\sigma+i\omega\varepsilon$, where $i=\sqrt{-1}$. In the Electrostatics module, the boundary conditions were prescribed uniform potentials of +250 V and -250 V for the positive DC and negative DC fluid electrodes, respectively. In the AC/DC module, the boundary conditions were +125 V and -125 V on the top and bottom AC fluid electrodes, respectively. This was done to evaluate the time averaged 0 V potential at the center of the sample channel as anticipated experimentally when a sinusoidal 250 V_{RMS} is applied. The resultant voltages were then summed and used to evaluate the electric field distribution within the sample channel.

All fluid electrodes were defined as phosphate buffered saline (PBS), the sample channel as DI water, and all remaining domains as PDMS. The values for the electrical conductivity and permittivity of the PDMS, DI water, and PBS that were used in this numerical modeling were similar to those reported earlier [52,53]. The DI water and PBS had a relative permittivity of 80 as assumed based on water content. The conductivity of the sample media and PBS were defined as 0.001 and 1.4 (S/m), respectively. The relative permittivity and conductivity of the PDMS were defined as 2.7 and $8.33\text{x}10^{-13}$ (S/m), respectively. The zeta-potential (ζ) between PDMS and the sample was approximated as 1, the viscosity (η) and permittivity (ε_m) of the sample were set to $8.9\ \text{x}10^{-4}$ [N·s/m^2] and 80 based on their water composition.

3.5 Experimental Parameters

The devices were placed into a vacuum jar for at least 30 minutes prior to experiments. The fluid electrode channels were filled with PBS, and then copper wire electrodes were placed in each side channel inlet. The sample channel was primed and 200 μL pipette tips filled with extra sample fluid were used to balance the pressure at the inlet and outlet.

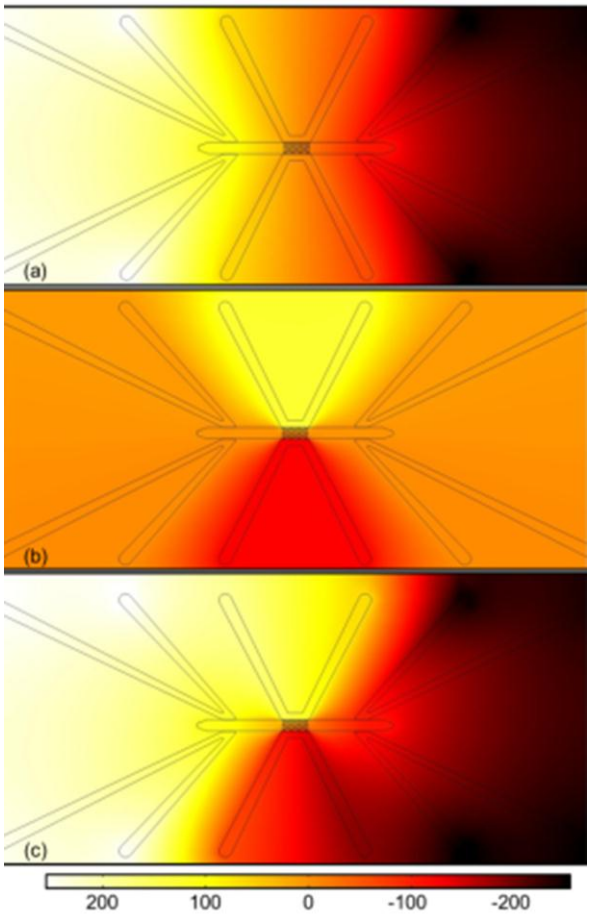

Figure 11-2: Computational results for the voltage distribution within the device when (a) only the DC fluid electrodes are energized (500 V_{DC}) , (b) only the AC fluid electrodes are energized (250 V_{RMS}), and (c) when the AC and DC fluid electrodes are simultaneously energized. The scale is presented in units of volts (V).

An inverted light microscope (Leica DMI 6000B, Leica Microsystems, Bannockburn, IL) was used to monitor the experiments. A high voltage, low current DC power supply (HVS448 6000D, Labsmith Inc., Livermore, CA) was used to apply +250 V and -250 V to the positive and negative DC fluid electrode channels, respectively. An independent channel was used for each polarity and the ground connections from the two channels were connected together. A 250 V_{RMS} 500 kHz signal was then applied across the AC fluid electrode channels. This high voltage, high frequency waveform was produced through a combination of waveform generation, amplification, and step up transformation. The output signal of a function generator (GFG-3015, GW Instek, Taipei, Taiwan) was pass through a wideband amplification system (AL-50HF-A, Amp-Line Corp., Oakland Gardens, NY, USA). A step up transformer was then used to achieve output voltages up to 300 V_{RMS}. Voltage and frequency were measured using an oscilloscope (TDS-1002B, Tektronics Inc. Beaverton, OR, USA) connected to the output stage of the transformer.

Particle enrichment was quantified using image analysis on data acquired before and after the

AC signal was applied. The Measure RGB plugin in ImageJ (version 1.43u, National Institutes of Health, USA) was used to quantify the red, green and blue intensity within the sample channel. These values were averaged and normalized to the area analyzed.

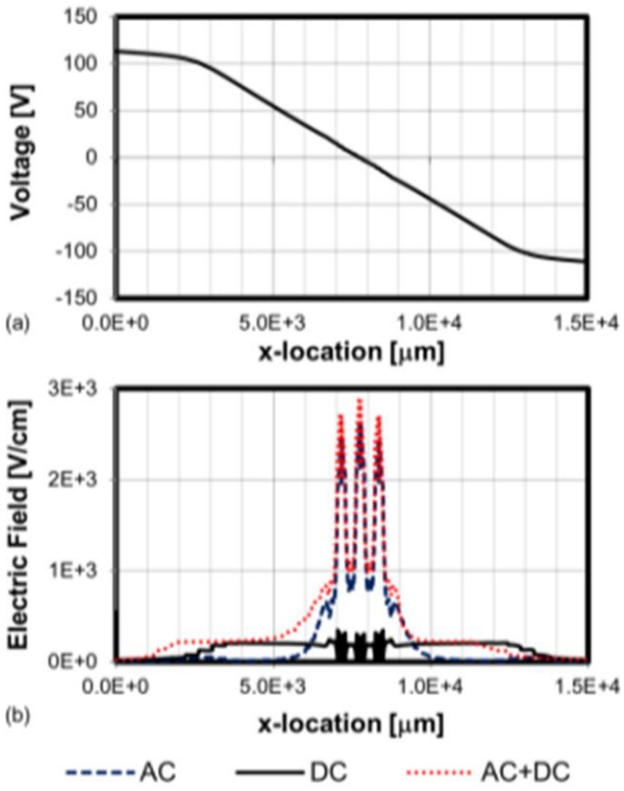

Figure 11-3: (a) Voltage distribution within the sample channel from inlet to outlet when a 500 V static potential is applied across the DC fluid electrodes. A linear regression of this curve shows a static electric field of 199 V/cm is generated within a large region of the device. (b) Electric field distribution along the length of the device when AC only (dashed line), DC only (solid line), and AC + DC electric fields (dotted line) are applied.

Results and Discussion

Simulation Results

Figure 11-2a shows the simulations results obtained by applying a static potential of 500 V_{DC} which was established across the DC fluid electrodes on the extreme ends of the sample channel. The voltage drop across the PDMS is nearly linear across the device (voltage drop at the center of the channel will be shown in Figure 11-3). As observed in Figure 11-2a, the voltage is nearly constant for the first 2.5 mm from the extreme edges of the sample channel. These segments are from the edges of the sample channel to the inner most edges of the DC fluid electrode channels. In the sample channel between the positive and negative DC fluid electrodes, the voltage drops linearly from approximately +100 V_{DC} to – 100 V_{DC}. A linear fit of this curve predicts that an electric field of 199 V/cm is established in the sample channel when 500 V_{DC} is applied across the fluid electrodes. As anticipated due to the symmetry of the device, the potential at the center of the sample channel is 0 V_{DC}.

Figure 11-2b shows the potential in the device when only an AC voltage of 250 V is applied to the AC fluid electrodes. There are regions of elevated (or lowered) potential in proximity to the energized fluid electrodes. The magnitude of the voltage drop at the center of the sample channel, from top to bottom, is approximately 20 $V_{RMS.}$ The remainder of the device, including a

large section of the sample channel, has no substantial change in potential. Figure 11-2c shows the potential distribution within the device when both AC and DC voltages are applied. In this scenario, the voltage drop across the length of the sample channel continues to be strongly influenced by the DC voltage. These results show that a DC voltage can be applied across 'contactless' fluid electrode channels and induce a strong electric field within a sample channel. This field can be used to set up an electroosmotic flow without direct contact between the sample and the electrodes. The application of an AC voltage perpendicular to this DC field appears to have little impact on the potential distribution along the length of the channel, but may potentially affect the flow.

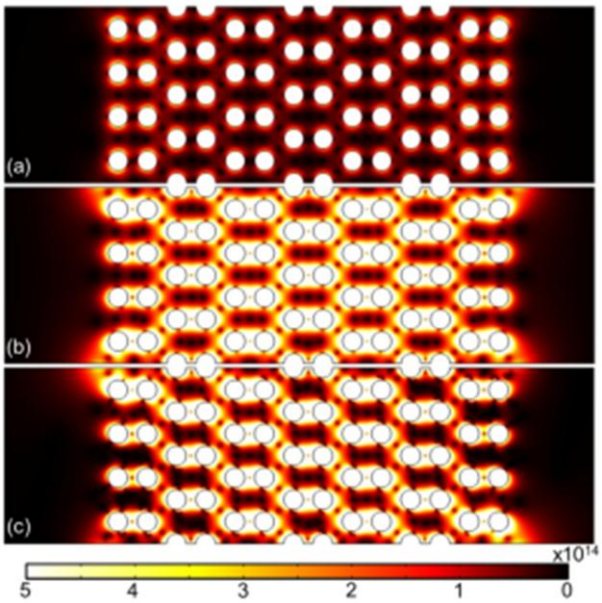

Figure 11-4: DEP field within the sample channel when (a) only the DC fluid electrodes are energized (500 V_{DC}), (b) only the AC fluid electrodes are energized (250 V_{RMS}), and (c) when the AC and DC fluid electrodes are simultaneously energized. The scale is presented in units of V^2m^{-3}.

Figure 11-3a and 3b show the voltage drop and the electric field distribution in the center of the sample channel from inlet to outlet, respectively. As it can be seen from Figure 11-3a there is DC voltage drop of approximately 200V across the length of the sample channel. Figure 11-3b shows the distribution of the electric field across the length of the sample channel, when applying only DC potential, only AC potential and both AC and DC potentials. From Figure 11-3b it is observed that electric field varies significantly only when the AC potential is applied and only in the region containing the insulating posts.

Figure 11-4a shows the gradient of the electric field squared (DEP field) when only the DC voltage is applied. A large DEP field is present close to the top and bottom of each of the pillars. These regions are co-located with regions of high fluid velocity (Figure 11-5). Figure 11-4b shows the DEP field for the scenario when only an AC voltage is applied. The volume of the device in which strong DEP forces occur is substantially larger than in the case of only DC voltage. In addition, the magnitude of the DEP field is elevated in regions between the pairs of posts. In these zones, the fluid velocity is anticipated to be low, improving the probability that particles will become trapped. When the AC and DC fluid electrodes are energized the resulting DEP field, shown in Figure 11-4c, becomes slightly distorted. This is due to the interaction of the AC and DC fields and the magnitude of the distortion is anticipated to change with the phase of the AC signal.

Figure 11-5 shows the ratio of drag to DEP forces when 500 V_{DC} and 250 V_{RMS} are applied. As anticipated, particle velocities are the greatest in regions where the pillars constrict the channel width. In contrast, there exist regions of relatively low fluid velocity between pillar horizontal pairs. This combined with the high DEP field (Figure 11-4c) creates a region of low particle velocity in which the probability of particle trapping is maximized.

Experimental Results

When a static voltage of 500 V_{DC} was applied across the DC fluid electrodes, electroosmotic flow was induced as shown in Figure 11-6a. As anticipated, since EK flow has a linear dependence with the electric field, the velocity of the particles increased as the applied voltage was elevated. At 350 V_{DC} the particles are mainly moving due to EK flow, only a small number of stray particles seem to be adhered to some of the posts and microchannel bottom, but this is not a DEP effect. At 350 V_{DC} and above a small counter current developed along the top edge of the sample channel. A population of particles was observed moving in the opposite

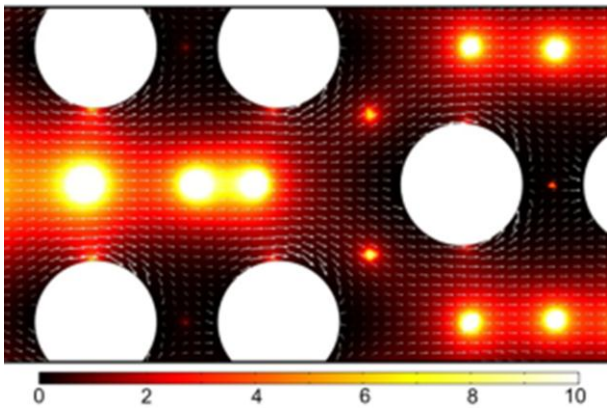

Figure 11-5: Surface plot of the ratio of Drag / DEP forces calculated using experimental parameters. Arrow plots show normalized simulated particle trajectories. Particle trapping is predicted to occur in the dark regions where the arrows turn and oppose the bulk flow.

direction of the bulk flow. The cause of this counter flow is currently unknown, but it may be a result of the development of pressure or thermal gradients.

As shown in Figure 11-6b, when a static voltage of 500 V was applied across the DC fluid electrodes and a 250 V_{RMS} signal was applied across the AC fluid electrodes, particles began to collect near the pillars due to dielectrophoretic trapping, this means that DEP overcame EK in those regions. In agreement with the theoretical predictions (Figure 11-5), most particles collected close to the left and right tangents of the pillars. However, some populations collected in vortices which formed in front of the pillars. The cause of these vortices is currently under investigation and is likely due to the interaction of the AC and DC fields as the AC phase changes. After one minute, the AC field was turned off while the DC potential was still on and the particles were released downstream (Figure 11-6c). Image analysis showed a 9.32 fold increase in per unit area intensity.

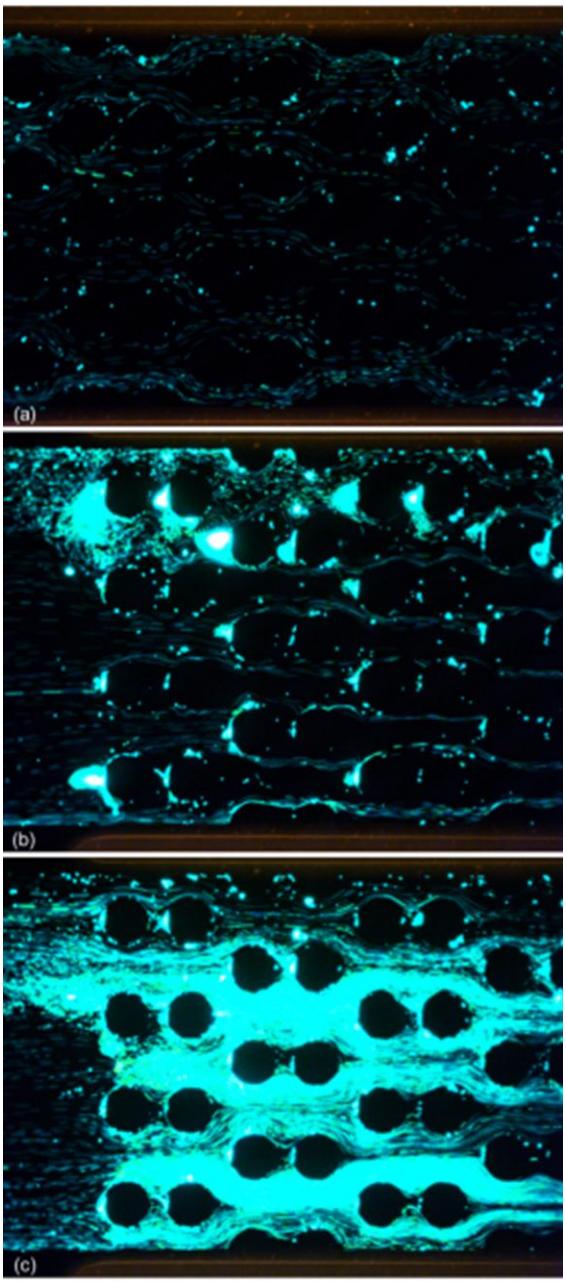

Figure 11-6: Experimental application of electric potentials to the device. (a) When only the DC fluid electrodes are energized to +/- 250 V_{DC}, EO pumping drives particles from left to right. (b) When the AC fluid electrodes are simultaneously energized to 250 V_{RMS}, particles between to trap around the insulating pillars. (c) After 1 minute, the AC potential is turned off and particles are released downstream.

Concluding Remarks

The device presented here is the first example of electrokinetic pumping using physically isolated fluid electrodes. This technique is advantageous as it eliminates sample-electrode contact and the need for platinum or silver-silver chloride electrodes. Another attractive feature of the combination of cDEP with EO flow is the potential

for highly controlled particle manipulation with DEP at much lower applied potentials than traditional iDEP, and with simpler systems that does not require the use of an external pump. This mode of static electric field generation has applications in a number of microfluidic microdevices including cell sorting, trapping, and migration studies. This technique eliminates the need for an external pump in cDEP designs, increasing the portability of the systems. Future work will focus on examination of the vortex phenomena observed during experimentation and investigating the viability of this technique for cell sorting.

Chapter 12: Effects of High Frequency and Pulsed Electric Fields on Cells in Suspension

Introduction

The application of an external electric field causes a redistribution of charge within a cell resulting in an increase in the cell's transmembrane potential (TMP). This, in turn, increases the free energy in the molecules in the cell membrane and the rate of transport of larger molecules into the cell. The process, known as electropermeabilization or electroporation, has been widely used in biology to transfer macromolecules, into cells while maintaining cell viability. Irreversible electroporation (IRE) results if the external field intensity increases past a certain threshold, such that the cell membrane is permanently destabilized and the cell cannot recover, IRE was first demonstrated by Davalos et al. [1] to be an effective means of non-thermally ablating tissue and tumors. Charge redistribution in presence of an electric field is not instantaneous. For a brief time, ions internal and external to the cell rearrange in response to the external field. This displacement current halts as the TMP reaches its maximum, after approximately 1 μs. If the electric field is pulsed or due to a high frequency AC voltage, a displacement current propagates through the cell giving rise to increased membrane potentials in the nucleus and organelles. In typical reversible and irreversible electroporation protocols the pulses are a single polarity with on times on the order of 100 to 1000 microseconds. In this chapter, we show that trains of sub-microsecond pulses can be used to disrupt the cell membrane causing instantaneous and delayed cell death.

Methods

Numerical Modeling

A numerical model of a cell in suspension was created in Comsol 4.2. Two schemes were used to model the cell as a membrane covered sphere. In the first model, individual domains were created representing the sample fluid, cell membrane, and cytoplasm. The 5 nm thick spherical shell domain representing the cell membrane required significant modification to the default meshing parameters and resulted in a large number of tetrahedral elements. Briefly, the entire geometry was assigned a single mesh with a predefined density of 'Extremely course'. The values for the default parameters were then changed for minimum element size (0.00025), maximum element growth rate (1.2), resolution of curvature (0.04), and resolution of narrow

regions (0.0001) to successfully mesh the geometry with 817184 tetrahedral elements. A computer with a quad core 3.0 GHz process and 8 GB of ram required 15 hours of computation time to solve a 14 μs transient model with 1,092,902 degrees of freedom (results shown in Figure 12-1). This model was used to calculate the frequency, sinusoidal, and pulse response of the TMP for conductivities between 0.01 and 10 S/m. This model was presumably the most accurate representation of the TMP; however, it was painfully computationally expensive. It also limited analysis of transmembrane potentials to the cell membrane.

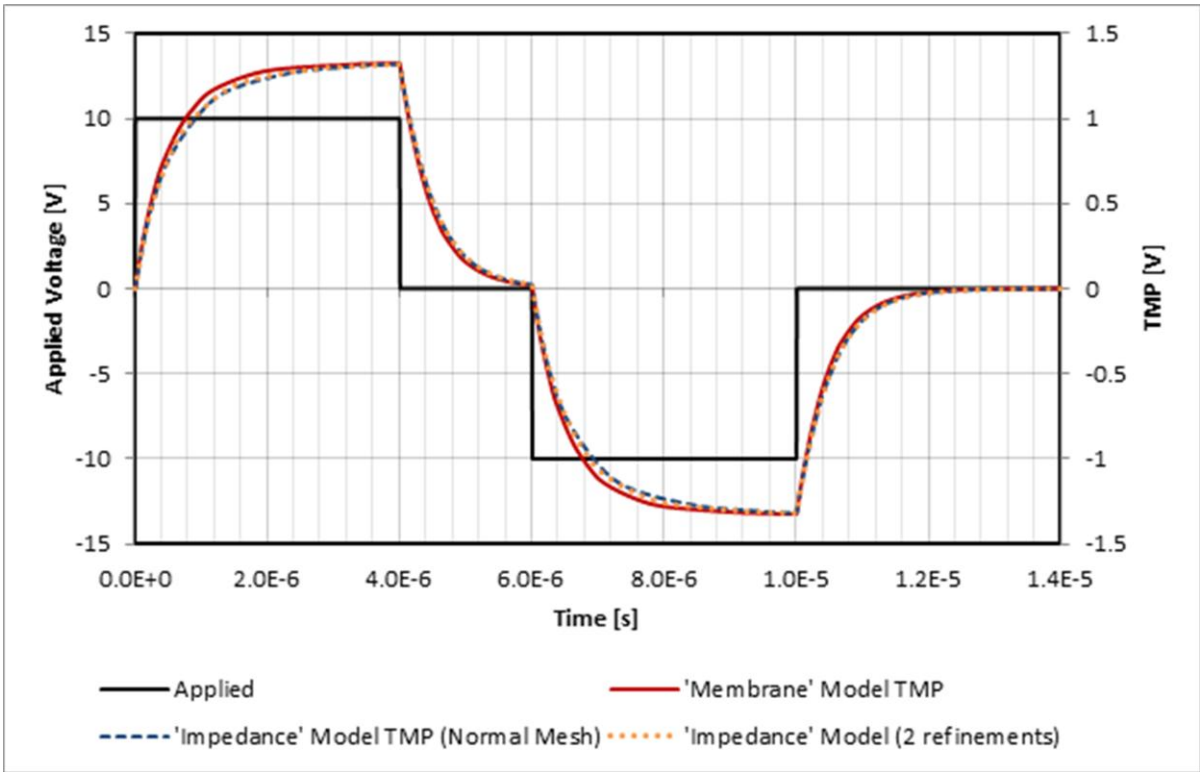

Figure 12-1: Numerical simulation of the transmembrane potential (TMP) of a cell suspended in 1.0 S/m solution under the influence of a 1000 V/cm pulsed electric field. The discrete membrane model solved in 15 hours while the refined and unrefined impedance boundary models solved in 27 and 14 minutes respectivly.

To model the effects of bursts of bipolar square waves and effects on the nuclear membrane, a more efficient impedance boundary condition model was used. In this method, a square domain represented the experimental media and two spheres represented the domains for the cytoplasm and nucleoplasm, respectively. For each domain, a separate Electric Currents physics module was used and the dependent voltage variables were defined as V_{media}, V_{cyto}, V_{nuc} for the media, cytoplasm, and nucleoplasm domains, respectively. Variables were then defined to calculate the cell membrane (TMP) and nuclear membrane (nTMP) as ($V_{media} - V_{cyto}$) and ($V_{cyto} - V_{nuc}$),

respectively. In the Electric Currents module, the boundaries representing membranes were defined as impedance boundary conditions with reference voltages prescribed as the voltage in the adjacent domain. For example, in the Media domain, the boundary representing the cell membrane was defined as an impedance boundary with reverence voltage of V_{cyto}. The layer specification was defined as a 'thin layer' and the electrical conductivity, relative permittivity, and surface thickness were defined using the values presented in Table 12-1.

Parameter	Value		Reference
membrane thickness	5	[nm]	Alberts 1994 'Mollecular Biology of the cell'
cell radius	8.88	[μm]	Sano 2011
membrane conductivity	3e-7	[S/m]	Miklavcic 2006 / Gascoyne 1993
membrane capacitance	0.01518	[F/m^2]	MDA-MB231 Sano 2011
cytoplasmic conductivity	0.3	[S/m]	Miklavcic 2006 / Hozel 1992
cytoplasmic permittivity	50		Sano 2011
nucleus-cytoplasm ratio	0.5		

Table 12-1: Parameter values used in parametric studies on the TMP

In the impedance boundary condition model, the mesh was defined as a single Free Tetrahedral group with 'Normal' sized elements resulting in 17825 tetrahedral elements. In a preliminary study of this model, an additional mesh refinement step (Number of refinements = 2) was also taken. With refinement, this computation of the same 14 μs simulation was completed in 27 minutes. Without refinement, the computation time was further reduced to 14 minutes. When compared to the physical boundary model, both impedance boundary configurations sufficiently reproduced similar results. The unrefined impedance boundary condition model was used to conduct the remaining parametric studies.

Cell Preparation and Experimentation

MDA-MB-231: MDA-MB-231 human breast cancer cells were suspended in buffer with conductivity of 0.1 S/m at a concentration of $2.5x10^6$ cells/mL. A custom pulse generation system capable of delivering 1000 V_{Peak} in each polarity was used to create electric field intensities of approximately 1000, 2000, and 4000 V/cm across cell suspensions in 1 or 2 mm electroporation cuvettes. MDA-MB-231 cells were exposed to 90 burst consisting of 200 bipolar square wave pulses 700 ns wide separated by 1.8 μs of dead time, shown in Figure **12-2** (top and middle) at a repetition rate of 1 Hz. Cell viability was assessed 1 and 16 hours post treatment using a Vi-Cell cell viability analyzer. Total viability after 16 hours was quantified as the ratio of live treated cells to live untreated (sham control) cells.

PPT8182: Additional experiments were conducted with to PPT8182 murine primary pancreatic tumor cells suspended in a buffer at a concentration of $5x10^6$ cells/mL with a conductivity of 0.2 S/m. 100 μL of cell suspension were added to a 2 mm gap cuvette and 80 bursts with 50 microseconds on time in each polarity (100 μs total) were applied. Within each burst, individual pulses had on times of 250 ns, 500 ns, 1, 2, 5, 10, or 50 μs. There was a 2 μs delay time between the end of a pulse and the beginning of the next pulse in the opposite polarity. The cells were exposed to electric fields with magnitudes of 1500, 3000, and 4000 V/cm.

Results and Discussion

Numerical Modeling

Figure 12-3 shows the maximum TMP for an MDA-MB-231 cell in a 400 V/cm electric field for frequencies between 1 Hz and 100 MHz. This is approximately the electric field experienced by cells as they pass through the constricted regions of the cDEP sorting devices presented in

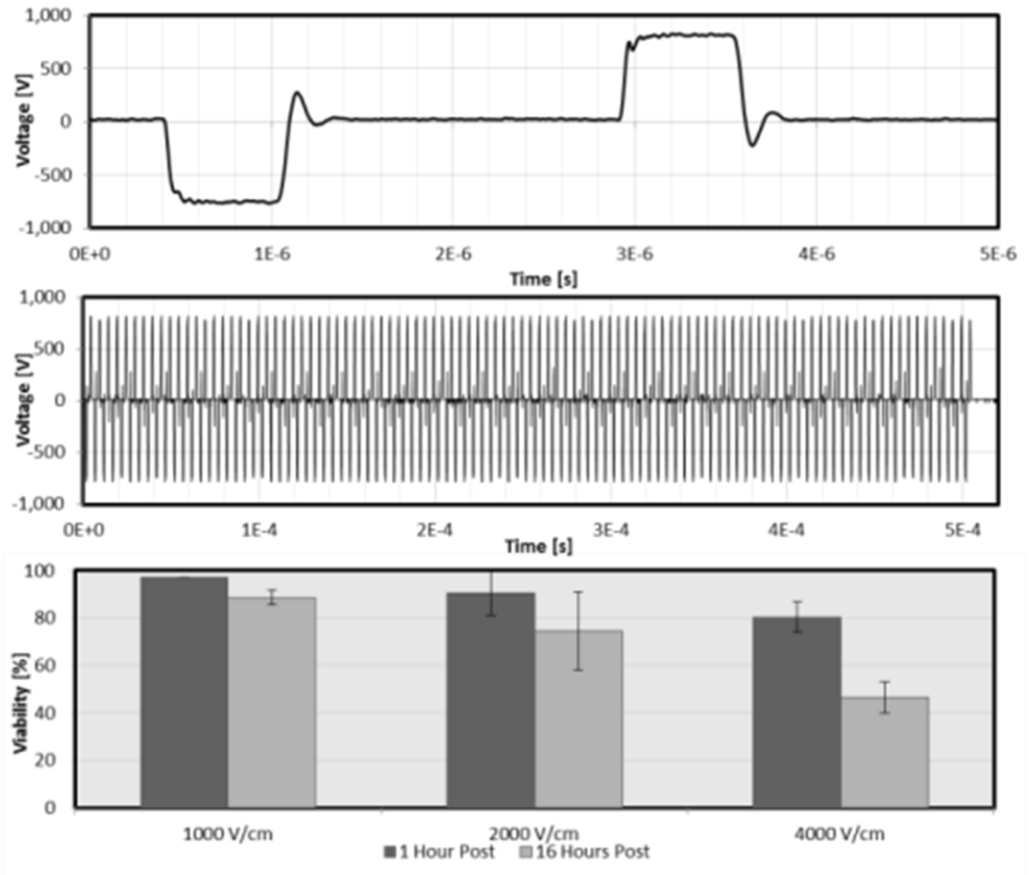

Figure 12-2: [Top] A Single sub-microsecond pulse waveform is repeated 200 times [Middle] to create an irreversible electroporation pulse train. [Bottom] These pulse trains cause immediate and delayed cell death *in-vitro*.

Chapter 8: and Chapter 9:. DC and low frequency sinusoidal voltages are very effective at increasing the TMP of the cell membrane. This is because the averaged energized time is much longer than the charging time of the cell membrane. As a result, for a low frequency sinusoidal voltage of 400 V/cm, the TMP is elevated and held at a value greater than the threshold for electroporation independent of the conductivity of the media. In low conductivity solutions, the cell membrane charges more slowly. As the frequency is increased above 1 kHz, the voltage is not on for long enough to fully charge the cell membrane in 0.01 S/m buffer. The results in Figure 12-3 show that the optimal frequency range for sorting cells without significantly altering their cell membrane occurs above 1 kHz. When operating above 100 kHz, very large magnitude electric fields can be used without significantly increasing the TMP.

Interestingly, experimental observations presented in Chapter 8: and Chapter 9: showed some degree of electroporation of cells below the first crossover frequency of their Clausius-Mossotti factor, but minimal electroporation above this frequency (i.e. cells were electroporated while experiencing negative DEP, but minimally impacted when experiencing positive DEP). Analysis of the results shown in Figure 12-3 shows that the cross-over frequency is collocated with the -

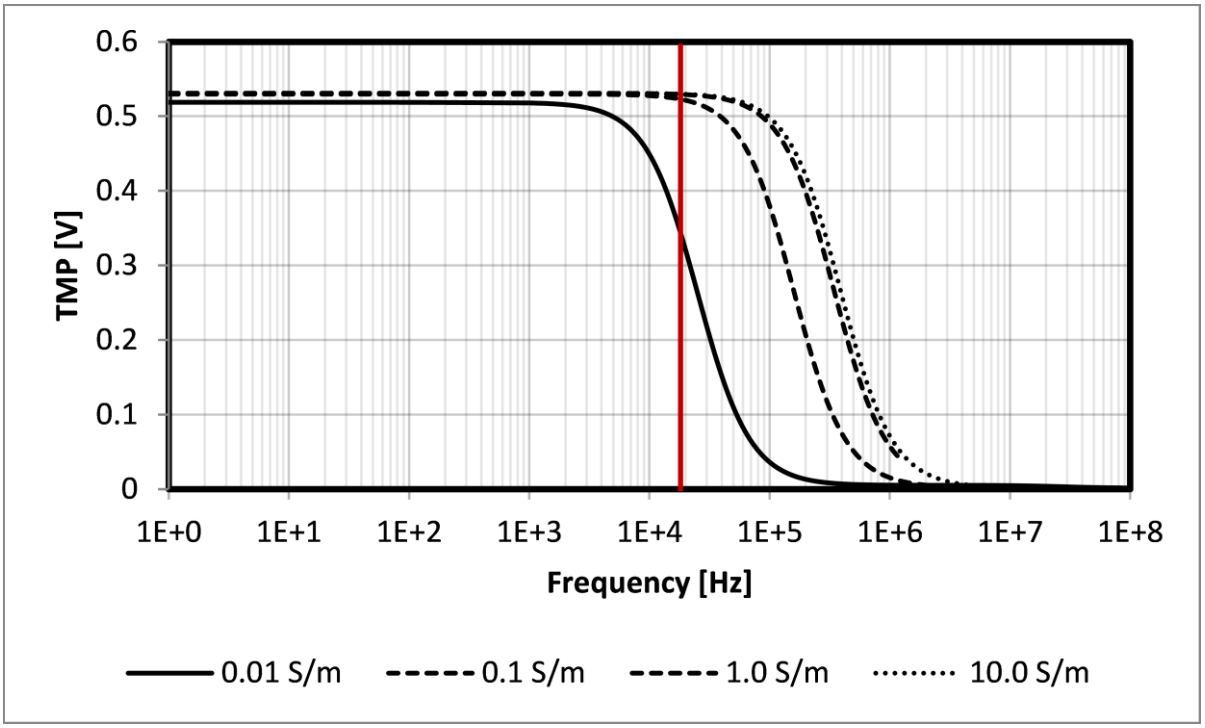

Figure 12-3: Steady state maximum TMP for a MDA-MB-231 cell under a 400 V/cm electric field verses frequency. The red vertical line represents the first crossover frequency of MDA-MB-231 cells in 0.01 S/m conductivity media.

3dB point on the TMP curve. This indicates that at the cross-over frequency, cells are absorbing approximately half of the maximum energy absorbed at lower frequencies and shows the strong dependence of membrane electrical characteristics on DEP and Electroporation effects.

As the conductivity of the media is increased, the charging time of the cell membrane decreases until the media conductivity reaches 1.0 S/m. Above this threshold increases in media conductivity negligibly impact the TMP charging time. At 0.1 S/m, the -3 dB frequency is not reached until approximately 100 kHz. At 1.0 and 10.0 S/m this frequency is shifted higher to approximately 300 kHz. If higher conductivity buffers are to be used in cDEP experiments, then the frequency range used must also be shifted to avoid damaging the analyzed cells.

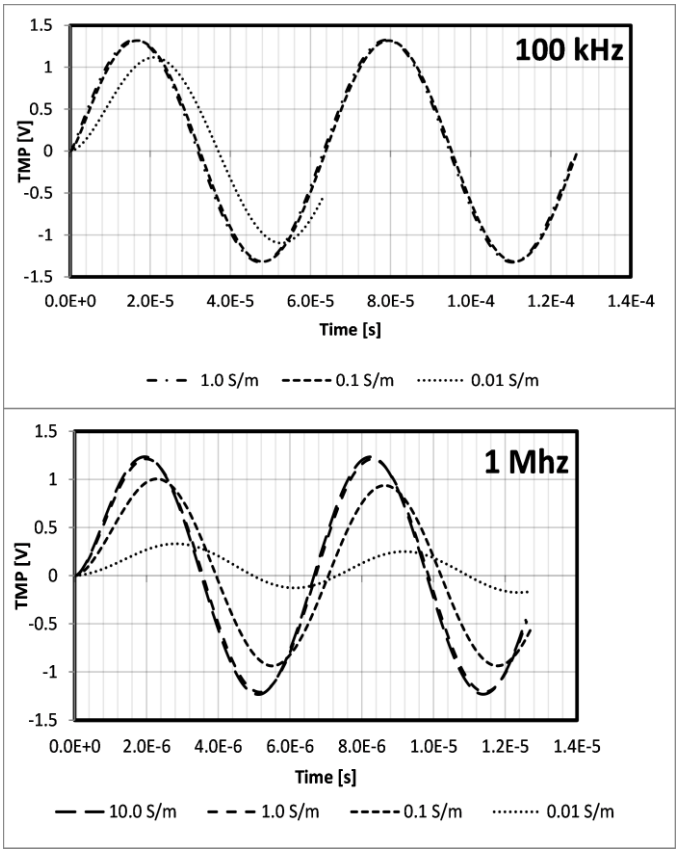

Figure 12-4: TMP response to a 1000 V/cm electric field at [top] 100 kHz and [bottom] 1 MHz. At 100 kHZ, media conductivity has a minimal impact on the maximum amplitude of the TMP. At 1 MHz, the lowest conductivity media (0.01 S/m) reduces the TMP.

Figure 12-4 shows the time dependent charging of the TMP for a 1000 V/cm electric field at frequencies of 100 kHz and 1 Mhz. At 1 kHz, the maximum TMP is negligibly affected by media conductivity. At 0.01 S/m there is a slight phase shift and decrease in the maximum value achieved. At 1 MHz, the TMP is drastically affected by media conductivity. A phase shift and decrease is evident for 0.01 and 0.1 S/m conductivity media. This again indicates that low conductivity media provide some measure of protection to cells against electroporation. In media with conductivity closer to physiological norms (1 S/m), the TMP increases significantly (and in phase) with the applied signal.

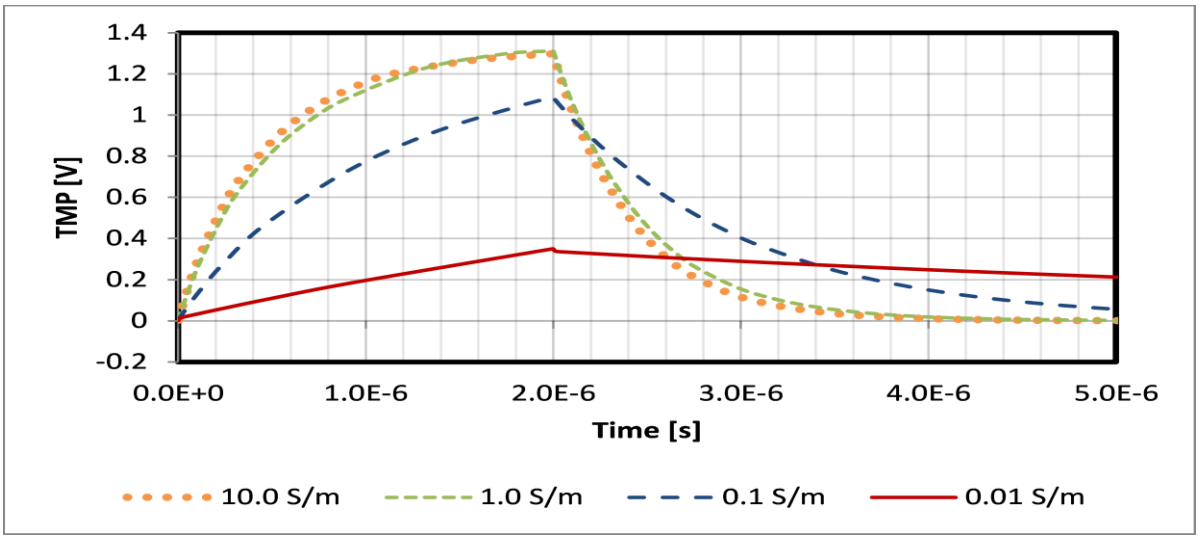

Figure 12-5: Transient response of a cell to a 1000 V/cm. The low conductivity media protects the cell from electroporation. In low conductivity solutions, the cell appears more conductive than the media and a small increase in the TMP occurs. As the media becomes more conductive, the TMP rises towards its maximum value more quickly.

Figure 12-6 and Figure 12-5 show the TMP response to 2 and 20 μs pulsed electric fields with 1000 V/cm magnitudes. As anticipated from the results with sinusoidal signals, the rate of TMP increase is highly dependent on media conductivity. For the lowest media conductivity (0.01 S/m), it takes longer than 20 μs for the TMP to reach its maximum value. This charging time reduces to approximately 2 μs for conductivities of 1.0 S/m or greater. These results show the exponential increase and decrease in TMP caused by electric fields. The slower charging rate in low conductivities is due a preference for currents to flow through the cell rather than around it resulting in a smaller electric field across cell. This highlights the need for low conductivity buffers when attempting to avoid cell damage. Conversely, when attempting to induce electroporation in low conductivity buffers, a much higher electric field is required if pulsed or high frequency fields are used.

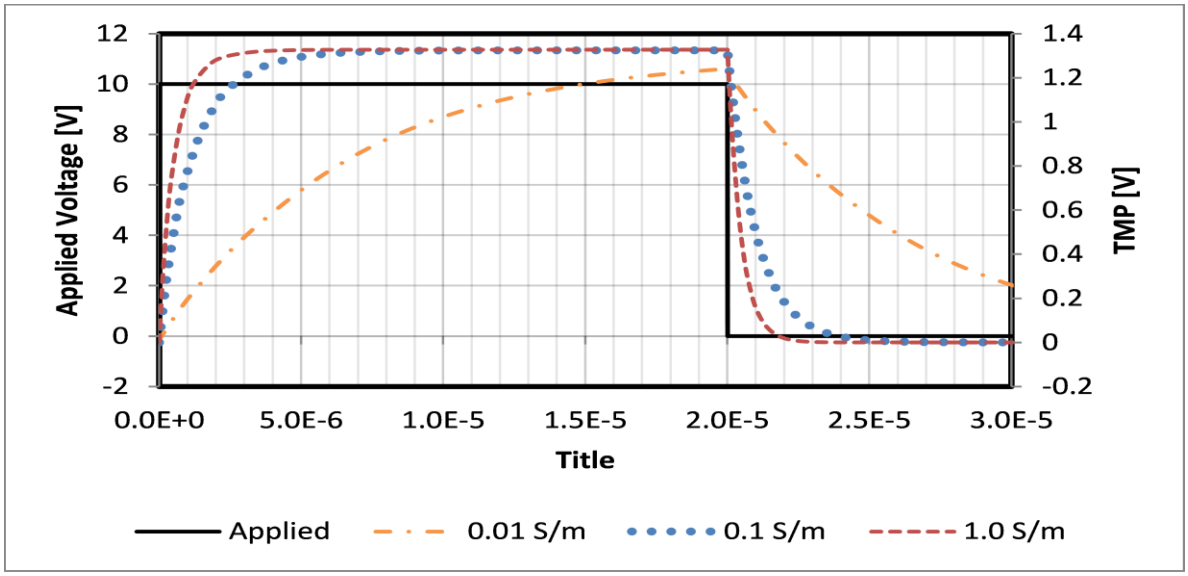

Figure 12-6: Transient response of a cell to a 1000 V/cm. For high conductivity buffers, the TMP rises rapidly. As the conductivity decreases, the rate of charging decreases. In the lowest conductivity, isotonic solution available (0.01 S/m) it takes more than 20 microseconds for the TMP to charge to its maximum

Effect of Pulsed Electric Fields on the Nuclear Trans-Membrane Potential (nTMP)

When a cell is exposed to a pulsed electric field, the capacitive nature of the cell membrane blocks the flow of current through the cell. However, the membrane cannot charge instantaneously and there is a brief time when ions and molecules are rearranging and current

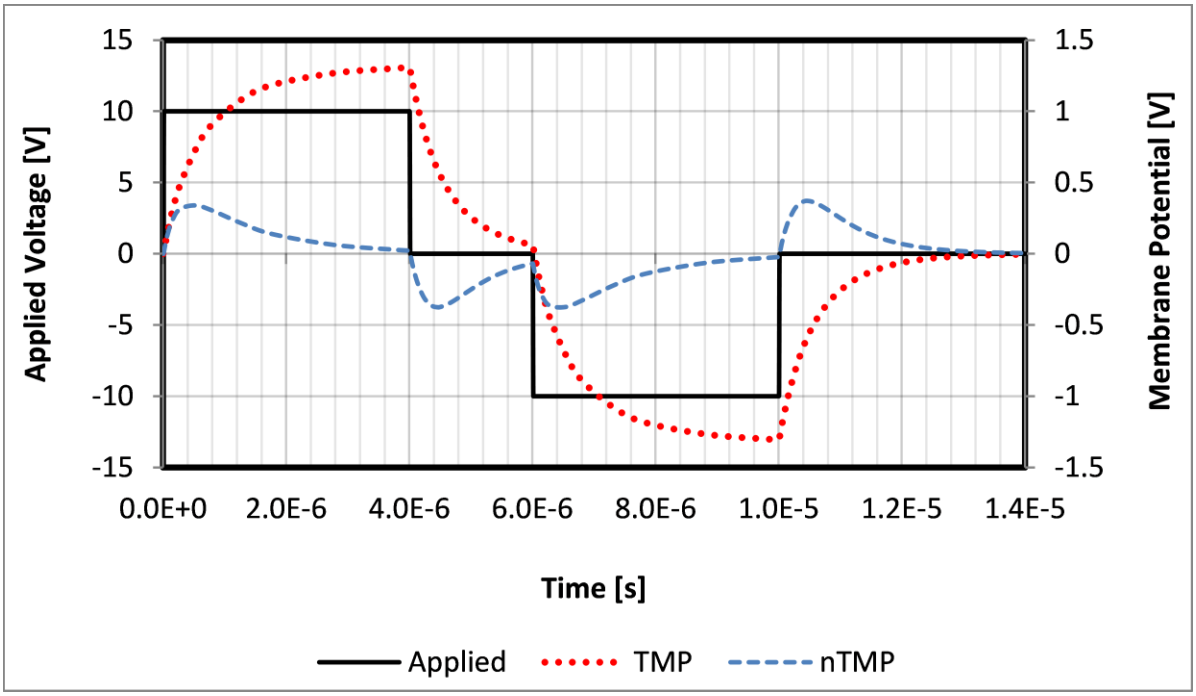

Figure 12-7: TMP and nTMP for a cell with a 0.5:1 nucleus to cytoplasm radius ratio.

flows through the cytoplasm of the cell. This displacement current increases the transmembrane potential of membranes surrounding the nucleus and organelles. These cellular components are much smaller than the cell and their theoretical maximum TMP within the same electric filed decreases linearly with their effective radius. Additionally, as a fully charged cell membrane blocks the flow of current through the cytoplasm, these internal membranes can charge for a period less than the TMP charging time.

Figure 12-7 shows the charging characteristics of the cell and nuclear membranes for a bipolar pulse with 4 μs on and 2 μs off times. For the first 500 ns, current flows through the cytoplasm and the nuclear transmembrane potential (nTMP) increases. After 500 ns, the cell membrane begins to block the flow of current and the nTMP begins to decay back to zero. As the positive going pulse turns off, the charge on the cell membrane begins to dissipate and ions redistributing cause a current to flow in the opposite direction, charging the nuclear membrane in the opposite polarity. This process repeats as the pulse switches polarity. In Figure 12-7 we can see that every bi-polar pulse results in four increases in nTMP with pattern + + - - + +. This pattern of successive nTMP increase in the same polarity suggests that there exists an optimal pulse configuration to increase the maximum nTMP value achievable.

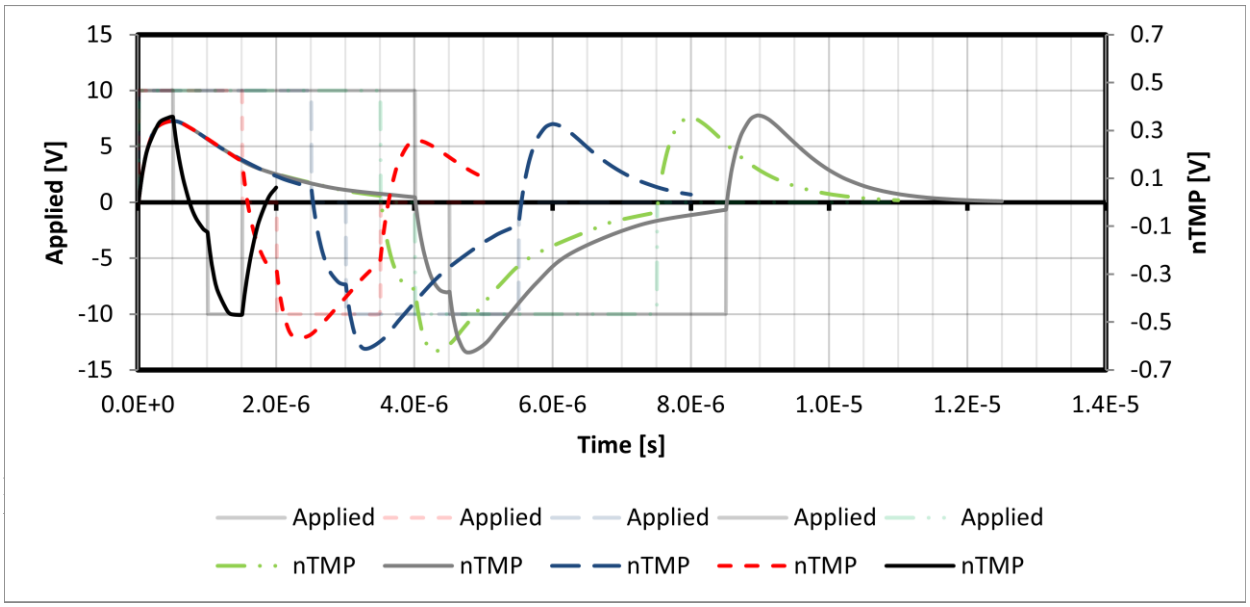

Figure 12-9: Effect that pulse on time has on the nTMP when the off time between pulses is held to 500 ns. These results suggest that there is an optimal minimal ontime to affect the nTMP (green) of 3.5 μs.

Figure 12-9 shows the impact of pulse on time on the nTMP when the pulse off time is held constant at 500 ns. At the onset of the first positive pulse, the nTMP charges up to a maximum of approximately 0.35 V in the first 500 ns before it starts to decay. At the end of the first pulse, displacement currents within the cytoplasm force the nTMP negative. The onset of the negative polarity pulse further increases the magnitude of the nTMP in the negative direction. This additive effect results in a negative nTMP value which is greater in magnitude than the first positive nTMP.

For very short on-time pulses, the nuclear membrane has not fully discharged before the positive pulse returns to zero. This diminishes the maximum negative nTMP achievable. For 500 ns on time pulses, the first positive nTMP reaches 0.35 V while the first negative nTMP reaches -0.47 V. This effect is further enhanced if the positive nTMP is given sufficient time to decay back to zero before the positive pulse is turned off. When the pulse length is increased to 3.5 and 4 μs, the nTMP reaches a maximum magnitude of 0.62 V, nearly double the value achieved by a

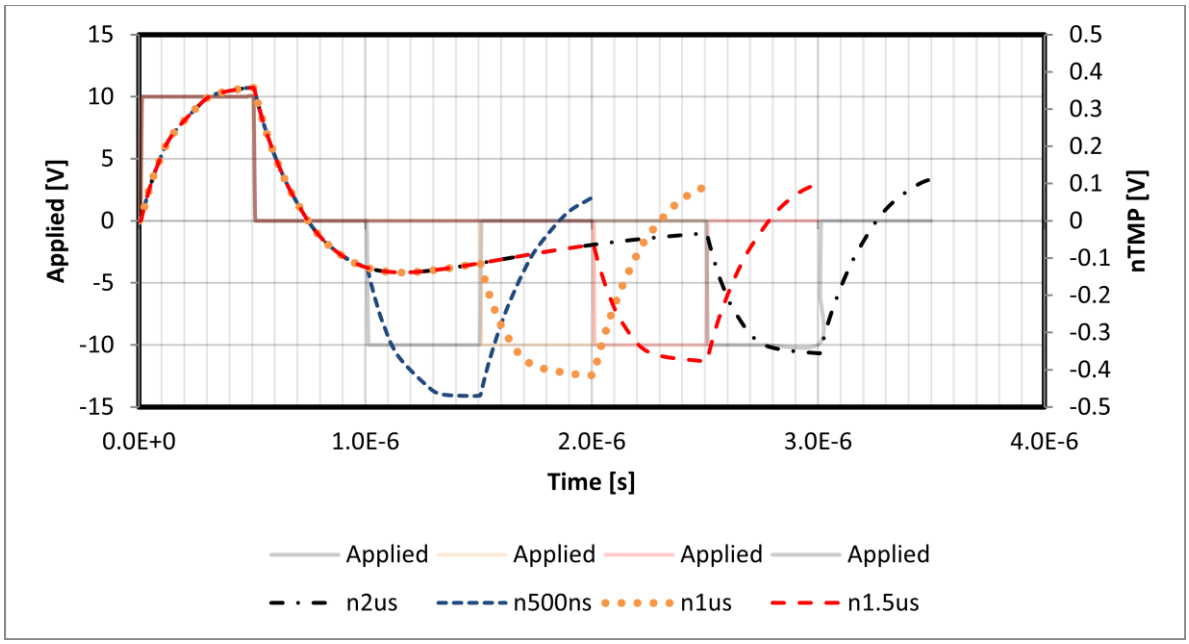

Figure 12-10: Effect of pulse delay on nTMP. Shorter delays result in an increase in the nTMP as the second pulse falls negative.

single mono-polar pulse. *Figure 12-9 shows the nuclear transmembrane potential can be doubled without increasing the magnitude of the applied field by carefully tuning the pulse parameters.*

Figure 12-10 shows the effect of delay time between pulses. At the end of the first positive pulse, the nTMP decays and becomes negative after approximately 250 ns. It reaches its maximum negative value approximately 500 ns after the end of the first positive pulse before decaying back towards zero.

If the negative pulse is initiated before the nTMP can decay back to zero, then the resulting increase in nTMP is greater than that achieved by a single mono-polar pulse. The maximum nTMP value is achieved when the delay between pulses is 500 ns. This optimum time is due to a combination of factors that contribute to the RC time constants for the cell and nuclear membranes. The results shown in Figure 12-9 and Figure 12-10 show that the pulse characteristics can be optimized to increase the maximum nTMP achievable for high frequency bipolar pulses.

Though further optimization and analysis is necessary, it appears that to maximize the nTMP, the optimal pulse on time is equivalent to the charging time of the cell membrane plus the discharge time of the nuclear membrane. This allows the nTMP to charge up, then return to zero before it is forced negative at the falling edge of the pulse. Similarly, the optimal off time is approximately equivalent to the charging time of the cell membrane. This allows the nTMP to be increased to its maximum opposite polarity value, without decaying, just as the second pulse is initiated.

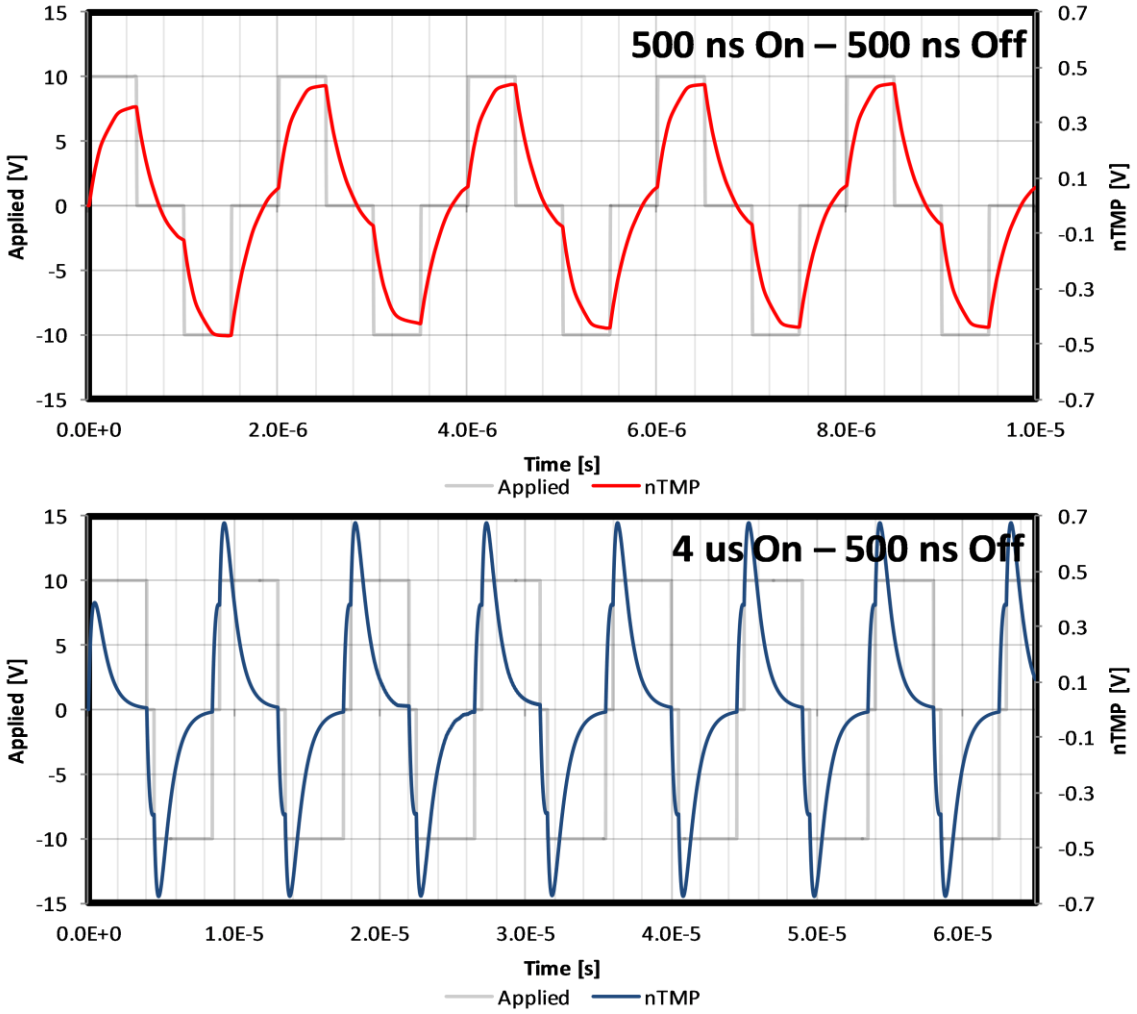

Figure 12-11: Pulse geometry can be optimized to increase the nTMP above the single pulse maximum. Pulse trains result in an increase in nTMP above the single pulse maximum. For off times of 500 ns, changing the pulse width from 500 ns to 4 us increases the maximum nTMP from approximately 0.5 V to 0.7

Figure 12-11 shows the effect of following this optimization scheme. In most cases, the use of a train of bipolar pulses will increase the nTMP above the single pulse maximum. For 500 ns pulses with 500 ns off times, the first pulse nTMP is approximately 0.33 V. Using a burst of

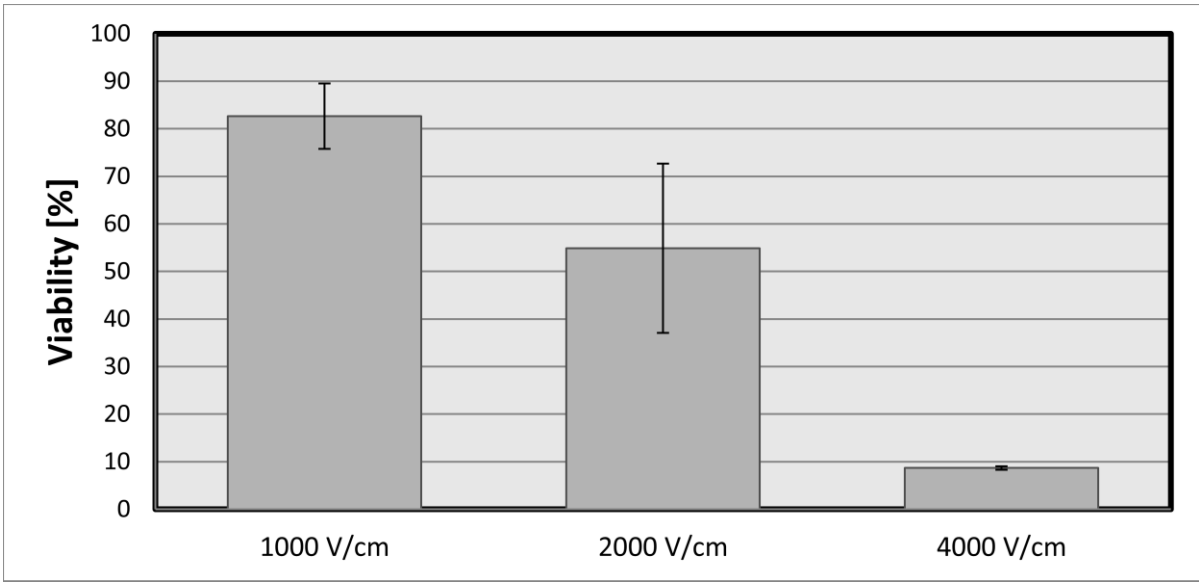

Figure 12-12: Viability of attached MDA-MB-231 cells exposed to 90 bursts of two hundred 700 ns pulses after 16 hours. After exposure to 4000 V/cm, a very small number of cells attached to the surface after 16 hours.

pulses, this value increases to 0.44 V. The use of an optimized pulse with 4 μs on time and 500 ns off time increases the maximum nTMP to almost 0.7 V. This optimized pulse configuration doubles the effect that the electric field has on the nuclear membrane without needing to increase the voltage applied to the system.

E*xperimental Results*

MDA-MB-231: Figure **12-2** [bottom] shows the viability of MDA-MB-231 cells exposed to bursts of 700 ns wide pulses in 0.1 S/m buffer. Viability was assessed by comparing the number of cells attached and floating in suspension to control at 1 and 16 hours post treatment. At 1000 V/cm there was minimal effect on the viability of the cells immediately and 16 hours post treatment. At 2000 V/cm and 4000 V/cm the viability reduced to 50% and 10% when considering only cells that attached to the well plates. Examination of the supinate revealed that for 4000 V/cm there was a large number of cells that failed to attach to the well plate surface. This indicates that the cytoskeletal network of the cells had become damaged or they were in various stages of apoptosis.

PPT8182: An extensive parametric study was conducted on PPT8182 murine pancreatic cancer cells in media with conductivity of 0.2 S/m. Eighty bursts with total on time of 100 μs consisting of pulses with widths between 250 ns and 50 μs were delivered at field strengths of 1500 V/cm, 3000 V/cm, and 4000 V/cm. At 1500 V/cm, pulse widths of 2 μs or greater were able to reduce

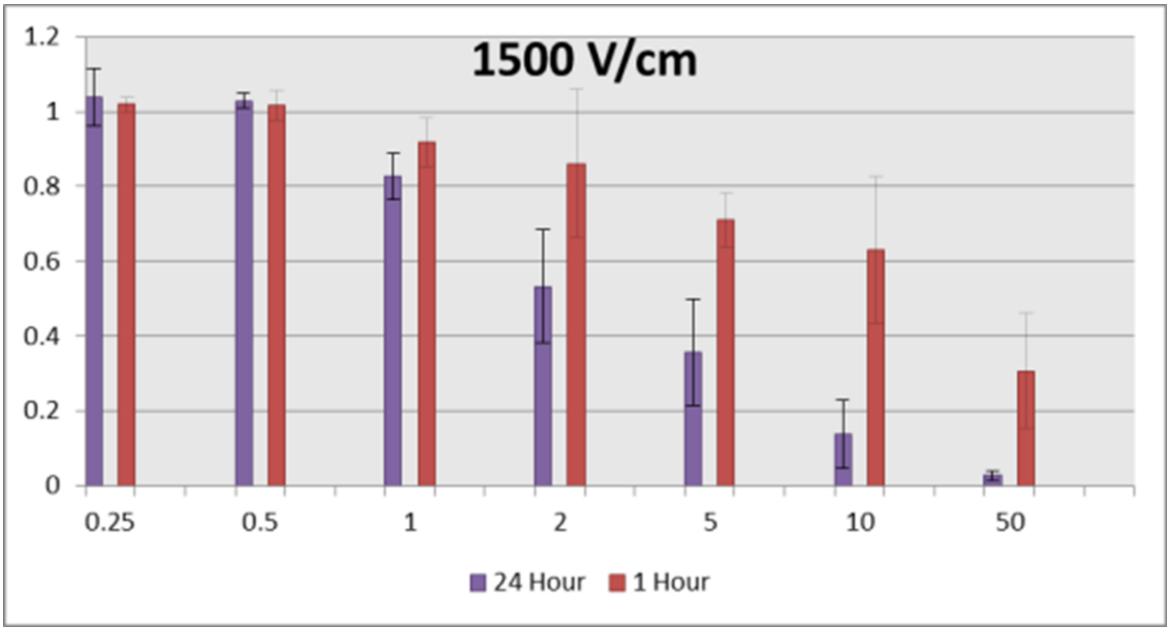

Figure 12-13: Cell viability for 1500 V/cm pulses. There is a clear decrease in viability after 24 hours for pulses greater than 2 us.

the total viability to less than 50 percent after 24 hours. For pulses of 5 microseconds or greater, the viability after 24 hours was significantly reduced indicating that the cells were undergoing some form of apoptosis or delayed cell death.

At 3000 V/cm pulses 1 μs or greater were reduced cell viability below 50 percent with 2 μs pulses and greater almost completely eliminating signs of cellular metabolic activity after 24 hours. At 4000 V/cm, 500 nanosecond pulses appear to induce immediate cell death (60% viability) after 1 hour and delayed cell death (30% viability) after 24 hours. Pulses greater than this induce immediate cell death (<30% viability) at one hour and further delayed cell death (<10% viability) at 24 hours. Cell viability was negligibly impacted by 250 ns pulse widths for all field strengths.

`

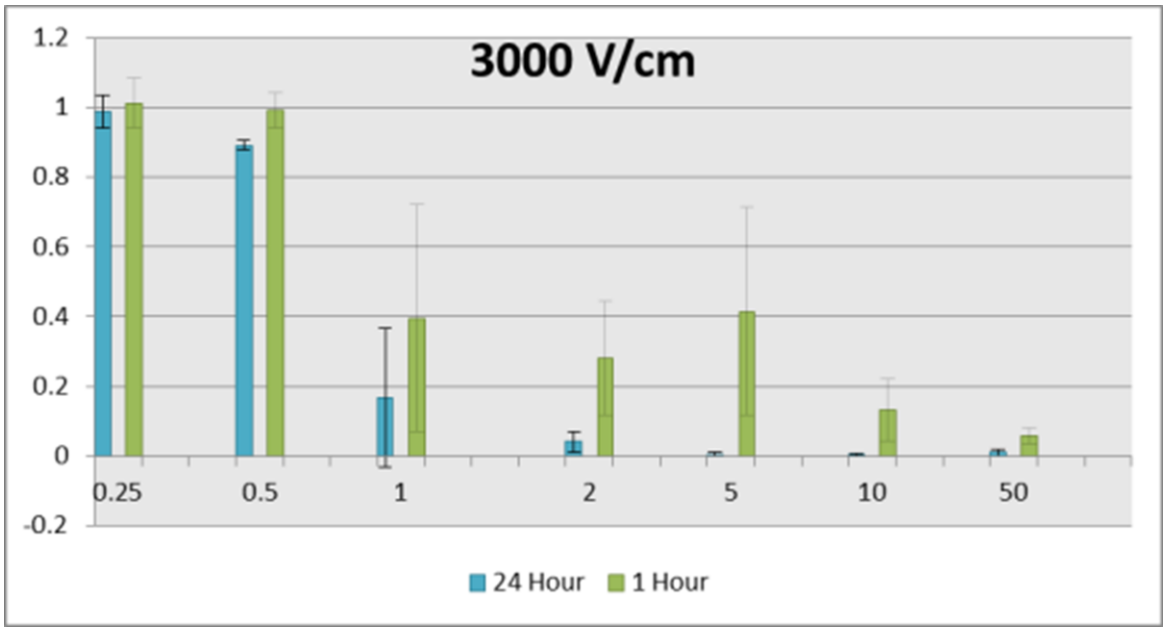

Figure 12-14: Viability of cells treated with 3000 V/cm. At this field strength, pulses of 1 us or greater duration induce substantial cell death, both immediate and delayed.

Conclusion

In this chapter we showed that the frequency of the applied field and the conductivity of the suspending medium play a large role in the buildup of the TMP. In the case where electroporation is not desirable, as in cDEP, the lowest conductivity physiologically suitable buffer should be used. Even at 0.01 S/m, the TMP will increase if continuous sine wave voltages are applied between DC and approximately 10 kHz. The extent of electroporation (both reversible and irreversible) should diminish significantly above this frequency if the field strength is held constant.

If electroporation is desirable, as in the case of tissue ablation, it is advantageous to operate within a sufficiently conductive media. Numerical analysis of the charging times for the cell membrane indicates that 1.0 S/m is an optimal conductivity. Above this, the charging time does not increase significantly, while below this, the cell may not reach its maximum TMP for short pulses. Due to limitations in of our current pulse generator, experiments were conducted in 0.1 or 0.2 S/m media. Increasing the conductivity of this media will almost certainly increase the lethality of the pulses.

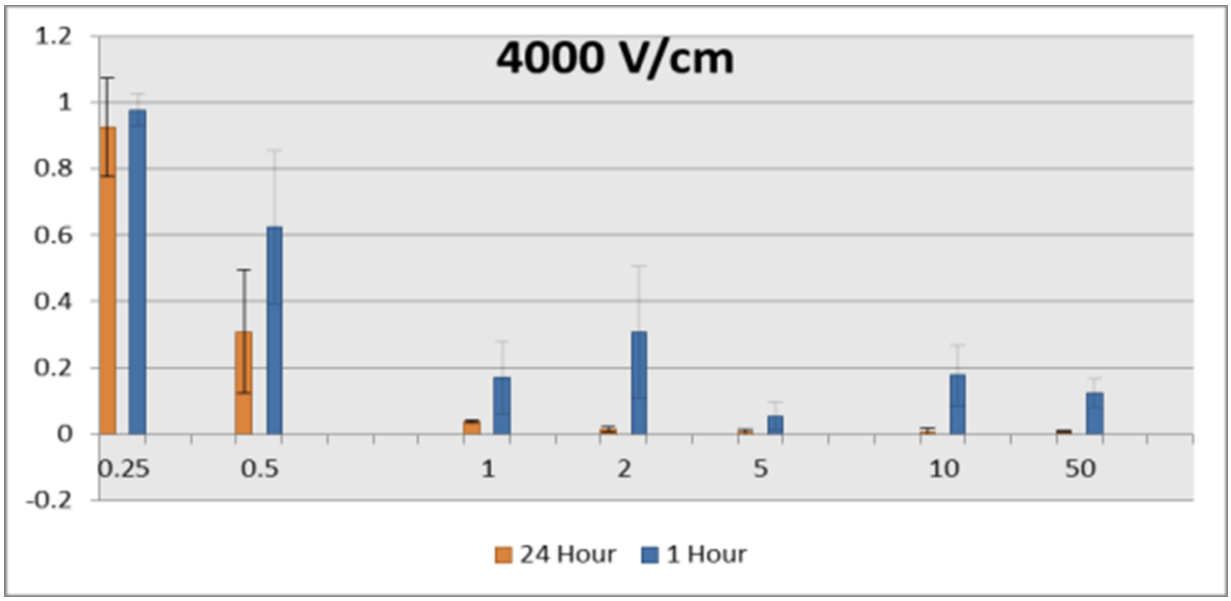

Figure 12-15: Cell viability after exposure to 4000 V/cm. At this field strength, 500 ns pulses begin to induce substantial cell death as well as all pulses with longer durations.

Theoretically, bursts of 4μs pulses with 500 ns off time will result in the largest effect on the nuclear transmembrane potential and may help to further increase the lethality of the high frequency pulses. Though theoretically possible with our current pulse generation system, these waveforms were not examined due to concerns about damaging the electronics. However, these waveforms will certainly be the focus of future work.

Chapter 13: Effects of High Frequency Pulsed Electric Fields on Tissue Mimics

Introduction

It has been observed that the electric field necessary to kill cells suspended in media is higher than for cells in tissue. For example, in Chapter 13, we observed that 50 microsecond pulses reduced cell viability to approximately 30% at 1500 V/cm. In contrast, Davalos first reported cell an electric field threshold of 650 V/cm to kill liver tissue *in-vivo*[1]. Arena et al. have recently demonstrated that cells suspended in a collagen hydrogel scaffold could be used to predict the electric field threshold needed to kill cells using 100 microsecond mono-polar pulses. In collagen hydrogel scaffolds, cells stretch out and assume a more natural morphology. When needle electrodes are placed within the scaffold and pulses are delivered, an oval shaped region of cell death is observed. The electric field necessary to induce cell death can be determined comparing the affected area to numerical simulations. Here we use hydrogel scaffolds to predict the *in-vivo* electric field threshold of high frequency bipolar bursts. Eighty pulse trains with 100 μs total on times were formed using pulses with 250 ns, 2 μs, 5 μs, and 50 μs widths. Live and dead cells

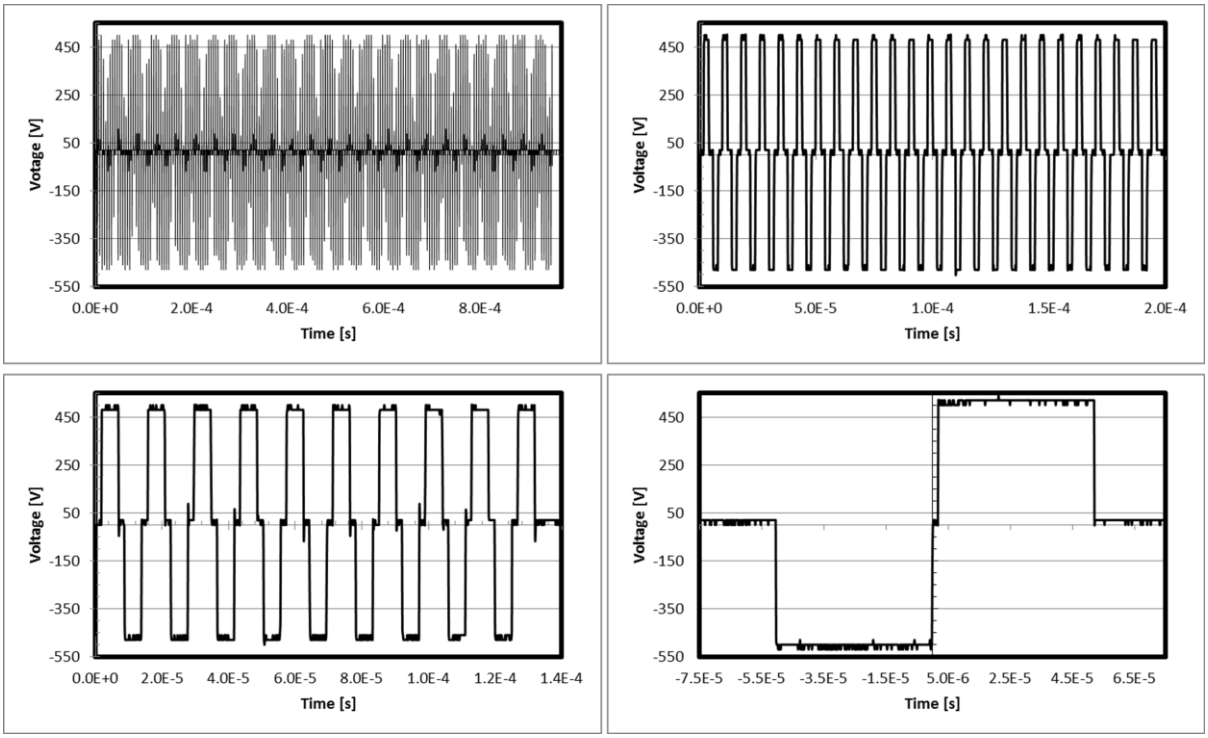

Figure 13-1: Oscilloscope readings of the bipolar bursts delivered to the hydrogel scaffolds. All pulses had a total on time of 10 μs and consisted of (a) 250 ns, (b) 2 μs, (c) 5 μs, or (d) 50 μs wide bipolar square waves

were observed by staining with Calcean AM and propidium iodide, respectively. Observations were made at 1 and 24 hours post treatment.

Methods

Hydrogels

Collagen I hydrogels were fabricated as described previously [2]. Briefly, Sprague Dawley rat tail tendons were excised and allowed to dissolve under agitation overnight in 10 mM HCl at room temperature. The resulting suspension was centrifuged at 22,500 g for 30 min, and the supernatant containing the collagen I was decanted. The collagen I solution was neutralized with a buffer containing 10x concentrated DMEM (supplemented with 4.5 g/L glucose, L-glutamine, sodium pyruvate, and sodium bicarbonate; Mediatech Inc., Manassas, VA, USA), 1N NaOH, and DI-H_20 to obtain a final concentration of 8 mg/mL. The U87 cells were suspended in the neutralizing buffer at a seeding density of 5 cells/ml and then mixed with the collagen I solution. The collagen-cell suspension, or collagen-only suspension for the control group, was pipetted into 10 mm diameter cylindrical molds to achieve a thickness of 3 mm. Following a 30 min gelation period at 37°C, the hydrogels were removed from the molds and cultured in complete media for 18 hours prior to IRE pulse delivery.

Electronics

A custom pulse generation system was used to deliver bursts of pulses with pulse widths of 250 ns, 2 μs, 5 μs, and 50 μs. A 500 Ω resistor was placed in parallel with the load to ensure proper pulse shaping and to protect against delivering pulses to an open circuit. Custom electrodes were made from hollow 1.27 mm diameter dispensing needles (Howard Electronic Instruments Inc., El Dorado, KS, USA) with a 2.0 mm edge-to-edge separation distance. The pulse generation system was set to deliver pulses with amplitude of 540 V_{peak} for a voltage to distance ratio of 2700 V/cm. The total on time for each burst was set to 100 μs (50 μs in each polarity).

Pulse Parameters (n = 2)			
Pulse Width	**Number of Bi-polar Pulses**	**Total On Time**	**Number of Pulses**
250 ns	200	100 µs	80
2 µs	25	100 µs	80
5 µs	10	100 µs	80
50 µs	2	100 µs	80

Sample Processing

At one or 24 hours after pulsing, normal culture media was replaced with 2.5 mL of media supplemented with 4µM Calcein AM (λ_{em} = 515 nm, Invitrogen, Eugene, Oregon) and incubated at 37 °C for 30 minutes. Five minutes prior to visualization, the media was supplemented with 75 µL of 1.5 mM propidium iodide (λ_{em} = 617 nm, Invitrogen, Eugene, Oregon) for 5 minutes. Finally, the hydrogels were rinsed with PBS to flush out any unabsorbed dyes and increase the signal to noise ratio. A Leica DMI 6000 fluorescent microscope (Leica Microsystems Inc., Buffalo Grove, IL, USA) was used to tile a set of images and reconstruct the entire surface of the HF-IRE treated scaffolds.

Numerical Modeling

The collagen hydrogels were modeled as a 3 mm thick cylinder with a 5 mm radius and

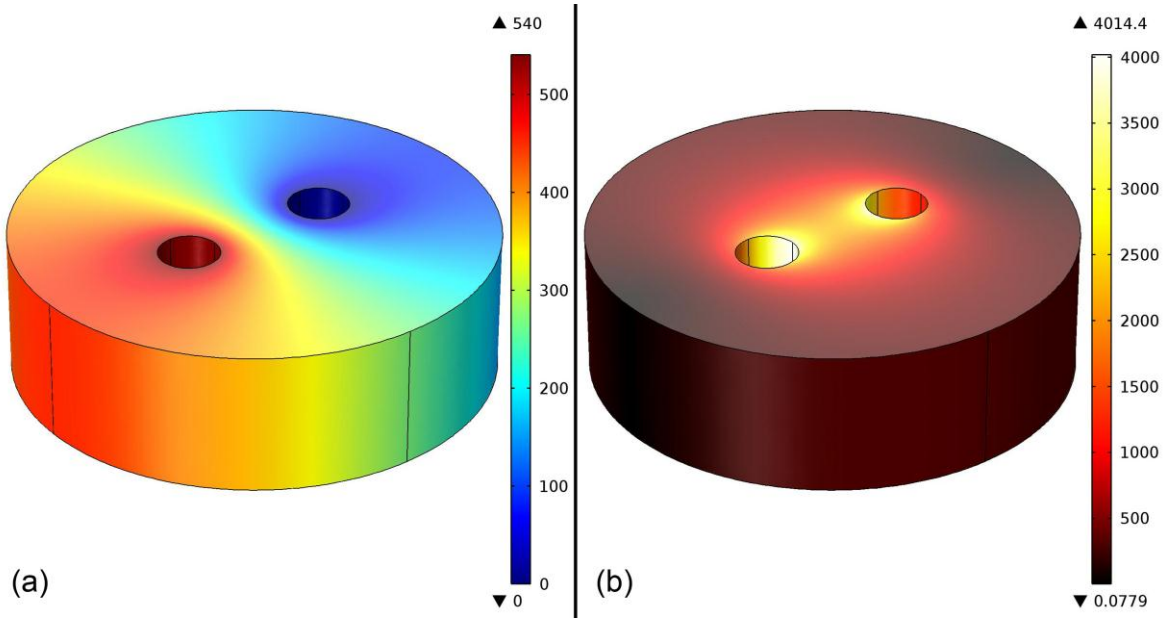

Figure 13-2: (a) Voltage [V] and (b) electric field [V/cm] distributions within the hydrogel scaffolds when 540 V_{peak} is applied. A maximum electric field of 4014.4 V/cm is observed directly adjacent to the electrodes.

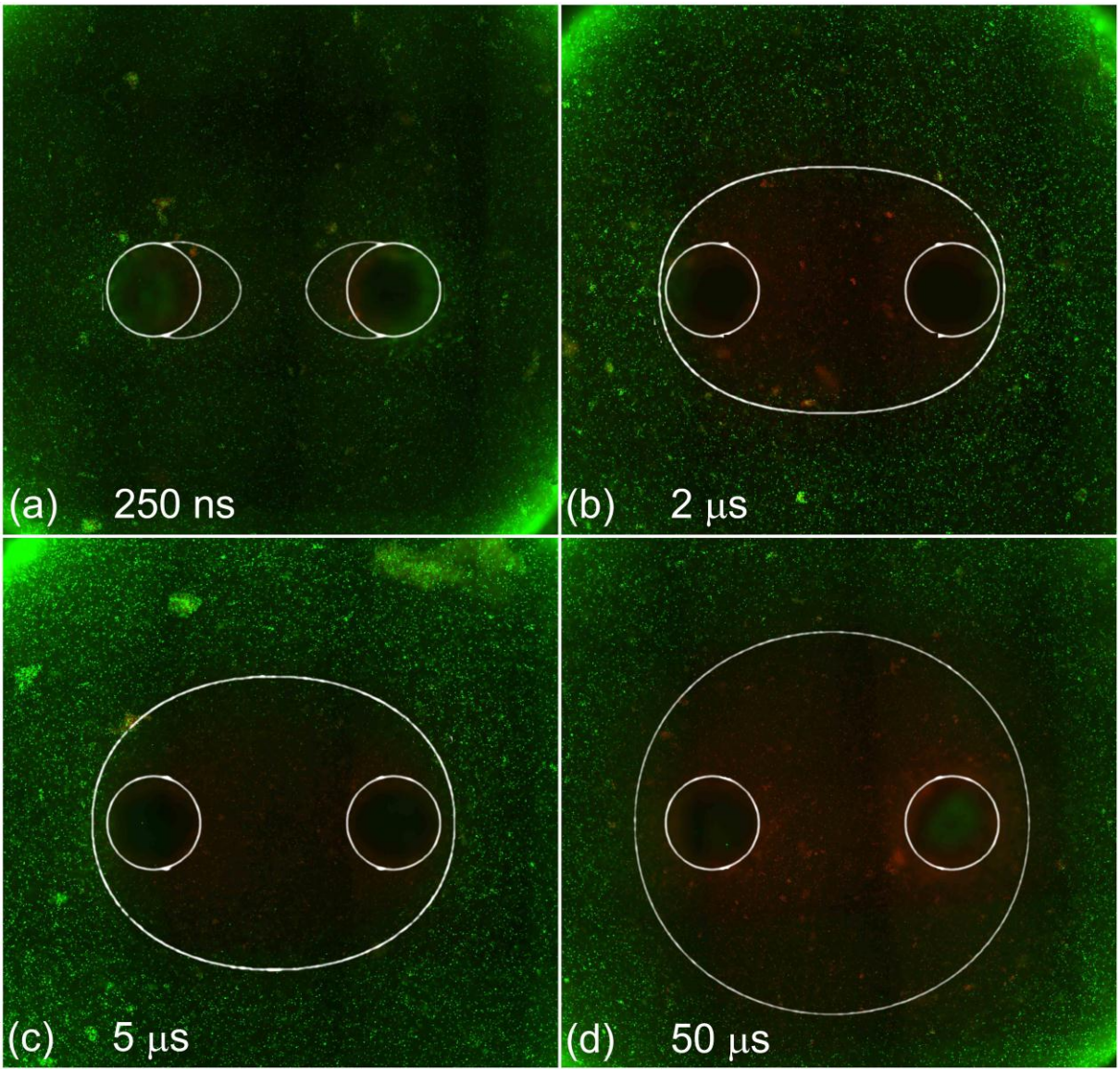

Figure 13-3: Lesions created by bipolar bursts with constituent pulses of (a) 250 ns, (b) 2 μs, (c) 5 μs, and (d) 50 μs 1 hour after treatment. Red regions contain cells which have taken up PI indicating that they have become electroporated. Green regions contain unaffected cells. The white outlines indicate regions where electric field is greater than the average threshold to induce cell death.

conductivity of 1.2 S/m. Cylinders representing the 1.27 mm outer diameter electrodes were offset such that their edge-to-edge distance was equal to 2 mm. These were then subtracted from the collagen domain. The boundaries of the subtracted cylinders were then set to 540 V and ground. Due to the low concentration of cells within the scaffold, changes in conductivity due to electroporation were neglected. Previous studies (results not shown) indicated minimal thermal effects due to the pulses and a negligible impact on the electric field distribution. Therefore, changes in conductivity due to temperature increases were neglected.

Analysis of Results

Tiled images of the surface of the hydrogels were examined using ImageJ (version 1.43u, National Institutes of Health, USA). At the 1 hour time point, the width and height of the region cells that had taken up PI was measured. After 24 hours, there were no cells remaining in the 'treated' region so measurements were taken of the region in the hydrogel not containing calcein. These values, shown in Figure 13-2 were then correlated to the electric field intensity from the numerical simulations to determine the electric field threshold required for cell death.

Results

As presented in Chapter 13, cell viability was negligibly affected by bursts with pulse widths of 250 ns, even at 4000 V/cm. In the hydrogel scaffolds, cells were irreversibly electroporated by bursts of 250 ns pulses when the electric field intensity was greater than 2500 V/cm. In the experiments presented here, this occured only in a small region adjacent to the electrodes as shown in Figure 13-3a**.** Future experiments at higher applied voltages will be necessary to confirm this preliminary electric field threshold. Figure 13-3**b-d** show the lesions created by bursts with pulse widths of 2, 5, and 50 μs and total on times of 100 μs. For a constant applied

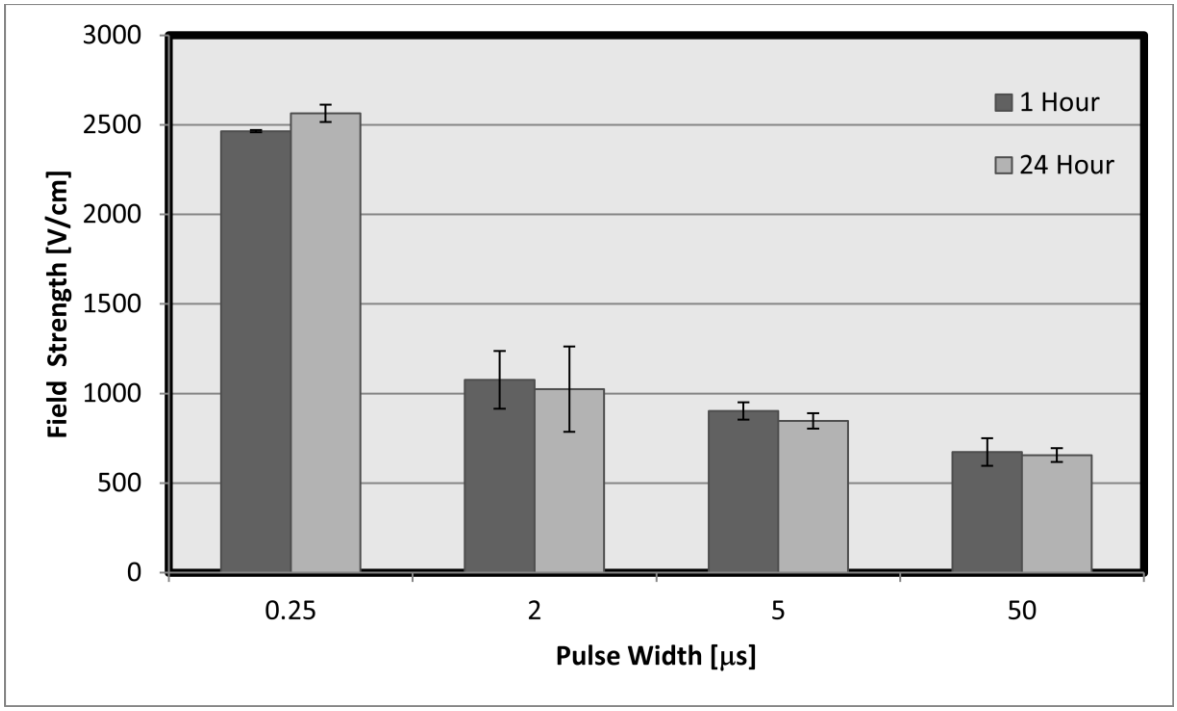

Figure 13-4: Electric field threshold to irreversibly electroporate cells using bursts of bi-polar pulses consisting of square waves with width of 250 ns, 2μs, 5μs, and 50μs.

voltage, the volume of cells electroporated increases as the width of the constituent pulses is increased. Figure 13-4 shows the average electric field intensity required to irreversibly electroporate cells. There is a minimal difference in the lesion size observed at the 1 and 24 hour time points. The absence of any nuclear material to bind to PI and fluoresce after 24 hours indicates that a majority of the cells up taking PI at 1 hour are irreversibly electroporated. Using this technique, we predict an *in-vivo* electric field threshold of approximately 1000 V/cm to irreversibly electroporate cells using bipolar bursts of 2 μs pulses. This is substantially lower than that predicted *in-vitro* (Chapter 13) of 3000 V/cm. This threshold decreases to approximately 900 and 675 V/cm for bursts consisting of 5 and 50 μs. The threshold predicted for 50 μs pulses is very close to the *in-vivo.*

Conclusions

In this chapter we demonstrated that the electric field necessary to irreversibly electroporate cells while they are imbedded in an artificial construct is lower than that observed *in-vitro*. The similarity in threshold between bipolar 50 μs pulses in a hydrogel scaffold and a 100 μs pulses in *in-vivo* liver tissue indicate that this is an effective method to determine the electric field threshold needed for HF-IRE treatment planning.

Chapter 14: Effects of Pulsed Electric Fields on Perfused Organs

Electroporation is a non-linear biophysical process in which the application of pulsed electric fields leads to an increase in permeability of cells, presumably through the creation of nanoscale pores in the lipid bilayer[154]. At low pulsing energy, this permeability is reversible and cellular health and function is maintained. Once a critical electric field intensity threshold is surpassed (approximately 500[155] to 700V/cm[156] for ninety 50μs pulses at 4 Hz in brain and eight 100µs pulses at 1 Hz in liver, respectively), the cell membrane is unable to recover and cell death is induced in a precise and controllable manner with sub-millimeter resolution[157,158]. This process is referred to as non-thermal irreversible electroporation (N-TIRE)[159]. N-TIRE does not rely on thermal mechanisms[159] and preserves the structure of the underlying extracellular matrix as well as nerve conduits and bile ducts[160]. Since N-TIRE cell death does not require any drugs, there should not be any creation or deposition of toxins in killing the cells from this technique.

Recently, we and others have determined, through the use of translational laboratory models, that capitalizing on the ability of N-TIRE to destroy cells without destroying the extracellular matrix might make N-TIRE a viable means for scaffold creation via organ decellularization[161,162]. We hypothesize that viable decellularized tissue scaffolds can be obtained using non-thermal irreversible electroporation (N-TIRE) on organs under continuous perfusion.

Machine-perfused porcine livers were treated with N-TIRE using external plate or needle electrodes within one hour of organ harvest and establishment of active perfusion. At varying time points after electroporation, livers were removed from perfusion, immediately after which samples were collected, preserved in 10% neutral buffered formalin, prepared for histology, and their microscopic structure was examined. Examination of the N-TIRE treated and control (untreated) regions of tissue demonstrated that N-TIRE was capable of decellularizing large volumes of tissue when performed in conjunction with active organ perfusion, suggesting that N-TIRE may be a viable method of decellularization for tissue engineering applications.

Methods

Tissue: Young mixed breed pigs were sacrificed via barbiturate overdose. Livers were harvested and placed on ice within 15 minutes of death. Vascular anastomosis with the perfusion system was created by inserting Luer lock syringe connections into the portal vein, hepatic artery, and major hepatic vein and then secured with zip ties. The livers were flushed with lactated Ringer's solution (LRS) to remove blood/clots before placement on the perfusion system.

Perfusion: The VasoWave™ Perfusion System (Smart Perfusion, Denver, NC) was used to perfuse the livers for 4 and 24 hours. This system produces a cardioemulating pulse wave to generate physiological systolic and diastolic pressures and flow rates within the organ. The system is capable of controlling the oxygen content of the perfusate above and below physiological norms. A perfusate, consisting of modified LRS, was delivered to the portal vein and hepatic artery and recycled back into the system via the hepatic vein. All livers were under active machine perfusion within one hour post-mortem and the perfusate was held at 4°C

Electroporation: The ECM 830 Square Wave BTX Electroporation System (Harvard Apparatus, Cambridge, MA) was used to deliver low-energy pulses to the liver tissue while it was on ice undergoing active perfusion with the solution maintained at 21°C. Two metal plate electrodes, 2 cm in diameter, were attached to a pair of ratcheting vice grips (38 mm, Irwin Quick-Grips) using Velcro. High voltage wire was used to connect the electrodes to the BTX unit. The electrodes were clamped gently to the liver and the center-to-center distance between the electrodes was measured. The voltage output on the BTX unit was adjusted such that the approximate applied electric field was 1000 V/cm. Then, ninety-nine individual 100-µs square pulses were administered at repetition rates of 0.25, 0.5, 1.0 and 4.0 Hz. Repetition rates trials were performed at random and repeated a minimum of three times. Sham controls were performed by placing the electrodes over the tissue without delivering any pulses. Since needle electrodes are typically employed in clinical applications of IRE, two additional trials were performed using needle electrodes separated by 0.5 cm, inserted into the tissue approximately 1cm, using a voltage-to-distance ratio of 1500 V/cm at rates of 1 and 4 Hz. The experimental setup for plate electrodes is illustrated in Figure 14-1a. All N-TIRE treatments were completed within two hours post mortem. The surface lesion created at each treatment site was measured at the end of the 24 hour perfusion period. Statistical analysis of the lesion diameters was

conducted using JMP 8.0 (SAS Institute Inc., South Cary, NC) via Student's t-test with a 0.1 α level. Histological images were imported into ImageJ (Version 1.43u, NIH, USA). For each sample, a binary image was created using the threshold tool based on a sample selected within an acellular region. An average pixel value for each image was calculated using the measure RGB plugin and a density score was created by normalizing these values to 1; where 1 corresponds to regions filled with cells and extracellular material and 0 to a region completely devoid of material. Samples were analyzed for statistical significance in JMP via Student's t-test with a maximum 0.05 α level and a minimum of 6 samples for each treatment group.

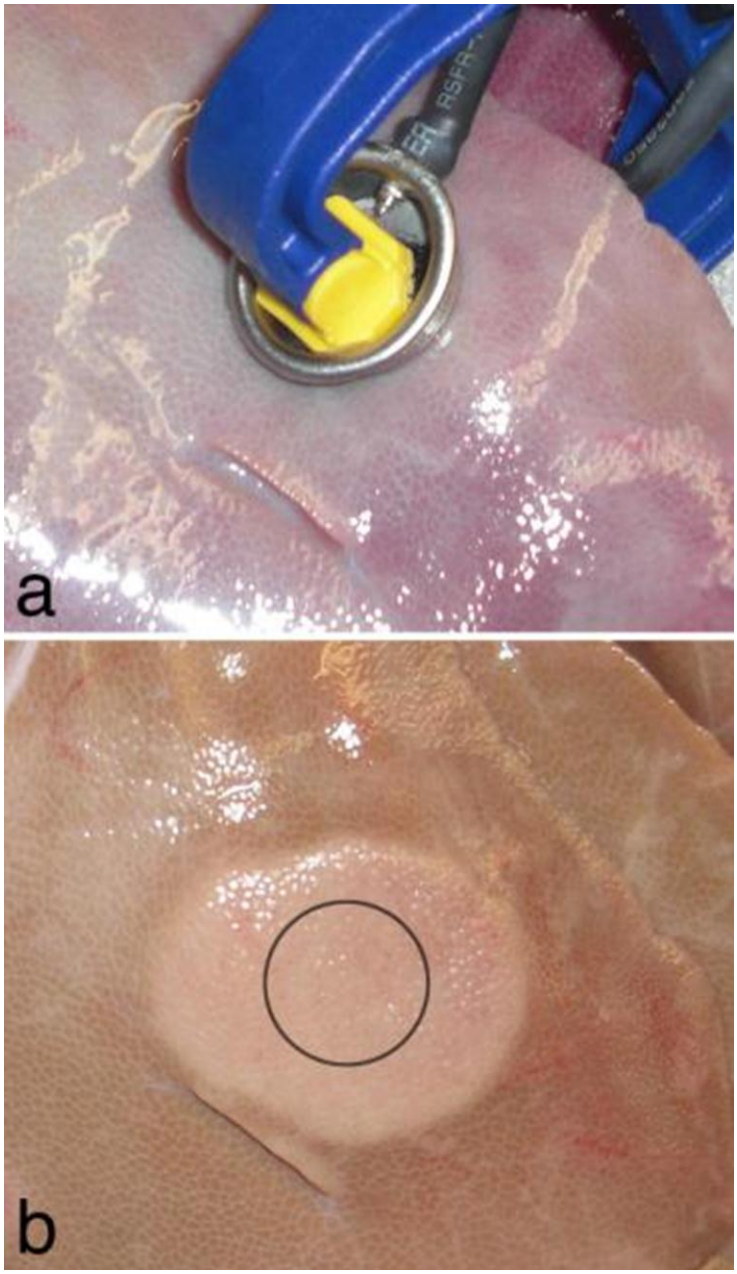

Figure 14-1:Experimental setup and IRE lesion. (a) Placement of the electrodes on actively perfused liver tissue and (b) the resultant lesion after treatment with 99, 100µs, 1500V/cm pulses and 4 hours of perfusion. The approximate area of the electrode is outlined in black.

Tissue preparation: Following N-TIRE treatment and machine perfusion, livers were disconnected from the VasoWave™ system, immediately sectioned to preserve lesions, and tissues were immediately fixed by immersion in 10% neutral buffered formalin solution. After fixation, tissues were trimmed and processed for routine paraffin embedding, then sectioned at 4 micrometers, and stained with hematoxylin-eosin (H&E) or Masson's trichrome stain. Tissue

sections were evaluated by a veterinary pathologist who had no knowledge of the N-TIRE treatment parameters.

Results

Surface lesions develop during perfusion within 30 minutes initiating of treatment. The area of these on the liver surface created by plate electrodes were larger than, but the same type as that from the needle electrodes. In Figure 14-1b, a 3.3 cm surface lesion produced from an applied voltage of 1500 V may be seen, taken 4 hours after treatment. Numerically modeled, this lesion size was produced within the region of tissue experiencing an electric field of 423 +/- 147 V/cm (average ± standard deviation).

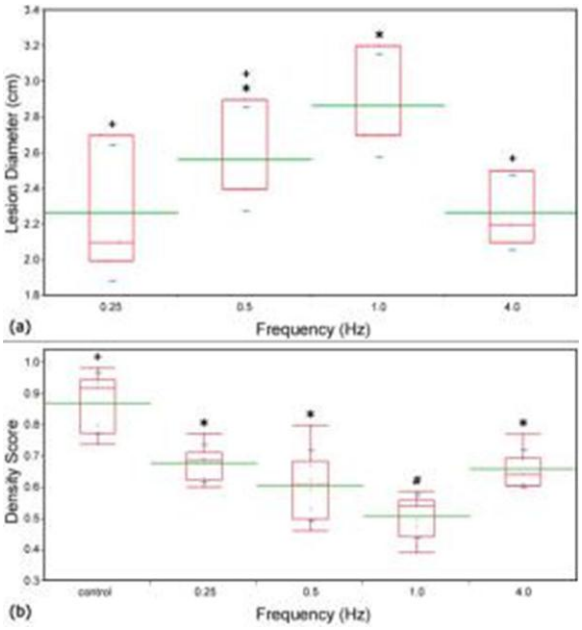

Figure 14-2:- Lesion diameter and density score vs. pulse frequency. Plots comparing the (a) measured lesion diameters for the plate electrodes and (b) density score for each experimental frequency. Box plots (red) which share a common symbol (+, *, or #) were not statistically different from each other for (a) $\alpha = 0.1$ and (b) $\alpha = 0.05$. The average value and standard deviations are represented by green and blue lines respectively. The box plots represent the interquartile range between the 25th and 75th data percentiles. The largest lesions developed and the lowest density score was observed when pulses were applied at a frequency of 1 Hz.

The average applied voltage to distance ratio between the plates for the frequency trials was 962 V/cm, corresponding to an average applied voltage and tissue thickness of 696.9 +/- 141.7 V and 7.3 +/- 1.5 mm, respectively. Lesions from these trials developed over 22 hours post-treatment, and were 2.5 cm in diameter on average (125% electrode diameter); with a minimum lesion of 2 cm occurring at 0.25 Hz and 936 V/cm, and maximum lesion of 3.2 cm occurring at 1.0 Hz and 950 V/cm. Though not dramatically significant, the results suggest that lesion sizes were on average greatest at 1 Hz and decreased as the frequency increased or decreased. The lesions which developed after treatments applied at 0.25 and 4 Hz were statistically smaller (α = 0.1) than those which developed for treatments applied at 1 Hz (Figure 14-2). Future studies will investigate the role of pulse parameters such as repetition rate, duration, magnitude and number on lesion volume.

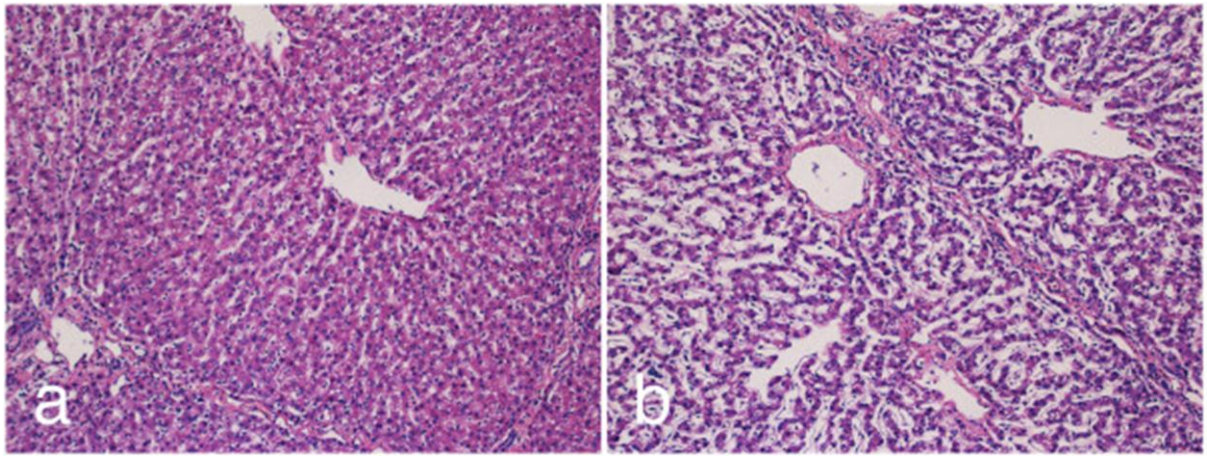

Figure 14-3: Histological comparison of untreated liver tissue to areas which have undergone mild IRE treatments showing preservation of connective tissue and blood vessels. Histological comparison of untreated liver tissue to areas which have undergone mild IRE treatments showing preservation of connective tissue and blood vessels. Samples stained with H&E from (a) untreated and (b) ninety nine, 100µs, 1000V/cm pulses using plate electrodes 24 hours of cardio emulation perfusion at 10x.

Analysis of the treated tissue reveals a uniform treatment region that extended cylindrically through the tissue with no visible damage distal to the treatment regions. This resulted in calculated treated volumes between 1.97 cm^3 and 6.37 cm^3 for corresponding tissue thicknesses of 0.628 and 0.792 cm.

Histological examination 24 hours post-treatment indicates that treated regions exhibit cell death (Figure 14-3b) compared to controls (Figure 14-3a). Hepatic acini in pigs are bordered by connective tissue, which contains blood vessels and biliary structures, and have a prominent cord architecture terminating in a hepatic venule. In areas adjacent to energy delivery, hepatic cell cords were well preserved, with mildly vacuolated hepatocytes (an expected finding at 24-hour *ex vivo* machine perfusion cycle). Sinusoidal structure in untreated areas is open, reflecting the flow of perfusate between hepatic artery/portal vein and hepatic vein. N-TIRE treatment disrupts hepatic cords and induces cell degeneration (Figure 14-3b). Preservation of major acinar features, including connective tissue borders and blood vessels, is evident. In zones of N-TIRE treatment, cell cords were indistinct and membranes lining sinusoids are fragmented to varying degrees.

Pigs, like humans, have substantial septation of liver acini by thin bands of fibrous connective tissue that run between portal triads. This macrostructure had an effect on the distribution of lesions induced by electroporation. Lesions are confined within structural acini in a manner that

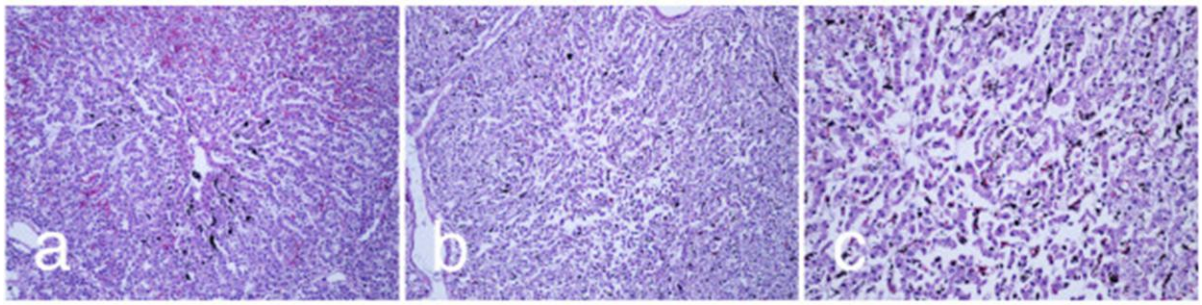

Figure 14-4: IRE treatments result in hepatocytic cord disruption and cell delamination. (a) A section of untreated liver after 24 hours of perfusion. Sections of the same liver treated with 90, 1500V/cm, 100µs pulses at 4Hz using needle electrodes after 24 hours of perfusion at (b) 10x and (c) 20x magnification.

at the edges of the electroporation field, acini with lesions could border normal or nearly normal acini. Thus, the bands of connective tissue act as insulation for the electrical pulsing, an important observation when considering procedures for treating focal liver lesions with electroporation or for evolving an intact connective tissue/duct/vascular matrix for subsequent tissue engineering. Figure 14-4a shows a portion of untreated porcine liver with normal sinusoidal cell cords arrayed from portal tracts to central vein. Cell morphology is well preserved. Some vascular congestion with red blood cells is noted and there is also mild centrilobular biliary stasis. Mildly damaged porcine acini are observed in regions subjected to electroporation from needle electrodes (Figure 14-4b). The center of the acinus shows disruption of cord architecture and some cell degeneration and clumping. A higher magnification view of this area is shown in Figure 14-4c, where cellular changes are more readily appreciated. These treated regions display mild lesions consisting of hepatocytic cord disruption and cells delaminating from cord basal laminae. Mild biliary stasis is noted (dark pigment).

Administration of N-TIRE treatment, either with needle electrodes or with plate electrodes produced lesions in some hepatic acini that are distinctive. The severity of lesions within individual acini ranges from mild to moderately severe. Mild lesions consisted of small clumps of hepatocytes that detach from basal membranes. These cells show a loss of organization of fine intracellular structure and clumping of cytoplasm/organelles (Figure 14-4b-c).

Moderately severe lesions are readily discerned (Figure 14-5)**.** Cells affected by the N-TIRE procedure show varying degrees of cell swelling and karyolysis (Figure 14-5)**.** Within individual acini, most cells are affected. In some acini, frank nuclear pyknosis and cellular degeneration is

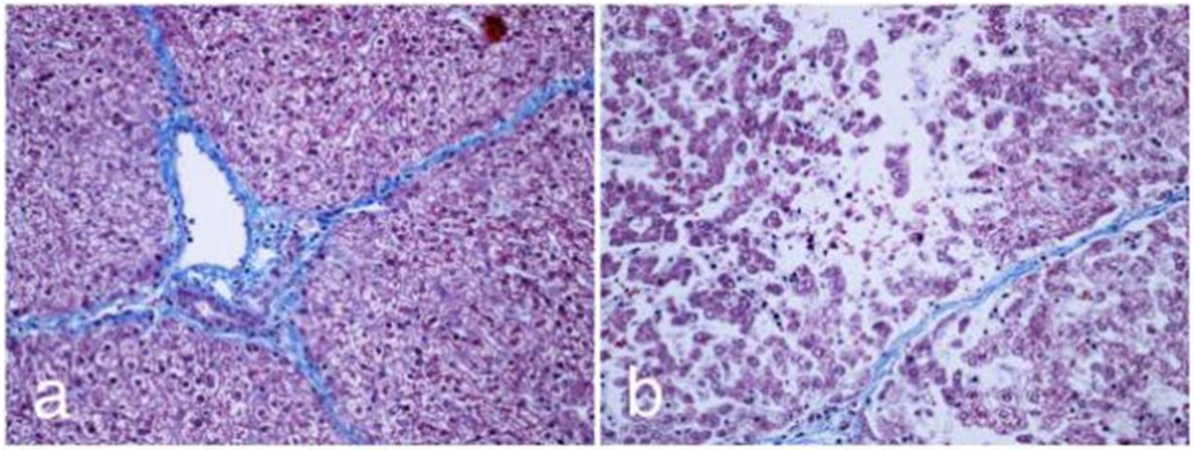

Figure 14-5: Moderately severe lesions maintain bile ducts and vascular structures. (a) A section of untreated liver after 24 hours of perfusion. (b) The same liver treated with 100, 1500V/cm, 100μs pulses at 1Hz using needle electrodes after 24 hours of perfusion at 20x magnification.

seen, with small clumps of hyperchromic cells unattached from basal membranes. In some acini, centrilobular biliary stasis is noted, with aggregation of bile pigments in distal sinusoidal spaces. In all cases, as noted, bridging bands of connective tissue, with intact bile ducts and vascular structures are seen, even immediately bordering acini with significant N-TIRE-induced tissue damage.

The density score for control samples was 0.87 +/- 0.0097 corresponding to approximately 87% of the histological tissue containing cells and extracellular material. Each treatment group had a statistically significant different density score versus the control (α = 0.01). The lowest density score of 0.509 +/- 0.069, was obtained for N-TIRE treatments where pulses were applied every 1.0 Hz. Additionally, treatments applied at 1.0 Hz resulted in a statistically significant lower density score as compared to all other treatment groups (α = 0.05).

Discussion

To the best of our knowledge, this is the first work reporting the effect of non-thermal irreversible electroporation in an actively perfused organ. This effort is the first step towards creating decellularized tissue scaffolds that could be used for organ transplantation. This paper is aimed as a proof of concept to show that the cells may be removed, and therefore we targeted our study towards treating centimeter-scale regions of tissue. However, because N-TIRE procedures are dependent on the electric field to which a region of tissue is exposed, and thermal effects are mitigated by brief pulses with intervals between pulses, it is possible to scale up N-TIRE procedures to treat larger regions of tissue and organs.

The clearance of cellular debris was analyzed in this study using an image analysis algorithm as a preliminary method to determine the effectiveness of this technique. A more comprehensive study will include staining for primary and secondary antibodies, apoptotic markers, and DNA[163] and analysis of these samples via electron microscopy. Assays to determine the quantity of sulfated glycosaminoglycans, elastin, and collagen will be used as a measure of success of this method to preserve the important proteins in the extracellular matrix[164]. Additionally, biodegradation evaluation[164] and analysis of the vascular structure[165] must be completed before cell seeding and animal studies can be conducted.

The results reported here were localized to volumes of tissue up to 6.37 cm^3 for a single N-TIRE treatment. This can readily be expanded into much larger volumes by performing multiple treatments with the goal of creating decellularized structures for partial and full liver transplants. Analysis of the pulse repetition rate shows that the largest treated area and the lowest density score was achieved for a pulse frequency of 1 Hz. After 24 hours of perfusion, a maximum density score reduction of 58.5 percent had been achieved and cellular debris remained within the tissue construct. Since cell viability in the treatment regions was minimal, this is likely due to the combination of three factors; adhesion of cellular debris to the extracellular matrix, low physiological flow rates and pressures at the lobule level, and possible damage to the microvasculature by the N-TIRE treatments.

Although electroporation has been shown to preserve major blood vessels, vascular occlusion after electroporation has been reported in the literature under multiple treatment regiments including work done by Edd et al.[166] (a single 20 ms, 1000 V/cm pulse) , Sersa et al.[167] (eight, 100 μs, 1300 V/cm pulses at 1 Hz) and Nuccitelli et al.[168] (three hundred, 300 ns, 40kV/cm pulses at 0.5 Hz) and is reportedly due to two mechanisms. The first is a rapid onset of temporary vasoconstriction due to reflex vasoconstriction of vascular endothelial cells lasting between 1 and 3 minutes[169]. The second, slower mechanism is due to the disruption of the microfilament and microtubule cytoskeletal networks which are necessary for maintaining cell function and structure[170]. This decrease in blood flow has been observed lasting up to 4 to 8 hours after electroporation of *in-vivo* tumors[171] before partially recovering to normal physiological values

after 24 hours[172,173]. Thus, electroporation induces profound but essentially transient and reversible decline in blood flow[171]. This phenomenon may have occurred during the course of perfusion *ex-vivo*, though it was not directly observed, and it may have an effect on the clearance of cellular debris from the vascular network.

Additionally, the branching network of vessels within the liver produces a system with low pressures and fluid velocities at the capillary level and within individual lobules. The combination of physiological geometry and the loss of fine capillary structure caused by the N-TIRE treatments may have resulted in local sheer stresses which were not significant enough to fully clear cellular debris from the tissue. Removal of this debris is essential in minimizing immune response of recipients. Future work will focus on optimizing treatment and perfusion protocols to minimize disruption of the microvasculature network while enhancing the clearance of debris. This may include the continuous application of sub 1000 V/cm pulses at 1 Hz and perfusion at higher than physiological pressures which we believe will enhance the decellularization process. Recently developed chemical decellularization processes require perfusion cycles of up to 72 hours[165] for the complete removal of cellular material from a rat liver matrix and extension of N-TIRE treatment and perfusion cycles to these durations may be necessary to achieve complete decellularization.

Both external plate electrodes and needles placed within the tissue produced clearly delineated regions of cell death. Plate electrodes produced circular surface lesions, which when appeared cylindrical in shape in sectioned samples and extended between the top and bottom electrodes. Sections of tissue treated with needle electrodes produced oval shaped surface lesions which extended through the tissue.

Needle punctures damaged the tissue structure and provided an alternative path for fluid to flow. Rather than returning through the vasculature, some perfusate escaped the organ through the punctures hindering the perfusion process. Due to this, treatment of an entire organ using needle electrodes is likely not possible and external electrodes appear to be the best method of inducing N-TIRE in large tissue volumes.

In N-TIRE areas, cell death was directly related to energy delivered. Close to electrode placements, over 90% of the cells were degenerate and in varying stages of lysis. In the more reversibly energized zone, cell disruption was 20- 30% of cells. Other cells may have been degenerate or leaky, but not morphologically abnormal. We have observed that the machine perfusion system can mobilize large amounts of cellular debris, a significant benefit for tissue engineering.

In addition to producing decellularized tissue scaffolds, this method provides an ideal platform to study the effects of pulse parameters such as pulse length, repetition rate, and field strength on whole organ structures. Additionally, since we have direct control over the electrical properties of the perfusate, this could serve as a model for examining the effects of N-TIRE on diseased or cancerous organs with unique electrical or physical properties.

The development of engineered materials to replicate the structure and function of thoracic and abdominal organs has achieved only limited success. Large volumes of poorly-organized cells and tissues cannot be implanted due to the initial limited diffusion of oxygen, nutrients and waste [174,175]. Despite this, researchers have made some progress toward complete organ regeneration. For instance, mouse renal cells, grown on decellularized collagen matrices and implanted into athymic mice, developed nephron-like structures after 8 weeks[176]. In addition, five millimeter thick porous polyvinyl-alcohol (PVA) constructs, implanted in mice and then injected with hepatocytes, developed liver-like morphology over the course of one year[177]. However, cell survival and proliferation in each of these structures was limited to a few millimeters from a nutrient source[177].

The resulting scaffolds from N-TIRE plus perfusion maintain the vasculature necessary for perfusion into structures far beyond the nutrient diffusion limit that exists for non-vascularized structures. Since the temperature of the perfusate used can be as low as 4°C, thermal aspects associated with Joule heating are negligible. This provides an ideal platform in which to explore the effects on the cells and tissue of electric fields in isolation from the effects of thermal damage. Additionally, the low temperature of the organ compared to *in vivo* applications may allow for the application of much higher voltages to attain appropriate electric fields for

decellularizing thicker structures without inducing thermal damage. This is important since the thickness of a human liver can exceed 10 cm in some regions.

When planning to decellularize tissues and organs undergoing active perfusion, the treatment region of decellularized tissue may be predicted through numerical modeling. From the lesion sizes and numerical model used here, when decellularizing an entire organ for a transplantable scaffold, the protocol should expose all of the tissue to an electric field of 423 +/- 147 V/cm. This will ensure complete cell death, allowing comprehensive reseeding of the scaffold with the desired cells, thus minimizing the effects of recipient rejection. The threshold found here is slightly lower than the approximate 500-700 V/cm values reported in previous investigations[155] [156]. This may be a result of the unique pulse parameters used or an inherent increased sensitivity of the cells to the pulses when under perfusion. The variability in the electric field threshold may result from the multiple inhomogeneous characteristics of the tissue anatomy and structure, such as the vascular system and tissue thickness, leading to lesions that were not perfectly circular.

The continuous active machine perfusion methods utilized here in the decellularization process may also be advantageous for recellularization. Once the decellularization process is complete, it should be possible to reseed the scaffold without risking damage attendant with removing the newly-created scaffold from the perfusion system. Since the arterial and venous supplies are individually addressable, multiple cell types can be delivered simultaneously to different regions of the organ. Similarly, retrograde perfusion through the biliary system may be the ideal pathway in which to deliver hepatocytes for the reseeding process.

Lesions seen microscopically are clearly indicative of a mechanism and morphology for cellular stripping using electroporation. It is very interesting that even at 24 hours, when using the N-TIRE parameters described here, there is only a modest loss of acinar architecture. More stringent conditions of energy delivery could likely alter this, but this might induce damage to important connective tissue and vascular structures. Addition of adjuvant cytotoxic agents, enzymes, and detergents in the perfusion fluid also might modulate the severity and temporal nature of cell stripping. Logically, it is much better to build on mild conditions, preserving important architecture for tissue engineering purposes, than to rapidly obliterate cells and stroma.

The ability to manage the period of perfusion and conditions of perfusion with the cardioemulation system has clear advantages for this gradual, evolutionary approach to decellularization and eventual recellularization of liver.

Conclusion

This study investigated the ability to develop decellularized tissue scaffolds using N-TIRE on organs undergoing active perfusion. Porcine livers were harvested and placed under active mechanical perfusion while N-TIRE electrical pulses were applied using plate and needle electrodes. Livers were removed from the perfusion system and the resultant lesions and control regions were examined histologically and a density score improvement of 58.5 percent was observed. Through numerical modeling of the electric field distribution from the pulse applications, it was found that an N-TIRE threshold of 423 +/- 147 V/cm may be used to predict the affected area. The continuous active machine perfusion method utilized during the decellularization process in this study provides the necessary platform for scaffold recellurization, a vital aspect required for practical organ transplantation techniques.

Chapter 15: Effects of Pulsed Electric Fields Dissipating through Vascular Networks

Introduction

Electroporation is a non-linear biophysical process in which the application of pulsed electric fields leads to an increase in permeability of cells, presumably through the creation of nanoscale pores in the lipid bilayer [154]. At low pulsing energy, this permeability is reversible and cellular health and function is maintained. Once a critical electric field intensity threshold is surpassed the cell membrane is unable to recover and cell death is induced in a precise and controllable manner with sub-millimeter resolution [159]. This process is referred to as irreversible electroporation (IRE). IRE does not rely on thermal mechanisms and preserves the structure of the underlying extracellular matrix (ECM) as well as nerve conduits and bile ducts [160].

IRE promotes cell necrosis [178], and is an independent means to destroy substantial volumes of targeted tissue without the use of harmful adjuvant chemicals [179]. Common protocols for IRE, involve delivering multiple, unipolar pulses with a duration on the order of microseconds through electrodes inserted directly into, or adjacent to, the malignant tissue [179]. When the tumor is located deep within an organ, a minimally invasive needle is needed for the electrodes to reach

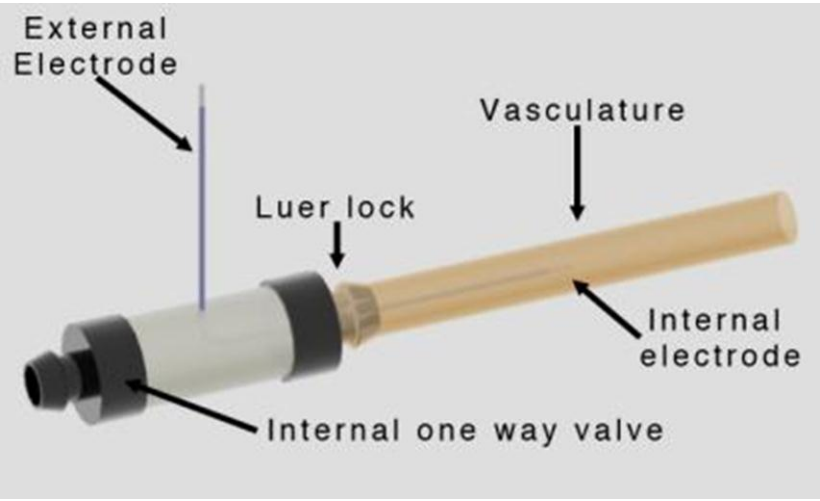

Figure 15-1: Ideal IRE-mechanical perfusion connection device. Connections to the vascualure and the perfusion system are made throught he use of Luer lock connections. A one way valve inside teh device prevents back-flow and isolates and elecrically isolates th organ between mechanically simulated heart beats.

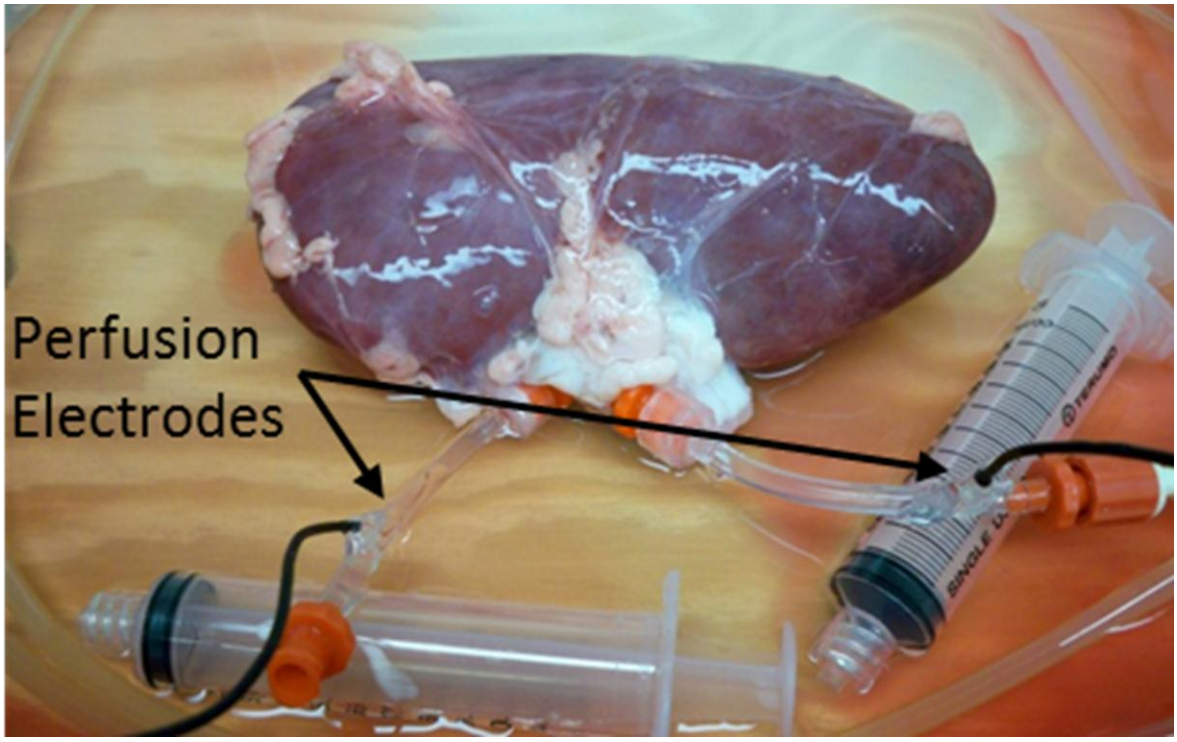

Figure 15-2: Porcine kidney simultaneously attached to vascular electrodes and nutrient perfusion system via the renal vein and artery.

the tumor. In some instances, the organ puncture required by these designs can, in itself, damage the surrounding healthy cells [180]. There is also the possibility of reseeding cancer cells upon needle removal. Therefore, the use of non-puncturing electrodes is desirable.

Here we present a method in which large volumes of tissue can be ablated without the use of puncturing electrodes. In this technique, the vasculature network acts as fluid electrodes through which the electroporation pulses are delivered. By isolating the vasculature and subsequently delivering pulsed electrical energy through venous and arterial pathways of an organ, we are able to ablate larger volumes of tissue in a single 200 second treatment than possible using needle or plate electrodes.

This technique delivers electrical energy to the micro-vascular bed of the organ. Here, the distance between the vascular source and arterial sink is minimized and small voltages result in large electric fields. Typically, due to constraints of pulse generation systems and the effects of Joule heating, needle and plate electrodes must be placed few centimeters apart at most. In this approach, the distance between the physical electrodes is inconsequential and the effective

Biomed Microdevices
DOI 10.1007/s10544-009-9317-5

Contactless dielectrophoresis: a new technique for cell manipulation

Hadi Shafiee · John L. Caldwell · Michael B. Sano · Rafael V. Davalos

Abstract Dielectrophoresis (DEP) has become a promising technique to separate and identify cells and microparticles suspended in a medium based on their size or electrical properties. Presented herein is a new technique to provide the non-uniform electric field required for DEP that does not require electrodes to contact the sample fluid. In our method, electrodes are capacitively-coupled to a fluidic channel through dielectric barriers; the application of a high-frequency electric field to these electrodes then induces an electric field in the channel. This technique combines the cell manipulation abilities of traditional DEP with the ease of fabrication found in insulator-based technologies. A microfluidic device was fabricated based on this principle to determine the feasibility of cell manipulations through contactless DEP (cDEP). We were able to demonstrate cell responses unique to the DEP effect in three separate cell lines. These results illustrate the potential for this technique to identify cells through their electrical properties without fear of contamination from electrodes.

Keywords BioMEMS · Biochip · Dielectrophoretic · Microfluidics · Sample handling · Electrorotation · Sample preparation

Electronic supplementary material The online version of this article (doi:10.1007/s10544-009-9317-5) contains supplementary material, which is available to authorized users.

H. Shafiee · M. B. Sano · R. V. Davalos
Engineering Science and Mechanics Department, Virginia Tech, Blacksburg, VA 24061, USA

J. L. Caldwell
Bradley Department of Electrical and Computer Engineering, Virginia Tech,
Blacksburg, VA 24061, USA

R. V. Davalos
School of Biomedical Engineering & Sciences, Virginia Tech—Wake Forest University,
Blacksburg, VA 24061, USA

H. Shafiee · J. L. Caldwell · M. B. Sano · R. V. Davalos (✉)
Cellular ElectroMechanical Systems (CEMS) Laboratory, Institute for Critical Technology and Applied Science (ICTAS), Virginia Tech,
Blacksburg, VA 24061, USA
e-mail: davalos@vt.edu

1 Introduction

Efficient biological particle separation and manipulation is a crucial issue in the development of integrated microfluidic systems. Current enrichment techniques for sample preparation include density gradient based centrifugation or membrane filtration (Giddings 1993), fluorescent and magnetic activated cell sorting (F/MACS) (Miltenyi et al. 1990), cell surface markers (Fu et al. 1999), and laser tweezers (Ashkin et al. 1987). Each of these techniques relies on different cell properties for separation and has intrinsic advantages and disadvantages. Typically, more sensitive techniques may require prior knowledge of cell-specific markers and antibodies to prepare target cells for analysis.

One alternative to these methods is dielectrophoresis (DEP) which is the motion of a particle due to its polarization in the presence of a non-uniform electric field (Pohl 1951, 1958). Currently, typical dielectrophoretic devices employ an array of thin-film interdigitated electrodes placed within the flow of a channel to generate a non-uniform electric field that interacts with particles near the surface of the electrode array (Yang et al. 1999). Such platforms have shown that DEP is an effective means to concentrate and differentiate cells rapidly and reversibly

Published online: 05 May 2009

based on their size, shape, and intrinsic electrical properties such as conductivity and polarizability. These intrinsic properties arise due to the membrane compositional and electrostatic characteristics, internal cellular structure, and the type of nucleus (Gascoyne and Vykoukal 2004) associated with each cell type.

The application of DEP to separate target cells from a solution has been studied extensively in the last two decades. Examples of the successful use of DEP include the separation of human leukemia cells from red blood cells in an isotonic solution (Becker et al. 1994), entrapment of human breast cancer cells from blood (Gascoyne et al. 1997), and separation of U937 human monocytic from peripheral blood mononuclear cells (PBMC) (Huang et al. 2002). DEP has also been used to separate neuroblastoma cells from HTB glioma cells (Huang et al. 2002), isolate cervical carcinoma cells (Cheng et al. 1998), isolate K562 human CML cells (Altomare et al. 2003), separate live yeast cells from dead (Markx et al. 1994), and segregate different human tumor cells (Das et al. 2005). Unfortunately, the microelectrode-based devices used in these experiments are susceptible to electrode fouling and require complicated fabrication procedures (Hughes 2002; Steffen Hardt 2007).

Insulator-based dielectrophoresis (iDEP) is a practical method to obtain the selectivity of DEP while overcoming the robustness issues associated with traditional DEP platforms. iDEP relies on insulating obstacles rather than the geometry of its electrodes to produce spatial non-uniformities in the electric field. The patterned electrodes at the bottom of the channel employed by conventional DEP create an electric field gradient near their surface such that only cells in their vicinity are affected. One advantage of iDEP, is that the insulating structures typically traverse the entire depth of the channel and provide a non-uniform electric field over their entire depth, thus increasing the affected area. This advantage typically results in a higher throughput for the technique when compared to traditional DEP. The basic concept of the iDEP technique was first presented by Masuda et al. (Masuda et al. 1988). Others have previously demonstrated with glass insulating structures and AC electric fields that iDEP can separate DNA molecules, bacteria, and hematapoietic cells (Chou et al. 2002). It has been shown that polymer-based iDEP devices are effective for selective trapping of a range of biological particles in an aqueous sample (Davalos et al. 2008). iDEP technology has also shown the potential for water quality monitoring (Simmons et al. 2006), separating and concentrating prokaryotic cells and viruses (Lapizco-Encinas et al. 2005), concentration and separation of live and dead bacteria (Lapizco-Encinas et al. 2004), sample concentration followed by impedance detection (Sabounchi et al. 2008), and manipulation of protein particles (Lapizco-Encinas et al. 2008).

While many have had success designing and fabricating different DEP and iDEP microdevices to manipulate particles in biological fluids, there are some potential drawbacks of these techniques. The traditional DEP technique suffers from fouling, contamination, bubble formation near integrated electrodes, low throughput, and an expensive and complicated fabrication process (Hughes 2002; Steffen Hardt 2007). The insulating obstacles employed by iDEP are meant to address these shortcomings and are less susceptible to fouling than integrated electrodes (Cummings and Singh 2003). iDEP's fabrication process is also much less complicated; the insulating obstacles can be patterned while etching the microchannel in one step. This technique has the added benefit of making the process more economical in that mass fabrication can be facilitated through the use of injection molding. Unfortunately, one of the primary drawbacks of an iDEP system is the presence of a high electric field intensity within the highly conductive biological fluid inside the microchannel (Sabounchi et al. 2008; Steffen Hardt 2007). The relatively high electrical current flow in this situation causes joule heating and a dramatic temperature increase. The ideal technique would combine iDEP's simple fabrication process and resistance to fouling with DEP's reduced susceptibility to joule heating all-the-while preserving the cell manipulation abilities of both methods.

We have developed an alternative method to provide the spatially non-uniform electric field required for DEP in which electrodes are not in direct contact with the biological sample. The absence of contact between electrodes and the sample fluid inside the channel prevents bubble formation and mitigates fouling. It is also important to note that without direct contact between the electrodes and the sample fluid, any contaminating effects of this interaction can be avoided. In fact, the only material in contact with the sample fluid is the substrate material on which the device is patterned. In our method, an electric field is created in the microchannel using electrodes inserted in a highly conductive solution which is isolated from the main channel by thin insulating barriers. These insulating barriers exhibit a capacitive behavior and therefore an electric field can be produced in the main channel by applying an AC electric field across them. Furthermore, non-uniformity of the electric field distribution inside the main channel is provided by the geometry of insulating structures both outside and inside the channel.

In order to demonstrate this new method for cell separation and manipulation, we have designed and fabricated a microfluidic device to observe the DEP response of cells to a non-uniform electric field created without direct contact from electrodes. Modeling of the non-uniform electric field distribution in the device was accomplished through an equivalent electronic circuit and

finite element analysis of the microfluidic device. The effects of different parameters such as total applied voltage, applied frequency, and the electrical conductivity of the fluid inside and outside of the main channel on the resulting DEP response were simulated and then observed through experimentation. DEP responses for three different cell lines (THP-1, MCF-7, and MCF-10A) were observed primarily as a change in cell trajectory or velocity as it traveled through the device. Further evidence of this DEP response to the non-uniform electric field is provided by the electrorotation of cells, and their aggregation in "pearl chain" formations.

2 Theory

DEP is the motion of polarized particles in a non-uniform electric field toward the high (positive DEP) or low (negative DEP) electric field. The direction of the force depends on the particle's polarizability compared with medium conductivity. The time-average dielectrophoretic force is described as (Pohl 1951, 1958):

$$\boldsymbol{F}_{DEP} = 2\pi\varepsilon_m \boldsymbol{r}^3 \mathrm{Re}\{\boldsymbol{K}(\omega)\}\nabla(\boldsymbol{E}_{\mathrm{rms}} \cdot \boldsymbol{E}_{\mathrm{rms}}) \tag{1}$$

where ε_m is the permittivity of the suspending medium, r is the radius of the particle, and $\boldsymbol{E}_{rms}$ is the root mean square electric field. $\mathrm{Re}\{\boldsymbol{K}(\omega)\}$ is the real part of the Clausius-Mossotti factor $\boldsymbol{K}(\omega)$. The Clausius-Mossotti is given by:

$$\boldsymbol{K}(\omega) = \frac{\varepsilon_p^* - \varepsilon_m^*}{\varepsilon_p^* + 2\varepsilon_m^*} \tag{2}$$

where ε_p^* and ε_m^* are the complex permittivities of the particle and the medium, respectively. Complex permittivity is defined as:

$$\varepsilon^* = \varepsilon + \frac{\sigma}{\boldsymbol{j}\omega} \tag{3}$$

where ε and σ are the real permittivity and conductivity of the subject, $j = \sqrt{-1}$ and ω is the radial frequency.

Electrorotation is the rotation of polarized particles suspended in a liquid due to an induced torque in a rotating electric field (Arnold 1982). The maximum magnitude of the torque is given by:

$$\Gamma = -4\pi\varepsilon_m \boldsymbol{r}^3 \mathrm{Im}\{\boldsymbol{K}(\omega)\}(\boldsymbol{E}_{\mathrm{rms}} \cdot \boldsymbol{E}_{\mathrm{rms}}) \tag{4}$$

where $\mathrm{lm}\{\boldsymbol{K}(\omega)\}$ is the imaginary part of the Clausius-Mossotti factor $\boldsymbol{K}(\omega)$.

Assuming the cells are spherical particles in the medium, the hydrodynamic frictional force, f_{Drag}, due to translation and hydrodynamic frictional torque, R, due to rotation are given by:

$$\boldsymbol{f}_{Drag} = 6\eta r\pi(\boldsymbol{u}_p - \boldsymbol{u}_f) \tag{5}$$

$$\boldsymbol{R} = 8\eta\pi r^3 \Omega \tag{6}$$

where r is the particle radius, η is the medium viscosity, u_p is the velocity of the particle, u_f is the medium velocity, R is induced torque, and Ω is the electrorotation rate (rad.S^{-1}).

The magnitude of the steady state electrorotation rate, Ω, and translational velocity, u_p, is determined by a balance between the induced torque and the hydrodynamic friction and between the induced dielectrophoretic force and Stoke's drag force on a cell, respectively. In this preliminary study it should be noted that the effect of the acceleration term is considered to be negligible. The relationship is given by:

$$\Omega(\omega) = \frac{\varepsilon_m}{2\eta}\mathrm{Im}\left(\frac{\varepsilon_p^* - \varepsilon_m^*}{\varepsilon_p^* + 2\varepsilon_m^*}\right)\boldsymbol{E}_{\mathrm{rms}} \cdot \boldsymbol{E}_{\mathrm{rms}} \tag{7}$$

$$\boldsymbol{u}_p = \boldsymbol{u}_f - \mu_{DEP}\nabla(E \cdot E) \tag{8}$$

where μ_{DEP} is the dielectrophoretic mobility of the particle and is defined as:

$$\mu_{DEP} = \frac{\varepsilon_m \boldsymbol{r}^2}{3\eta}\mathrm{Re}\left(\frac{\varepsilon_p^* - \varepsilon_m^*}{\varepsilon_p^* + 2\varepsilon_m^*}\right) \tag{9}$$

3 Methods

3.1 Microfabrication process

3.1.1 Deep reactive ion etching (DRIE)

A silicon master stamp was fabricated on a <100> silicon substrate. AZ 9260 (AZ Electronic Materials) photoresist was spun onto a clean silicon wafer and softbaked at 114°C for 45 s (Fig. 1(a)). The wafer was then exposed to UV light for 45 s with an intensity of 12 W/m through a chrome-plated glass mask. The exposed photoresist was then removed using Potassium-based buffered developer AZ400K followed by another hard baking at 115°C for 45 s (Fig. 1(b)). Deep Reactive Ion Etching (DRIE) was used to etch the silicon master stamp to depths ranging from 50-100 microns (Fig. 1(c)). The silicon master stamp was then cleaned with acetone to remove any remaining photoresist (Fig. 1(d)). The scalloping effect, a typical effect of the

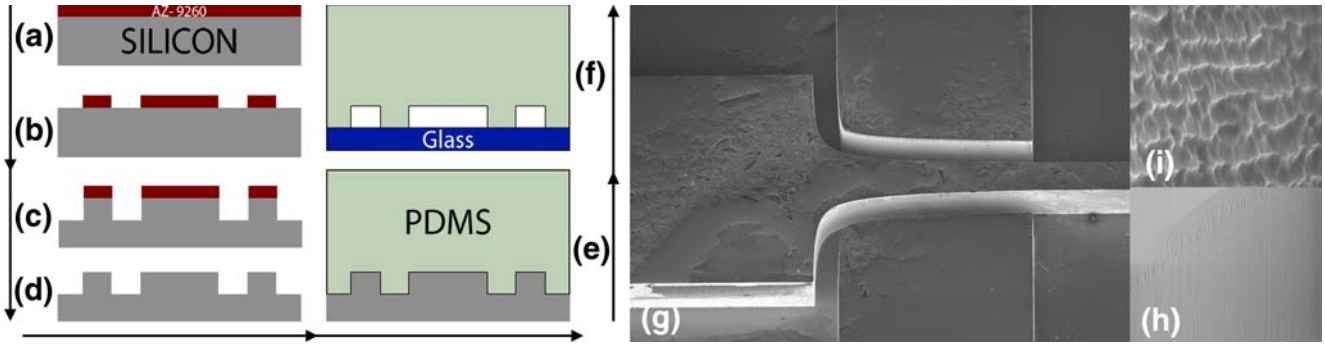

Fig. 1 (**a**–**i**) Schematic of the fabrication process used to create the microfluidic chambers and the SEM image of the scalloping effect on the silicon master. Steps (**a**) through (**d**) are followed only once to create a master stamp. Steps (**e**) and (**f**) are repeated to produce an indefinite number of experimental devices. (**g**) SEM image of the silicon wafer mold at the intersection between the side and the main channel of the microfluidic device. (**h**) Surface roughness of the wafer after growing and removing the oxide layer. (**i**) Scalloping effect after DRIE

DRIE etching method, creates a surface roughness which is detrimental to the stamping process. In order to reduce the surface roughness, silicon oxide was grown on the silicon master using thermal oxidation and then was removed (Fig. 1(g–i)).

3.1.2 PDMS

The liquid phase PDMS was made by mixing the PDMS monomers and the curing agent in a 10:1 ratio (Sylgrad 184, Dow Corning, USA). Bubbles in the liquid PDMS were removed by exposing the mixture to vacuum for an hour. An enclosure was created around the wafer using aluminum foil in order to contain the PDMS on the wafer as well as to ensure the proper depth for the PDMS portion of the device. The clean PDMS liquid was then poured onto the silicon master and 15 min was allowed for degassing. The PDMS was then cured for 45 min at 100°C (Fig. 1(e)) and then removed from the mold. Finally, fluidic connections to the channels were punched with 15 gauge blunt needles (Howard Electronic Instruments, USA).

3.1.3 Bonding

Microscope glass slides (3" × 2" × 1.2 mm, Fisher Scientific, USA) were cleaned with soap and water, rinsed with distilled water and isopropyl alcohol, then dried with a nitrogen gun. The PDMS replica was bonded with the clean glass slides after treating with oxygen plasma for 40 s at 50 W RF power (Fig. 1(f)). A schematic with dimensions and equivalent circuit model of our device is presented in (Fig. 2(a)). The channel depth in this device is 100 μm and

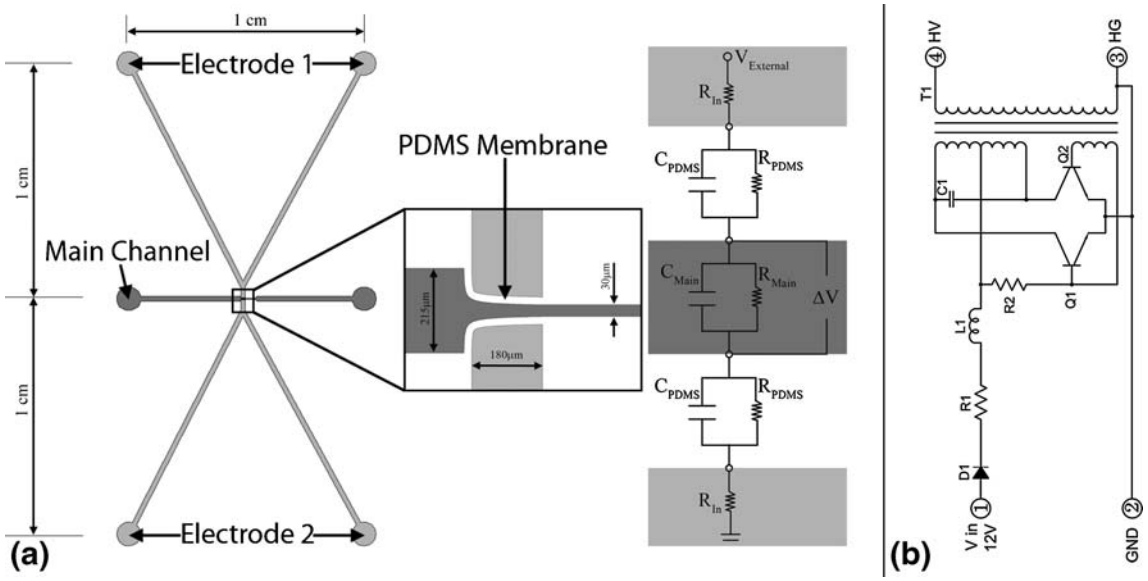

Fig. 2 (**a**) Schematic of the microfluidic device and the equivalent circuit model. (**b**) Schematic of the two transistor inverter circuit provided by JKL Components Corp

Table 1 Electrical properties of the materials and fluids

Electrical Properties Materials	Electrical Conductivity (S/m)	Relative Electrical Permittivity
PDMS	0.83 e-12	2.65
PBS	1.4	80
DEP Buffer	0.01	80

the thickness of the PDMS barrier between the side channels and the main channel is 20 μm.

3.1.4 Experimental setup

Pipette tips, inserted in the punched holes in the PDMS portion of the device, were used as reservoirs for fluidic connections to the channels. Pressure driven flow (10 to 15 μl/hr) was provided by an imbalance in the amount of the sample in these reservoirs of the main channel. An inverted light microscope (Leica DMI 6000B, Leica Microsystems, Bannockburn, IL) equipped with a digital camera (Hamamatsu EM-CCD C9100, Hamamatsu Photonics K.K. Shizuoka Pref., 430-8587, Japan) was used to monitor cells in the main channel. Microfluidic devices were placed in a vacuum jar for at least half an hour before running the experiments to reduce priming issues and then the side and main microchannels were filled with PBS and DEP buffer, respectively.

3.1.5 Cells and buffer

The THP-1 human Leukemia monocytes, MCF-7 breast cancer cells, and MCF-10A breast cells were washed twice and resuspended in our prepared DEP buffer (8.5% sucrose [wt/vol], 0.3% glucose [wt/vol], and 0.725% [vol/vol] RPMI) (Flanagan et al. 2008). The electrical conductivity of the buffer was measured with a Mettler Toledo SevenGo Pro conductivity meter (Mettler-Toledo, Inc., Columbus, OH) to ensure that its conductivity was 100 μS/cm. These cells were observed to be spherical when in suspension. The measured diameters of the cells with the corresponding standard deviations (n=30) are given in Table 2.

3.1.6 Electronics

A commercially available two-transistor inverter circuit (BXA-12576, JKL Components Corp., USA) was modified to provide a high-frequency and high-voltage AC signal for the device (Fig. 2(b)). The circuit relies on the oscillation created by the two-transistors and passive components to create an AC voltage on the primary side of a transformer. This voltage is then stepped-up by the transformer to give a high-output voltage on the secondary side to which the microfluidic device was connected.

The resonant frequency at which the circuit operates is highly dependent on the load impedance connected to the secondary side of the transformer. Two high-voltage power supplies were fabricated with resonant frequencies of 85 kHz and 125 kHz. A DC input voltage was provided by a programmable DC power supply (PSP-405, Instek America Corp., USA) which allowed adjustment of the output voltage by varying the input voltage. This technique allowed the output voltage of the power supplies to be varied from approximately 100 Vrms to 500 Vrms. A three-resistor voltage divider network, with a total impedance of one megaohm, was added to the output of the inverter circuit in order to provide a scaled (100:1) output voltage to an oscilloscope (TDS-1002B, Tektronix, USA) which facilitated monitoring the frequency and magnitude of the signal applied to the microfluidic device. All circuitry was housed in a plastic enclosure with proper high-voltage warnings on its exterior and connections were made to the microfluidic device using high-voltage test leads.

3.1.7 Translational and rotational velocity measurement

The average velocity of the THP-1, MCF-7 and MCF-10A cells in our microfluidic device was measured along the centerline a-b in Fig. 3 from point 1 to point 4. Time-lapse videos were recorded of the cells motion before and after applying an AC electric field through the platinum electrodes inserted in the side channels. These recorded videos then were converted to JPEG files using the Leica software, (Leica DMI 6000B, LAS AF 1.6.3Leica Micro-

Table 2 The measured average velocity from point 1 to point 4 (Fig. 3) of five different cells before and after applying the electric field at the zone of trapping

Cell Velocity Cell line	Diameter (μm)	Uon (μm/s)	Uoff (μm/s)	Uoff- Uon(μm/s)	Uon/Uoff	Ω (rad/s)
THP-1	15.4 ±2	240±13	392±21	152±19	0.61±0.08	8.1±0.66
MCF-7	18.5±2.5	387±7	476±17	89±17	0.81±0.04	19.4±2.9
MCF-10A	18.2±2.1	310±17	313±16	3±24	0.99±0.076	N.A.

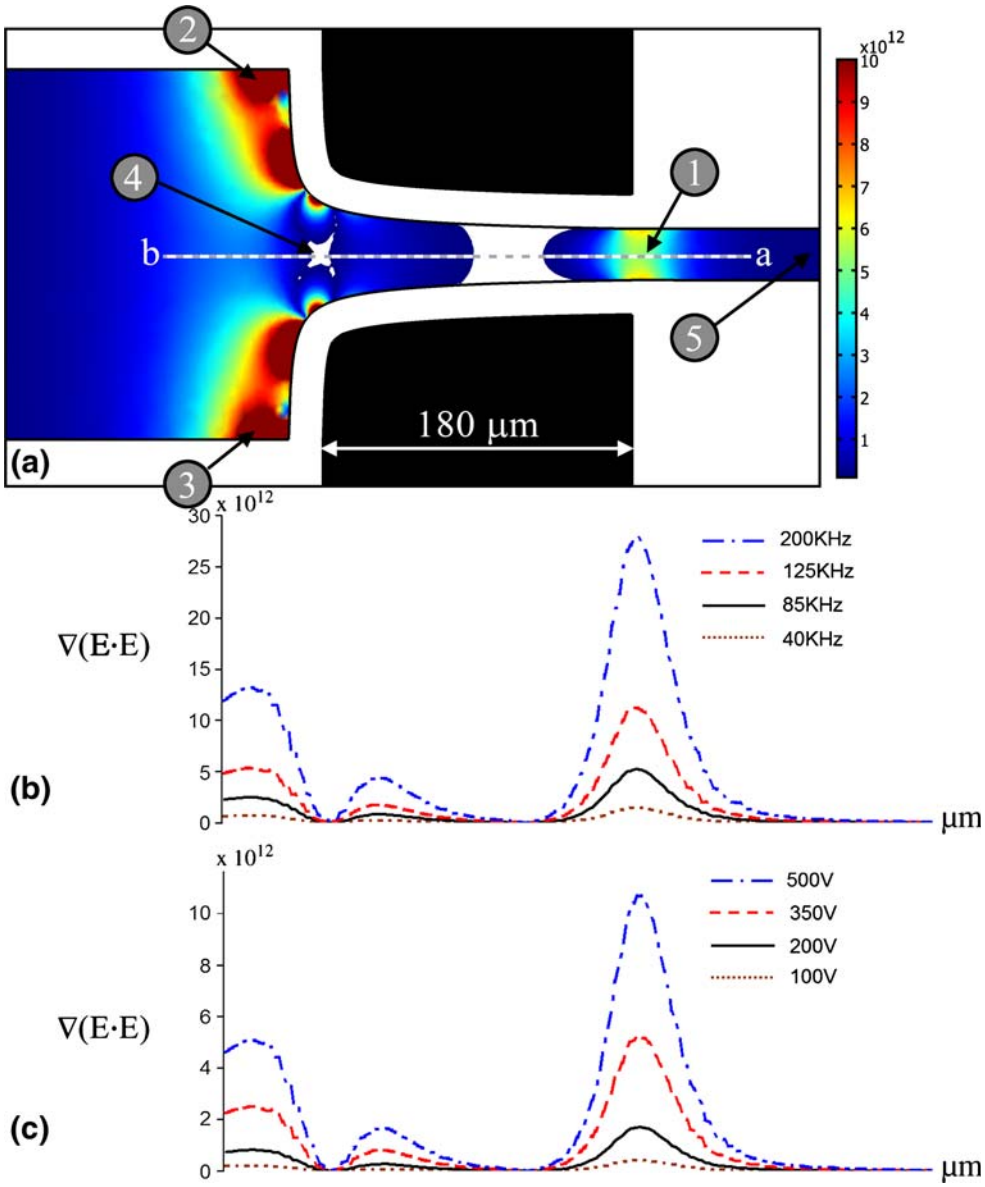

Fig. 3 Numerical results of the electric field gradient within the sample channel (**a**) Surface plot of the gradient of the field ($kg^2mC^{-2}S^{-4}$)within the main microchannel (**b**) Line plot of the gradient ($kg^2mC^{-2}S^{-4}$) along the line a-b (mm) for four different frequencies (40 kHz, 85 kHz, 125 kHz, and 200 kHz) at 250 Vrms (**c**) The line plot of the gradient of the electric field along the line a-b for four different applied voltages (100 V, 200 V, 350 V, and 500 V) at 85 kHz

systems, Bannockburn, IL), in order to measure the traveling time of the target cells for a known specific distance in the main channel. These measurements were performed before and after inducing the electric field in the main microfluidic channel.

3.2 Numerical modeling

The microfluidic device was modeled numerically in Comsol multi-physics 3.4 using the AC/DC module (Comsol Inc., Burlington, MA, USA). Because DEP

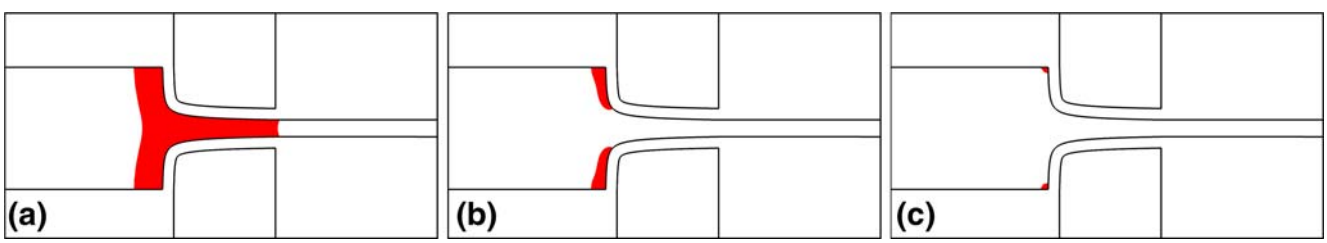

Fig. 4 Electric field surface plot for an applied AC field at 85 kHz and 250 Vrms. Areas with the induced electric field intensity higher than (**a**) 0.1 kV/cm, (**b**) 0.15 kV/cm, (**c**) 0.2 kV/cm

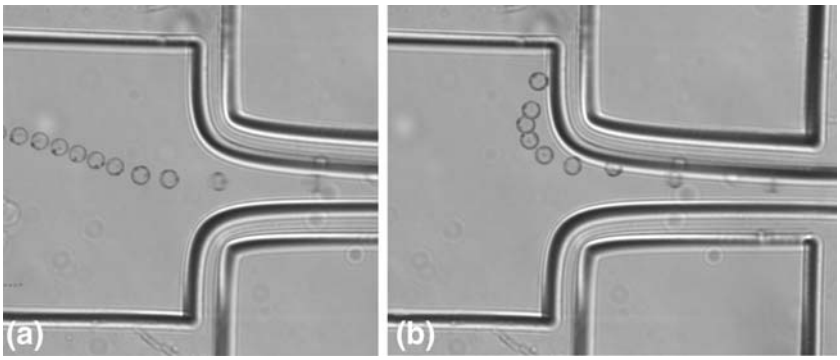

Fig. 5 Superimposed images showing the trajectory of one cell through the device. (**a**) The cell is moving from right to left under an applied pressure (**b**) with an applied voltage of 250 Vrms at 85 kHz. The superimposed images were approximately 250 ms apart

depends on the gradient of the electric field, $\nabla E = -\nabla(\nabla\phi)$ the first step in modeling was to determine the electric field distribution within a channel's geometry. This was done by solving for the potential distribution, ϕ, using the Laplace equation, $\nabla^2\phi = 0$. The boundary conditions used are prescribed uniform potentials at the inlet or outlet of the side channels.

The values for the electrical conductivity and permittivity of the PDMS, PBS, and DEP buffer that were used in this numerical modeling are given in Table 1. PBS and DEP buffer electrical properties are used for the side and main microfluidic channels, respectively.

The effect of the external voltage and the frequency on the gradient of the induced electric field has been studied. The gradient of the electric field along the center line of the main channel is investigated numerically for different applied voltages (100 V, 200 V, 350 V, and 500 V) at 85 kHz and for different frequencies (40 kHz, 85 kHz, 125 kHz, and 200 kHz) at 250 Vrms applied voltage. Based on our current available electronic circuit (250Vrms at 85 kHz), the electric field distribution and the gradient of the electric field was mapped in our microfluidic device.

4 Results and discussion

4.1 Numerical results

Figure 3 shows the surface and line plot of the gradient of the electric field inside the main microfluidic channel at the intersection between the main and the side channels. There is a high gradient of the electric field at the corners (points 2 and 3) as well as point 1, which can provide a strong DEP force. These results indicate that changes in the thickness of the PDMS barrier have a more significant effect on the gradient of the induced electric field inside the main channel than changes in the channel's geometry which is in agreement with our analytical results.

In (Fig. 3(b)) the gradient of the electric field along the line a-b is plotted for different applied frequencies (40 kHz, 85 kHz, 125 kHz, and 200 kHz) at 250 Vrms. The effect of the total external voltage across the microfluidic device on the gradient of the electric field (along the line a-b) is also investigated in (Fig. 3(c)). DEP response of the system is plotted for four different voltages (100 V, 200 V, 350 V, and 500 V) at 85 kHz.

An increased gradient of the electric field can be obtained by increasing the applied frequency or increasing the total applied voltage although it should be noted that adjusting the frequency will also affect the Clasius-Mossotti factor of the microparticles and needs to be considered. Also the induced gradient of the electric field in the main microfluidic channel is on the order of 10^{12} ($kg^2mC^{-2}S^{-4}$) which is strong enough for particle manipulations.

Based on this numerical modeling, the voltage drop across the 20 μm PDMS barrier was 250 V for an applied total voltage of 500 V across the microfluidic electrode channels. This voltage drop is lower than the 400 V break down voltage for a 20 μm PDMS channel wall. Thus, the DEP force can be amplified by adjusting the input voltage with some tolerance.

4.1.1 Electric field surface plot

Figure 4(a-c) shows the induced electric field intensity distribution inside the main microfluidic channel filled with the DEP buffer with a conductivity of 100μS/cm. The highest electric field is induced at the zone of intersection between the main and the side channels and between the PDMS barriers. Figure 4(c) also shows that with an applied AC electric field of 250 Vrms and 85 kHz the electric field does not significantly exceed 0.2 kV/cm in the main microfluidic channel.

4.2 Experimental results

4.2.1 Cell trapping-contactless DEP evidence

Figure 5 shows the experimental results we attained using MCF-7 breast cancer cells and THP-1 leukemia cells in our device. The behavior of cells traveling through the device under static conditions was observed to be significantly different than when an electric field was applied to the device. Three induced DEP responses were studied, rotation, velocity changes, and chaining.

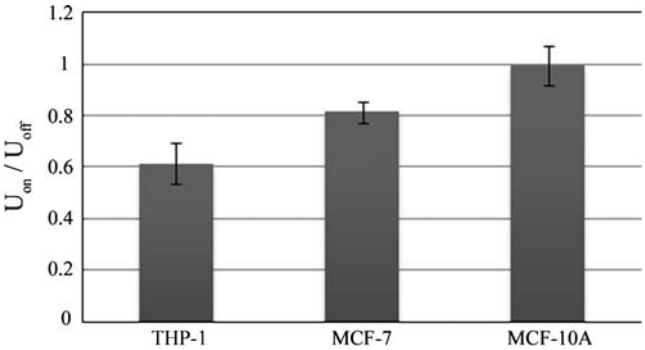

Fig. 6 The normalized velocity of THP-1, MCF-7, and MCF-10A cells. U_{on} is the velocity of the cells while applying e-field and U_{off} is the velocity of the cells while the power is off

Under a pressure driven flow, without an applied electric field, it was observed that THP-1 leukemia and MCF-7 breast cancer cells flow through the main microfluidic channel from right to left without any disruption or trapping. The cells were observed to be trapped, experiencing a positive DEP force, once an AC electric field at 85 kHz and 250 Vrms was applied. A representative video is given in the supplemental online data (supplemental online Video 1). Their velocity decreased at the intersection between the main and the side channels where the thin PDMS barriers are located. With the same electrical boundary conditions we did not observe any trapping or cell movement disruption for MCF-10A normal breast cells. These results indicate that the cells exhibited positive DEP at 85 kHz in our device. Furthermore, our results indicate that contact-less DEP may be an alternative method to DEP and iDEP to distinguish and separate cell types based on their Clausius-Mossotti factor.

Since the positive DEP force in the main microchannel depends on the electrical properties of the cells, different cell lines experience different forces at the same electrical boundary conditions (external voltage and frequency) in the same buffer. Cell bursting or lysis was not observed during cDEP trapping.

4.2.2 Translational velocity

The cells were observed to move faster along the centerline of the sample channel in (Fig. 3(a)) from point 5 to point 1 when the electric field was applied as compared to their velocity due to pressure driven flow. As shown in (Fig. 3), the magnitude of the DEP force is high at point 1. Because the DEP force is positive at 85 kHz, the cells are attracted to this point. Therefore, as the cells approach point 1 from the right, the positive DEP force is in the direction of the pressure driven flow, causing the cells to move faster down the channel. Conversely, the average velocity of the cells in the area between the thin PDMS barriers (from 1 to 4) decreases when the voltage is applied because the positive DEP force now acts in the opposite direction of the pressure driven flow.

Table 2 compares the average induced velocities of the cells with respect to their average velocities under pressure driven flow. The normalized velocity (U_{on} /U_{off}) for the three cell lines under the same electrical boundary conditions (250 Vrms at 85 kHz) are also reported in (Fig. 6). The results show that there is a statistically significant difference in the cells velocities when the field is applied. Furthermore, when the experiments are normalized for comparison, the results suggest that this technique can be used to differentiate cells based on their electrical properties.

The same experiments with the same buffers and electrical boundary conditions were performed on MCF-10A breast cells without noticeable trapping or disruption, which shows that the electrical properties of the normal breast cells are different compared to the MCF-7 breast cancer cells. It also shows the sensitivity of the cDEP technique to isolate cells with close electrical properties.

There was a great tendency for cells to move towards the corners in the main channel. This agrees with our numerical results, which show there is a high gradient of the induced electric field at the corners, which causes a strong positive DEP force and pulls cells towards these zones of the main microfluidic channel.

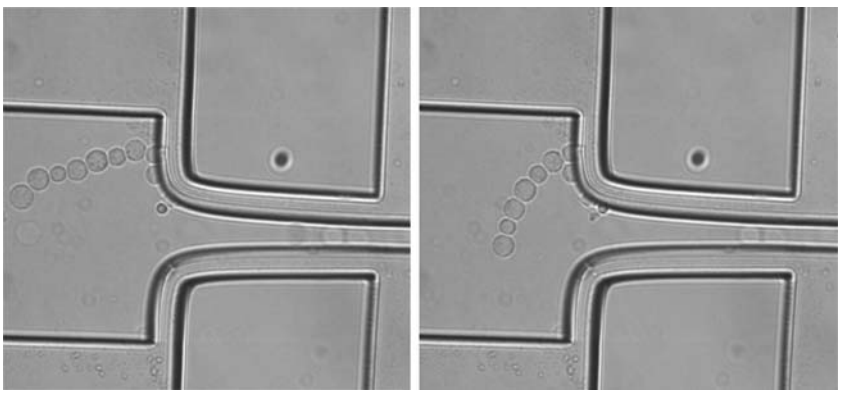

Fig. 7 Two, single-frame, showing several cells arranged in the "pearl-chain" phenomena often associated with DEP. These images show the grouping of cells into a chain configuration in areas of the main channel with a high gradient of the electric field. Images were captured with an applied field of 250 Vrms at 85 kHz

4.2.3 Rotational velocity

Cell rotation in the main channel at the zone of trapping and between the thin PDMS barriers was present with an applied electric field. The rotational velocity of the cell is a function of its electrical properties, the medium permittivity, the medium dynamic viscosity as well as the properties of the electric field. We measured the rotational velocity of the trapped THP-1, and MCF-7 cancer cells in different experiments at one spot of the main microfluidic channel. No cell rotation was observed without an applied electric field. The reported rotational velocities in Table 2 are the average rotational velocities of five different cells of each of the cancer lines. These results imply that the average rotational velocities of the THP-1 and MCF-7 cancer cell lines are significantly different. Cell rotation for the MCF-10A cells with the same electrical boundary conditions in the same buffer solution was not observed.

4.2.4 Pearl-chain

Cell aggregation and chain formation in DEP experiments with an AC field have been frequently observed and can be attributed to dipole-dipole interactions as well as local distortions of the electric field due to the cells' presence (Dussaud 2000; Pohl 1951, 1958; Wong 2004). Particles parallel to the electric field attract each other because of this dipole-dipole force, resulting in pearl-chaining of the trapped cells in the direction of the electric field in the microfluidic channel. The cell chain formation was observed for the MCF-7 and THP-1 cancer cell lines in our experiments with an applied AC electric field at 85 kHz and 250 Vrms (Fig. 7).

5 Conclusion

We have demonstrated a new technique for inducing electric fields in microfluidic channels in order to create a dielectrophoretic force. Our method relies on the application of a high-frequency AC electric signal to electrodes that are capacitively coupled to a microfluidic channel. In our device, the geometry of the electrode channels create the spatial non-uniformities in the electric field required for DEP. Three separate DEP responses were observed in our device, namely, translational velocity, rotational velocity, and chaining. In order to observe the devices effects in these three categories, three different cell lines were inserted into the devices and their individual responses recorded. Each cell line exhibited a response unique to its type due to the cell's specific electrical properties. This result highlights the ability of our technique to differentiate cells by their intrinsic electrical properties.

We believe this technique may help overcome many of the challenges faced with traditional DEP and iDEP. Because the induced electric field is not as intense as comparable methods and is focused just at the trapping zones, we theorize the joule heating within the main microfluidic channel is negligible. This could mitigate the stability and robustness issues encountered with conventional iDEP (Sabounchi et al. 2008), due to the conductivity distribution's strong dependence on temperature. Furthermore, challenges associated with cell lysing due to high temperatures (Kang et al. 2008) or irreversible electroporation due to high field strengths (Davalos et al. 2005; Edd and Davalos 2007) are overcome with our new design approach under these conditions.

Acknowledgements This work was supported by the Institute for Critical Technology and Applied Science (ICTAS). Also the authors would like to acknowledge Dr. Eva M. Schmelz at the department of Human Nutrition, Foods, & Exercise and Phillip Andrew Zellner for their cooperation.

References

L. Altomare, M. Borgatti, G. Medoro, N. Manaresi, M. Tartagni, R. Guerrieri, R. Gambari, Biotechnol. Bioeng. **82**, 474 (2003). doi:10.1002/bit.10590

W. M. K. J. G. m. b. H. Arnold, Juelich (Germany, F.R.). Inst. fuer Medizin); Zimmermann, U. Plant Physiol. Biochem. **37**, 908 (1982)

A. Ashkin, J.M. Dziedzic, T. Yamane, Nature **330**, 769 (1987). doi:10.1038/330769a0

F.F. Becker, X.-B. Wang, Y. Huang, R. Pethig, J. Vykoukal, P.R.C. Gascoyne, J. Phys. D. Appl. Phys. (Berl.) **27**, 2659 (1994)

J. Cheng, E.L. Sheldon, L. Wu, M.J. Heller, J.P. O'Connell, Anal. Chem. **70**, 2321 (1998). doi:10.1021/ac971274g

C. Chou, J. Tegenfeldt, O. Bakajin, S. Chan, E. Cox, N. Darnton, T. Duke, R. Austin, Biophys. J. **83**, 2170 (2002). doi:10.1016/S0006-3495(02)73977-5

E.B. Cummings, A.K. Singh, Anal. Chem. **75**, 4724 (2003). doi:10.1021/ac0340612

C.M. Das, F. Becker, S. Vernon, J. Noshari, C. Joyce, P.R. Gascoyne, Anal. Chem. **77**, 2708 (2005). doi:10.1021/ac048196z

R.V. Davalos, G.J. McGraw, T.I. Wallow, A.M. Morales, K.L. Krafcik, Y. Fintschenko, E.B. Cummings, B.A. Simmons, Anal. Bioanal. Chem. **390**, 847 (2008). doi:10.1007/s00216-007-1426-5

R.V. Davalos, L.M. Mir, B. Rubinsky. Ann. Biomed. Eng. **33**, 223 (2005). doi:10.1007/s10439-005-8981-8

A.D. Dussaud, J. Appl. Phys. **88**, 5463 (2000). doi:10.1063/1.1315617

J.F. Edd, R.V. Davalos, Technol. Cancer Res. Treat. **6**, 275 (2007)

L.A. Flanagan, J. Lu, L. Wang, S.A. Marchenko, N.L. Jeon, A.P. Lee, E. S. Monuki, Stem Cells **26**, 656 (2008). doi:10.1634/stemcells.2007-0810

A.Y. Fu, C. Spence, A. Scherer, F.H. Arnold, S.R. Quake, Nat. Biotechnol. **17**, 1109 (1999). doi:10.1038/15095

P.R.C. Gascoyne, J.V. Vykoukal, Proc. IEEE **92**, 22 (2004). doi:10.1109/JPROC.2003.820535

P.R.C. Gascoyne, X.-B. Wang, Y. Huang, F.F. Becker, IEEE Trans. Ind. Appl. **33**, 670 (1997). doi:10.1109/28.585856

J.C. Giddings, Science **260**, 1456 (1993). doi:10.1126/science.8502990

Y. Huang, S. Joo, M. Duhon, M. Heller, B. Wallace, X. Xu, Anal. Chem. **74**, 3362 (2002). doi:10.1021/ac011273v

M.P. Hughes, Electrophoresis **23**, 2569 (2002). doi:10.1002/1522-2683(200208) 23:16<2569::AID-ELPS2569>3.0.CO;2-M

Y. Kang, D. Li, S.A. Kalams, J.E. Eid, Biomed. Microdevices **10**, 243 (2008). doi:10.1007/s10544-007-9130-y

B.H. Lapizco-Encinas, R.V. Davalos, B.A. Simmons, E.B. Cummings, Y. Fintschenko, J. Microbiol. Methods **62**, 317 (2005). doi:10.1016/j.mimet.2005.04.027

B.H. Lapizco-Encinas, S. Ozuna-Chacon, M. Rito-Palomares, J. Chromatogr. A **1206**, 45 (2008). doi:10.1016/j.chroma.2008.05.077

B.H. Lapizco-Encinas, B.A. Simmons, E.B. Cummings, Y. Fintschenko, Anal. Chem. **76**, 1571 (2004). doi:10.1021/ac034804j

G.H. Markx, M.S. Talary, R. OPethig, J. Biotechnol. **32**, 29 (1994). doi:10.1016/0168-1656(94)90117-1

S. Masuda, T. Itagaki, M. Kosakada, IEEE Trans. Ind. Appl. **24**, 740 (1988). doi:10.1109/28.6130

S. Miltenyi, W. Muller, W. Weichel, A. Radbruch. Cytometry **11**, 231 (1990). doi:10.1002/cyto.990110203

H.A. Pohl, J. Appl. Phys. **29** (1958)

H.A. Pohl, J. Appl. Phys. **22**, 869 (1951)

P. Sabounchi, D.E. Huber, A.E. Harris, B.A. Simmons, MicroTAS Conference, San Diego (2008).

P. Sabounchi, A.M. Morales, P. Ponce, L.P. Lee, B.A. Simmons, R.V. Davalos, Biomed Microdevices **10**, 661 (2008). doi:10.1007/s10544-008-9177-4

B.A. Simmons, G.J. McGraw, R.V. Davalos, G.J. Fiechtner, Y. Fintschenko, E.B. Cummings, MRS BULLETIN **31**, 120 (2006)

F. S. Steffen Hardt, *Microfluidic Technologies for Miniaturized Analysis Systems* (Springer, 2007). doi:10.1007/978-0-387-68424-6

P.K. Wong, IEEE/ASME Transactions on Mechatronics **9**, 366 (2004). doi:10.1109/TMECH.2004.828659

J. Yang, Y. Huang, X.B. Wang, F.F. Becker, P.R. Gascoyne, Anal Chem **71**, 911 (1999). doi:10.1021/ac981250p

Erin A. Henslee[1]
Michael B. Sano[1]*
Andrea D. Rojas[2]*
Eva M. Schmelz[3]
Rafael V. Davalos[1,2]

[1]School of Biomedical Engineering and Sciences, Virginia Tech-Wake Forest University, Blacksburg, VA, USA
[2]Department of Materials Science and Engineering, Virginia Tech, Blacksburg, VA, USA
[3]Department of Human Nutrition, Foods and Exercise, Virginia Tech, Blacksburg, VA, USA

Received January 27, 2011
Revised May 2, 2011
Accepted May 2, 2011

Research Article

Selective concentration of human cancer cells using contactless dielectrophoresis

This work is the first to demonstrate the ability of contactless dielectrophoresis (cDEP) to isolate target cell species from a heterogeneous sample of live cells. Since all cell types have a unique molecular composition, it is expected that their dielectrophoretic (DEP) properties are also unique. cDEP is a technique developed to improve upon traditional and insulator-based DEP devices by replacing embedded metal electrodes with fluid electrode channels positioned alongside desired trapping locations. Through the placement of the fluid electrode channels and the removal of contact between the electrodes and the sample fluid, cDEP mitigates issues associated with sample/electrode contact. MCF10A, MCF7, and MDA-MB-231 human breast cells were used to represent early, intermediate, and late-staged breast cancer, respectively. Trapping frequency responses of each cell type were distinct, with the largest difference between the cells found at 20 and 30 V. MDA-MB-231 cells were successfully isolated from a population containing MCF10A and MCF7 cells at 30 V and 164 kHz. The ability to selectively concentrate cells is the key to development of biological applications using DEP. The isolation of these cells could provide a workbench for clinicians to detect transformed cells at their earliest stage, screen drug therapies prior to patient treatment, increasing the probability of success, and eliminate unsuccessful treatment options.

Keywords:
Clausius–Mossotti factor / Dielectrophoresis / Enrichment / Microfluidics / Sample isolation
DOI 10.1002/elps.201100081

1 Introduction

Dielectrophoresis (DEP) has been increasingly investigated as a method for particle separation and isolation. The potential of DEP as a biological tool for sample isolation and enrichment for drug screening, disease detection and treatment, as well as on-chip applications lies in its inherent advantages over current concentration and detection techniques. These techniques typically maintain an inverse relationship between specificity and sensitivity forcing the compromise of high-throughput and highly specific isolation. Concentration methods such as density gradient-based centrifugation or filtration [1], fluorescent and magnetic-activated cell sorting (FACS/MACS) [2, 3] and laser tweezers [4], as well as detection techniques such as PCR and immunochemistry are all examples that demonstrate this basic problem encountered by the current detection techniques. Commonly, the more sensitive techniques may require prior knowledge of cell-specific markers and antibodies to prepare target cells for analysis. Additionally, the complex sample handling required by these techniques may compromise gene expression, contaminate samples, reduce cell populations, as well as add to experimental time and cost [5].

Since DEP response, the resultant motion of a particle due to its polarization in a non-uniform electric field [6, 7], is dependent upon physical and electrical properties of a particle, it presents an advantage over the current techniques in the ability to be highly specific with minimal sample preparation. Several applications to isolate target cells based on their biophysical properties have been successfully demonstrated through the separation of leukemia, breast cancer, and other targeted cells from blood [8–10], cancer cells from $CD34^+$ hematopoietic stem cells [11],

Correspondence: Dr. Rafael V. Davalos, School of Biomedical and Engineering Sciences, Virginia Tech-Wake Forest University, 329 ICTAS Building, Stanger Street (MC 0298) Blacksburg, VA 24061 Office, USA
E-mail: davalos@vt.edu
Fax: +1-540-231-9738

Abbreviations: AC, alternating current**; cDEP,** contactless dielectrophoresis**; DEP,** dielectrophoresis**; iDEP,** insulator-based dielectrophoresis

*These authors contributed equally to this work.

Colour Online: See the article online to view Figs. 1,3,4 in colour.

neuroblastoma cells from HTB glioma cells [10], as well as cervical carcinoma cells [8], K562 human CML cells [12], and mammalian cells based on their cell-cycle phase [13, 14]. The selectivity of DEP has been further demonstrated through the distinction of cells of the same type based on their activation state [15, 16].

Insulator-based DEP (iDEP) was investigated as a means to simplify the fabrication process of more traditional DEP methods relying on patterned electrodes within the sample channel, making DEP more appealing for mass production. iDEP relies on a direct current (DC) voltage, or low-frequency alternating current (AC) voltage, applied across the sample channel, where insulating structures within the microfluidic channel create the electric field non-uniformities necessary for DEP, as opposed to the electrode geometry required in traditional DEP [17–19]. Since these insulating structures typically traverse the entire depth of the channel, a greater area of the sample channel is affected by the gradient of the inner product of the electric field, greatly improving the device throughput. In addition, the DC field creates electrokinetic flow across the length of the sample channel, alleviating the need for a pump in pressure-driven flow [18, 20–28].

Contactless dielectrophoresis (cDEP) is a promising new DEP technique [29] that exploits the intrinsic advantages of DEP, while also mitigating the challenges associated with sample/electrode contact in the traditional DEP and iDEP. Rather than metal electrodes, cDEP utilizes fluid electrodes to develop electric field non-uniformities within a separate sample channel. The fluid electrode channels, containing a high-conductive solution, are isolated from the sample channel by thin insulating membranes [29, 30]. The geometry of the fluid electrode channels as well as the sample channel, which incorporates insulating barriers, creates the electric field non-uniformities necessary for DEP. This technique eliminates cell–electrode contact, minimizing contamination of the biological sample, joule heating, bubble formation, as well as electrochemical effects [29, 30]. As with iDEP, cDEP lends itself to mass fabrication techniques such as hot embossing and injection molding. cDEP has successfully been proven able to trap particles and selectively isolate viable leukemia cells from non-viable cells [29, 30].

This study is the first to assess the ability of cDEP to distinguish viable cell types. Specifically, trapping frequencies of human breast cancer cells representing early, intermediate, and advanced stages of the disease were determined for a range of voltages. The DEP responses of MCF10A, MCF7, and MDA-MB-231 cells were investigated using a cDEP device previously shown to isolate viable from non-viable human leukemia cells [30]. This study, through theoretical modeling, numerical simulations, and experimental results, demonstrates the ability of this particular cDEP device to distinguish dielectric properties of breast cancer at various stages. Additionally, this study can be used as a platform to further cDEP development towards applications such as isolation of cells from the same lineage, detection techniques, and individualized medicine.

2 Theory

DEP is the motion of a particle due to its polarization within a non-uniform electric field and is dependent on a particle's physical and electrical properties. By exploiting these differences in various cell types, DEP can be used as a method for separation. Different cells will have varying DEP responses to the same gradient of the inner product of the electric field determined by Pohl [6, 7]

$$F_{\mathrm{DEP}} = 2\pi\varepsilon_{\mathrm{M}} r^3 \mathrm{Re}\{K(\omega)\}\nabla(E \cdot E) \tag{1}$$

where ε_{M} is the permittivity of the suspending medium, r is the radius of the particle, and E is the root mean-square electric field. $\mathrm{Re}\{K(\omega)\}$ is the real part of the Clausius–Mossotti factor given by

$$K(\omega) = \frac{\varepsilon_{\mathrm{p}}^* - \varepsilon_{\mathrm{M}}^*}{\varepsilon_{\mathrm{p}}^* + 2\varepsilon_{\mathrm{M}}^*} \tag{2}$$

where $\varepsilon_{\mathrm{p}}^*$ and $\varepsilon_{\mathrm{M}}^*$ are the complex permittivities of the particle and the medium, respectively. Complex permittivity is defined as

$$\varepsilon^* = \varepsilon + \frac{\sigma}{j\omega} \tag{3}$$

where ε and σ are the real permittivity and conductivity of the subject, $\mathrm{j} = \sqrt{-1}$ and ω is the radial frequency. From the single shell dielectric model [31] the effective permittivity and conductivity of the particle (ε_{p} and σ_{p} respectively) can be expressed as

$$\varepsilon_{\mathrm{p}} = \varepsilon_{\mathrm{m}} \frac{\gamma^3 + 2\left(\frac{\varepsilon_{\mathrm{c}} - \varepsilon_{\mathrm{m}}}{\varepsilon_{\mathrm{c}} + 2\varepsilon_{\mathrm{m}}}\right)}{\gamma^3 - \left(\frac{\varepsilon_{\mathrm{c}} - \varepsilon_{\mathrm{m}}}{\varepsilon_{\mathrm{c}} + 2\varepsilon_{\mathrm{m}}}\right)} \tag{4}$$

$$\sigma_{\mathrm{p}} = \sigma_{\mathrm{m}} \frac{\gamma^3 + 2\left(\frac{\sigma_{\mathrm{c}} - \sigma_{\mathrm{m}}}{\sigma_{\mathrm{c}} + 2\sigma_{\mathrm{m}}}\right)}{\gamma^3 - \left(\frac{\sigma_{\mathrm{c}} - \sigma_{\mathrm{m}}}{\sigma_{\mathrm{c}} + 2\sigma_{\mathrm{m}}}\right)} \tag{5}$$

where the subscripts m and c denote membrane and cytoplasm respectively and $\gamma = (r/r - d)$ where r is the particle radius and d is the membrane thickness. By substituting Eqs. (4) and (5) into Eq. (3), the real part of Clausius–Mossotti factor in Eq. (2) is given by

$$\mathrm{Re}[K(\varepsilon_{\mathrm{p}}^*, \varepsilon_{\mathrm{M}}^*, \omega)] = \frac{(\sigma_{\mathrm{p}} - \sigma_{\mathrm{M}})}{(1 + \omega^2\tau_{\mathrm{MW}}^2)(\sigma_{\mathrm{p}} + 2\sigma_{\mathrm{M}})} + \frac{\omega^2\tau_{\mathrm{MW}}^2(\varepsilon_{\mathrm{p}} - \varepsilon_{\mathrm{M}})}{(1 + \omega^2\tau_{\mathrm{MW}}^2)(\varepsilon_{\mathrm{p}} + 2\varepsilon_{\mathrm{M}})} \tag{6}$$

where $\tau_{\mathrm{MW}} = \frac{\varepsilon_{\mathrm{p}} + 2\varepsilon_{\mathrm{M}}}{\sigma_{\mathrm{p}} + 2\sigma_{\mathrm{M}}}$ is the Maxwell–Wagner relaxation time.

It is important to note that $\mathrm{Re}\{\mathrm{K}(\omega)\}$ can take both positive and negative values based on the sign of Eq. (6). When the particle is more polarizable than the medium, the particle will move toward regions containing the highest gradient of the inner product of the electric field (positive DEP). If the medium is more polarizable than the particle, the electric field will be distorted around the particle inducing the dipole in the opposite direction pushing the particle away from regions containing the highest gradient of the

inner product of the electric field (negative DEP). The frequency at which the force changes direction is known as a crossover frequency. At this frequency, the medium and particle have the same complex permittivity and thus there is no net force on the particle. By using the relation Re{K(ω)}, unknown dielectric properties can be determined from particles' DEP responses [32–34]. Conversely, if dielectric properties of a particle are known, the crossover frequency can be calculated and exploited for separation of one particle type from a heterogeneous sample [8, 9, 11, 13, 14, 16, 35].

3 Methods

3.1 Device fabrication

A silicon master stamp was fabricated on a <100> working-grade silicon substrate (University Wafer, South Boston, MA, USA). The wafer was coated with AZ 9260 photoresist (AZ Electronic Materials, Branchburg, NJ, USA) and exposed to UV light through a chrome-plated glass mask for 45 s with an intensity of 12 W/m. To remove the exposed photoresist, a potassium-based buffered developer AZ 400K (AZ Electronic Materials) was used. The silicon master stamp was etched to 50 μm using Deep Reactive Ion Etching (Alcatel Micro Machining Systems, Annecy, France). Silicon oxide was grown on the master stamp using thermal oxidation for 4 h at 1000°C and removed with buffered oxide etch (BOE) solvent. This was repeated twice to adequately reduce surface scalloping and reduce adhesion of the polymer replicas.

Replicas of the master stamp were molded using polydimethylsiloxane (PDMS). Liquid-phase PDMS was made using a 10:1 ratio of the PDMS monomers and curing agent (Sylgrad 184, Dow Corning, USA) respectively. Once degassed, the liquid PDMS was poured onto the silicon wafer and cured for 45 min at 100°C. Upon cooling, the PDMS mold was peeled from the master stamp, fluidic connections were punched using 1.5 mm hole punchers (Harris Uni-Core, Ted Pella, Redding, CA, USA) and excess PDMS was cut off. The PDMS mold was then bonded to cleaned 3×3 cm microscope glass slides after treating with air plasma for 2 min.

3.2 Cell preparation

For these experiments, established human cell lines that represent the broad spectrum of breast cancer disease were used. As a model for non-transformed cells, MCF10A (ATCC, Manassas, VA, USA) cells were chosen. MCF10A is a spontaneously immortalized breast epithelial cell line that expresses breast-specific antigens and normal breast epithelial markers, such as cytokeratin and milk fat globule antigen, but shows only the modest gene alterations found in cultured cells. MCF10A do not form tumors in mice, thus serve as the non-transformed control. Intermediate stages were represented by the MCF7 (ATCC, Manassas, VA, USA) cells that express the estrogen receptor. Aggressive, metastatic disease was represented by MDA-MB-231 (ATCC) human breast cancer cells.

Cells were cultured in DMEM/F12 media (Invitrogen, Grand Island, NY, USA). For MDA-MB-231 and MCF7 cells, the medium was supplemented with 10% fetal bovine serum (Invitrogen, Grand Island, NY, USA) and 1% of a penicillin/streptomycin (Invitrogen) solution. In addition, the MCF7 medium was suppplemented with 0.5 nM estradiol (Sigma-Aldrich, Saint Louis, MO, USA) and 2 mL of 2.5 mg/mL insulin (Sigma-Aldrich). MCF10A medium contained 5% horse serum (Invitrogen), 1% penicillin/streptomycin solution, and 2 mL of 2.5 mg/mL insulin, 0.215 mL of 50 μg/mL epidermal growth factor (Sigma-Aldrich), 0.1 mL of 2.5 mg/mL hydrocortisone (Sigma-Aldrich), and 100 ng/mL cholera toxin (Sigma-Aldrich). All cells were cultured at 37°C in 5% CO_2 in a humidified atmosphere.

All cells were harvested by trypsinization at 80% confluence. Each cell type was resuspended in DEP buffer [30], washed twice, and resuspended again in fresh DEP buffer to achieve a solution conductivity of 100 μS/cm and a cell concentration of 10^6 cells/mL. They were then pipetted with a 300 μL pipetter to reduce cell clumping. Fifty cell radii for each cell type were measured from a calibrated image of the cells under a microscope slide. Initially, each cell type was tested individually to measure their frequency and voltage responses, then a new sample of cells for each type were stained with either calcein AM or CellTrace™ calcein red/orange (Invitrogen, Eugene, OR, USA) and mixed together to evaluate the extent of cDEP separation.

3.3 Experimental set-up

The devices were placed into a vacuum jar for at least 30 min prior to experiments. To reduce fouling in the pillar region of the device, the main channel was primed with a filtered DEP solution containing 5% BSA for 1 h. The channel was then washed with DEP buffer using pressure-driven flow. Side channels were filled with PBS and aluminium electrodes were placed in each side channel inlet (Fig. 1). Teflon tubing was inserted into the inlet and outlet of the main channel. The inlet tubing was connected to a 1 mL syringe containing the cell suspension. The syringe was fastened to a syringe pump set to 0.02 mL/h. A calibrated, inverted light microscope (Leica DMI 6000B, Leica Microsystems, Bannockburn, IL, USA) was used to monitor the cells. Once the flow rate was maintained for 5 min, an AC electric potential was applied to the electrodes.

Experiments to determine initial DEP response and at least 90% trapping were conducted at $20V_{rms}$, $25V_{rms}$, $30V_{rms}$, $35V_{rms}$, $40V_{rms}$, and $50V_{rms}$ for each cell line. These voltages were chosen due to the absence of an observed DEP force on the cells below $20V_{rms}$, while above $50V_{rms}$, no trapping distinction could be observed. For each experiment, the frequency was adjusted by intervals of 2 kHz until

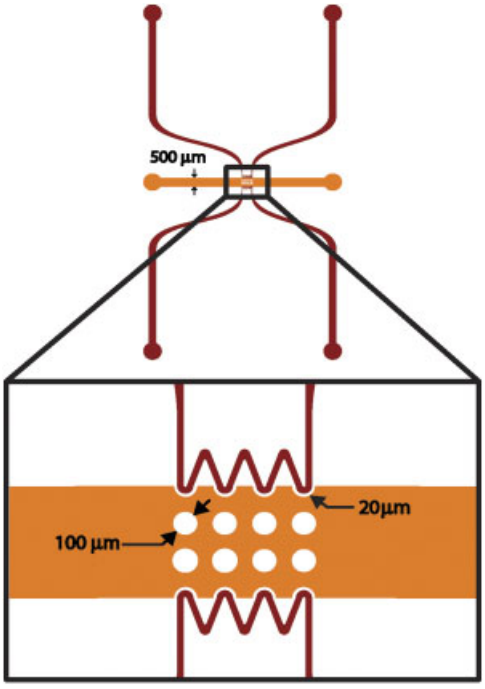

Figure 1. Schematic of experimental device. The side channels are filled with high-conductive PBS.

an initial DEP response was observed. Similarly, 90% trapping was measured by initial observation. After each initial observation at 90%, ±5 kHz were also tested. Thirty second video footage was captured for each trial and replayed in slow motion while the amount of cells flowing in and out of the trapping region were counted. Eight trials were conducted at each voltage in a random order.

3.4 Numerical modeling

The real part of the Clausius–Mossotti factor, $K(\omega)$, was theoretically calculated and graphed for each cell line using a MATLAB script (R2010a, The MathWorks, Natick, MA). The Clausius–Mossotti factor was found for frequencies between 100 Hz and 100 MHz using a logarithmic sampling rate in MATLAB with the parameters in Table 1.

The gradient of the inner product of the electric field was modeled using COMSOL Multiphysics (3.5a, COMSOL, Burlington, MA, USA). The electrical potential, ϕ, was found using the governing equation, $\nabla \cdot (\sigma^* \nabla \phi) = 0$, where σ^* is the complex conductivity $\sigma^* = \sigma + j\omega\varepsilon$ of the sub-domains in the microfluidic devices. The sub-domains were grouped into three areas: fluid electrode, sample channel, and PDMS, where the conductivities of these materials are 1.4 S/m, 1.0×10^{-2} S/m, and 8.3×10^{-13} S/m, respectively. The permittivity used for the fluid electrode and the sample channel was $80\varepsilon_0$ while the permittivity of the PDMS was $2.65\varepsilon_0$. The boundary conditions used were prescribed uniform potentials at the inlets of one fluid electrode and ground at the inlets of the other fluid electrode.

4 Results

Experimentally, the onset of cell trapping from MDA-MB-231 cells occurred at voltages as low as $20V_{rms}$ when a minimum frequency of 174.67 kHz was applied. As the applied voltage increased, the frequency necessary to induce cell trapping decreased, reaching a minimum of 125.78 kHz when $50V_{rms}$ was applied. Similarly, 90% of MDA-MB-231 cells could be trapped at $20V_{rms}$ when a minimum frequency of 267.93 kHz was applied. This decreased to a frequency of 176.02 kHz when $50V_{rms}$ was applied.

At $20V_{rms}$, the onset of cell trapping did not occur for MCF7 cells until a 209.97 kHz signal was applied. Complete trapping of these cells at this voltage was not seen until at least 302.76 kHz was applied. Similar to the MDA-MB-231 cells, the frequency necessary for the onset and 90% trapping thresholds could be reduced by increasing the applied voltage. At $50V_{rms}$, these frequencies had dropped to a minimum of 131.48 and 198.67 kHz respectively.

At all voltage levels, MCF10A required the highest average applied frequency to induce trapping and achieve 90% or greater trapping (Fig. 2). At $20V_{rms}$ this corresponded to minimum of 224.67 and 311.00 kHz, respectively. At $50V_{rms}$ a minimum of 130.39 kHz was needed to induce trapping and 208.81 kHz was required to trap at least 90% of the MCF10A cells.

The largest zone in which only MDA-MB-231 cells were influenced by DEP forces occurred at 20 and $30V_{rms}$. In this region, it was possible to isolate MDA-MB-231 cells from a heterogeneous mixture of MCF7 and MCF10A cells as shown in Fig. 2. At $20V_{rms}$ this region was approximately between 180 and 210 kHz. For $30V_{rms}$, the bandwidth was slightly smaller falling approximately between 155 and 175 kHz. Experimentally, voltages greater than $50V_{rms}$ occasionally induced cell lysing. Voltages about $65V_{rms}$ typically caused the formation of defects within the insulating barriers, which negatively altered the device performance.

Table 1. Literature values of cell dielectric properties. Cell radii and media conductivity were experimentally measured

Cell type	Average radius (µm)	Membrane capacitance (F/m^2)	Cytoplasm conductivity (S/m)	Cytoplasm permittivity (F/m)	Media conductivity (S/m)	Media permittivity (F/m)
MCF10A	9.25	0.0194 [40]	1 [41]	$50\varepsilon_0$ [41]	1.00E−02	$80\varepsilon_0$
MCF7	9.1	0.0186 [40]	1 [41]	$50\varepsilon_0$ [41]	1.00E−02	$80\varepsilon_0$
MDA-MB-231	8.93	0.0163 [40]	1 [41]	$50\varepsilon_0$ [41]	1.00E−02	$80\varepsilon_0$

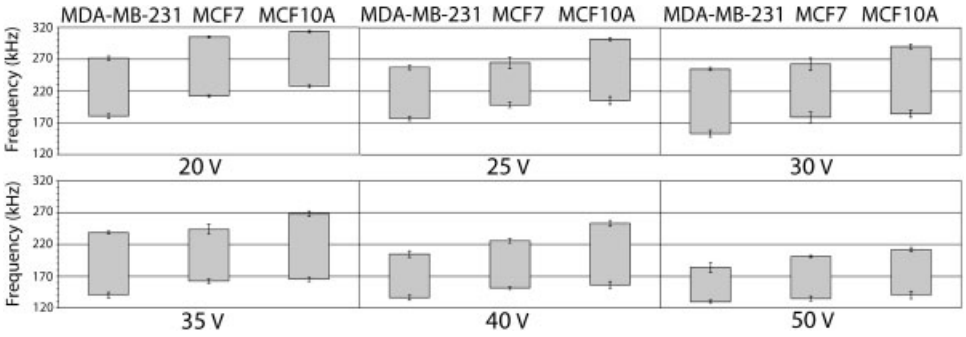

Figure 2. Frequencies between which, the onset of trapping and 90% trapping was observed for MDA-MB-231, MCF7, and MCF10A cells. At 20–30 V_{rms} MDA-MB-231 cells could be trapped while the other cell types passed through the device unaffected. The onset of trapping and 90% trapping of MCF7, MCF10A, and MDA-MB-231 cells occurred over different overlapping frequency bands.

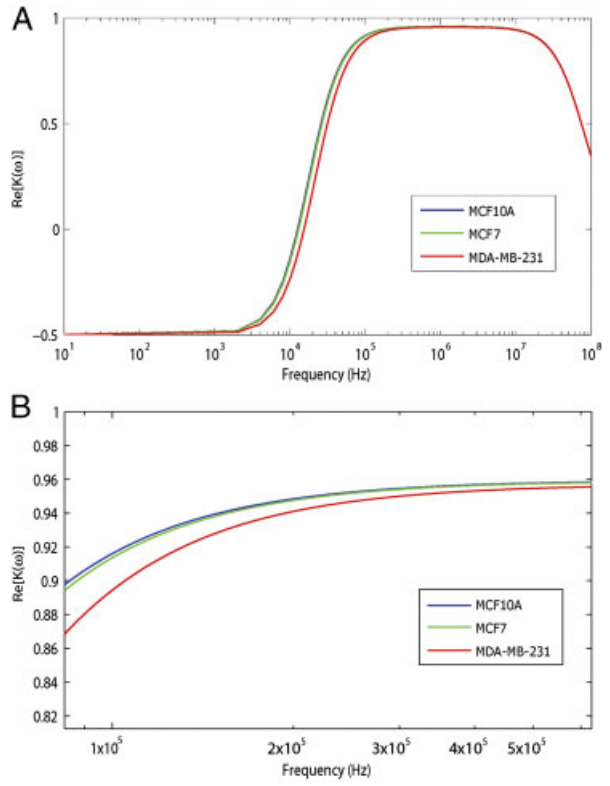

Figure 3. (A) The real part of the Clausius–Mossotti factor for MCF10A, MCF7, and MDA-MB-231 cells using estimated parameters in Table 1. (B) Zoomed in image of the curve at experimental frequencies.

The Clausius–Mossotti factor for MCF7, MCF10A, and MDA-MB-231 cells were distinct with each cell type having its own unique crossover frequency between 12.5 and 15.5 kHz. For these cells, the Clausius–Mossotti factor was within 98% of the global maxima by 200 kHz. Between 100 and 500 kHz, a unique curve of the Clausius–Mossotti factor for each cell type can be distinguished as shown in Fig. 3A and B.

Between the ranges of 100 kHz and 1 MHz, the cells experience the maximum DEP force necessary to be manipulated. In our device models, a frequency of 100 kHz was applied to demonstrate specific areas of local maxima and local minima of the DEP force (Fig. 4A). Within the sample channel, local maxima in the gradient of the inner product of the electric field were found to be in the regions closest to the left and right of the insulating pillars. The gradient of the inner product of the electric field is the greatest near the quadrants of the four inner pillars closest to $x = 0$. Local minima were found to exist at the middle of the center-to-center spacing of the pillars from left to right and top to bottom (Fig. 4A).

The DEP force acting on cells passing through the center of the device was found to have the same pattern for all of the cell types. The magnitude of the DEP force was the greatest for MCF7 cells and the lowest for MDA-MB-231 cells with MCF10 cells between the two (Fig. 4B). To validate the individual results of Fig. 2, experiments with a heterogeneous sample containing an equal number of each cell type were conducted at 30 V and at frequencies <180 kHz (frequency at which initial trapping of the MCF7 and MCF10A cells began). It was found the target cell line, MDA-MB-231, could be trapped with no trapping of the other two cell lines at 164 kHz (Fig. 4C).

5 Discussion

Current cell-sorting techniques generally suffer from a lack of sensitivity, non-specificity, and throughput. Each of these techniques relies on prior knowledge of specific cell properties for separation and has intrinsic advantages and disadvantages. Typically, more sensitive techniques may require prior knowledge of cell-specific markers and antibodies to prepare target cells for analysis. Additionally, the large amount of sample handling required by these techniques greatly increases the likeliness of cell loss and contamination, therefore increasing the error involved in the application of these techniques [5].

DEP has been shown to be a promising technique to overcome these challenges. The dielectric properties of a cell are determined by the distribution of surface charges, cell size, and morphology, as well as conductivity and permittivity of their membranes, cell walls, and internal structure. Cells are made of complex structures adjacent to one another with their own unique electrical properties. For example, the cell membrane consists of a lipid bilayer, which is a very thin insulator that contains proteins. This

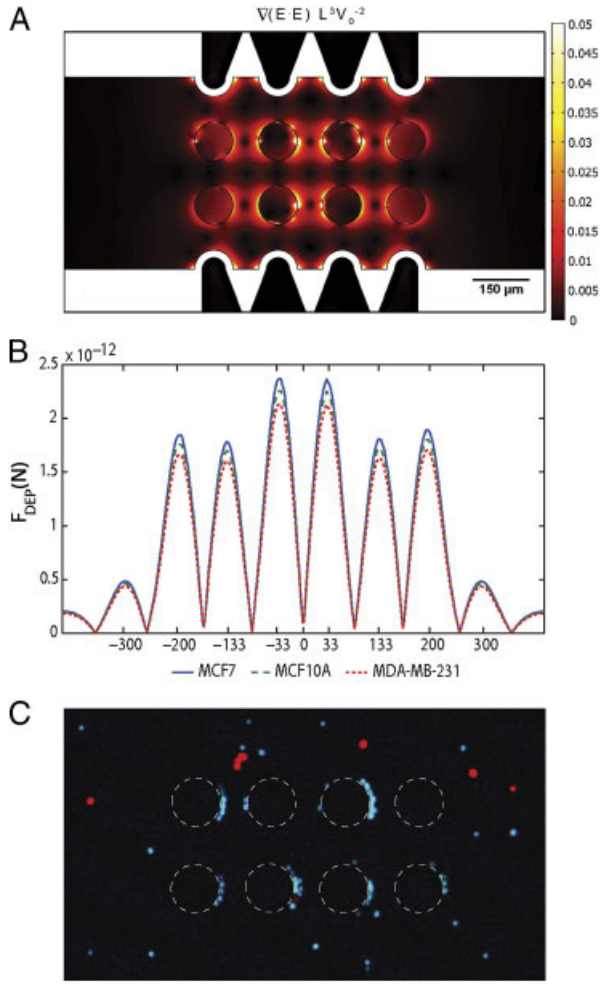

Figure 4. (A) Non-dimensionalized computational model of the gradient of the inner product of the electric field used to predict trapping regions within the cDEP device where L and V correspond to the width of the sample channel (500 μm) and the applied AC voltage (100 V_{rms}). Regions in yellow generate the highest DEP force and are the regions in which targeted cells are held. (B) DEP force on MCF7, MCF10A and MDA-MB-231 cells versus location from the center of the microfluidic channel. The DEP force within the sample channel at 100 kHz was numerically calculated to be the greatest for MCF7 cells. All cell types would experience a similar pattern of DEP forces as they traverse the device. (C) MDA-MB-231 cells (green/blue) trapping along the circumference of the insulating posts that are outlined with white dotted lines with no MCF7 or MCF10A (both red) trapping. Cells are moving from right to left under pressure-driven flow at 30 V and 164 kHz.

layer has a conductivity around 10^{-7} S/m whereas the conductivity of the inside of the cell can be as high as 1 S/m. The Clausius–Mossotti factor is a powerful parameter that relates cells' effective permittivities and conductivities to ultimately decide the magnitude and direction of DEP force. Unfortunately, the current DEP techniques suffer from their own disadvantages such as complex fabrication, cell contamination, and joule heating. For biological applications, it is crucial to overcome these hurdles. cDEP has proven to be a viable enhancement of current DEP technology through investigations of particle separation [36] as well as live/dead separation [30]. This study demonstrates the sensitivity of this current cDEP device to detect minute differences within the cell through their DEP responses.

Numerical modeling of MCF7, MCF10A, and MDA-MB-231 cells showed that the cells had unique Clausius–Mossotti curves. These curves were substantially different at frequencies near the crossover frequencies of the cells. In this region, it is likely that one cell type will experience negative DEP forces, movement away from regions containing a high gradient of the inner product of the electric field, while the others experience a positive DEP force. It should be noted however, that in this region, the magnitude of the Clausius–Mossotti factor is small in comparison to the global maximum and the resulting force experienced by the cells will be significantly lower.

Thorough examination of the cells' behavior at frequencies between 120 and 320 kHz and voltages between 20 and 50 V_{rms} showed that MDA-MB-231 cells can be isolated from a heterogeneous mixture of cells. At frequencies between 155 and 175 kHz and voltages between 20 and 30 V_{rms}, a portion of the MDA-MB-213 cells were successfully trapped while MCF7 and MCF10A cells passed by unaffected. This is the first demonstration of cDEP to isolate a specific cell type from a heterogeneous population of live cells.

Future work will focus on improving the sensitivity and removal efficiency of cDEP devices. One particular extension of this will be to investigate breast cancer cells from the same lineage, as a more clinically relevant sample mixture. Not only could this provide a basis for detection, but also the ability to isolate the most aggressive cells from a heterogeneous sample will have a profound impact on cancer therapies. The isolation of these cells could offer a workbench for clinicians to screen drug therapies prior to patient treatment, which will increase the probability of success and eliminate unsuccessful treatment options. This would enable oncologists to tailor a treatment on a patient-specific level and to ensure the most effective treatment is being utilized [37–39].

This work has been funded in part by the Institute for Critical and Applied Sciences (ICTAS) at Virginia Tech, Blacksburg, VA.

Conflict of interest: Sano and Davalos have a pending patent in Contactless Dielectrophoresis.

6 References

[1] Giddings, J., *Science* 1993, *260*, 1456–1465.

[2] Fu, A. Y., Spence, C., Scherer, A., Arnold, F. H., Quake, S. R., *Nat. Biotech.* 1999, *17*, 1109–1111.

[3] Miltenyi, S., Muller, W., Weichel, W., Radbruch, A., *Cytometry* 1990, *11*, 231–238.

[4] Ashkin, A., Dziedzic, J. M., Yamane, T., *Nature* 1987, *330*, 769–771.

[5] Adams, A. A., Okagbare, P. I., Feng, J., Hupert, M. L., Patterson, D., Gottert, J., McCarley, R. L., Nikitopoulos, D., Murphy, M. C., Soper, S. A., *J. Am. Chem. Soc.* 2008, *130*, 8633–8641.

[6] Pohl, H. A., *J. Appl. Phys.* 1951, *22*, 869–871.

[7] Pohl, H. A., *J. Appl. Phys.* 1958, *29*, 1182–1188.

[8] Cheng, J., Sheldon, E. L., Wu, L., Uribe, A., Gerrue, L. O., Carrino, J., Heller, M. J., O'Connell, J. P., *Nat. Biotech.* 1998, *16*, 541–546.

[9] Gascoyne, P. R. C., Xiao-Bo, W., Ying, H., Becker, F. F., *IEEE Trans. Indl. Appl.* 1997, *33*, 670–678.

[10] Huang, Y., Joo, S., Duhon, M., Heller, M., Wallace, B., Xu, X., *Anal. Chem.* 2002, *74*, 3362–3371.

[11] Stephens, M., Talary, M. S., Pethig, R., Burnett, A. K., Mills, K. I., *Bone Marrow Transplant.* 1996, *18*, 777–782.

[12] Altomare, L., Borgatti, M., Medoro, G., Manaresi, N., Tartagni, M., Guerrieri, R., Gambari, R., *Biotechnol. Bioeng.* 2003, *82*, 474–479.

[13] Huang, Y., Wang, X. B., Becker, F. F., Gascoyne, P. R., *Biophys. J.* 1997, *73*, 1118–1129.

[14] Kim, U., Shu, C.-W., Dane, K. Y., Daugherty, P. S., Wang, J. Y. J., Soh, H. T., *Proc. Natl. Acad. Sci. USA* 2007, *104*, 20708–20712.

[15] Toner, M., Irimia, D., *Annu. Rev. Biomed. Eng.* 2005, *7*, 77–103.

[16] Griffith, A. W., Cooper, J. M., *Anal. Chem.* 1998, *70*, 2607–2612.

[17] Cummings, E. B., Singh, A. K., *Anal. Chem.* 2003, *75*, 4724–4731.

[18] Davalos, R. V., McGraw, G. J., Wallow, T. I., Morales, A. M., Krafcik, K. L., Fintschenko, Y., Cummings, E. B., Simmons, B. A., *Anal. Bioanal. Chem.* 2008, *390*, 847–855.

[19] Baylon-Cardiel, J. L., Jesus-Perez, N. M., Chavez-Santoscoy, A. V., Lapizco-Encinas, B. H., *Lab Chip* 2010, *10*, 3235–3242.

[20] Jen, C.-P., Huang, C.-T., Shih, H.-Y., *Microsystem Technol.* 2010, *16*, 1097–1104.

[21] Ozuna-Chacón, S., Lapizco-Encinas, B. H., Rito-Palomares, M., Martínez-Chapa, S. O., Reyes-Betanzo, C., *Electrophoresis* 2008, *29*, 3115–3122.

[22] Du, F., Baune, M., Thöming, J., *J. Electrostat.* 2007, *65*, 452–458.

[23] Lapizco-Encinas, B. H., Simmons, B. A., Cummings, E. B., Fintschenko, Y., *Electrophoresis* 2004, *25*, 1695–1704.

[24] Lapizco-Encinas, B. H., Simmons, B. A., Cummings, E. B., Fintschenko, Y., *Anal. Chem.* 2004, *76*, 1571–1579.

[25] Lapizco-Encinas, B. H., Davalos, R. V., Simmons, B. A., Cummings, E. B., Fintschenko, Y., *J. Microbiol. Methods* 2005, *62*, 317–326.

[26] Lapizco-Encinas, B. H., Ozuna-Chacón, S., Rito-Palomares, M., *J. Chromatogr. A* 2008, *1206*, 45–51.

[27] Jen, C.-P., Chen, T.-W., *Biomed. Microdev.* 2009, *11*, 597–607.

[28] Masuda, S., Itagaki, T., Kosakada, M., *IEEE Trans. Indl. Appl.* 1988, *24*, 740–744.

[29] Shafiee, H., Caldwell, J. L., Sano, M. B., Davalos, R. V., *Biomed. Microdev.* 2009, *11*, 997–1006.

[30] Shafiee, H., Sano, M. B., Henslee, E. A., Caldwell, J. L., Davalos, R. V., *Lab Chip* 2010, *10*, 438–445.

[31] Jones, T. B., *Electromechanics of Particles*, Cambridge University Press,USA 1995.

[32] Arnold, W. M., Zimmermann, U., *Z Naturforsch C* 1982, *37*, 908–915.

[33] Wang, X. B., Huang, Y., Becker, F. F., Gascoyne, P. R. C., *J. Phys. D Appl. Phys.* 1994, *27*, 1571–1574.

[34] Arnold, W. M., Zimmermann, U., *J. Electrostat.* 1988, *21*, 151–191.

[35] Becker, F. F., Wang, X. B., Huang, Y., Pethig, R., Vykoukal, J., Gascoyne, P. R. C., *J. Phys. D Appl. Phys.* 1994, *27*, 2659–2662.

[36] Shafiee, H., Caldwell, J. L., Davalos, R. V., *J. Assoc. Lab. Automat.* 2010, *15*, 224–232.

[37] Tatosian, D. A., Shuler, M. L., *Biotechnol. Bioeng.* 2009, *103*, 187–198.

[38] Ntouroupi, T. G., Ashraf, S. Q., McGregor, S. B., Turney, B. W., Seppo, A., Kim, Y., Wang, X., Kilpatrick, M. W., Tsipouras, P., Tafas, T., Bodmer, W. F., *Br. J. Cancer* 2008, *99*, 789–795.

[39] Del Bene, F., Germani, M., De Nicolao, G., Magni, P., Re, C. E., Ballinari, D., Rocchetti, M., *Cancer Chemother. Pharmacol.* 2009, *63*, 827–836.

[40] Han, A., Yang, L., Frazier, A. B., *Clin. Cancer Res.* 2007, *13*, 139–143.

[41] Sancho, M., Martinez, G., Munoz, S., Sebastian, J. L., Pethig, R., *Biomicrofluidics* 2010, *4*, 022802.

Dielectrophoretic differentiation of mouse ovarian surface epithelial cells, macrophages, and fibroblasts using contactless dielectrophoresis

Alireza Salmanzadeh,[1,2,3] Harsha Kittur,[1] Michael B. Sano,[1,3]
Paul C. Roberts,[4] Eva M. Schmelz,[3,5] and Rafael V. Davalos[1,2,3,a)]
[1]*School of Biomedical Engineering and Sciences, Virginia Tech-Wake Forest University, Blacksburg, Virginia 24061, USA*
[2]*Department of Engineering Science and Mechanics, Virginia Tech, Blacksburg, Virginia 24061, USA*
[3]*Center for Multi-scale Bio-Engineered Devices and Systems (M-BEDS), Institute for Critical Technology and Applied Science (ICTAS), Virginia Tech, Blacksburg, Virginia 24061, USA*
[4]*Department of Biomedical Sciences and Pathobiology, Virginia Tech, Blacksburg, Virginia 24061, USA*
[5]*Human Nutrition, Foods, and Exercise, Virginia Tech, Blacksburg, Virginia 24061, USA*

(Received 17 January 2012; accepted 13 March 2012; published online 3 April 2012)

Ovarian cancer is the leading cause of death from gynecological malignancies in women. The primary challenge is the detection of the cancer at an early stage, since this drastically increases the survival rate. In this study we investigated the dielectrophoretic responses of progressive stages of mouse ovarian surface epithelial (MOSE) cells, as well as mouse fibroblast and macrophage cell lines, utilizing contactless dielectrophoresis (cDEP). cDEP is a relatively new cell manipulation technique that has addressed some of the challenges of conventional dielectrophoretic methods. To evaluate our microfluidic device performance, we computationally studied the effects of altering various geometrical parameters, such as the size and arrangement of insulating structures, on dielectrophoretic and drag forces. We found that the trapping voltage of MOSE cells increases as the cells progress from a non-tumorigenic, benign cell to a tumorigenic, malignant phenotype. Additionally, all MOSE cells display unique behavior compared to fibroblasts and macrophages, representing normal and inflammatory cells found in the peritoneal fluid. Based on these findings, we predict that cDEP can be utilized for isolation of ovarian cancer cells from peritoneal fluid as an early cancer detection tool. © *2012 American Institute of Physics*. [http://dx.doi.org/10.1063/1.3699973]

I. INTRODUCTION

Epithelial ovarian cancer is the leading cause of death from gynecological malignancies and the fourth leading cause of death in women in the United States among all cancers.[1,2] The World Health Organization estimates that approximately 225,500 women worldwide are diagnosed with ovarian cancer[3] and 140,200 women die from it annually. In the U.S., it was estimated that 21,990 new cases of ovarian cancer would be diagnosed in 2011 and 15,460 women would die from this disease.[4] Much of this lethality is attributable to its late detection due to the lack of symptoms of earlier stages, and routine screening methods are not established. However, early detection improves the survival rates of women to more than 90%,[5] highlighting the importance of early detection and treatment of ovarian cancer. Ideally, screening tests should

a)Author to whom correspondence should be addressed. Electronic mail: davalos@vt.edu.

be non-invasive and highly specific to reduce false-positive results, the associated risks, and costs for the affected women.[2]

Ovarian cancer cells exfoliate from the primary tumor and disseminate throughout the peritoneal cavity. The changing peritoneal microenvironment, characterized by increasing numbers of immune cells, mostly monocytes/macrophages,[6] and increased protein and bioactive lipid levels in the ascites fluid[7,8] promotes tumor cell survival, proliferation, and metastasis. Ascites fluid can also contain benign cell populations of macrophages and fibroblasts.[6,9] The percentage of tumor cells versus non-tumor cells can vary greatly in women from 1 to >60%.[10] Because of the different physical characteristics of these cells, we theorize that resident and recruited peritoneal cells can be separated from ovarian cancer cells. Unlike cancers of other sites, ovarian cancer cells rarely enter systemic distribution. Thus, the peritoneal fluid is the appropriate source for detection of disseminating ovarian cancer cells.

Traditionally, specific biomarkers expressed mainly by the target tumor cell population are used to isolate cells from each other. CA-125, the most popular biochemical marker for ovarian cancer, is found in 50% of early stage patients and 80% of late stage patients.[11] Other markers can vary greatly. Detection techniques include ultrasound and color-flow Doppler imaging, using morphological and vascular markers, respectively.[11] Recently, proteomics has become a promising means by which new potential biomarkers are identified. Several of these biomarkers have to be used in combination to improve sensitivity, but at the cost of reduced specificity.[11,12]

Roberts *et al*. have established a mouse cell model for progressive ovarian cancer from C57BL/6 mice.[13] Isolated primary mouse ovarian surface epithelial (MOSE) cells undergo progressive changes during culturing.[13,14] Based on their phenotype (size, growth rate, morphology) and their tumorigenic potential, MOSE cells were categorized into early, early-intermediate, intermediate, and late aggressive stages. During neoplastic progression, increased dysregulation of the cytoskeleton organization was observed, which[14] was recently found to be associated with stage specific changes in their biomechanical properties.[15] The MOSE model exemplifies an alternative to human cell lines since comparable human cell lines providing different stages of ovarian cancer derived from the same woman are not available.

It has been reported that malignant cells are distinguishable from normal and healthy cells based on differences in their electrical properties.[16–22] For example, breast tumors have different electrical impedance compared to their surrounding tissues,[21] and transformed cells have higher effective cell membrane capacitance than normal cells.[17–20,22] Leukemia and breast cancer cells lines have higher effective membrane capacitance than normal T lymphocytes and erythrocytes.[17,18] Also, transformed rat kidney cells,[20] murine erythroleukemia cells,[19] and oral cancer cells[22] have higher effective membrane capacitance than non-transformed counterparts. However, it is not known if this also applies to a progressive cancer cell model derived from syngeneic non-transformed cells. Studying the electrical properties of these cells, thereby eliminating potential inter-individual differences that are inherent to human cell lines, may lead to novel cancer detection techniques. The first step towards this goal is investigating the dielectrophoretic response of cancer cells derived from a non-transformed, spontaneously immortalized mouse ovarian epithelium to determine the changes in their electrical properties during progression.

Dielectrophoresis (DEP), a non-destructive electrokinetic transport mechanism, is a technique employed to manipulate cells in microdevices. DEP has been a very successful technique for the manipulation,[23] separation,[24] and detection[25] of bioparticles. In contrast to techniques such as fluorescence activated cell sorting (FACS),[26] chemically functionalized pillar-based microchips,[27] and magnetic bead cell separation,[28] DEP does not require the use of target specific antibodies. Traditionally, DEP utilizes arrays of electrodes to produce non-uniform electric fields to polarize particles and thereby induce movement. However, there are some challenges with bubble formation due to electrolysis, electrode fouling and delamination, and sample contamination.[29,30] In addition, the electric field deteriorates exponentially as distance from the electrode surface increases.[31]

Modified DEP techniques, such as insulator-based dielectrophoresis (iDEP), have been developed to overcome challenges of conventional DEP. In iDEP, insulating structures are straddled between two electrodes to cause regions of high and low electric field intensity,

resulting in non-uniformity of the electric field.[29] Such systems were proposed by Cummings and Singh[29] and have been applied successfully for manipulation of DNA,[30] separation of live and dead cells,[32,33] and separation of different species of cells.[34]

Contactless dielectrophoresis (cDEP) is a new technique for manipulating cells which eliminates direct contact between the sample and electrodes. In cDEP, an electric field is generated in the sample channel by using two fluid electrode channels which are filled with a conductive fluid. These electrode channels are separated from the main channel by thin insulating barriers. The absence of metal electrodes minimizes sample contamination[35] and bubble formation, and resolves issues associated with joule heating.[36,37] We have shown previously that the viability of prostate cancer cells did not change through characterization or isolation by cDEP.[38] cDEP has been used to isolate tumor initiating cells (TICs) from non-initiating cells[38] and to separate living cancer cells from dead cells[37] and from red blood cells.[39] It has also been shown recently with cDEP that breast cancer cells from different cell lines exhibit unique dielectrophoretic responses and highly metastatic cell lines can be isolated from less metastatic lines.[40]

In this work, we examined the changes in dielectrophoretic response of MOSE cells as they progress from benign to aggressive stages of ovarian cancer. Previously, MOSE cells were characterized as stiffer and more viscous when they are benign,[15] confirming reports in other cells.[41–44] This suggests that changes in gene expression during progression of ovarian cancer correspond to an altered morphology, decreased cell size, and altered cellular architecture,[14] which together not only affect the biological behavior of the cells, but also modulates their biomechanical and, perhaps, their bioelectrical properties.

To our knowledge, there is no information about changes in the electrical properties of ovarian cancer cells as the disease progresses. In this study we demonstrate for the first time that different stages of cancer, progressed from the same progenitor cells, have different dielectrophoretic responses. We also compare the signal parameters (voltage and frequency) required to selectively capture and isolate MOSE cells at different cancer stages from normal fibroblast and macrophages that can be found in the peritoneal fluid. These results demonstrate the potential of cDEP as a method of early detection and diagnosis of ovarian cancer.

II. THEORY

The DEP force acting on a spherical particle in a non-uniform electric field is given by[45]

$$\vec{F}_{DEP} = 2\pi\varepsilon_m r^3 Re\left\{\frac{\varepsilon_p^* - \varepsilon_m^*}{\varepsilon_p^* + 2\varepsilon_m^*}\right\}\nabla(\vec{E}_{RMS}\cdot\vec{E}_{RMS}), \tag{1}$$

$$\varepsilon^* = \varepsilon + \frac{\sigma}{j\omega}, \tag{2}$$

where ε_p^* and ε_m^* are the complex permittivity of the particle and suspending medium, respectively, r is the radius of the particle, σ is the real conductivity, and $\vec{E}_{RMS}$ is the root mean square electric field. $j^2 = -1$, and ω is the radial frequency of the applied voltage.

The Clausius-Mossotti factor, $K(\omega) = (\varepsilon_p^* - \varepsilon_m^*)/(\varepsilon_p^* + 2\varepsilon_m^*)$, is a complex function with a real value between -0.5 and 1, and is dependent on the bioelectric properties of the cell. Depending on the sign of $K(\omega)$, the DEP force can either be positive, in which case it is directed towards high electric field gradient regions, or negative, in which case it is directed towards low electric field gradient regions.

Frequencies at which the DEP force is zero are called the crossover frequency, f_{xo}. These are the frequencies at which the real part of K changes sign, $Re\{K(\varepsilon_p^*, \varepsilon_m^*)\} = 0$. The first crossover frequency of mammalian cells happens between 10–100 kHz, and the second crossover frequency is typically on the order of 10 MHz for a sample with conductivity of 100 μS/cm.[46] Cell size, shape, cytoskeleton, and membrane morphology affect the first crossover frequency; and cytoplasm conductivity, nucleus-cytoplasm volume ratio, and endoplasmic reticulum affect the second crossover frequency.[47]

The material properties of cells and biological tissues change with the applied frequency. This disparity in properties is known as dispersion. At frequencies less than 10 kHz, counterion polarization happens along the cell membrane (α dispersion). In the MHz frequency range, interfacial polarization of the cell membrane occurs, which can develop because of the polarization of proteins and other macromolecules (β dispersion).[48] The applied frequencies in our experiments are in the range of 200–600 kHz, which is in between α and β dispersion regimes. Thus, both the counterion polarization along cell membrane (α dispersion) and interfacial polarization of cell membrane (β dispersion) should both be considered as potential reasons for observing differing DEP signature between cells.

As particles move under the influence of the DEP force, they interact with the surrounding fluid and experience hydrodynamic drag

$$\vec{F}_{Drag} = 6\eta r\pi(\vec{u}_p - \vec{u}_f), \tag{3}$$

where r is the particle radius and $\vec{u}_p$ and $\vec{u}_f$ are the velocities of the particle and the medium, respectively.

III. MATERIALS AND METHODS

A. Device layout

Figure 1 shows the top view schematic of the microdevice. Electrode channels, which are approximately 1 cm long, are separated from the sample channel by 20 μm barriers. Insulating pillars, 100 μm in diameter, in the sample channel increase the non-uniformity of the electric field and enhance the DEP force.

B. Fabrication process

Experimental devices were fabricated using standard soft lithography techniques. Photoresist, AZ 9260 (AZ Electronic Materials, Somerville, NJ, USA), was spun onto a clean silicon

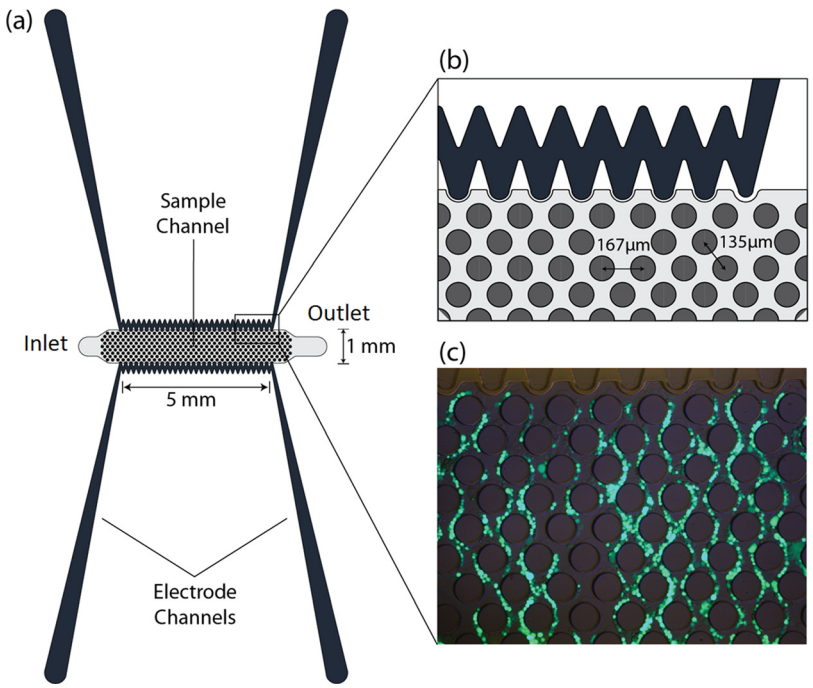

FIG. 1. (a) 2D top view schematic of the microdevices. (b) A section of the microdevice and pillars. Each pillar is 100 μm in diameter. (c) Complete trapping of cells. Calcein AM, enzymatically converted to green fluorescent calcein, is added to the cell sample at 2 μL per mL of cell suspension.

substrate. Then, the silicon wafer was exposed to UV light for 60 s through a mask patterned with the design. Using AZ 400 K (AZ Electronic Materials, Somerville, NJ, USA) developer, the exposed photoresist was removed. The silicon master stamp was etched to a depth of 50 microns with deep reactive ion etching (DRIE). Wet etching with tetramethylammonium hydroxide (TMAH) 25% at 70 °C was used for 5 minutes to smooth the surface of the wafer. Then, a thin layer of Teflon was deposited on the silicon master to ease the replication process using typical DRIE parameters.

The liquid PDMS was made by mixing PDMS monomers and a curing agent in a 10:1 ratio (Sylgard 184, Dow Corning, Midland, MI, USA). Bubbles were removed from liquid PDMS by exposing the mixture to vacuum for 1 h. PDMS liquid was poured onto the silicon master, cured for 45 minutes at 100 °C, and then peeled off from the silicon mold. Fluidic connections to the channels were punched with a 1.5 mm puncher (Harris Uni-Core, Redding, CA, USA). After treating with air plasma for 2 minutes, the PDMS replica was bonded to clean glass slides using air plasma (Harrick Plasma, Ithaca, NY, USA).

C. Experimental set-up

Prior to experimentation, the microfluidic devices were placed in a vacuum jar for 20 minutes to reduce issues with bubble formation within the channels. The fluid electrode channels were filled with phosphate buffered saline (PBS). Externally, pipette tips formed fluid reserviors at the inlet and outlet of each fluid electrode channel. Metal electrodes were inserted into these reserviors as a means of electrical connection. The main channel was then primed with the sample and a microsyringe pump (Harvard Apparatus Syringe Pumps, Plymouth Meeting, PA, USA) was used to achieve a flow rate of 0.02 mL/h. Once the required flow rate was maintained for 2 minutes, an AC voltage was applied to the electrodes.

A combination of waveform generation and amplification equipment was used to create AC electric fields in the microfluidic devices. Waveforms were produced with a function generator (GFG-3015, GW Instek, Taipei, Taiwan), and the output was fed to a wideband power amplifier (AL-50HF-A, Amp-Line Corp., Oakland Gardens, NY, USA). A high-voltage transformer was used to step-up the voltage of the signal before it was applied across the fluid electrodes via external electrodes. An inverted light microscope (Leica DMI 6000B, Leica Microsystems, Bannockburn, IL, USA) equipped with a color camera (Leica DFC420) was used to monitor the particles flowing through the main channel.

The dielectrophoretic responses of early (MOSE-E), early-intermediate (MOSE-E/I), intermediate (MOSE-I), and late stage ovarian cells (MOSE-L), as well as macrophages (PC1) and fibroblasts (OP9), were studied separately using the device shown in Fig. 1. The frequency of the AC signal was set as indicated in each experiment for five selected frequencies: 200, 300, 400, 500, and 600 kHz. These frequencies were selected at random, and the associated voltages required to observe trapping of the first two cells (onset of trapping) and trapping of all cells (complete trapping) were recorded (Figs. 1(b)–1(c)). Each experiment was repeated 10 times using cells from biological replicates. The student t-test method was used to determine if data from different cell lines were statistically different. The purpose of these experiments was to investigate if there is a difference in onset of and complete trapping between these cell types.

D. Cell preparation

Different stages of MOSE cells, early (passage number 15–16), early-intermediate (passage number 33–34), intermediate (passage number 70–71), and late (passage number 188–189), were cultured in Dulbecco's modified eagle's medium (DMEM)-high glucose medium supplemented with 4% fetal bovine serum (FBS, Atlanta Biological, Atlanta, GA) and 100 μg/ml each of penicillin and streptomycin, at 37°C in a humidified atmosphere as described previously.[13,14]

PC1 macrophages were grown in DMEM–low glucose (Sigma-Aldrich, St. Louis MO), containing 5 mL of penicillin and streptomycin (Invitrogen, Carlsbad, CA), and 10% FBS (Atlanta Biological). OP9 fibroblast were maintained in α-MEM (Invitrogen, Carlsbad CA),

containing 5 mL of penicillin and streptomycin (Invitrogen, Carlsbad CA), and 20% FBS (Atlanta Biological).

The MOSE cells, fibroblasts (OP9), and macrophages (PC1) were grown separately, harvested, washed twice, and resuspended in a low conductivity buffer for the experiments (8.5% sucrose [wt./vol.], 0.3% glucose [wt./vol.], and 0.725% [vol./vol.] RPMI)[49] to 1×10^6 cells per mL. The electrical conductivity of all samples was $105 \pm 3\ \mu$S/cm as measured with a conductivity meter (Horiba B-173 Twin Conductivity/Salinity Pocket Testers, Cole-Parmer) prior to each experiment.

E. Computational modeling

COMSOL Multiphysics 4.2 (Comsol Inc., Burlington, MA, USA) was used to investigate the effect of different geometrical parameters, such as pillar arrangements, the gap between the pillars, and pillar diameter on $\nabla(\vec{E}\cdot\vec{E})$ and fluid flow.

The electrical properties of PDMS were reported as $\sigma_{\mathrm{PDMS}} = 0.83 \times 10^{-12}$ S/m and $\varepsilon_{\mathrm{PDMS}} = 2.65$.[27] The electrical conductivities of PBS and DEP buffer were defined as $\sigma_{\mathrm{PBS}} = 1.4$ S/m and $\sigma_{\mathrm{DEP}} = 0.01$ S/m, respectively. Their relative permittivities were defined as $\varepsilon_{\mathrm{PBS}} = \varepsilon_{\mathrm{DEP}} = 80$, as assumed based on their water content. The properties of PBS and DEP buffer were prescribed for the electrode and sample channels, respectively. The boundary conditions were prescribed as uniform potentials at the inlet and outlet of the electrode channels and insulating on the outside surrounding boundaries.

The fluid dynamics within the sample channel were also modeled to find the velocity field and the shear rate. No slip boundary conditions were applied to the walls of the channel and the pillars. Based on past experiments, the inlet velocity was set to 110 μm/s, approximately corresponding to 0.02 mL/h.[38] The outlet was set to no viscous stress (the Dirichlet condition for pressure), and the Navier-Stokes equation was solved for an incompressible laminar flow. The viscosity and density of water, 0.001 Pa.s and 1000 kg/m^3, respectively, were used.

IV. RESULTS AND DISCUSSION

A. Computational results

The insulating structures inside the main channel are essential tools to enhance the dielectrophoretic force by increasing the electrical resistance of the sample channel, as well as increasing the non-uniformity of the electric field. Without these structures, gradients in the electric field would be limited to areas close to the side walls of the sample channel, and most cells would not experience a strong enough dielectrophoretic force to be trapped. Adding the insulating structures allows for wider channels with uniform $\nabla(\vec{E}\cdot\vec{E})$, which consequently increases the throughput and selectivity of the devices.

To compare microdevices with different circular pillar geometries, a diagonal line located on the center of the device has been drawn (line A-B on Fig. 2(a)). Only the values on A-B′ are shown in Figs. 2(b)–2(d) because these values are repeated periodically on other parts of line A-B. Figure 2(a) shows the contour plot of $\nabla(\vec{E}_{RMS}\cdot\vec{E}_{RMS})$. For the designs presented here, frequencies from 100–600 kHz and voltages from 0–300 V_{RMS} where studied.

Line plots of $\nabla(\vec{E}_{RMS}\cdot\vec{E}_{RMS})$ inside the sample channel for two different pillar arrangements, triangular (staggered, similar to Fig. 2(a)), and rectangular arrangements are shown in Fig. 2(b). These demonstrate that the triangular arrangement creates higher $\nabla(\vec{E}_{RMS}\cdot\vec{E}_{RMS})$ compared to the rectangular arrangement. This arrangement has the added benefit that the calculated hydrodynamic efficiency for capturing cells is better in triangular than in rectangular arrangements.[27] Additionally, the triangular arrangement increases the probability of cell trapping since there is a higher frequency of cell collisions with the pillars. Based on these results, a triangular arrangement was selected.

Figure 2(c) shows the line plot of $\nabla(\vec{E}_{RMS}\cdot\vec{E}_{RMS})$ for three devices with 100 μm diameter and different gaps between the circular pillars: 30, 60, and 120 μm. This shows that $\nabla(\vec{E}_{RMS}\cdot\vec{E}_{RMS})$ has an inverse relation with the distance between the pillars, i.e., the DEP force increases by

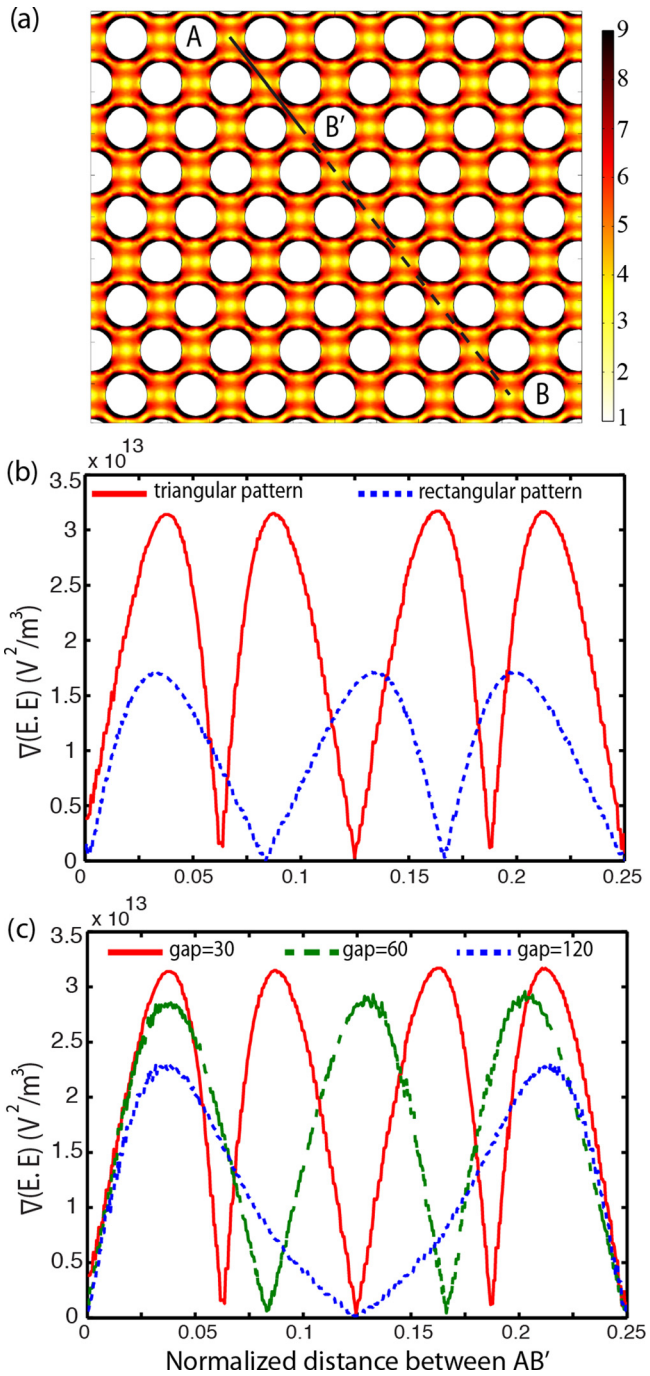

FIG. 2. (a) The gradient of the electric field squared ($V^2\,m^{-3}$) at 300 V_{rms} and 600 kHz. The line plot of $\nabla(\vec{E}_{rms}\cdot\vec{E}_{rms})$ on a normalized diagonal line A-B is presented for (b) triangular and rectangular pillar arrangements, (c) circular pillars with 30, 60, and 120 μm gap and diameter of 100 μm, at 100 V_{rms} and 500 kHz.

decreasing the gap between the pillars, although this increase is not significant. To avoid mechanically filtering the cells, the distance between pillars was not reduced to less than 30 μm. A spacing of 30 μm was used for the remainder of this study because decreasing the gap between pillars increases the number of pillars per unit area, which increases the probability of cell trapping.

Computational results predict that the maximum shear rate in the device has a maximum value of 52 s^{-1} which is two orders of magnitude less than the cell lysis limit of approximately 5000 s^{-1}.[50,51] In order to trap a cell in a moving fluid, the dielectrophoretic force should

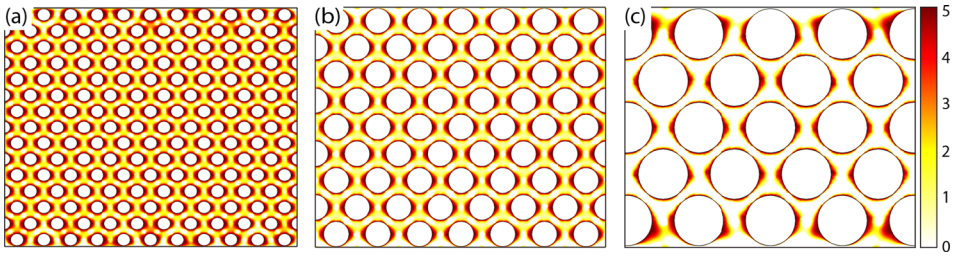

FIG. 3. Ratio of drag force to dielectrophoretic force for microdevices with equal channel width and circular pillars with diameter of (a) 50 μm, (b) 100 μm, and (c) 200 μm. In dark areas DEP force is dominant, and in light areas drag force prevails.

overcome the drag force. Figure 3 presents drag force to dielectrophoretic force ratios for pillars with diameter of 50, 100, and 200 μm. It was found that 50 μm pillars have 2.25 times smaller DEP dominant area than devices with 200 μm pillars.

In contrast, increasing the size of pillars reduces the total number of pillars per unit area, which decreases the probability of a cell entering a DEP dominant area. As a compromise between these two results, a diameter of 100 μm was chosen. It is also important to note that the size of the trapping area should be sufficiently large to encompass several particles and avoid saturation; otherwise, the captured cells may be released by small fluctuations in the fluid flow and thus decrease the trapping efficiency.

B. Experimental results

To determine the individual voltages for trapping the MOSE cells, we used the device shown in Fig. 1. Figure 4 shows the onset and complete trapping voltages for four different stages of MOSE cells. The voltages required to trap different stages were statistically different among most stages. The largest variation in trapping between cell types was seen when comparing the voltage required for complete trapping. Between 200 and 500 kHz, the voltage required for complete trapping of MOSE cells increased as the cell type became more tumorigenic. For all cell types, the complete trapping voltages were significantly different with p-values of 0.005 or less.

At 500 kHz, MOSE-L cells were trapped at a higher voltage than MOSE-I cells, while at 600 kHz the reverse occurred. This result did not occur for complete trapping at any other frequencies or for the other cell types, and we predict that the Clausius-Mossotti factor values for MOSE-L and MOSE-I cells intersected at a frequency between 500 and 600 kHz.

The onset and complete trapping of macrophages (PC1) and fibroblasts (OP9) are compared with different stages of MOSE cells in Fig. 5. Voltages for complete trapping of PC1 and OP9 cells are statistically different from the various stages of MOSE cells at almost all applied frequencies in the range of 200–600 kHz. Similarly to Fig. 4, the voltages for onset of trapping are statistically different.

Figures 6(a) and 6(b) present the difference between the complete trapping voltage of fibroblasts (OP9) and macrophages (PC1), respectively, with different stages of MOSE cells as a function of applied frequency. These results show that the difference between the complete trapping voltage of PC1 and OP9 and different stages of MOSE cells increases with increases in malignancy and stage of the MOSE cells.

Radius and viability of cells were measured using Cell Viability Analyzer (Vi-Cell, Beckman Coulter). The average radius of MOSE-E, -E/I, -I, and -L cells were 7.185 ± 1.004, 7.163 ± 1.245, 7.292 ± 1.493, and 7.050 ± 1.195 μm, respectively. The radii of PC1 macrophages and OP9 fibroblasts were 6.451 ± 1.530 and 6.673 ± 1.211 μm, respectively.

C. Discussion

The dielectrophoretic properties of cells are influenced by cell membrane morphologies, membrane surface permeability, cytoplasm conductivity, and cell size.[52,53] In this study, the cell

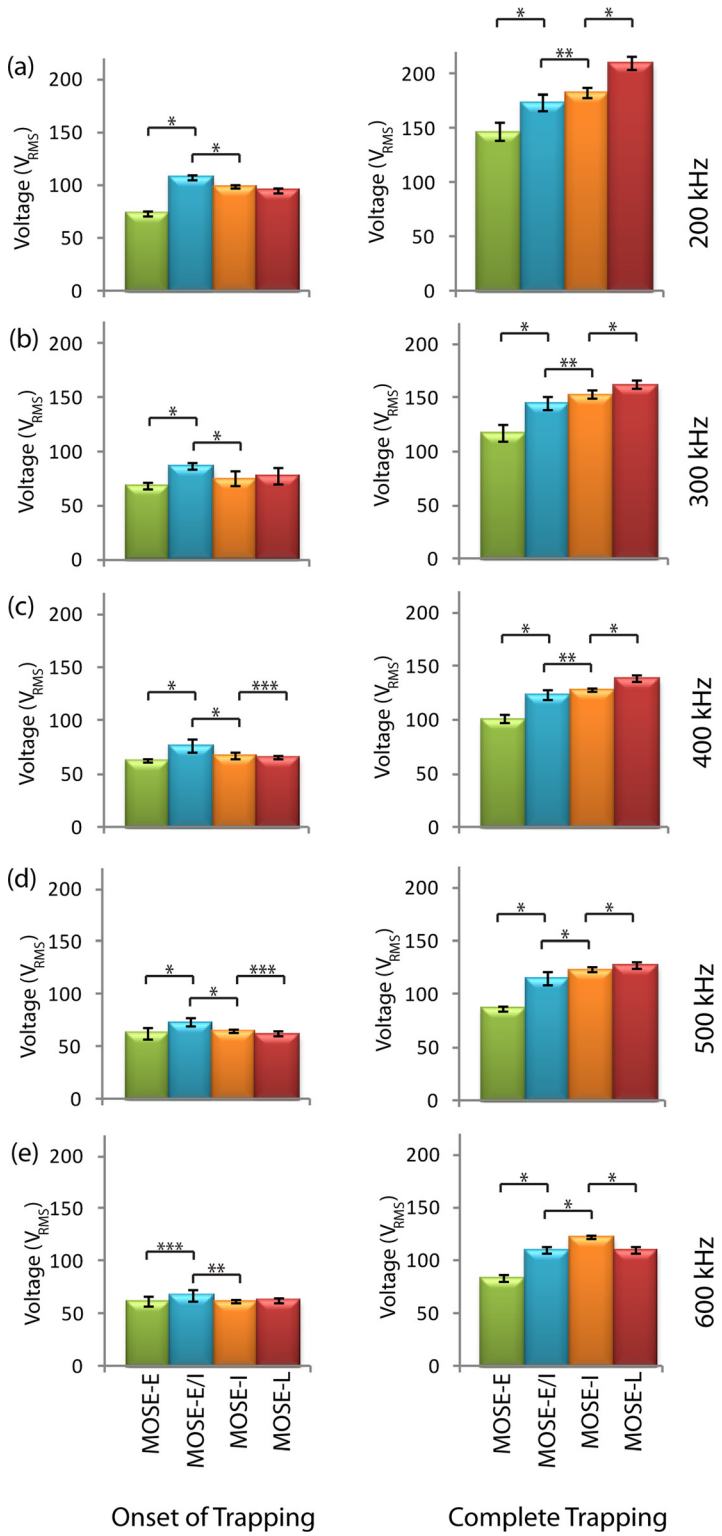

FIG. 4. Onset and complete trapping voltages of early (MOSE-E), early-intermediate (MOSE-E/I), intermediate (MOSE-I), and late (MOSE-L) cells at (a) 200 kHz, (b) 300 kHz, (c) 400 kHz, (d) 500 kHz, and (e) 600 kHz. Left and right columns present the onset of trapping and complete trapping, respectively. *, **, and *** indicate that data are significantly different with $p < 0.0005$, $p < 0.005$, and $p < 0.05$, respectively, ($n = 10$).

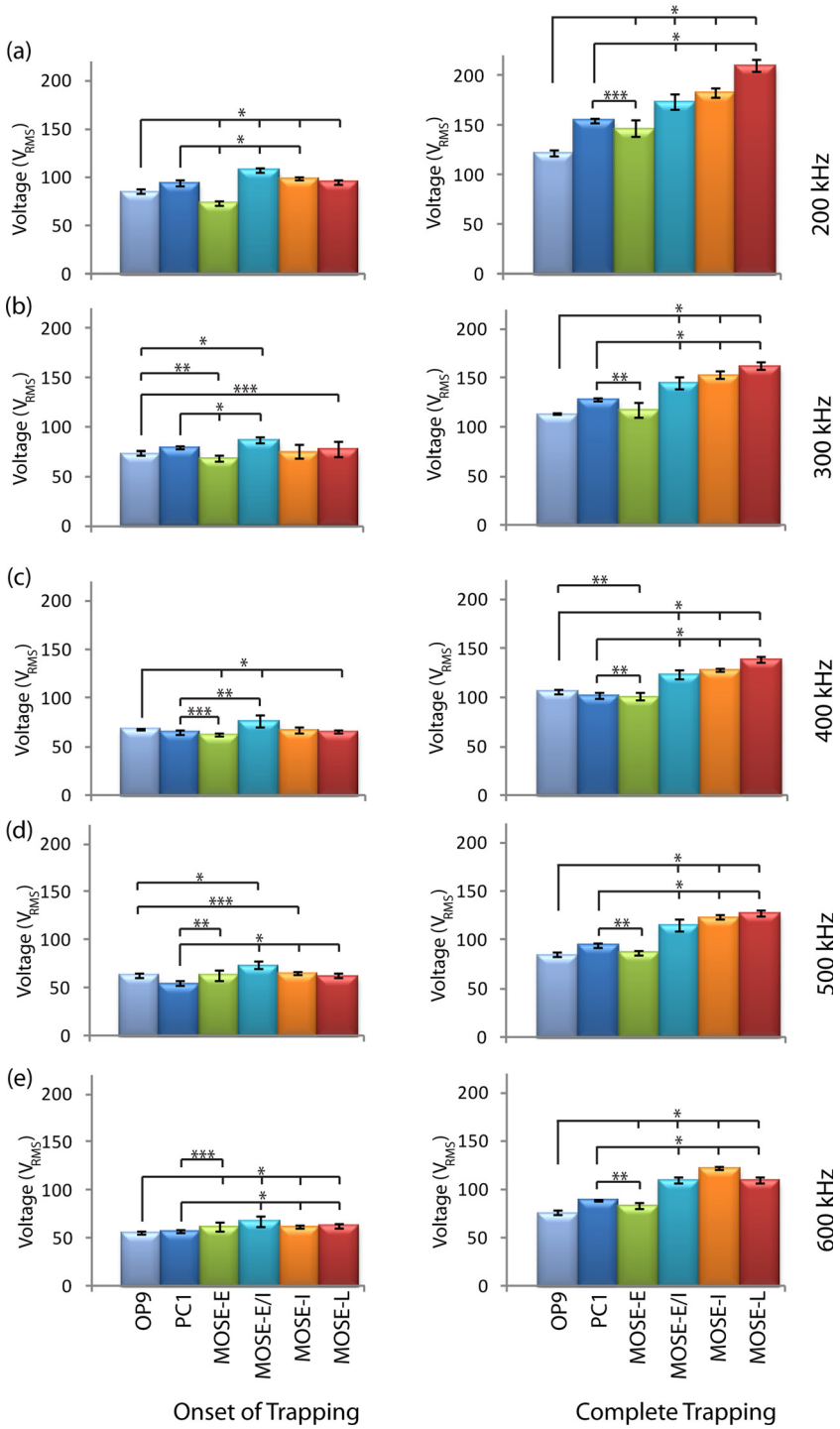

FIG. 5. Onset and complete trapping voltages of different stages of MOSE cells compared with macrophages (PC1) and fibroblasts (OP9) cells at (a) 200 kHz, (b) 300 kHz, (c) 400 kHz, (d) 500 kHz, and (e) 600 kHz. Left and right columns present the onset of trapping and complete trapping, respectively. *, **, and *** indicate that data are significantly different with $p < 0.0005$, $p < 0.005$, and $p < 0.05$, respectively, ($n = 10$).

size did not dominate the response because the radii of different stages of MOSE cells were in a similar range. Thus, we believe that the observed differences in the DEP response of different stages of MOSE cells (Fig. 4) are due to the intrinsic difference between the cells and not their size, as will be discussed below.

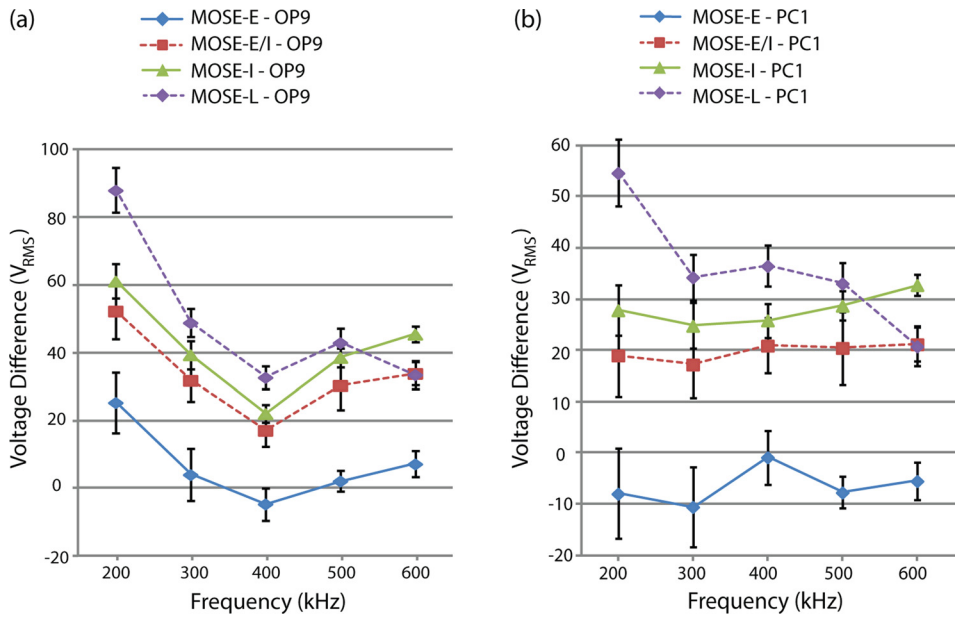

FIG. 6. (a) Difference between complete trapping voltage of (a) fibroblasts (OP9) and (b) macrophages (PC1) and different stages of MOSE cells as a function of applied frequency (n = 10).

The complex dielectric properties of living cells may result from the expression levels of various surface proteins and interfacial polarization of ions at cell membrane surfaces.[54] Since different cells have dissimilar properties, they can be selectively manipulated using DEP. Cell size, shape, and membrane morphology affect the first crossover frequency, and cytoplasm conductivity and nucleus-cytoplasm volume ratio affect the second crossover frequency.[31] The first crossover frequency of mammalian cells is typically less than 100 kHz (Ref. 46), and the second crossover frequency is normally in the order of 10 MHz for the sample with conductivity of 100 μS/cm.[46] The frequency range used in this study was limited between 200 and 600 kHz; thus, all of the aforementioned biophysical properties, especially membrane morphology, could play a role as to why different stages of MOSE cells exhibit different DEP properties.

The electrical capacitance of the cell membrane is a function of structural features, such as membrane folding, microvilli, and blebs.[47] It has been reported that there are more protrusions on the surface of transformed cells than normal cells, which results in transformed cells having a higher effective membrane capacitance than normal cells.[17–20] For instance, leukemia and breast cancer cells lines have higher effective membrane capacitance than normal T lymphocytes and erythrocytes.[17,18] This was also reported for rat kidney cells,[20] murine erythroleukemia cells,[19] and oral cancer cells.[22]

It has been reported that there is an increase in membrane ruffles in MOSE cells as they progress to a more aggressive phenotype.[14] MOSE-E cells show a more typical cobblestone-like phenotype. MOSE-E/I cells change to more spindle-shape morphology and are smaller than MOSE-E cells. In general, MOSE cells become more spindle-shape and smaller as they progress into MOSE-I and then MOSE-L.[14] Among other functional categories, the cytoskeleton and its regulators are significantly altered during MOSE progression, which affects both cell morphology[14] and viscoelasticity.[15] Based on the presented results (Figs. 4–6), we hypothesize that these morphological changes, including the increase in surface ruffling in later stages, could be the main reasons of dielectrophoretic changes between different stages of cancer cells. This will be investigated in more detail.

In addition, membrane proteins can be related to cells' dielectrophoretic properties. For instance the dielectrophoretic properties of erythrocytes from different blood types are determined by the diverse ABO-Rh antigens on the red blood cell membrane surface; thus blood cell membranes from donors with different blood types polarize differently.[4] In yeast cells, DEP properties

are modulated by the binding of lectin which can change the permittivity of the cell.[55] These observed differences in DEP response could be due to the expression levels of different, perhaps specific surface proteins or to a change in the total electrical charge and the conductivity of the cell membrane. Clearly, more in depth investigations are needed to identify changes in the MOSE cell membranes that are causal for the changes in their dielectrophoretic properties.

Most studies compare non-transformed cells with highly aggressive cancer cells, often derived from different patients.[17,18,22,56] In two other studies, a normal and a malignant cell, derived from the same cell line, have been compared.[19,20] The MOSE model allows for detection of step-wise changes during progression of syngeneic cancer cells, avoiding inter-individual differences that may affect the membrane organization, and thereby influence the dielectrophoretic properties. Thus, this model is more applicable to identify differences between progressive stages of transformed cells derived from the same cell line as would occur in the clinical setting. The current study is the first study that compares the dielectrophoretic responses of different stages of cancer cells, which are extracted from one cell line.

Furthermore, MOSE cells display unique behavior compared to fibroblasts and macrophages, representing normal and inflammatory cells found in the peritoneal fluid. These varying physical properties between MOSE cells, OP9 fibroblasts, and PC1 macrophages can be used to explain the distinct trapping regions among these cells, as shown in Fig. 5. From these data, it would seem possible to selectively screen for ovarian cells in the midst of background peritoneal cells, which is a likely scenario in true patient samples. Thus, these preliminary results suggest that cDEP technique has the potential to be used as a tool for early detection of ovarian cancer.

V. CONCLUSIONS

The current study is the first study that compares the dielectrophoretic response of different stages of ovarian cancer cells which are derived from one precursor cell line. The results presented here demonstrate that aggressive ovarian cancer cells display a significantly different voltage that allows them to be dielectrophoretically distinguished and trapped from their non-transformed progenitor cells as well as from other cell types that may be found in peritoneal serous exudate fluid. Studying the dielectrophoretic responses of these cells is the first step in developing a clinical diagnostics system centered on contactless dielectrophoresis to separate ovarian epithelial cells from peritoneal fluid to potentially detect even early and intermediate stages of the disease. Early diagnosis will result in early treatment and may increase the survival rates of the affected women. Future work will focus on optimizing device performance and building towards a clinically applicable method for early detection of ovarian cancer.

ACKNOWLEDGMENTS

This material is based upon work supported in part by the National Science Foundation under Grant No. EFRI 0938047, by the Virginia Tech Institute for Critical Technology and Applied Science (ICTAS), by the Diversity Summer Research Program (DSRP), and by NIH RO1 CA118846 (to EMS and PCR). The authors would like to thank Dr. Mark A. Stremler, Bioelectromechanical Systems (BEMS) laboratory members, Hadi Shafiee, Roberto Gallo, Elizabeth Savage, and Andrea Rojas, and Dr. Schmelz laboratory members, Amanda Shea and Chun Cao, for their contributions.

[1]I. Visintin, Z. Feng, G. Longton, D. C. Ward, A. B. Alvero, Y. Lai, J. Tenthorey, A. Leiser, R. Flores-Saaib, H. Yu, M. Azori, T. Rutherford, P. E. Schwartz, and G. Mor, Clin. Cancer Res. **14**, 1065–1072 (2008).
[2]I. J. Jacobs and U. Menon, Mol. Cell. Proteomics **3**, 355–366 (2004).
[3]A. Jemal, F. Bray, M. M. Center, J. Ferlay, E. Ward, and D. Forman, Ca-Cancer J. Clin. **61**, 69–90 (2011).
[4]K. M. Leonard and A. R. Minerick, Electrophoresis **32**, 2512–2522 (2011).
[5]A. Jemal, R. Siegel, J. Xu, and E. Ward, Ca-Cancer J. Clin. **60**, 277–300 (2010).
[6]X. Wang, M. Deavers, R. Patenia, R. L. Bassett, Jr., P. Mueller, Q. Ma, E. Wang, and R. S. Freedman, J. Trans. Med. **4**, 30 (2006).
[7]L. Gortzak-Uzan, A. Ignatchenko, A. I. Evangelou, M. Agochiya, K. A. Brown, P. St Onge, I. Kireeva, G. Schmitt-Ulms, T. J. Brown, J. Murphy, B. Rosen, P. Shaw, I. Jurisica, and T. Kislinger, J. Proteome Res. **7**, 339–351 (2008).
[8]A. M. Westermann, E. Havik, F. R. Postma, J. H. Beijnen, O. Dalesio, W. H. Moolenaar, and S. Rodenhuis, Annals Oncol. **9**, 437–442 (1998).
[9]S. P. Langdon, Methods Mol. Med. **88**, 133–139 (2004).

[10]J. K. Chan, C. A. Hamilton, E. M. Anderson, M. K. Cheung, J. Baker, A. Husain, N. N. Teng, C. S. Kong, and R. S. Negrin, Am. J. Obstet. Gynecol. **197**, 507 e501–505 (2007).
[11]V. Nossov, M. Amneus, F. Su, J. Lang, J. M. Janco, S. T. Reddy, and R. Farias-Eisner, Am. J. Obstet. Gynecol. **199**, 215–223 (2008).
[12]Z. Zhang, R. C. Bast, Jr., Y. Yu, J. Li, L. J. Sokoll, A. J. Rai, J. M. Rosenzweig, B. Cameron, Y. Y. Wang, X. Y. Meng, A. Berchuck, C. Van Haaften-Day, N. F. Hacker, H. W. de Bruijn, A. G. van der Zee, I. J. Jacobs, E. T. Fung, and D. W. Chan, Cancer Res. **64**, 5882–5890 (2004).
[13]P. C. Roberts, E. P. Mottillo, A. C. Baxa, H. H. Heng, N. Doyon-Reale, L. Gregoire, W. D. Lancaster, R. Rabah, and E. M. Schmelz, Neoplasia **7**, 944–956 (2005).
[14]A. L. Creekmore, W. T. Silkworth, D. Cimini, R. V. Jensen, P. C. Roberts, and E. M. Schmelz, PloS one **6**, e17676 (2011).
[15]A. N. Ketene, E. M. Schmelz, P. C. Roberts, and M. Agah, Nanomed.: Nanotechnol., Biol., Med. **8**(1), 93 (2011).
[16]Y. Zou and Z. Guo, Med. Eng. Phys. **25**, 79–90 (2003).
[17]F. F. Becker, X. B. Wang, Y. Huang, R. Pethig, J. Vykoukal, and P. R. C. Gascoyne, J. Phys. D: Appl. Phys. **27**, 2659–2662 (1994).
[18]F. F. Becker, X. B. Wang, Y. Huang, R. Pethig, J. Vykoukal, and P. R. C. Gascoyne, Proc. Natl. Acad. Sci. U.S.A. **92**, 860–864 (1995).
[19]P. R. C. Gascoyne, J. Noshari, F. F. Becker, and R. Pethig, IEEE Trans. Ind. Appl. **30**, 829–834 (1994).
[20]Y. Huang, X. B. Wang, F. F. Becker, and P. R. C. Gascoyne, Bba-Biomembranes **1282**, 76–84 (1996).
[21]A. J. Surowiec, S. S. Stuchly, J. R. Barr, and A. Swarup, IEEE Trans. Bio-Med. Eng. **35**, 257–263 (1988).
[22]H. J. Mulhall, F. H. Labeed, B. Kazmi, D. E. Costea, M. P. Hughes, and M. P. Lewis, Anal. Bioanal. Chem. **401**, 2455–2463 (2011).
[23]N. Lewpiriyawong, C. Yang, and Y. C. Lam, Biomicrofluidics **2**, 34105 (2008).
[24]Z. Gagnon, J. Mazur, and H. C. Chang, Biomicrofluidics **3**, 44108 (2009).
[25]I. F. Cheng, H. C. Chang, and D. Hou, Biomicrofluidics **1**, 21503 (2007).
[26]A. Lostumbo, D. Mehta, S. Setty, and R. Nunez, Exp. Mol. Pathol., **80**, 46–53 (2006).
[27]S. Nagrath, L. V. Sequist, S. Maheswaran, D. W. Bell, D. Irimia, L. Ulkus, M. R. Smith, E. L. Kwak, S. Digumarthy, A. Muzikansky, P. Ryan, U. J. Balis, R. G. Tompkins, D. A. Haber, and M. Toner, Nature **450**, 1235–1239 (2007).
[28]K. Kato and A. Radbruch, Cytometry **14**, 384–392 (1993).
[29]E. B. Cummings and A. K. Singh, Anal. Chem. **75**, 4724–4731 (2003).
[30]C. F. Chou, J. O. Tegenfeldt, O. Bakajin, S. S. Chan, E. C. Cox, N. Darnton, T. Duke, and R. H. Austin, Biophys. J. **83**, 2170–2179 (2002).
[31]R. Martinez-Duarte, R. A. Gorkin III, K. Abi-Samra, and M. J. Madou, Lab Chip **10**, 1030–1043 (2010).
[32]B. H. Lapizco-Encinas, B. A. Simmons, E. B. Cummings, and Y. Fintschenko, Anal. Chem. **76**, 1571–1579 (2004).
[33]R. C. Gallo-Villanueva, V. H. Perez-Gonzalez, R. V. Davalos, and B. H. Lapizco-Encinas, Electrophoresis **32**, 2456–2465 (2011).
[34]R. V. Davalos, G. J. McGraw, T. I. Wallow, A. M. Morales, K. L. Krafcik, Y. Fintschenko, E. B. Cummings, and B. A. Simmons, Anal. Bioanal. Chem. **390**, 847–855 (2008).
[35]A. Gencoglu and A. Minerick, Lab Chip **9**, 1866–1873 (2009).
[36]H. Shafiee, J. L. Caldwell, M. B. Sano, and R. V. Davalos, Biomed. Microdevices **11**(5), 997 (2009).
[37]H. Shafiee, M. B. Sano, E. A. Henslee, J. L. Caldwell, and R. V. Davalos, Lab Chip **10**, 438–445 (2010).
[38]A. Salmanzadeh, L. Romero, H. Shafiee, R. C. Gallo-Villanueva, M. A. Stremler, S. D. Cramer, and R. V. Davalos, Lab Chip **12**, 182–189 (2012).
[39]M. B. Sano, J. L. Caldwell, and R. V. Davalos, Biosens. Bioelectron **30**, 13–20 (2011).
[40]E. A. Henslee, M. B. Sano, A. D. Rojas, E. M. Schmelz, and R. V. Davalos, Electrophoresis **32**, 2523–2529 (2011).
[41]M. Lekka, P. Laidler, D. Gil, J. Lekki, Z. Stachura, and A. Z. Hrynkiewicz, Eur. Biophys. J. Biophy. **28**, 312–316 (1999).
[42]S. E. Cross, Y. S. Jin, J. Rao, and J. K. Gimzewski, Nat. Nanotechnol. **2**, 780–783 (2007).
[43]E. M. Darling, S. Zauscher, J. A. Block, and F. Guilak, Biophys. J. **92**, 1784–1791 (2007).
[44]M. J. Rosenbluth, W. A. Lam, and D. A. Fletcher, Biophys. J. **90**, 2994–3003 (2006).
[45]T. B. Jones, *Electromechanics of Particles* (Cambridge University Press, Cambridge, New York, 2005).
[46]R. Pethig, *BioMEMS and Biomedical Nanotechnology* (SpringerLink, 2007), pp. 103–126.
[47]R. Pethig, Biomicrofluidics **4**, 022811 (2010).
[48]D. Miklavčič, N. Pavšelj, and F. X. Hart, *Wiley Encyclopedia of Biomedical Engineering* (John Wiley & Sons, 2006).
[49]L. A. Flanagan, J. Lu, L. Wang, S. A. Marchenko, N. L. Jeon, A. P. Lee, and E. S. Monuki, Stem Cells **26**, 656–665 (2008).
[50]R. Skalak and S. Chien, *Handbook of Bioengineering* (McGraw-Hill, New York, 1987).
[51]*Biomechanics, its Foundations and Objectives*, edited by Y. C. Fung, N. Perrone, M. Anliker (University of California San Diego, Office of Naval Research, Prentice-Hall, Englewood Cliffs, N.J., 1972).
[52]V. L. Sukhorukov, W. M. Arnold and U. Zimmermann, J. Membr. Biol. **132**, 27–40 (1993).
[53]X. B. Wang, Y. Huang, P. R. Gascoyne, F. F. Becker, R. Holzel, and R. Pethig, Biochim. Biophys. Acta **1193**, 330–344 (1994).
[54]P. R. Gascoyne and J. Vykoukal, Electrophoresis **23**, 1973–1983 (2002).
[55]I. Ikeda, S. Tsukahara, and H. Watarai, Anal. Sci. **19**, 27–31 (2003).
[56]J. An, J. Lee, S. H. Lee, J. Park, and B. Kim, Anal. Bioanal. Chem. **394**, 801–809 (2009).

Theoretical Considerations of Tissue Electroporation With High-Frequency Bipolar Pulses

Christopher B. Arena, Michael B. Sano, Marissa Nichole Rylander, and Rafael V. Davalos*, *Member, IEEE*

***Abstract*—This study introduces the use of high-frequency pulsed electric fields for tissue electroporation. Through the development of finite element models and the use of analytical techniques, electroporation with rectangular, bipolar pulses is investigated. The electric field and temperature distribution along with the associated transmembrane potential development are considered in a heterogeneous skin fold geometry. Results indicate that switching polarity on the nanosecond scale near the charging time of plasma membranes can greatly improve treatment outcomes in heterogeneous tissues. Specifically, high-frequency fields ranging from 500 kHz to 1 MHz are best suited to penetrate epithelial layers without inducing significant Joule heating, and cause electroporation in underlying cells.**

***Index Terms*—Bipolar pulses, electroporation, nanosecond pulsed electric field, oscillating electric field, transmembrane potential.**

I. Introduction

ELECTROPORATION is a nonlinear, biophysical mechanism in which the application of an external pulsed electric field leads to an increase in the permeability of cellular membranes. While direct evidence for the exact mechanism of electroporation has yet to be discovered [1], early *in vitro* experiments suggest that the extent of electroporation is attributed to the induced buildup of charge across the plasma membrane, and consequently, transmembrane potential (TMP) [2]–[7]. The applied field strength and pulse duration control the TMP development and the extent to which transient permeabilizing defects are allowed to reseal. If the pulse parameters are tuned such that the membrane defects are only temporary, and the cell remains viable, the process is termed reversible electroporation. Reversible electroporation can be used to introduce molecules into cells that, under normal conditions, would not permeate cellular membranes [8]. Irreversible electroporation (IRE) results when membrane defects are irrecoverable, leading to cell death presumably through a loss of homeostasis [9], [10]. Recently, electroporation has been utilized *in vivo* as a means to destroy cancer cells within tissues in both reversible and irreversible modalities. Reversible electroporation is being studied to facilitate the delivery of anticancer drugs and DNA into cancer cells through the plasma membrane in the form of electrochemotherapy (ECT) and electrogenetherapy (EGT), respectively. IRE promotes cell necrosis [11] and is an independent means to destroy substantial volumes of targeted tissue without the use of harmful adjuvant chemicals, if used prior to the onset of thermal injury [12].

Common protocols for IRE, ECT, and EGT involve delivering multiple, unipolar pulses with a duration on the order of microseconds through electrodes inserted directly into, or adjacent to, the malignant tissue [12]–[15]. When the tumor is located deep within an organ, a minimally invasive needle or catheter-based device is needed for the electrodes to reach the tumor. In some instances, the organ puncture required by these designs can, in itself, damage the surrounding healthy cells [16], [17]. There is also the possibility of reseeding cancer cells upon device removal. Therefore, the use of nonpuncturing plate electrodes placed around the organ is desirable in some instances. Plate electrodes are best suited to treat tumors lying close to the skin, because a high potential drop occurs across the skin, where the field is the largest, limiting the amount of deeper tissue that can be permeabilized without first permeabilizing the skin [14], [15]. However, the high electric field in the skin can lead to deleterious thermal damage through the mechanism of Joule heating [18]. Plate electrodes will have similar problems when placed around internal organs to treat tumors. Most organs are covered by the peritoneum, where the presence of tight junctions concentrates the field across epithelial cells, because extracellular current pathways are reduced [19]. We hypothesize that these problems can be mitigated by implementing high-frequency bursts of bipolar pulses with a burst width on the order of microseconds and a duration of single polarity on the order of nanoseconds.

To the best of our knowledge, the benefits of bipolar pulses have only been studied for electroporation applications at the single-cell level. Theoretically, Talele *et al*. have shown that asymmetrical electroporation due to the resting TMP ($\sim$0.1 V) [20] of cells seen when unipolar pulses are delivered [21], [22] can be alleviated by switching to bipolar pulses [23]. Experimentally, this leads to increased efficiency of macromolecule uptake through the membrane [21], [22]. Depending on the extracellular conductivity, bipolar pulses with a frequency of 1 MHz (i.e., 500 ns duration of single polarity) can also lessen

Manuscript received October 2, 2010; revised November 22, 2010; accepted December 15, 2010. Date of publication December 23, 2010; date of current version April 20, 2011. This work was supported by the National Science Foundation (NSF), Arlington, VA, under Award CBET-0933335. *Asterisk indicates corresponding author*.

C. B. Arena and M. B. Sano are with the Virginia Tech-Wake Forest School of Biomedical Engineering and Sciences, Bioelectromechanical Systems Laboratory, Virginia Polytechnic Institute and State University, Blacksburg, VA 24061 USA (e-mail: carena@vt.edu; sano@vt.edu).

M. N. Rylander is with the Virginia Tech-Wake Forest School of Biomedical Engineering and Sciences and the Virginia Tech Department of Mechanical Engineering, Bioheat Transfer and Nanotherapeutics Laboratory, Virginia Polytechnic Institute and State University, Blacksburg, VA 24061 USA (e-mail: mnr@vt.edu).

*R. V. Davalos is with the Virginia Tech-Wake Forest School of Biomedical Engineering and Sciences, Bioelectromechanical Systems Laboratory, Virginia Polytechnic and State University, Blacksburg, VA 24061 USA (e-mail: davalos@vt.edu).

Digital Object Identifier 10.1109/TBME.2010.2102021

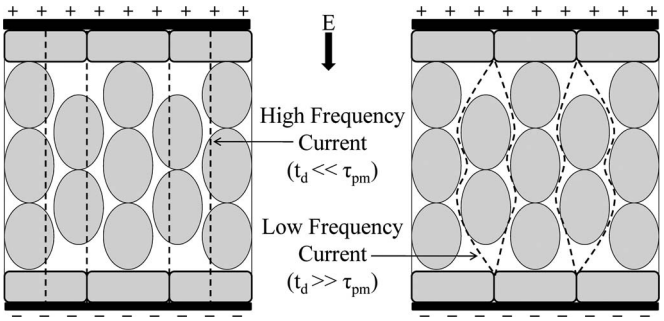

Fig. 1. Illustration of current pathways through epithelial layers and bulk tissue prior to the onset of electroporation. When the pulse duration t_d is much less than the plasma membrane time constant $\tau_{\rm pm}$, current flows through both intracellular and extracellular spaces (left). In the case that t_d is much more than $\tau_{\rm pm}$, current flow is restricted to the narrower extracellular spaces (right).

the dependence of electroporation on cell size, allowing more cells to be electroporated [24], [25]. In general, pore formation increases as long as the TMP is sustained above a critical threshold (∼1 V) [20]. One potential drawback of bipolar pulses is that they require higher field strengths to induce a given TMP as compared to a unipolar pulse of equivalent duration. This is apparent when the frequency of the bipolar pulses is increased, because the time interval above the critical TMP is reduced [25]. Kotnik *et al*. have explored the benefits of bipolar pulse trains at significantly lower frequencies, up to 1 kHz (i.e., 500 μs duration of single polarity). At lower frequencies, theoretical results show that the pore formation asymmetry can also be normalized with bipolar pulses [26]. Experimentally, bipolar pulses reduce electrolytic contamination [27] and the required field strength for reversible electroporation, while the field strength required for IRE remains unchanged [26]. The authors attribute this to the fact that when the duration of single polarity is much longer than the plasma membrane charging time, permeabilized area differences on the membrane between unipolar and bipolar pulses decreases as pulse amplitude increases.

Here, the benefits of high-frequency bipolar pulses for electroporation of tissue enclosed by an epithelium are studied. Epithelial layers containing tight junctions are preferred sites of electroporation for pulses with duration on the order of microseconds [28], [29]. This has to do with the fact that the electric current associated with pulses longer than the charging time of the plasma membrane (∼1 μs) [20] is confined to narrow, high-resistance extracellular spaces prior to the onset of electroporation (see Fig. 1) [30], [31]. It is possible for the field to penetrate epithelial layers when nanosecond pulsed electric field are employed, because current can flow through both extracellular and intracellular spaces [29], [31]. In this case, all cells present in the organ, regardless of their packing and morphology, experience a macroscopically homogeneous electric field distribution [32] (microscopic nonuniformities in the electric field are still present due to the packing of individual cells comprising the tissue). Therefore, high-frequency bipolar pulses with a duration of single polarity on the order of nanoseconds can be applied to treat tissue layers underlying the skin (see Fig. 2). Further, because the field is not concentrated across

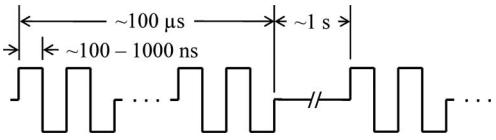

Fig. 2. Typical pulsing protocol for the proposed electroporation-based therapy. The total burst width of the high-frequency pulses (∼100 to 1000 ns duration of single polarity) is on the order of hundreds of microseconds, the time delay in between bursts is on the order of seconds, and the total number of bursts can be adjusted.

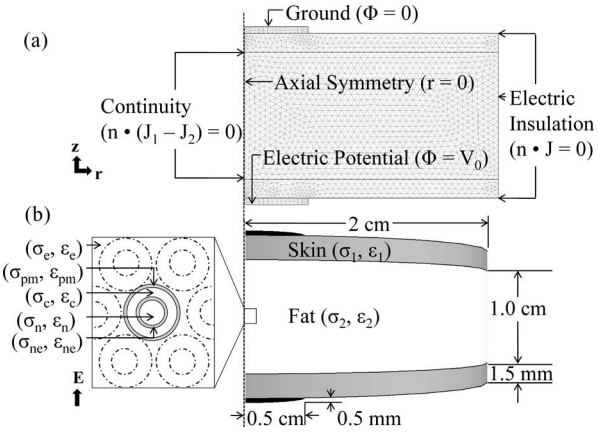

Fig. 3. (a) Meshed geometry of the FEM with boundary settings. The mesh consists of 3028 elements and was refined until there was $< 0.1\%$ change in the magnitude of the electric field at the center of the tissue. (b) Schematic diagram of the geometry with dimensions. The box represents an expanded view of the tissue that describes the link between the macroscopic electric field *E* and the microscopic analysis of TMP. Adjacent cells are drawn with dashed lines, indicating that their role was ignored in calculating TMP.

the epithelial cells, the potential for thermal damage in the skin should be reduced.

To quantify these apparent benefits, a finite element model (FEM) simulating plate electrodes surrounding a cylindrical tissue section through the center of a skin fold was constructed. Electroporation is often used to treat tumors that arise in fat tissue lying close to the skin [33]. The FEM incorporates physics for determining the electric field and temperature distribution within the heterogeneous system. Additionally, the electric field data generated were substituted into analytical calculations of TMP in order to determine the relationships between the pulse frequency and the extent of electroporation in the different tissue layers.

II. Methods

A 2-D axisymmetric FEM representative of a cylindrical section of noninfiltrated fat encapsulated by dry skin (see Fig. 3) was simulated using COMSOL 3.5a (Burlington, MA). The electric potential distribution within the tissue was obtained by transiently solving

$$-\nabla \cdot (\sigma \nabla \Phi) - \varepsilon_0 \varepsilon_r \nabla \cdot \left(\frac{\partial \nabla \Phi}{\partial t} \right) = 0 \qquad (1)$$

where Φ is the electric potential and σ and ε_r are the conductivity and relative permittivity of each tissue layer, respectively, which

TABLE I
DIELECTRIC PROPERTIES OF THE FEM SIMULATION DOMAIN

Frequency (Pulse Duration)	Waveform	Property	Tissue	
			Skin	Fat
250 kHz (2 μs)	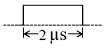	σ (S/m)	0.00216	0.0263
		ε_r	888	47
500 kHz (1 μs (×2))		σ (S/m)	0.00485	0.0265
		ε_r	851	33
1 MHz (500 ns (×4))	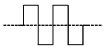	σ (S/m)	0.0119	0.0267
		ε_r	792	25
2 MHz (250 ns (×8))	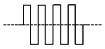	σ (S/m)	0.0290	0.0270
		ε_r	700	20

TABLE II
THERMAL PROPERTIES OF THE FEM SIMULATION DOMAIN

Property	Tissue		
	Blood	Skin	Fat
ρ (kg/m^3)	1069	1085	850
C (J/(kg·K))	3650	3680	2300
k (W/(m·K))	-	0.47	0.16
ω_b(1/s)	-	1.1	0.0036
Q_m (W/m^3)	-	368	58

depends on frequency (see Table I). Equation (1) is obtained from Maxwell's equations assuming no external current density (current density $J = \sigma E$), no remnant displacement (electric displacement $D = \varepsilon_0 \varepsilon_r E$), and the electro-quasistatic approximation. This approximation neglects magnetic induction ($\nabla \times E = 0$), which allows for the expression of the electric field only in terms of the electric potential:

$$E = -\nabla \Phi. \tag{2}$$

The dielectric properties of the bulk tissue were chosen from the data generated by Gabriel *et al*. [34] available online (http://niremf.ifac.cnr.it/docs/dielectric/home.html). The data were interpolated in Mathematica 7 (Wolfram Research, Inc., Champaign, IL) in order to estimate the dielectric properties at the desired frequencies. Dielectric properties of the electrode were chosen to be stainless steel, as incorporated in the Comsol material library. All electrical boundary conditions are shown in Fig. 3.

Because rectangular waveforms are comprised of components with various frequencies and amplitudes, tissue properties at frequencies associated with the carrier frequency, defined as the inverse of twice the duration of single polarity, are chosen. Intuitively, the duration of single polarity defines the frequency at which the current changes direction in the tissue. The pulses were constructed by multiplying the applied voltage by a function consisting of two smoothed Heaviside functions with a continuous second derivative and a tolerance of 5 ns (rise and fall times). The electro-quasistatic assumption is confirmed based on the fact that the primary frequency of the pulses is lower than 200 MHz (rise and fall times), which corresponds to a wavelength and skin depth that is greater than the longest dimension in the geometry [35]. The inclusion of a permittivity term in (1) differs from previous, simplified models [36], [37], and accounts for the reactive component of tissue to time-dependent pulsing, which is required for obtaining accurate potential distributions in heterogeneous models [38].

The temperature distribution in the tissue was obtained by transiently solving a modified version of the Pennes bioheat equation [39] with the inclusion of a Joule heating term:

$$\rho C \frac{\partial T}{\partial t} = \nabla \cdot (k \nabla T) + \rho_b \omega_b C_b (T_b - T) + Q_m + |J \cdot E| \tag{3}$$

where T is the tissue temperature, T_b is the blood temperature, k is the thermal conductivity of the tissue, C and C_b are the tissue and blood specific heat, respectively, ρ and ρ_b are the tissue and blood density, respectively, Q_m is the metabolic heat source term, ω_b is the blood perfusion coefficient, and $|J \cdot E|$ is the Joule heating term. All thermal tissue properties are given in Table II [40]. Due to the presence of different tissue layers and the high frequencies under consideration (250 kHz to 2 MHz), displacement currents are considered along with conduction currents in the formulation of Joule heating

$$J = J_D + J_C = \varepsilon_0 \varepsilon_r \frac{\partial E}{\partial t} + \sigma E \tag{4}$$

where J is the total current density, J_D is the displacement current density, and J_C is the conduction current density. In order to ensure that negative current components due to polarity changes add to the total current in the tissue, the absolute value of the resistive heating term was taken prior to temperature calculations. It was assumed that all subdomains were initially at physiologic temperature ($T_0 = 310.15$ K). The boundaries between the electrode–skin interface and the skin–fat interface were treated as continuous [$n \cdot (k_1 \nabla T_1 - k_2 \nabla T_2) = 0$], the centerline was defined as axial symmetry ($r = 0$), and the remaining boundaries were thermally insulated [$n \cdot (k \nabla T) = 0$] for conservative temperature estimates. Temperature profiles were investigated along the centerline ($r = 0$ mm) in the middle of the fat ($z = 0$ mm) and skin ($z = 5.75$ mm) layers. Data were imported into Mathematica, and a moving average with a period of 100 ns was taken to smooth the plots. Additionally, the data were fit with a linear trendline in order to extrapolate to longer burst widths and predict the onset of thermal damage.

By treating cells as a series of spherical, dielectric shells containing and surrounded by a conductive medium, the analytical solution for induced TMP across the plasma membrane ($\Delta \Phi$) can be obtained according to the law of total current [41]:

$$\nabla \cdot \left(\varepsilon_0 \varepsilon_r \frac{\partial E}{\partial t} + \sigma E \right) = \Lambda_k \nabla \cdot E = 0 \tag{5}$$

$$\Lambda_k = \sigma + \varepsilon_0 \varepsilon_r \frac{\partial}{\partial t} \tag{6}$$

where Λ is the admittivity operator and the subscript k denotes cellular regions including the nucleoplasm n, nuclear envelope

TABLE III
DIELECTRIC PROPERTIES OF ANALYTICAL TMP CALCULATION

Region	σ (S/m)	ε_r	Dimensions (m)
Extracellular Space	0.6	80.0	-
Plasma Membrane	5.3×10^{-6}	7.0	7.0×10^{-9} (thickness)
Cytoplasm	0.13	60.0	5.0×10^{-6} (radius)
Nuclear Envelope	4.3×10^{-3}	22.8	40.0×10^{-9} (thickness)
Nucleoplasm	0.18	120.0	2.5×10^{-6} (radius)

ne, cytoplasm *c*, plasma membrane *pm*, and extracellular space *e*. Transforming (2), (5), and (6) into the frequency domain [41]

$$E = -\nabla\Phi(s) \tag{7}$$

$$\Lambda_k \nabla \cdot E(s) = 0 \tag{8}$$

$$\Lambda_k(s) = \sigma + \varepsilon_0 \varepsilon_r s \tag{9}$$

where $s = j\omega = j2\pi f$, and applying the appropriate boundary conditions of potential continuity and normal vector continuity of current density at the interface between the different regions yields the solution for TMP [41]

$$\Delta\Phi(s) = F(\Lambda_n, \Lambda_{\rm ne}, \Lambda_c, \Lambda_{\rm pm}, \Lambda_e) E(s) \cos\theta \tag{10}$$

where θ represents the polar angle at the cell center between the electric field and the point of interest along the membrane. TMP is defined as the potential directly outside the membrane minus the inside. The natural, resting component of the plasma membrane TMP was ignored in all simulations, because it is typically an order of magnitude less than the induced TMP [20]. Further, the TMP across the nuclear envelope never reached a permeabilizing threshold with the chosen pulsing protocols, and reference to TMP from this point forward refers only to the plasma membrane. The term $F(\Lambda_k)$ represents a transfer function of the TMP that reflects the geometric and dielectric properties of the cellular regions (see Table III) [42] as a function of the admittivity. Dielectric properties at the cellular level are assumed to be frequency independent, which is valid for predicting TMP up to ~100 MHz [43]. The exact formulation for $F(\Lambda_k)$ is lengthy and can be found in [44], but is not included here for brevity. The term *E(s)* represents the Laplace transform of the pulsed electric field as a function of time.

The analytical model was utilized in two instances. In the first scenario, the frequency dependence of the induced TMP was investigated. Both rectangular and sinusoidal electric fields with identical maximum amplitude were compared. Rectangular waveforms were constructed with a series of step functions (ideal rise time) of alternating polarity and duration, and sinusoidal waveforms were constructed with a single sine function of varying frequency. The electric fields were substituted into (10), and the equations were solved directly in Mathematica.

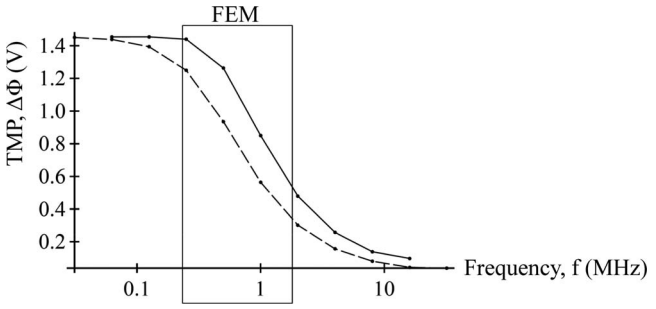

Fig. 4. Frequency *f* response of the TMP at the cell pole ($\theta = 0$) for rectangular bipolar pulses (–) and sinusoidal waveforms (– –). The box illustrates the frequency window implemented in the FEM.

This analysis provided insight as to which pulse waveforms and frequencies should be simulated by the FEM.

In the second case, TMP profiles were investigated around a hypothetical cell located along the centerline ($r = 0$ mm) in the middle of the fat ($z = 0$) and skin ($z = 5.75$ mm) layers of the FEM. The equations for TMP are derived under the assumption that there is no influence on the microscopic electric field from neighboring cells. Therefore, the macroscopic electric field in the bulk tissue predicted by the FEM dictates the microscopic electric field experienced by the cell. The vertical *z*-component of the electric field was imported from specific locations within the FEM into Mathematica to account for polarity changes. The radial *r*-component was neglected due to the fact that it never surpassed 3 V/cm as a current traveled primarily in the *z*-direction. Nonuniform electric field data were fit with a series of step functions (50-ns duration), such that the Laplace transform of the field could be performed and the solution for TMP could be obtained in the frequency domain as the summation of individual steps. The inverse Laplace transform of the data was then taken to obtain the complete time courses.

III. RESULTS

Results of the parametric study on TMP for frequencies spanning from 62.5 kHz to 16 MHz are shown in Fig. 4. The maximum amplitude of the sinusoidal and bipolar rectangular electric fields was 2000 V/cm (peak). For this applied field and the given geometric and dielectric properties of the modeled cell, the TMP never exceeds 1.46 V. Additionally, the time constant of the plasma membrane is 345 ns. All measurements were taken at the cell pole ($\theta = 0$) to depict the maximum achieved TMP after the system reached a steady oscillatory state. From the curve, as the frequency increases, the magnitude of the TMP is reduced. For the sinusoidal waveform, the reduction is evident at lower frequencies compared to the rectangular waveform. This has to do with the fact that the rectangular waveform maintains its maximum amplitude for a longer period of time than the sinusoidal waveform. It is not until the frequency of the rectangular waveform surpasses 250 kHz that a dramatic decrease in TMP occurs. For this reason, only rectangular pulses in a frequency window of 250 kHz to 2 MHz were investigated in the FEM, since they are best suited for electroporation with high-frequency bipolar pulses.

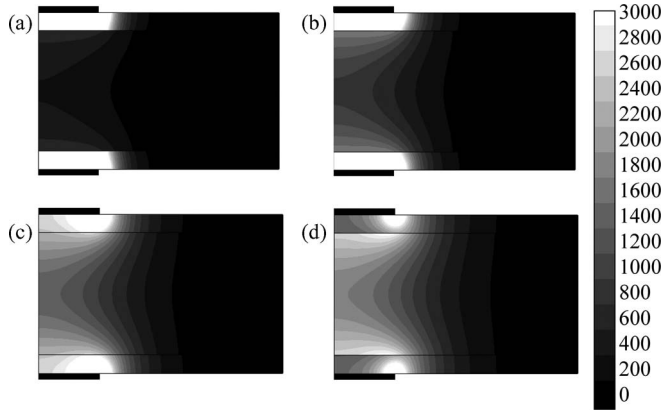

Fig. 5. Electric field, norm (V/cm) contours predicted by the FEM at the end of a 2-μs burst with an amplitude of 2600 V and a frequency of (a) 250 kHz, (b) 500 kHz, (c) 1 MHz, and (d) 2 MHz.

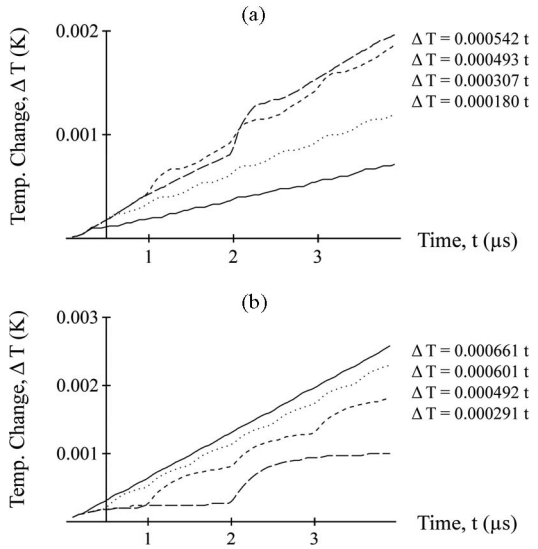

Fig. 6. Temperature changes predicted by the FEM at the center of the (a) skin and (b) fat for frequencies of 250 kHz (——), 500 kHz (- - -), 1 MHz (· · ·), and 2 MHz (–). Equations represent a linear fit to the data.

Fig. 5 shows the electric field distribution at the end of a 2-μs burst with various frequencies given in Table I. In each case, the maximum applied voltage was set to 2600 V (peak) in order to set up a voltage to distance ratio of 2000 V/cm between the electrodes (1.3-cm spacing). From the surface contour map, as frequency is increased, the electric field in the fat rises while the field in the skin drops. This trend extends to the point that at 2 MHz the field in the skin is lower than the fat, which is a direct result of the tissue dielectric properties at that frequency (greater conductivity and permittivity of skin as compared to fat). Therefore, high-frequency fields, are better suited to penetrate epithelial layers, such as the skin, and reach underlying tissue.

Temperature changes predicted by the FEM at the center of the skin and fat are shown in Fig. 6. In this case, a burst width of 4 μs was simulated in order to capture the trends in temperature development. Polarity of the 2-μs pulse (250 kHz) was switched between pulses to maintain consistency with the

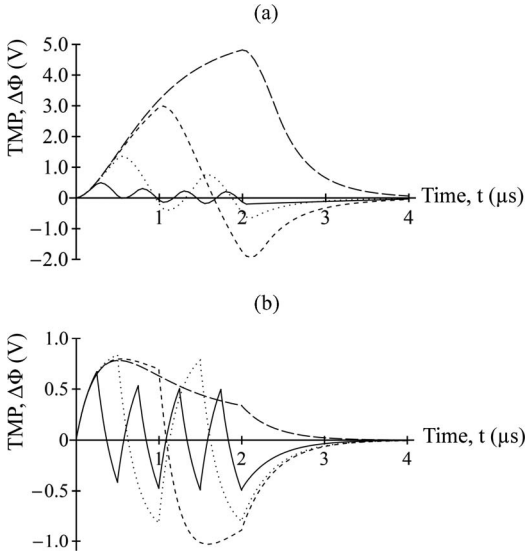

Fig. 7. TMP predicted by the FEM at the center of the (a) skin and (b) fat for frequencies of 250 kHz (——), 500 kHz (- – -), 1 MHz (· · ·), and 2 MHz (–).

other waveforms that are inherently bipolar. With respect to the skin, as the frequency of the applied field increases, the temperature rises at a slower rate. This is a consequence of the fact that the electric field within the skin also decreases with increasing frequency. In the case of the fat, the temperature rises at a faster rate when the frequency of the applied field is increased. At first glance, this seems to be detrimental; however, it is merely an indication that energy is preferentially being deposited into the fat at higher frequencies. Again, this can be correlated with the electric field profile. In both tissues, the sharp rises in temperature are due to the spikes in displacement current that occur at the onset and offset of each pulse (data not shown). The total temperature increase in all cases is less than 0.003 K for a burst width of 4 μs. As explained in Section IV, even for bursts of longer widths, the temperature increase is not enough to promote thermal damage.

TMP profiles as predicted by the FEM on a hypothetical cell at the center of the skin and fat for a 2-μs burst width are shown in Fig. 7. All measurements were taken at the pole ($\theta = 0$) to depict the maximum induced TMP around the cell. With respect to the skin, as the frequency of the applied field increases, the maximum oscillation amplitude of the TMP decreases. This occurs for two reasons. First, as seen in Fig. 5, the electric field in the skin decreases with increasing frequency. Second, as seen in Fig. 4, even with constant field amplitude, the TMP decreases with increasing frequency, because the time during which the membrane has to charge before the polarity switches is less at higher frequencies. In the case of the fat, the behavior is slightly more complex. At lower frequencies, a majority of the voltage drop occurs across the skin, resulting in a reduced electric field in the fat. This shielding effect is best shown in Fig. 7 along the 250-kHz trace. According to Fig. 4, at 250 kHz, the maximum TMP should be reached. However, due to the shielding effect from the skin, a reduction in the TMP prior to the polarity change is seen. This reduction in TMP can be alleviated by increasing the frequency of the applied field. However, the

TABLE IV
PULSE FREQUENCY–TMP COMPARISON IN THE FAT LAYER

Frequency (pulse duration)	Time (μs), |TMP| > 0.5 (V)	% of Pulse, |TMP| > 0.5 (V)
250 kHz (2 μs)	1.2	60
500 kHz (1 μs (×2))	1.9	95
1 MHz (500 ns (×4))	1.3	65
2 MHz (250 ns (×8))	0.1	5

tradeoff between increased frequency and reduced TMP is still evident at a frequency of 2 MHz (250-ns pulse duration).

IV. DISCUSSION

As mentioned, electric current associated with pulses longer than $\sim$1 μs is confined to extracellular spaces prior to the onset of electroporation (see Fig. 1) [30], [31]. This can be attributed to the migration of charges toward biological membranes following the application of an external electric field. The time required for a membrane to become charged to 63% of its steady-state value is defined as the charging time constant of the membrane τ_{pm}. Based on the analytical model for TMP in this study, the time constant of the plasma membrane for a constant field is 345 ns. Additionally, steady state is not reached until after 1 μs. Displacement currents across the plasma membrane allow organelles to be exposed to fields during the time that it takes the plasma membrane to reach steady state [32]. Once steady state is achieved, the counterfield developed along the plasma membrane due to the accumulation of charges is significant enough to shield the field from entering the cell, and current is directed through extracellular spaces. Only after permeabilization of the membrane does ionic conduction allow the field to re-enter the cell [45]. If extracellular current pathways between cells are reduced, as in layers of epithelial cells connected by tight junctions [19], the field is highly concentrated across the layer, and the extent of electroporation in underlying cells is reduced.

There is a balance between employing pulses that are delivered on a short enough timescale to flow through epithelial cells but are long enough to induce electroporation in underlying cells. The time constant of 345 ns falls between the 2 MHz (250-ns pulse duration) and 1 MHz (500-ns pulse duration) bursts. Further, the 500-kHz burst (1-μs pulse duration) is close to the time it takes the TMP to reach steady state. Table IV summarizes the results based on the time that the TMP on a hypothetical cell at the center of the fat layer is above 0.5 V. This amplitude was chosen such that even the highest frequency burst was above the set voltage level for a certain amount of time. The results would hold if the applied field was doubled and the voltage level was set to the 1-V threshold for pore formation, due to the linear dependence of TMP on the electric field. Based on this criterion, a frequency of 500 kHz is best suited to treat cells in the fat layer, followed by 1 MHz and 250 kHz. As frequency is increased, the dielectric properties and electric field distribution in the skin and fat become more macroscopically homogeneous, but above 1 MHz, the pulse duration is not adequate for the cell to charge.

According to *in vitro* experiments that utilize bipolar rectangular pulses, the typical burst width required to induce either reversible electroporation or IRE increases with the frequency of the applied field. For EGT, a 60-kHz bipolar square wave with a burst width of 400 μs and an amplitude of 1600 V/cm has a six times greater transfection efficiency than a 1-MHz bipolar square wave with equal amplitude and width [22]. In terms of IRE, a 60-kHz bipolar square wave with a burst width of 400 μs and an amplitude of 4000 V/cm results in 19% cell viability [22]. These results were obtained when a single burst was delivered to the sample, and we were unable to find any data on high-frequency electroporation with rectangular pulses that implemented multiple bursts. Similar to how multiple unipolar pulses are typically delivered in ECT, EGT, or IRE protocols to enhance the desired outcome [46], [47], multiple bipolar bursts would likely produce similar trends. Data are also available for burst sinusoidal waveforms in the frequency range of 2 kHz to 50 MHz [48], [49], but the results are inconclusive, and sinusoidal waveforms are less efficient than rectangular bipolar pulses for inducing electroporation [50].

The onset of protein denaturation and loss of cell structure occur above 318.15 K [51], which correlates with an increase in temperature of 8 K above physiological temperature. Using this information, we can calculate the maximum energy delivery period (number of pulses multiplied by pulse duration) for an amplitude of 2000 V/cm at each of the frequencies investigated using the trendlines generated by the FEM data (see Fig. 6). In the skin layer, heating is reduced by increasing the frequency of the applied field. This confirms our initial hypothesis that the potential for thermal damage in the skin is reduced when the frequency of the applied field is increased. At higher frequencies, the energy is preferentially deposited in the fat layer. For 2 MHz, the total energy delivery period required to cause an 8-K increase in temperature is 12 ms. An example treatment plan would then be 12, 1-ms bursts separated by a delay of 1 s. If the frequency is reduced to 500 kHz, which shows the greatest electroporation efficiency (see Table IV), the allowable energy delivery period increases to 16 ms, which would permit the delivery of an additional 4, 1-ms bursts before the onset of thermal damage. The restrictions could be increased if less conservative estimates are obtained that account for heat dissipation between pulses and heat convection at the tissue surface [52]. These projected protocols represent a maximum, and it is likely that the desired effects will be induced at a significantly lower energy [46], [47].

This work has been geared toward developing a better way to deposit electrical energy through the skin, but similar structures are seen in underlying tissue layers. For example, pancreatic ducts are lined by epithelial cells that can give rise to tumors, and tumors of the breast are often surrounded by fatty tissue [53]. These features will play an important role in how the electric field is distributed within the tissue. This complicates treatment planning, where the goal is to predict the electric field distribution in the tissue in order to select an appropriate pulsing protocol. A benefit of high-frequency bursts with nanosecond-order pulses is their ability to penetrate tissue heterogeneities, resulting in more predictable treatment outcomes. These pulsing

protocols would then be useful if implemented not only with plate electrodes, but also with the alternative needle electrodes. Additionally, IRE treatments are often preceded by a nerve blocker or paralytic agent to minimize muscle contraction during treatment. *Ex vivo* muscle stimulation experiments indicate that the electric field threshold required to induce muscle contractions increases as the pulse duration decreases [54]. Therefore, the nanosecond-order pulses proposed here may allow the use of these paralytic agents to be averted.

Detailed geometric considerations, such as the individual tissue layers comprising the skin, layers of conductive gel used clinically to improve electrical contact, and the outer curvature of a typical skin fold, have been ignored in order to simplify our initial investigation. To be conservative in our estimates, dry skin was used in the model and the use of a conductive gel to wet the skin was not employed. The use of a gel and the properties of wet skin should further enhance the benefits of this technique. In this initial study, our goal was to elicit the benefit of high-frequency electroporation for overcoming impedance barriers without superimposing the effects from geometric intricacies and electroporation nonlinearities in the analysis. Future work should be directed toward expanding this focus.

In the analytical model for TMP, it was assumed that the electric field was applied across an isolated cell. In reality, tissues comprise a network of cells that create nonuniformities in the electric field at the microscopic level. In general, as the packing density of cells increases, the TMP decreases [55]. Thus, the overall trends presented here are valid, but the specific values for TMP should be scaled accordingly if the packing density is known. Additionally, dynamic dielectric tissue properties were neglected in both the analytical model and the FEM. At the macroscale, changes in tissue dielectric properties due to electroporation [14], [15] and temperature should be incorporated in the FEM. At the microscale, in order to prevent the development of unrealistic TMP in regions of high electric field, as seen here in the skin layer, the analytical calculation of TMP could be supplemented with equations for pore formation. Pores allow current to flow through the membrane, which limits the increase in TMP [23]–[25].

V. Conclusion

Our results indicate that bursts of bipolar, nanosecond pulses can maintain a critical TMP beneath epithelial layers, while minimizing heating in the epithelial layer. This has to do with the ability of nanosecond pulses to achieve a macroscopically homogeneous field distribution in a heterogeneous system. At high frequencies, tissues with a low passive DC conductivity become more conductive. This has implications not only for skin, as presented here, but also for other tissues, such as bone and lung. Experimental work needs to be conducted to optimize the total burst width, time between bursts, and total number of bursts required for inducing electroporation with high-frequency rectangular pulses. This study serves as the first step in assessing the feasibility of implementing high-frequency bipolar pulses for tissue electroporation. Based on the theoretical analysis presented here, the predicted benefits of high-frequency electroporation will translate experimentally to enhance the efficacy of ECT, EGT, or IRE for treating electrically isolated tumors, such as those encapsulated by the skin, pancreas, breast, bone, or lung.

Acknowledgment

The authors would like to thank P. A. Garcia for his expertise in modeling with Comsol, J. L. Caldwell for his knowledge on high-frequency electronics, and G. S. Brown, R. E. Neal II, and S. L. Matrangola for their general support.

References

[1] J. C. Weaver and Y. A. Chizmadzhev, "Theory of electroporation: A review," *Bioelectrochem. Bioener.*, VA, vol. 41, pp. 135–160, Dec. 1996.
[2] I. G. Abidor, V. B. Arakelyan, L. V. Chernomordik, Y. A. Chizmadzhev, V. F. Pastushenko, and M. P. Tarasevich, "Electric breakdown of bilayer lipid-membranes 1. Main experimental facts and their qualitative discussion," *Bioelectrochem. Bioenerg.*, vol. 6, pp. 37–52, 1979.
[3] R. Benz, F. Beckers, and U. Zimmermann, "Reversible electrical breakdown of lipid bilayer membranes: A charge-pulse relaxation study," *J. Membr. Biol.*, vol. 48, pp. 181–204, Jul. 16, 1979.
[4] E. Neumann and K. Rosenheck, "Permeability changes induced by electric impulses in vesicular membranes," *J. Membr. Biol.*, vol. 10, pp. 279–90, Dec. 29, 1972.
[5] J. Teissie and T. Y. Tsong, "Electric-field induced transient pores in phospholipid-bilayer vesicles," *Biochem.*, vol. 20, pp. 1548–1554, 1981.
[6] U. Zimmermann, G. Pilwat, and F. Riemann, "Dielectric breakdown of cell membranes," *Biophys. J*, vol. 14, pp. 881–899, Nov. 1974.
[7] K. Kinosita and T. Y. Tsong, "Formation and resealing of pores of controlled sizes in human erythrocyte-membrane," *Nature*, vol. 268, pp. 438–441, 1977.
[8] T. K. Wong and E. Neumann, "Electric field mediated gene transfer," *Biochem. Biophys. Res. Commun.*, vol. 107, pp. 584–587, Jul. 30, 1982.
[9] B. Rubinsky, "Irreversible electroporation in medicine," *Technol. Cancer Res. Treat.*, vol. 6, pp. 255–260, Aug. 2007.
[10] R. V. Davalos and B. Rubinsky, "Temperature considerations during irreversible electroporation," *Int. J. Heat Mass Transfer*, vol. 51, pp. 5617–5622, Nov. 2008.
[11] L. M. Mir and S. Orlowski, "Mechanisms of electrochemotherapy," *Adv. Drug Deliv. Rev.*, vol. 35, pp. 107–118, Jan. 4, 1999.
[12] R. V. Davalos, L. M. Mir, and B. Rubinsky, "Tissue ablation with irreversible electroporation," *Ann. Biomed. Eng.*, vol. 33, pp. 223–231, Feb. 2005.
[13] R. Nuccitelli, X. Chen, A. G. Pakhomov, W. H. Baldwin, S. Sheikh, J. L. Pomicter, W. Ren, C. Osgood, R. J. Swanson, J. F. Kolb, S. J. Beebe, and K. H. Schoenbach, "A new pulsed electric field therapy for melanoma disrupts the tumor's blood supply and causes complete remission without recurrence," *Int. J. Cancer*, vol. 125, pp. 438–45, Jul. 15, 2009.
[14] N. Pavselj, V. Preat, and D. Miklavcic, "A numerical model of skin electroporation as a method to enhance gene transfection in skin," in *Proc. 11th Mediterranean Conf. Med. Biol. Eng. Comput.*, 2007, vol. 16, pp. 597–601.
[15] N. Pavselj, Z. Bregar, D. Cukjati, D. Batiuskaite, L. M. Mir, and D. Miklavcic, "The course of tissue permeabilization studied on a mathematical model of a subcutaneous tumor in small animals," *IEEE Trans. Biomed. Eng.*, vol. 52, no. 8, pp. 1373–1381, Aug. 2005.
[16] T. Lamsa, H. Jin, J. Mikkonen, J. Laukkarinen, J. Sand, and I. Nordback, "Biocompatibility of a new bioabsorbable radiopaque stent material ($BaSO_4$ containing poly-LD-lactide) in the rat pancreas," *Pancreatology*, vol. 6, pp. 301–305, 2006.
[17] T. Lämsä, H. Jin, P. H. Nordback, J. Sand, T. Luukkaala, and I. Nordback, "Pancreatic Injury Response is Different Depending on the Method of Resecting the Parenchyma," *J. Surgical Res.*, vol. 154, no. 2, pp. 203–211, 2009.
[18] R. C. Lee and R. D. Astumian, "The physicochemical basis for thermal and non-thermal 'burn' injuries," *Burns*, vol. 22, pp. 509–519, Nov. 1996.
[19] D. M. Jones, R. H. Smallwood, D. R. Hose, B. H. Brown, and D. C. Walker, "Modelling of epithelial tissue impedance measured using three different designs of probe," *Physiol. Meas.*, vol. 24, pp. 605–623, May 2003.
[20] T. R. Gowrishankar, A. T. Esser, Z. Vasilkoski, K. C. Smith, and J. C. Weaver, "Microdosimetry for conventional and supra-electroporation

in cells with organelles," *Biochem. Biophys. Res. Commun.*, vol. 341, pp. 1266–1276, Mar. 24, 2006.
[21] D. C. Chang, "Cell poration and cell-fusion using an oscillating electric-field," *Biophys. J.*, vol. 56, pp. 641–652, Oct. 1989.
[22] E. Tekle, R. D. Astumian, and P. B. Chock, "Electroporation by using bipolar oscillating electric-field—an improved method for DNA transfection of Nih 3t3 cells," *Proc. Nat. Acad. Sci. U.S.A.*, vol. 88, pp. 4230–4234, May 1991.
[23] S. Talele and P. Gaynor, "Non-linear time domain model of electropermeabilization: Response of a single cell to an arbitrary applied electric field," *J. Electrostatics*, vol. 65, pp. 775–784, Nov. 2007.
[24] S. Talele and P. Gaynor, "Non-linear time domain model of electropermeabilization: Effect of extracellular conductivity and applied electric field parameters," *J. Electrostatics*, vol. 66, pp. 328–334, May 2008.
[25] S. Talele, P. Gaynor, M. J. Cree, and J. van Ekeran, "Modelling single cell electroporation with bipolar pulse parameters and dynamic pore radii," *J. Electrostatics*, vol. 68, pp. 261–274, Jun. 2010.
[26] T. Kotnik, L. M. Mir, K. Flisar, M. Puc, and D. Miklavcic, "Cell membrane electropermeabilization by symmetrical bipolar rectangular pulses. Part I: Increased efficiency of permeabilization," *Bioelectrochemistry*, vol. 54, pp. 83–90, Aug. 2001.
[27] T. Kotnik, D. Miklavcic, and L. M. Mir, "Cell membrane electropermeabilization by symmetrical bipolar rectangular pulses. Part II. Reduced electrolytic contamination," *Bioelectrochemistry*, vol. 54, pp. 91–95, Aug. 2001.
[28] T. R. Gowrishankar, C. Stewart, and J. C. Weaver, "Electroporation of a multicellular system: Asymptotic model analysis," in *Proc. IEEE 26th Annu. Int. Conf. Eng. Med. Biol. Soc.*, 2004, vol. 26, pp. 5444–5446.
[29] T. R. Gowrishankar and J. C. Weaver, "An approach to electrical modeling of single and multiple cells," *Proc. Nat. Acad. Sci. U.S.A.*, vol. 100, pp. 3203–3208, Mar. 18, 2003.
[30] A. T. Esser, K. C. Smith, T. R. Gowrishankar, and J. C. Weaver, "Towards solid tumor treatment by irreversible electroporation: intrinsic redistribution of fields and currents in tissue," *Technol. Cancer Res. Treatment*, vol. 6, pp. 261–74, Aug. 2007.
[31] A. Ivorra, Ed.,,"Tissue Electroporation as a Bioelectric Phenomenon: Basic Concepts," Irreversible Electroporation. Berlin, Germany: Springer, 2010.
[32] A. T. Esser, K. C. Smith, T. R. Gowrishankar, and J. C. Weaver, "Towards Solid Tumor Treatment by Nanosecond Pulsed Electric Fields," *Technol. Cancer Res. Treatment*, vol. 8, pp. 289–306, Aug. 2009.
[33] L. M. Mir, P. Devauchelle, F. Quintin-Colonna, F. Delisle, S. Doliger, D. Fradelizi, J. Belehradek, and S. Orlowski, "First clinical trial of cat soft-tissue sarcomas treatment by electrochemotherapy," *Brit. J. Cancer*, vol. 76, pp. 1617–1622, Dec. 1997.
[34] S. Gabriel, R. W. Lau, and C. Gabriel, "The dielectric properties of biological tissues. 2. Measurements in the frequency range 10 Hz to 20 GHz," *Phys. Med. Biol.*, vol. 41, pp. 2251–2269, Nov. 1996.
[35] M. T. Chen, C. Jiang, P. T. Vernier, Y. H. Wu, and M. A. Gundersen, "Two-dimensional nanosecond electric field mapping based on cell electropermeabilization," *PMC Biophys.*, vol. 2, p. 9, 2009.
[36] J. F. Edd and R. V. Davalos, "Mathematical modeling of irreversible electroporation for treatment planning," *Technol. Cancer Res. Treatment*, vol. 6, pp. 275–286, Aug. 2007.
[37] R. E. Neal and R. V. Davalos, "The feasibility of irreversible electroporation for the treatment of breast cancer and other heterogeneous systems," *Ann. Biomed. Eng.*, vol. 37, pp. 2615–2625, Dec. 2009.
[38] N. Yousif, R. Bayford, and X. Liu, "The influence of reactivity of the electrode-brain interface on the crossing electric current in therapeutic deep brain stimulation," *Neuroscience*, vol. 156, pp. 597–606, Oct. 15, 2008.
[39] H. H. Pennes, "Analysis of tissue and arterial blood temperatures in the resting human forearm," *J. Appl. Physiol.*, vol. 1, pp. 93–122, Aug. 1948.
[40] D. Fiala, K. J. Lomas, and M. Stohrer, "A computer model of human thermoregulation for a wide range of environmental conditions: The passive system," *J. Appl. Physiol.*, vol. 87, pp. 1957–1972, Nov. 1999.
[41] C. G. Yao, D. B. Mo, C. X. Li, C. X. Sun, and Y. Mi, "Study of transmembrane potentials of inner and outer membranes induced by pulsed-electric-field model and simulation," *IEEE Trans. Plasma Sci.*, vol. 35, no. 5, pp. 1541–1549, Oct. 2007.
[42] Q. Hu, S. Viswanadham, R. P. Joshi, K. H. Schoenbach, S. J. Beebe, and P. F. Blackmore, "Simulations of transient membrane behavior in cells subjected to a high-intensity ultrashort electric pulse," *Phys. Rev. E*, vol. 71, no. 3, p. 031914, Mar. 2005.
[43] T. Kotnik and D. Miklavcic, "Theoretical evaluation of the distributed power dissipation in biological cells exposed to electric fields," *Bioelectromagn.*, vol. 21, pp. 385–394, Jul. 2000.
[44] T. Kotnik and D. Miklavcic, "Theoretical evaluation of voltage inducement on internal membranes of biological cells exposed to electric fields," *Biophys. J.*, vol. 90, pp. 480–491, Jan. 2006.
[45] J. F. Kolb, S. Kono, and K. H. Schoenbach, "Nanosecond pulsed electric field generators for the study of subcellular effects," *Bioelectromagn.*, vol. 27, pp. 172–187, Apr. 2006.
[46] J. Belehradek, S. Orlowski, L. H. Ramirez, G. Pron, B. Poddevin, and L. M. Mir, "Electropermeabilization of cells in tissues assessed by the qualitative and quantitative electroloading of bleomycin," *Biochimica Et Biophysica Acta-Biomembranes*, vol. 1190, pp. 155–163, Feb. 23, 1994.
[47] P. A. Garcia, J. H. Rossmeisl, R. E. Neal, T. L. Ellis, J. D. Olson, N. Henao-Guerrero, J. Robertson, and R. V. Davalos, "Intracranial nonthermal irreversible electroporation: *In vivo* analysis," *J. Membrane Biol.*, vol. 236, pp. 127–136, Jul. 2010.
[48] D. W. Jordan, R. M. Gilgenbach, M. D. Uhler, L. H. Gates, and Y. Y. Lau, "Effect of pulsed, high-power radiofrequency radiation on electroporation of mammalian cells," *IEEE Trans. Plasma Sci.*, vol. 32, no. 4, pp. 1573–1578, Aug. 2004.
[49] S. Katsuki, N. Nomura, H. Koga, H. Akiyama, I. Uchida, and S.-I. Abe, "Biological effects of narrow band pulsed electric fields," *IEEE Trans Dielectr. Electr. Insulat.*, vol. 14, no. 3, pp. 663–668, Jun. 2007.
[50] T. Kotnik, G. Pucihar, M. Rebersek, D. Miklavcic, and L. M. Mir, "Role of pulse shape in cell membrane electropermeabilization," *Biochimica Et Biophysica Acta-Biomembranes*, vol. 1614, pp. 193–200, Aug. 7, 2003.
[51] A. J. Bilchik, T. F. Wood, and D. P. Allegra, "Radiofrequency ablation of unresectable hepatic malignancies: Lessons learned," *Oncologist*, vol. 6, pp. 24–33, 2001.
[52] I. Lackovic, R. Magjarevic, and D. Miklavcic, "Three-dimensional finite-element analysis of joule heating in electrochemotherapy and in vivo ge," *IEEE Trans. Dielectr. Electr. Insul.*, vol. 16, no. 5, pp. 1338–1347, Oct. 2009.
[53] A. J. Surowiec, S. S. Stuchly, J. R. Barr, and A. Swarup, "Dielectric-properties of breast-carcinoma and the surrounding tissues," *IEEE Trans. Biomed. Eng.*, vol. 35, no. 4, pp. 257–263, Apr. 1988.
[54] W. R. Rogers, J. H. Merritt, J. A. Comeaux, C. T. Kuhnel, D. F. Moreland, D. G. Teltschik, J. H. Lucas, and M. R. Murphy, "Strength-duration curve for an electrically excitable tissue extended down to near 1 nanosecond," *IEEE Trans. Plasma Sci.*, vol. 32, no. 4, pp. 1587–1599, Aug. 2004.
[55] R. Susil, D. Semrov, and D. Miklavcic, "Electric field-induced transmembrane potential depends on cell density and organization," *Electro Magnetobiol.*, vol. 17, pp. 391–399, 1998.

Christopher B. Arena received the B.S. degree in biomedical engineering from the University of Virginia, Charlottesville, in 2008. He is a Graduate Student at the Virginia Tech-Wake Forest University School of Biomedical Engineering and Sciences.

He works in the Bioelectromechanical Systems Laboratory at Virginia Polytechnic Institute and State University, Blacksburg. His research interests include high frequency electroporation and irreversible electroporation combined with nanoparticles for cancer treatment.

Michael B. Sano received the B.S. degree in mathematics and electrical engineering from the University at Buffalo in 2007 and the M.S. degree in engineering mechanics from Virginia Polytechnic Institute and State University, Blacksburg. He is a Graduate Student at the Virginia Tech-Wake Forest University School of Biomedical Engineering and Sciences.

He works in the Bioelectromechanical Systems Laboratory at Virginia Polytechnic Institute and State University. His research interests include contactless dielectrophoresis and tissue decellularization with irreversible electroporation.

Marissa Nichole Rylander received the B.S. degree in 2000, M.S. degree in 2002, and the Ph.D. degree in 2005 from the University of Texas-Austin.

She is an Assistant Professor jointly appointed in the Virginia Tech - Wake Forest University School of Biomedical Engineering and Sciences and the Virginia Tech Department of Mechanical Engineering. She directs the Bioheat Transfer and Nanotherapeutics Laboratory at Virginia Tech. Her research interests include nanotechnology for therapeutics and heat shock protein expression in tumors.

Rafael V. Davalos (M'05) received the B.S. degree in 1994 from Cornell University, Ithaca, NY and the Ph.D. degree in 2002 from the University of California, Berkeley.

He is an Assistant Professor in the Virginia Tech - Wake Forest University School of Biomedical Engineering and Sciences. He directs the Bioelectromechanical Systems Laboratory and holds Adjunct Appointments at the Wake Forest Institute of Regenerative Medicine, the Wake Forest University Comprehensive Cancer Center, and the Virginia Tech Engineering Science and Mechanics Department.

BioMedical Engineering OnLine

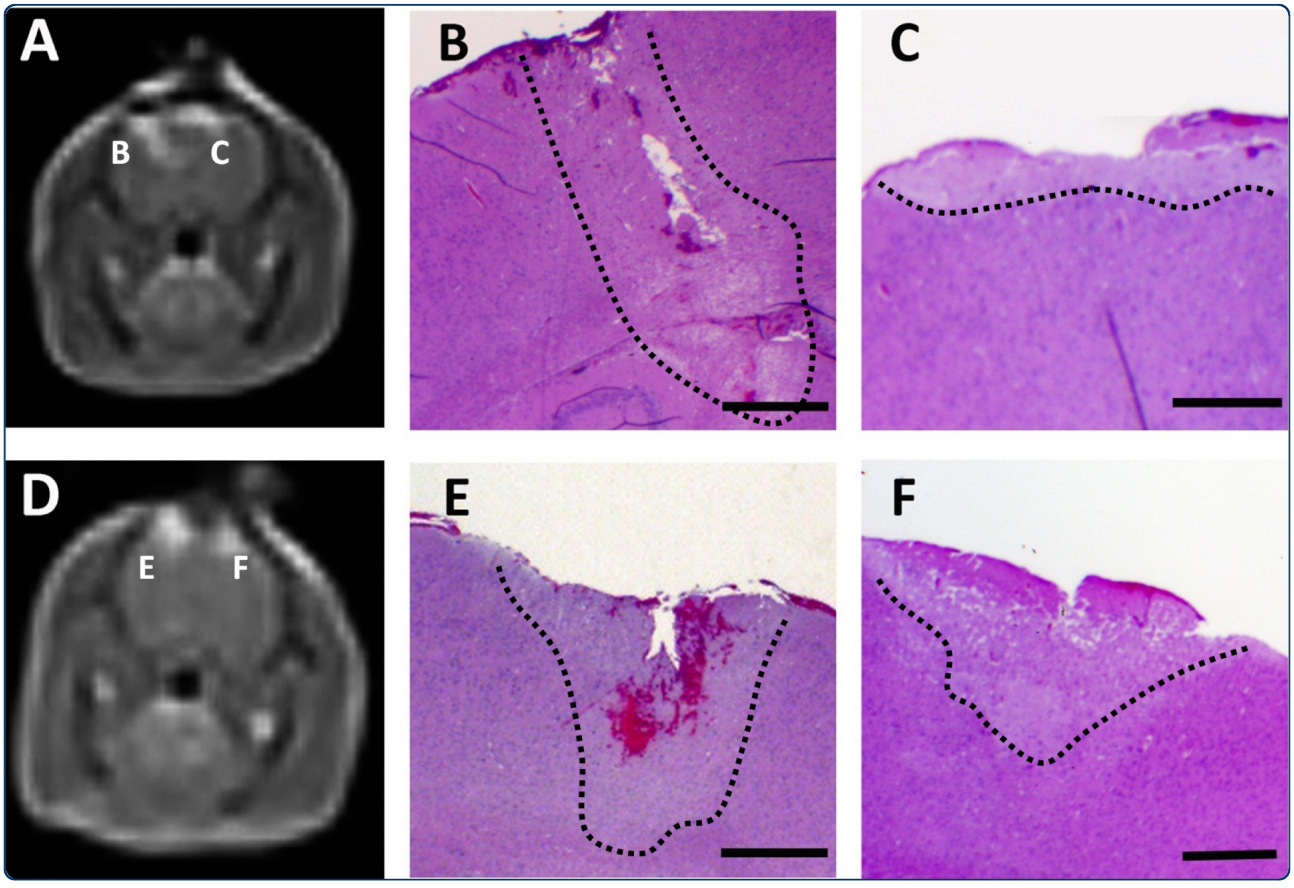

High-frequency irreversible electroporation (H-FIRE) for non-thermal ablation without muscle contraction

Arena *et al.*

BioMed Central

Arena *et al. BioMedical Engineering OnLine* 2011, **10**:102
http://www.biomedical-engineering-online.com/content/10/1/102 (21 November 2011)

BioMedical Engineering OnLine

RESEARCH Open Access

High-frequency irreversible electroporation (H-FIRE) for non-thermal ablation without muscle contraction

Christopher B Arena[1], Michael B Sano[1], John H Rossmeisl Jr[2], John L Caldwell[3], Paulo A Garcia[1], Marissa Nichole Rylander[4] and Rafael V Davalos[1*]

* Correspondence: davalos@vt.edu
[1]Bioelectromechanical Systems Lab, Virginia Tech-Wake Forest University School of Biomedical Engineering and Sciences, 330 ICTAS Building (MC0298), Blacksburg, VA. 24061, USA
Full list of author information is available at the end of the article

Abstract

Background: Therapeutic irreversible electroporation (IRE) is an emerging technology for the non-thermal ablation of tumors. The technique involves delivering a series of unipolar electric pulses to permanently destabilize the plasma membrane of cancer cells through an increase in transmembrane potential, which leads to the development of a tissue lesion. Clinically, IRE requires the administration of paralytic agents to prevent muscle contractions during treatment that are associated with the delivery of electric pulses. This study shows that by applying high-frequency, bipolar bursts, muscle contractions can be eliminated during IRE without compromising the non-thermal mechanism of cell death.

Methods: A combination of analytical, numerical, and experimental techniques were performed to investigate high-frequency irreversible electroporation (H-FIRE). A theoretical model for determining transmembrane potential in response to arbitrary electric fields was used to identify optimal burst frequencies and amplitudes for *in vivo* treatments. A finite element model for predicting thermal damage based on the electric field distribution was used to design non-thermal protocols for *in vivo* experiments. H-FIRE was applied to the brain of rats, and muscle contractions were quantified via accelerometers placed at the cervicothoracic junction. MRI and histological evaluation was performed post-operatively to assess ablation.

Results: No visual or tactile evidence of muscle contraction was seen during H-FIRE at 250 kHz or 500 kHz, while all IRE protocols resulted in detectable muscle contractions at the cervicothoracic junction. H-FIRE produced ablative lesions in brain tissue that were characteristic in cellular morphology of non-thermal IRE treatments. Specifically, there was complete uniformity of tissue death within targeted areas, and a sharp transition zone was present between lesioned and normal brain.

Conclusions: H-FIRE is a feasible technique for non-thermal tissue ablation that eliminates muscle contractions seen in IRE treatments performed with unipolar electric pulses. Therefore, it has the potential to be performed clinically without the administration of paralytic agents.

Keywords: Bipolar pulses, Biphasic pulses, Focal ablation, Focal therapy, Heterogeneous tissue, Nerve stimulation, Thermal damage, Electropermeabilization, Electrochemotherapy, nanosecond Pulsed Electric Field

Background

Irreversible electroporation (IRE) has recently emerged as a non-thermal treatment modality to destroy tumors [1-3] and other non-cancerous pathologies [4-6]. The protocol involves delivering a series of short and intense electric pulses through electrodes inserted directly into, or placed around, the target tissue. The pulses are designed to generate an electric field between the electrodes capable of inducing a rapid buildup of charge across the plasma membrane of cells, commonly referred to as a transmembrane potential (TMP). Once the TMP reaches a critical voltage, it is thought that electrically conductive pores form in the membrane in attempt to prevent permanent damage by shunting current and limiting further TMP rise [7]. If the pulse amplitude and duration are tuned to permit pore resealing, and cell viability is maintained following exposure, the process is categorized as reversible electroporation. This phenomenon has shown great promise in biotechnology and in medicine as a cancer therapy when combined with chemotherapeutic agents (Electrochemotherapy) [8,9] or plasmid DNA (Electrogenetherapy) [10]. IRE results if excess current is applied, and the extent of pore formation is such that the cell cannot recover. Macroscopically, this results in the creation of a tissue lesion without a dependence on thermal processes or the requirement of adjuvant drugs [1,4,11].

Despite requiring electric field strengths on the order of 1000 V/cm, the extent of thermal damage during IRE is negligible due to the short duration of the pulses (on the order of 100 μs) [1,12,13], the low repetition rate of the pulses (on the order of 1 Hz) [14], and the brief treatment time (a few minutes) [14]. These parameters mitigate the associated Joule heating in a majority of the treated tissue, excluding localized regions of elevated electric field adjacent to electrode edges. Due to its inherent non-thermal nature, protein rich tissue components, such as extracellular matrix, are unaffected by IRE. This promotes sparing of sensitive structures, including major blood vessel [5] and nerve [15] architecture. Further, because the mechanism of cell death is non-thermal and relies mainly on the induced TMP, treatment outcomes are not subject to heat sink effects from nearby blood vessels [16]. The induced TMP is predominantly a function of the electric field distribution in the tissue, in addition to cell specific variables. Therefore, knowledge of the field distribution can be used to accurately predict the lesion volume [17,18], which forms with a sharp delineation between treated and unaffected areas in homogenous tissue [4].

In heterogeneous tissues, information on multiple tissue types, including their electrical properties and often times intricate geometrical arrangement complicates treatment planning. For example, subcutaneous tumors treated over the skin non-invasively with IRE using plate electrodes may experience sub-lethal electric fields. This can be attributed to the low conductivity of the skin, which results in a large potential drop across it that increases the likelihood of thermal damage [19]. Up until this point, IRE pulses have been unipolar, meaning that they have a strong DC frequency component (0 Hz). Recently, we have theoretically shown that by delivering high-frequency, bipolar bursts, the impedance barrier of the skin or other epithelial layers can be overcome [20]. Specifically, squarewave bursts with a center frequency around 500 kHz (duration of single polarity equal to one microsecond) produce more homogenous, predictable electric field distributions in a heterogeneous geometry and reduce the potential for thermal damage. This is due to the fact that tissue contains both resistive and capacitive

components, resulting in a lower bulk electrical impedance as the frequency of the applied field is increased.

One aspect of the current work was to build on our theoretical results and investigate the *in vivo* potential of high-frequency, bipolar bursts to kill tissue through IRE. As opposed to traditional IRE that uses unipolar pulses (Figure 1A) delivered at a repetition rate of one pulse per second, we postulate that IRE can be achieved with a series of high-frequency, bipolar bursts (Figure 1B and 1C) delivered at the same repetition rate. To the best of our knowledge, these types of waveforms have not been investigated for therapeutic IRE applications. Here, we demonstrate lesion development in a rat brain model at center frequencies up to 500 kHz, which maintain the potential to overcome impedance barriers posed by epithelial layers [20]. Similar waveforms have been studied *in vitro* for reversible applications of electroporation, and were shown to counterbalance both electrolytic reactions for the prevention of electrode breakdown [21] and asymmetrical electroporation caused by the resting TMP [22]. Additionally, for a constant electric field applied to cell suspensions or monolayers, as the center frequency of the squarewave is increased up to 1 MHz (duration of single polarity equal to 500 ns), cell death decreases [23]. We explore this trend *in silico* with an analytical model that predicts the TMP in response to an arbitrary electric field and *in vivo* with the treatment of brain tissue using high-frequency IRE (H-FIRE) with bipolar bursts at frequencies of 250 kHz and 500 kHz.

In conjunction with investigating the ability of H-FIRE to kill tissue, this work serves to evaluate its potential for reducing nerve stimulation. Currently, clinical applications of IRE require the administration of general anesthesia and paralytic agents in order to eliminate muscle contractions during each pulse [24]. In some cases, without a sufficient dose of the paralytic agent, muscle contractions are still visible [3]. Muscle contractions may affect the location of implanted needle electrodes, which can invalidate treatment planning algorithms and prove harmful in treatments near vital structures. The threshold for nerve stimulation increases as the center frequency of bipolar waveforms is increased [25]. In this study, an accelerometer based recording system was

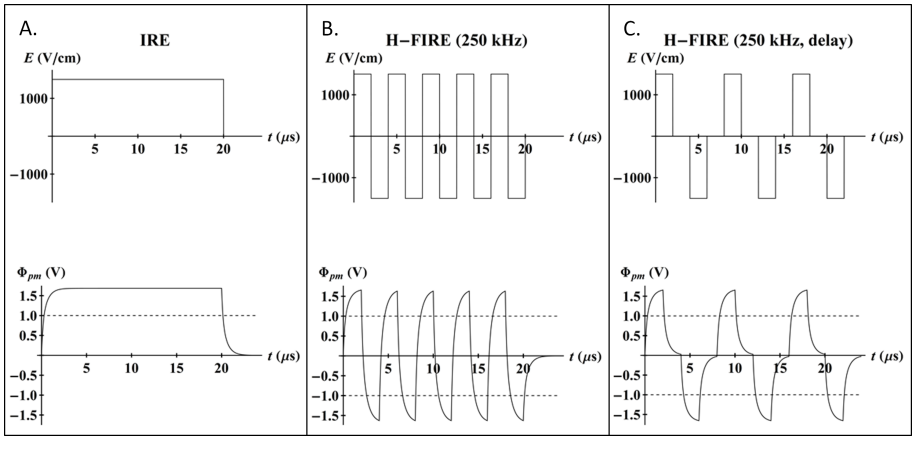

Figure 1 Characteristic waveforms of IRE and H-FIRE with the corresponding TMP development across the plasma membrane (Φ_{pm}). The 1500 V/cm unipolar pulse (A) causes the TMP to rise above the critical threshold for IRE (1 V, dashed line). The 1500 V/cm bipolar burst without a delay (B) and with a delay (C) causes the TMP to oscillate around the same critical threshold.

used to quantify muscle contractions during conventional IRE with unipolar pulses and H-FIRE at frequencies of 250 kHz and 500 kHz. Our results indicate that H-FIRE can non-thermally ablate tissue without causing muscle contractions. The non-thermal nature of the treatment is confirmed through both histological comparison to IRE controls and the development of a finite element model (FEM) for evaluating potential thermal damage in H-FIRE therapy of the brain.

Methods

Analytical Modeling of Transmembrane Potential

TMP development in response to a high-frequency electric field has been described in detail for a spherical cell with an organelle by Kotnik and Miklavčič [26]. Here we extend this model to include squarewave bursts with a delay between the positive polarity and negative polarity pulses. This delay was implemented experimentally as a protective measure for the MOSFET based pulse generation system described below. Under the assumption that cells can be represented by dielectric shells containing and surrounded by a conductive medium, the spatial distribution of electric potential (Φ) in a uniform electric field is described by the general solution to the Laplace equation for an arbitrary number of concentric shells [27]:

$$\Phi(r,\theta) = \left(A_i r + \frac{B_i}{r^2}\right)\cos(\theta) \tag{1}$$

where r is the distance from the origin to a point on the cell, θ is the angle between the electric field and a point on the cell, and A and B are constants specific to different cellular regions (i), including the extracellular space (e), plasma membrane (pm), cytoplasm (c), nuclear envelope (ne), and nucleoplasm (n). The constants are determined by solving the boundary conditions of continuity of electric potential (Eq. 2, 3, 4, 5) and electric current density (Eq. 6, 7, 8, 9), in addition to the assumptions of a finite field at $r = 0$ and a uniform field at $r = \infty$. In order to accurately predict the TMP in a time-varying electric field, the admittivity operator ($\Lambda_i = \sigma_i + \varepsilon_i (\partial/\partial t)$) is used in the formulation for the boundary conditions [28]:

$$\Phi_n(R_n - d_{ne}, \theta) = \Phi_{ne}(R_n - d_{ne}, \theta) \tag{2}$$

$$\Phi_{ne}(R_n, \theta) = \Phi_c(R_n, \theta) \tag{3}$$

$$\Phi_c(R_c - d_{pm}, \theta) = \Phi_{pm}(R_c - d_{pm}, \theta) \tag{4}$$

$$\Phi_{pm}(R_c, \theta) = \Phi_e(R_c, \theta) \tag{5}$$

$$\Lambda_n \left.\frac{\partial \Phi_n}{\partial r}\right|_{R_n - d_{ne}} = \Lambda_{ne} \left.\frac{\partial \Phi_{ne}}{\partial r}\right|_{R_n - d_{ne}} \tag{6}$$

$$\Lambda_{ne} \left.\frac{\partial \Phi_{ne}}{\partial r}\right|_{R_n} = \Lambda_c \left.\frac{\partial \Phi_c}{\partial r}\right|_{R_n} \tag{7}$$

$$\Lambda_c \left.\frac{\partial \Phi_c}{\partial r}\right|_{R_c - d_{pm}} = \Lambda_{pm} \left.\frac{\partial \Phi_{pm}}{\partial r}\right|_{R_c - d_{pm}} \tag{8}$$

$$\Lambda_{pm} \left.\frac{\partial \Phi_{pm}}{\partial r}\right|_{R_c} = \Lambda_e \left.\frac{\partial \Phi_e}{\partial r}\right|_{R_c} \tag{9}$$

where d represents membrane thickness, R represents radius, and ε and σ in the admittivity operator are the dielectric permittivity and conductivity, respectively, of the different cellular regions (Table 1). To avoid working with differential operators, the admittivity operator is transformed into the frequency domain ($\Lambda_i = \sigma_i + s\varepsilon_i$), where s is the complex frequency ($j\omega$) of the applied field. The resulting solutions for TMP ($\Delta\Phi$) across the plasma membrane and nuclear envelope can then be expressed as [28]:

$$\Delta\Phi_{pm}(s) = \Phi_e(R_c, \theta) - \Phi_c(R_c - d_{pm}, \theta) = H_{pm}(s)\, E(s)\, \cos(\theta) \tag{10}$$

$$\Delta\Phi_{ne}(s) = \Phi_c(R_n, \theta) - \Phi_n(R_n - d_{ne}, \theta) = H_{ne}(s)\, E(s)\, \cos(\theta) \tag{11}$$

where $H_{pm}(s)$ and $H_{ne}(s)$ are transfer functions that reflect the geometric and dielectric properties of the various cellular regions, the exact formulations of which are given in detail in [26]. $E(s)$ was obtained by taking the Laplace transform ($\mathcal{L}$) of the time-varying electric field, which was composed of a series of step functions. Equations 10 and 11 were solved in Wolfram Mathematica 8.0 (Champaign, IL, USA), and the inverse Laplace Transform ($\mathcal{L}^{-1}$) was taken to produce the time course of TMP in response to bipolar pulses with various frequencies.

Numerical Modeling of Temperature and Thermal Damage

A 3D finite element model (FEM) for calculating the temperature and potential thermal damage in brain tissue during IRE has been described in detail by Garcia *et al*. [29]. A similar model has been developed here in COMSOL Multiphysics 4.2 (Stockholm, Sweden) for predicting the thermal response to the *in vivo* H-FIRE treatments. Specifically, the electric potential distribution in the tissue was obtained by solving the time-harmonic continuity equation:

Table 1 Parameter values for TMP simulation

Quantity	Parameter	Value	Units	Reference
Conductivity	σ_e	1.2	S m^{-1}	[50]
	σ_{pm}	3×10^{-7}		[51]
	σ_c	0.3		[52]
	σ_{ne}	3×10^{-7}		set equal to σ_{pm}
	σ_n	0.3		set equal to σ_c
Permittivity	ε_e	6.4×10^{-10}	A s V^{-1} m^{-1}	[53]
	ε_{pm}	4.4×10^{-11}		[51]
	ε_c	6.4×10^{-10}		[53]
	ε_{ne}	4.4×10^{-11}		set equal to ε_{pm}
	ε_n	6.4×10^{-10}		[53]
Radius	R_c	7.5×10^{-6}	m	estimated from [54]
	R_n	5×10^{-6}		estimated from [54]
Thickness	d_{pm}	5×10^{-9}	m	[55]
	d_{ne}	5×10^{-9}		set equal to [55]

$$-\nabla \cdot \left[\left(\sigma + j\omega\varepsilon\right)\nabla\Phi\right] = 0 \tag{12}$$

where ω is the angular frequency of the field. Equation 12 is developed from Maxwell's equations under the electro-quasistatic approximation, which neglects magnetic induction and allows for the expression of the electric field only in terms of electric potential:

$$E = -\nabla\Phi \tag{13}$$

Dielectric tissue properties were chosen at 250 kHz to match the center frequency of the waveform delivered experimentally in a majority of the H-FIRE trials. Data generated by Gabriel *et al*. for the conductivity and permittivity of grey matter [30] was interpolated in Mathematica in order to estimate the values at 250 kHz (Table 2). The electro-quasistatic assumption is validated based on the fact that the frequency of the field corresponds to a wavelength (3.5 m) and skin depth (0.5 m) that are greater than the longest dimension in the geometry [31]. The brain subdomain was modeled as a 0.75 cm × 0.75 cm × 0.425 cm ellipsoid having a total volume of 1 cm^3 [32]. The maximum applied voltage, electrode dimensions, exposure length, and spacing were modeled to match the *in vivo* configuration described below. Electric potential boundary conditions of Φ = 400 V and Φ = 0 V were applied on the energized and grounded portions of the electrodes, respectively, while the remaining boundaries were treated as electrically insulating ($-n \cdot J = 0$), where J is the current density. The electrode subdomain was subtracted from the brain subdomain for conservative temperature estimates by preventing any heat dissipative fin effects. A fine mesh was utilized, which consisted of 23989 elements and resulted in less than a 0.5% difference in Joule heating between the electrodes upon further refinements.

Following a time-harmonic analysis of the electric field distribution, the temperature distribution in the brain was obtained by transiently solving the heat conduction equation with the inclusion of the predetermined Joule heating term ($J \cdot E = (\sigma + j\omega\varepsilon)E \cdot E$) as a heat source:

$$\frac{\partial T}{\partial t} = \frac{1}{\rho\, c_p}\left[\nabla \cdot (k\nabla T) + (J \cdot E)\right] \tag{14}$$

where c_p is the specific heat capacity at constant pressure, k is the thermal conductivity, and ρ is the density of the tissue (Table 2). Terms associated with the Pennes' Bioheat equation that account for blood perfusion and metabolism commonly used to assess tissue heating during IRE have been neglected for conservative temperature

Table 2 Parameter values for FEM simulation

Physics	Parameter	Value	Units	Reference
Heat conduction	k	0.565	W m^{-1} K^{-1}	[56]
	c_p	3680	J kg^{-1} K^{-1}	[56]
	ρ	1039	kg m^{-3}	[56]
Electric Currents	σ	0.145	S m^{-1}	[30]
	ε	1.95×10^{-8}	A s V^{-1} m^{-1}	[30]
Damage Processes	E_a	8.033×10^5	J mol^{-1}	[33]
	ζ	1.676×10^{129}	s^{-1}	calculated from [33,34]

estimates [29]. Additionally, it was assumed that all subdomains were initially at physiologic temperature (37°C) and all boundaries were thermally insulating ($-n \cdot (-k \nabla T) = 0$).

Three different methods were evaluated for calculating Joule heating to determine which method was computationally efficient while generating accurate solutions during a 10 s test treatment. One method simulated ten IRE pulses (200 μs duration) at a repetition rate of one pulse per second. Another method modeled ten, 250 kHz H-FIRE bursts (200 μs on-time) at a repetition rate of one burst per second. In the last method, voltage was held constant, but the Joule heating term was scaled by the duty cycle of the burst (200×10^{-6}) for a 10 s simulation. The parameters chosen had identical energized times, ensuring that equal quantities of energy were delivered to the tissue independent of the method used. The scaled Joule heating approach was eventually adapted for predicting the temperature increase during the entire H-FIRE protocol implemented experimentally, due to the slightly conservative yet accurate temperature distributions that were calculated in a fraction of the simulation time of the other two methods (data not shown). This technique also eliminates the need for an adaptive time stepping algorithm required to resolve microsecond order pulses that occur on the order of seconds. To account for the experimental condition of 180 bursts delivered at a rate of one per second, the Joule heating term was multiplied by the duty cycle (200×10^{-6}) and the simulation was run for 180 s.

Based on the temperature distribution, the extent of potential thermal damage in the brain was quantified at each time step using the Arrhenius equation:

$$\Omega(t) = \int \zeta e^{-E_a/(R\,T(t))} dt = \int F\, dt \tag{15}$$

where ζ is the frequency factor, E_a is the activation energy, R is the universal gas constant, and $T(t)$ is the temperature distribution for a given time (t). Due to a lack of data in the literature on Arrhenius parameters for healthy brain, parameters were chosen from glioblastoma cells in the temperature range 40°C to 45°C [33] (Table 2). It is important to note that only E_a is presented in [33], and ζ was calculated based on a linear relationship between E_a and $\ln(\zeta)$ for mammalian cells [34]. Thermal damage can include a variety of processes including cell death, microvascular blood flow stasis, and protein coagulation [35], each of which have different parameter values. Here, we have chosen to model the Arrhenius parameters associated with cell death. In terms of finite element modeling of tissue damage, a damage integral value $\Omega = 1$ corresponds to a 63% probability of cell death at a specific point, and a damage integral value $\Omega = 4.6$ corresponds to 99% probability of cell death at that point [36]. Equation 15 was incorporated into Comsol by adding a general PDE solver mode and writing the forcing function (F) in logarithmic form:

$$F = e^{\ln(\zeta) - E_a/(R\,T(t))} \tag{16}$$

in order to prevent abrupt changes in the solver. Additionally, all boundaries in the domain were assumed to be insulating ($-n \cdot \Gamma = 0$), where Γ is the general flux vector, which was assumed to be zero.

In Vivo Experiments

H-FIRE was performed using a custom pulse generator (Figure 2). Two commercially available monopolar high voltage MOSFET switches (HV1000, Directed Energy, Inc.,

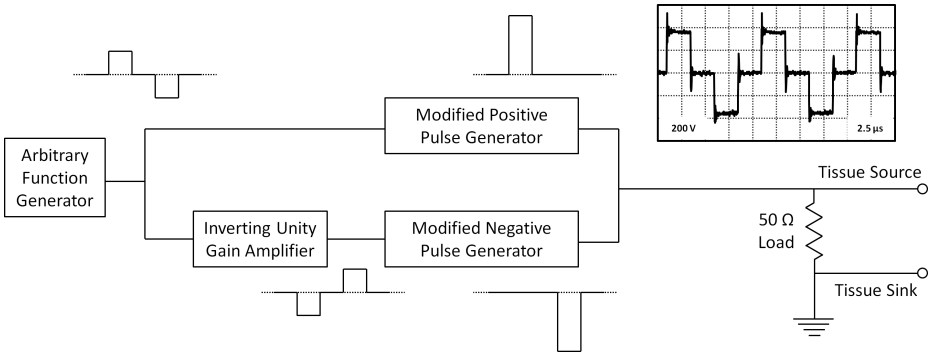

Figure 2 Schematic diagram of the pulse generation system. The example output is a portion of the bipolar burst delivered during *in vivo* H-FIRE of the brain.

Fort Collins, CO, USA) were modified so that their outputs would withstand a pulse of opposite polarity. When triggered with a positive 5 V signal, these generators deliver a corresponding positive (HV1000P) or negative (HV1000N) pulse. An unregulated DC power supply was constructed to maintain a sufficient level of charge to deliver 20 A over a 100 μs burst. A center tapped 400 VA transformer (AS-4T320, Antek, Inc., North Arlington, NJ, USA) was rectified and smoothed by a capacitor bank to provide positive and negative power rails to the HV1000P and HV1000N, respectively. The voltage rails were controlled by adjusting the input voltage using a variable transformer, and the maximum output rating of the system was +/- 450 V. For each treatment, an arbitrary function generator (AFG3011, Tektronix, Beaverton, OR, USA) was used to define the parameters of the pulse train to be delivered. A delay equal to the duration of single polarity was included between the pulses in order to protect the MOSFETs from ringing. A unity gain inverting amplifier (AD844, Analog Devices, Norwood, MA, USA) was used to invert this signal and appropriately trigger the negative pulse generator. The outputs of the two monopolar pulse generators were terminated into a 50 Ω load in parallel with the electrodes. This load was used to maintain appropriate pulse characteristics and as a safety to ensure the system was never triggered without an attached load. For comparison, the IRE treatments were performed using the BTX ECM 830 electroporation system (Harvard Apparatus, Holliston, MA, USA).

All study procedures were conducted following Institutional Animal Care and Use Committee approval and performed in a GLP compliant facility. Four, Fischer 344 male rats weighing 200-240 g were anesthetized by intraperitoneal injection of 10 mg/kg xylazine and 60 mg/kg ketamine hydrochloride, and a surgical plane of anesthesia was assessed by loss of the tail pinch reflex. To monitor muscle contractions, a 3-axis accelerometer breakout board (ADXL335, Adafruit Industries, New York, NY, USA) with a sensing range of ± 3 g's was sutured to the dorsum of each rat in the interscapular region at the cervicothoracic junction using 5-0 monocryl suture. Low-pass filter capacitors (0.1 μF) were included at the x, y, and z outputs of the accelerometer for noise reduction. The hair of the skull was clipped and aseptically prepared using povidone-iodine and alcohol solutions. Anesthetized rats were placed in a small animal stereotactic head frame (Model 1350M, David Kopf Instruments, Tungisten, CA, USA). A routine lateral rostrotentorial surgical approach to the skull was made, and 6 mm by 3 mm rectangular parieto-occipital craniectomy defects were created in the right and

left aspects of the skull of each rat using a high-speed electric drill. Custom electrodes were inserted into the center of the forelimb area of the sensorimotor cortex of each rat (coordinates relative to Bregma: 1 mm anterior, 2.5 mm lateral, 2 mm dorsoventral) and advanced to a depth of 2 mm beneath the surface of the exposed dura. The electrodes were fashioned by blunting stainless steel acupuncture needles (0.45 mm diameter, Kingli Medical Appliance Co., Wuxi, China) with high grade sandpaper. Exposure length was set to 1 mm by insulating the electrodes with miniature polyimide tubing (25 AWG, Small Parts, Seattle, WA, USA), and the edge-to-edge electrode spacing was set to 1 mm by molding the electrodes in liquid phase polydimethylsiloxane (PDMS) cured in a 10:1 ratio with Sylgard 184 (Dow Corning Corp., Midland, MI, USA) at 150°C for 30 min.

Pulse parameters were chosen based on the results from the analytical and numerical models to ensure the greatest potential for non-thermal tissue ablation. Following electrode insertion, pulses were applied to the right and left cerebral hemispheres, resulting in two treatments per rat (Table 3). All H-FIRE experiments were performed using 180 bursts with a pulse on-time of 200 μs within each burst, and all bursts were delivered at a rate of one per second. In Rat #1 and Rat #2, H-FIRE was applied at voltages of 100 V and 200 V, respectively, to the right hemisphere with a center frequency of 250 kHz (duration of single polarity equal to two microseconds). The left hemisphere of Rat #1 and Rat #2 were treated with 180 IRE pulses (200 μs duration) of equivalent energy. In Rat #3, H-FIRE was applied to the left and right hemispheres at voltages of 300 V and 400 V, respectively, with a frequency of 250 kHz. In Rat #4, H-FIRE was applied at a voltage of 400 V to the right hemisphere with a frequency of 500 kHz (duration of single polarity equal to one microsecond). The left hemisphere of Rat #4 was treated with 90 IRE pulses (200 μs) and an applied voltage of 50 V. This lower energy scenario was designed to compare H-FIRE treatment outcomes to traditional IRE protocols in the brain [37].

Immediately following treatment, Rats #3 and #4 were subjected to MRI examinations of the brain while under general anesthesia. The MRI was performed with a 0.2 T MRI scanner using a dual phased array hand/wrist coil for RF signal transmission and reception. Sequence acquisition parameters were as follows: T1-weighted images were acquired using spin echo pulse sequence (TR = 200 ms, TE = 16 ms, FOV = 6 cm, matrix = 256 × 196, slice thickness = 2 mm), and T2-weighted images were acquired using a gradient echo pulse sequence (TR = 3000 ms, TE = 90 ms, FOV = 6 cm, matrix = 256 × 196, slice thickness = 3 mm). T1-weigthed images were obtained following intraperitoneal injection of 0.1 mmol/kg of gadopentetate dimeglumine

Table 3 Treatment matrix for *in vivo* experiments

Rat Number	Treatment	Hemisphere	Frequency (kHz)	Voltage (V)
1	IRE	Left	-	100
	H-FIRE	Right	250	100
2	IRE	Left	-	200
	H-FIRE	Right	250	200
3	H-FIRE	Left	250	300
	H-FIRE	Right	250	400
4	IRE	Left	-	50
	H-FIRE	Right	500	400

(Magnevist, Berlex Laboratories, NJ, USA). In all rats, humane euthanasia was performed by cervical dislocation approximately 1 hr post-treatment, and the brain was removed and fixed intact in 10% neutral buffered formalin. Following fixation for 48 hours, an adult rat brain matrix slicer (Zivic Instruments, Pittsburg, PA) was used to obtain contiguous 2 mm coronal brain sections from each animal. Brain and sections were embedded routinely in paraffin, sectioned at 5 μm, and stained with hematoxylin and eosin (H&E).

Results

Analytical Modeling of Transmembrane Potential

The critical TMP (Φ_{cr}) across the plasma membrane required to induce IRE is approximately 1 V [38]. This threshold is illustrated in Figure 1 by the dashed, horizontal line on the TMP profiles. All results are presented at the cell pole (θ = 0) to show the maximum TMP around the cell. Further, results are only shown for TMP across the plasma membrane, as the TMP across the nuclear envelope never approached the permeabilizing threshold. For an electric field of 1500 V/cm, results indicate that a unipolar pulse (Figure 1A), a 250 kHz bipolar burst (Figure 1B), and 250 kHz bipolar burst that includes delays between the pulses (Figure 1C) are all capable of inducing IRE. However, the time above the threshold TMP varies between the different cases. This is investigated further in Figure 3 for center frequencies of 0, 100, 250, 500, and 1000 kHz, with the 0 kHz case representing the unipolar pulse, and electric fields of 1000 V/cm and 1500 V/cm. The burst width of the bipolar waveform that included delays was twice as long (40 μs) as the corresponding burst with no delays in order to generate an equivalent pulse on-time (20 μs). The amount of time that the TMP was above the critical value was normalized by the on-time and converted to a percentage. Figure 3 illustrates that, for a given frequency, as the electric field is increased from 1000 V/cm to 1500 V/cm, the percentage of the burst above the critical TMP also increases. At 250 kHz, IRE is possible during all waveforms, but at 500 kHz, only the waveforms with amplitudes of 1500 V/cm are capable of inducing IRE. As the center frequency of the burst increases, the percentage of the burst above the critical TMP decreases. However, with the inclusion of delays between the pulses, this characteristic dispersion is shifted towards higher frequencies. At 1 MHz, only the 1500 V/cm waveform with delays can theoretically cause IRE.

Numerical Modeling of Temperature and Thermal Damage

Results from the simulated H-FIRE treatment of brain tissue are shown in Figure 4. The FEM was developed in 3D, as visualized by the mesh (Figure 4A), and 2D slices were taken in the x-z plane through the center of the brain geometry to display the electric field (Figure 4B) and temperature (Figure 4C) distributions. The electric field decays rapidly with increasing distance from the electrodes, due to their relatively small diameter. The applied voltage-to-distance ratio of 4000 V/cm resulted in a peak electric field of 2979 V/cm along the centerline between the electrodes. Because the electric field relates directly to temperature through the Joule heating term, the application of 180, 200 μs long bursts causes only a 3.5°C increase in temperature near the electrode boundaries. This resulted in a maximum damage integral value of 0.003 at the electrode/tissue interface, which corresponds to a 0.3% probability of cell death

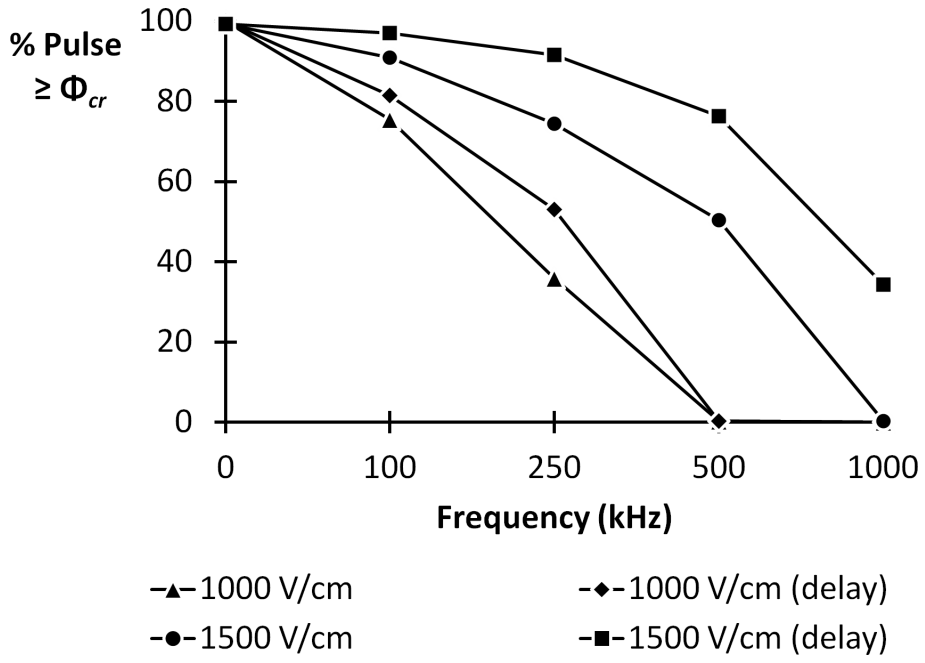

Figure 3 Comparison of time above the critical threshold (Φ_{cr}) for IRE at various center frequencies. Bipolar bursts were simulated with an electric field of 1000 V/cm and 1500 V/cm and an on-time of 20 μs. As the frequency of the applied field is increased, the time above the critical threshold diminishes. This characteristic dispersion is shifted towards higher frequencies for bursts that have a delay between the positive and negative polarity pulses. A conventional IRE pulse is depicted by the 0 kHz data point.

from thermal processes. Therefore, all cell death *in vivo* is likely to be a direct result of IRE and not thermal modes.

In Vivo Experiments

All IRE pulsing protocols were associated with macroscopic muscular contractions of the cervicothoracic junction, which were also palpable to the neurosurgeon, while no

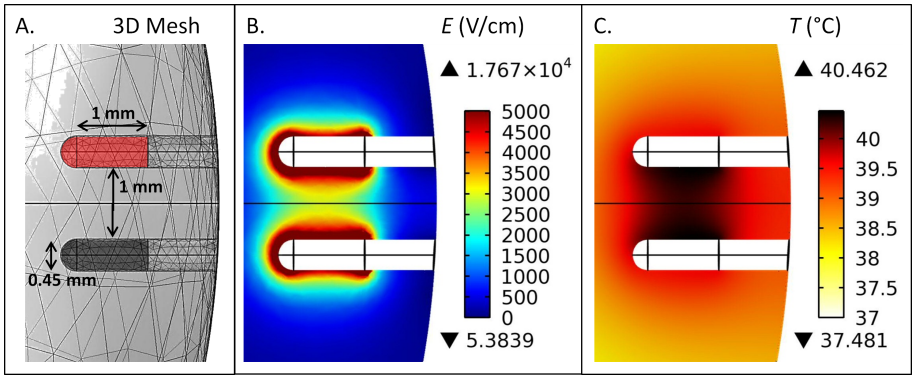

Figure 4 Schematic diagram of the FEM alongside the predicted electric field (*E*) and temperature (*T*) distributions in brain tissue. The 3D mesh (A) consisted of 23989 elements. An energized electrode (red) and ground electrode (black) with a 0.45 mm diameter were spaced 1 mm apart (edge-to-edge) and had an exposure length of 1 mm (not including the blunt tip). (B) The resulting electric field distribution in the x-z plane for an applied voltage of 400 V along the energized electrode. (C) The resulting temperature distribution in the x-z plane following the simulation of 180, 200 μs pulses. Upper and lower triangles in the legends depict maximums and minimums within the entire subdomain, respectively.

visual or tactile evidence of muscular contraction was seen during any of the H-FIRE bursts (Additional File 1). These results were quantitatively confirmed by the data recordings from the accelerometer (Figure 5). Peak acceleration was determined during the first 90 bursts of the highest energy H-FIRE protocol (400 V/250 kHz) and the first 90 pulses of each IRE protocol (50 V, 100 V, 200 V). A one-way ANOVA was used to investigate the effects of each protocol on the ranks of peak acceleration at the cervicothoracic junction. In the event of a significant main effect, pairwise comparisons were completed using Tukey's Honestly Significant Difference (HSD). All statistical analyses were conducted using JMP 7 (Cary, North Carolina, USA) with a significance level of $p \leq 0.05$. Results indicate that, even in the highest energy H-FIRE protocol, there are no detectable peaks in acceleration above the inherent noise of the system. However, in all IRE protocols, peaks in acceleration associated with each pulse are detectable above the baseline noise. Further, pairwise comparisons between the various IRE protocols indicated that the mean peak acceleration during each treatment was energy dependent. Specifically, the mean peak acceleration decreased as the applied voltage decreased (Figure 6).

All treatments evaluated in this study produced ablative lesions in brain tissue, as evaluated with MRI examinations (Figure 7) and pathologic preparations (Figure 8). In Rats #3 and #4, the MRI characteristics of both H-FIRE and IRE lesions were similar. Lesions appeared as focal, ovoid to elliptical, T1 iso- to hypo-intense, uniformly and markedly contrast enhanced (Figure 7A, B, C, D, F), and T2 hyper-intense (Figure 7E). All lesions were well demarcated from adjacent, normal brain tissue and appeared similar in size. A comparable size IRE lesion was produced at lower energy, as

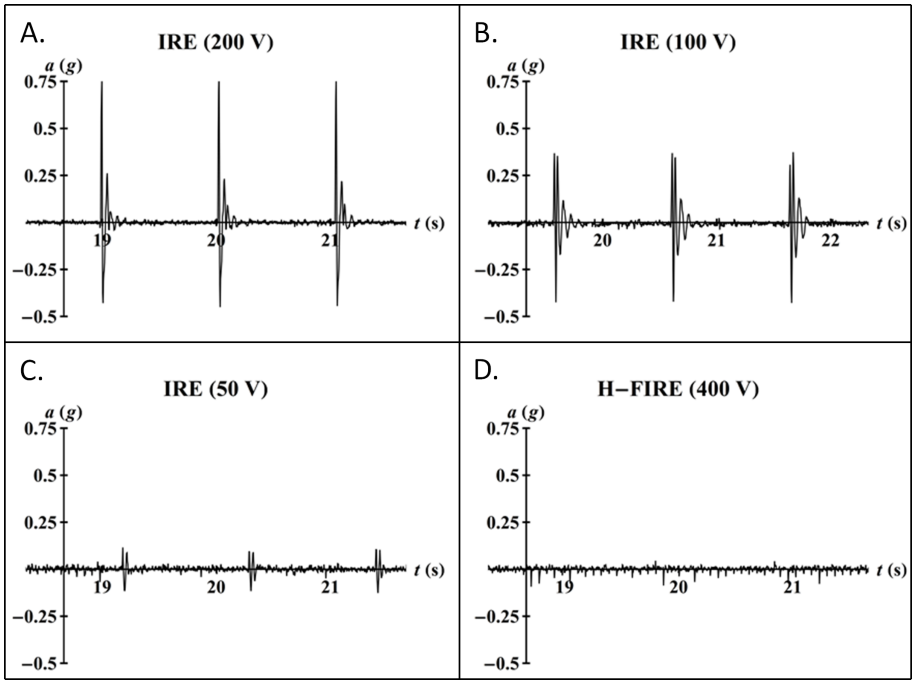

Figure 5 Snapshot of acceleration (*a*) versus time during IRE and H-FIRE treatments. Acceleration at the cervicothoracic junction was detected by the accelerometer based recording system during all IRE protocols. None of the H-FIRE protocols resulted in detectable acceleration of the cervicothoracic junction (e.g. shown, 400 V/250 kHz).

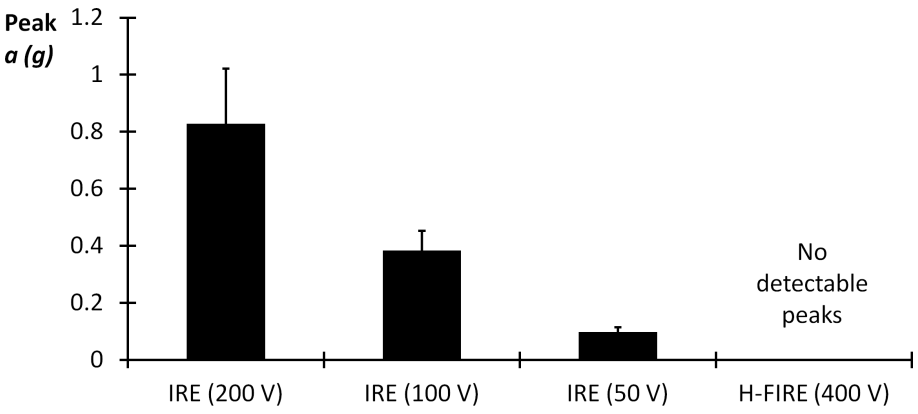

Figure 6 Peak acceleration (*a*) during IRE protocols averaged over the first 90 pulses. Mean peak acceleration during IRE treatments at the cervicothoracic junction for each applied voltage was significantly different from each other. H-FIRE resulted in no detectable acceleration of the cervicothoracic junction.

compared to the H-FIRE lesions. However, as mentioned, IRE even at the lowest energy scenario produced muscle contractions, while the highest energy H-FIRE protocol did not (Figure 6).

Compared to untreated brain (Figure 8A and 8B), histopathologic examination of brain sections from all treatments demonstrated clear areas of ablation indicated by

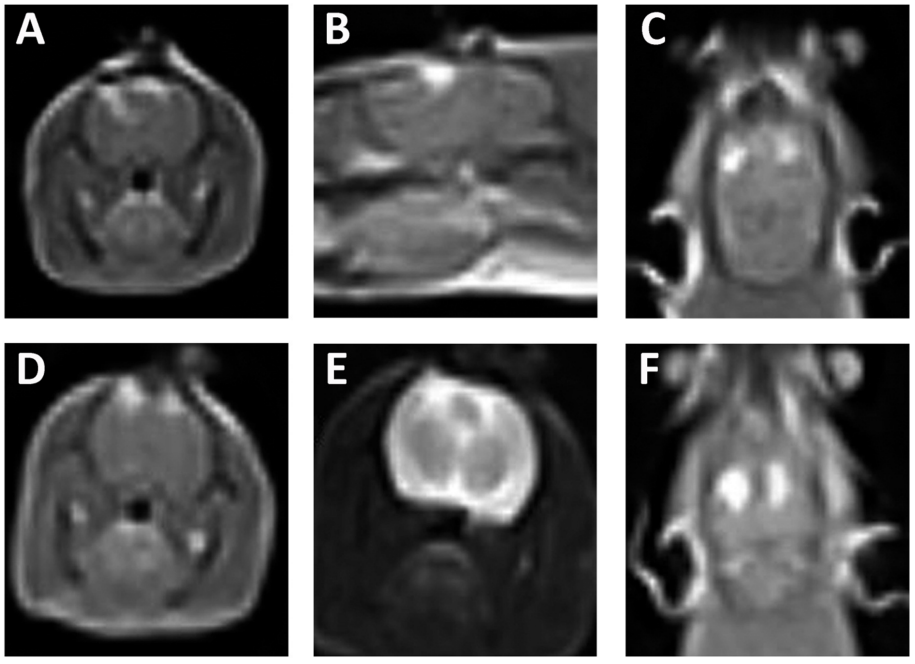

Figure 7 MRI appearance of H-FIRE and IRE lesions in rat brain. In all panels, IRE and H-FIRE induced lesions appear as focal hyper-intense regions (white) compared to adjacent untreated cerebrocortical tissue (gray). Top Panels (A-C) obtained from Rat #3, in which both the left and right cerebral hemispheres were treated with H-FIRE at 300 V/250 kHz and 400 V/250 kHz, respectively. Bottom Panels (D-F), Rat #4, which underwent H-FIRE in the right cerebrum at 400 V/500 kHz, and IRE at 50 V in the left cerebrum. Panels A and D, post-gadolinium T1-weighted MRI sequences in the axial plane. Panel B, post-gadolinium T1-weighted MRI sequences in the right parasagittal plane. Panels C and F, post-gadolinium T1-weighted MRI sequences in the dorsal plane. Panel D, T2-weighted MRI sequence in the transverse plane. In all panels, the right side of the brain is on the left side of the panel.

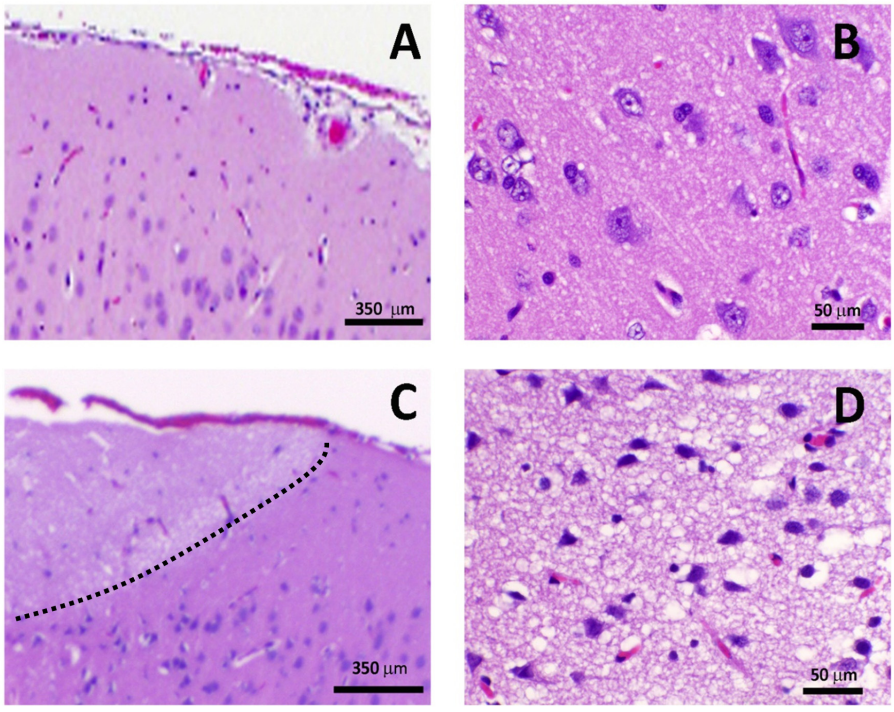

Figure 8 Histopathology of rat brain tissue. Untreated (A and B) and H-FIRE treated at 200 V/250 kHz (C and D, Rat #2, right hemisphere). Hematoxylin and eosin stain. The delineation between treated and untreated tissue is shown in Panel C (black, dotted line)

pallor of the treated tissue that was sharply delineated from adjacent normal brain (Figure 8C, Figure 9). H-FIRE and IRE lesions were predominantly characterized by areas of complete obliteration of cerebrocortical architecture by an eosinophilic, vacuolated amorphous debris (Figure 8C and 8D). In Rat #1, the H-FIRE ablation zone was confined to regions of elevated electric field surrounding the electrodes, whereas all other pulsing protocols resulted in ablation zones spanning the entire region between the electrodes. Cavitary cerebrocortical defects were induced with H-FIRE in Rat #1 and IRE in Rat #4. Variably sized regions of intraparenchymal hemorrhage were most pronounced immediately adjacent to and within electrode insertion tracks (Figure 9B and 9E). The morphology of remnant neuronal and glial elements within H-FIRE ablated regions demonstrated features of both apoptosis and necrosis, including shrunken and hypereosinophilic cytoplasm, nuclear chromatin condensation, and nuclear pyknosis and karyolysis (Figure 8D). Free glial and neuronal nuclei in various states of degeneration were scattered throughout ablation zones. Inflammation was not a significant feature of IRE or H-FIRE lesions at the time point brains were examined.

Discussion

The results presented above demonstrate the feasibility of H-FIRE for non-thermally ablating tissue without causing any associated muscle contractions. Specifically, we have shown the ablation of brain tissue by applying bipolar bursts at center frequencies up to 500 kHz. While the pilot data gathered here was not designed to locate an upper limit in terms of frequency at which IRE could still be achieved *in vivo*, the theoretical model of TMP suggests that IRE should be possible up to 1 MHz for an electric field

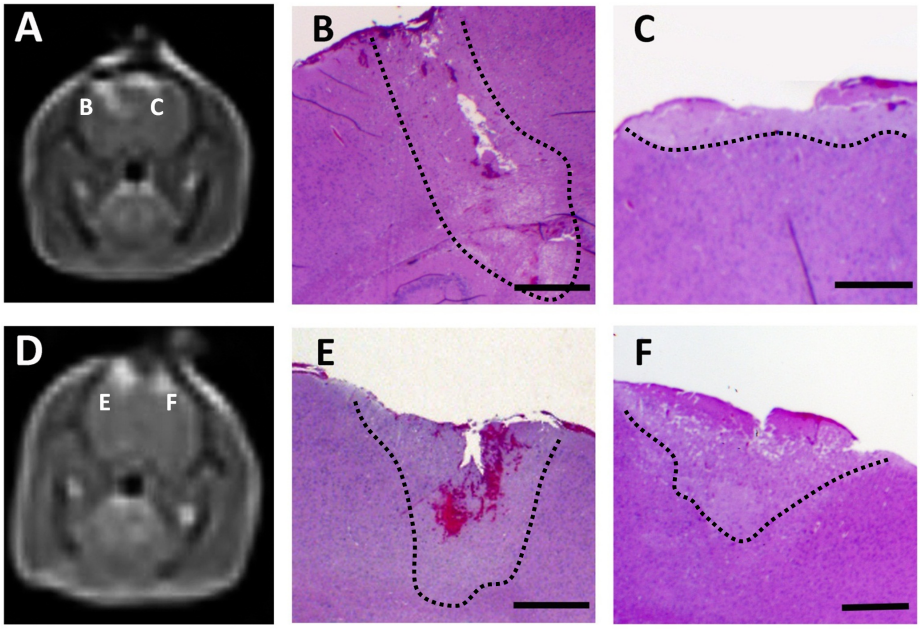

Figure 9 MRI and corresponding neuropathology of rat brain tissue lesioned with H-FIRE and IRE. Top Panels (A-C) obtained from Rat #3, in which both the right (Panel B) and left (Panel C) cerebral hemispheres were treated with H-FIRE at 400 V/250 kHz and 300 V/250 kHz, respectively. Bottom Panels (D-F), Rat #4, which underwent H-FIRE in the right cerebrum at 400 V/500 kHz (Panel E), and IRE in the left cerebrum at 50 V (Panel F). Panels A and D are the same as those presented in Figure 7A and D, with an outline of the lesions that are further represented in Panels B, C, E, and F (Hematoxylin and eosin stain, bar = 1 mm). In Panels B, C, E, and F, the delineation between treated and untreated tissue is shown (black, dotted line). In Panels A and D, the right side of the brain is on the left side of the panel.

of 1500 V/cm. Interestingly, including a delay between the positive and negative pulses comprising the bipolar burst offers a therapeutic advantage in addition to protecting the MOSFETs in the pulse generation system from ringing. By not forcing a discharge of the TMP with an immediate reversal of polarity, the cell is allowed to return to the resting TMP according to its characteristic time constant. As a result, the TMP is maintained above the critical voltage required for IRE for a longer amount of time. This metric has been recognized before as a potential indicator of treatment outcomes in electroporation based therapies with bipolar waveforms [39].

Due to the small number of observations chosen to assess feasibility, quantitative comparisons between pulse parameters and ablation volumes were not performed. Qualitatively, the fact that IRE was performed with a lower applied voltage in Rat #4 suggests that H-FIRE requires a greater electric field strength than conventional IRE for inducing necrosis, as observed under MRI (Figures 7 and 9). However, even at higher fields, H-FIRE produced no muscle contractions either tactilely, visibly, or through accelerometer recordings at the cervicothoracic junction (Figures 5 and 6). In Rat #1, histopathologic examination revealed that ablation due to H-FIRE occurred only in regions of elevated electric field surrounding the electrodes. This may be explained due to the rapid decline in electric field away from the electrodes predicted by the FEM, and the relatively low percentage of the burst above the critical TMP for the 1000 V/cm waveforms predicted by the analytical model.

The gross histological lesions from the *in vivo* H-FIRE treatments, along with the results of the FEM for predicting the temperature increase in brain tissue during H-FIRE, support the claim that the ablation is not thermally mediated and a direct result of IRE. There is complete uniformity of tissue destruction within targeted H-FIRE areas (Figures 8 and 9), which is in contrast to thermal ablation procedures, such as radiofrequency (RF) ablation [40]. Additionally, H-FIRE results in a sharp transition zone between lesioned and normal brain (on the order of 10-20 μm), which is in agreement with previous intracranial studies on traditional non-thermal IRE [37,41]. The transition zone in RF ablation is characterized by regions of partial tissue damage of anywhere from 100 μm to a few millimeters [42].

Due to the greater electric field strength required to induce IRE with high-frequency, bipolar bursts, evaluating the thermal damage probability in the tissue gains importance in H-FIRE treatment planning. Here, the FEM was conservative in the sense that all boundaries were thermally insulating, no electrodes were present in the subdomain to dissipate heat, and the duty cycle approach was implemented for calculating Joule heating as opposed to simulating individual pulses. The *in vivo* treatments resulted in no predictable thermal damage, due to the small diameter of the electrodes and small exposure length. In the future, temperature predictions should be validated by direct measurements, and the effects of H-FIRE on the electrical conductivity of the tissue should be incorporated into the FEM, as this will have implications for Joule heating. However, it is possible that H-FIRE will produce more subtle changes in tissue conductivity compared to IRE, due to its ability to enhance the capacitive coupling across epithelial layers [20].

The brain was chosen here as a model system due to our expertise and specific interest in advancing electroporation based therapies for the treatment of malignant glioma, including glioblastoma multiforme [43]. Despite attempts to selectively target efferent pathways to the limbs based on electrode placement, all IRE treatment protocols produced contractions of the head, truncal, and limb musculature. Therefore, movement may be caused by direct stimulation of motor regions in the brain, as well as leak currents that directly excite muscle. No hemorrhage occurred, other than an anticipated microhemorrhage along the electrode tracks, and no inadvertent penetration into cerebrospinal fluid pathways occurred, other than traversing of the subarachnoid space at the point of electrode insertion, which might influence leak currents. It is expected that the results obtained in the brain will translate to other tissues, such as the liver, prostate, kidney, and breast, which warrant further investigations. Additionally, studies performed directly in muscle would help elucidate the mechanism responsible for a reduction in nerve stimulation in response to H-FIRE, as the presence of the skull may provide a certain degree of electrical isolation from nearby muscle.

According to classic literature, bipolar waveforms have a higher current threshold for action potential stimulation as compared to monopolar waveforms, which becomes more evident as pulse duration is reduced [25], and bipolar waveforms reduce muscle twitch forces as compared to monopolar waveforms [44]. No electrically induced movement was seen in any of the H-FIRE treatment protocols, ruling out the possibility of tonic contraction. Elimination of patient motion through the delivery of high-frequency, bipolar bursts confers several significant advantages over IRE to both the neurosurgeon and neurosurgical patient that warrants higher energy demands required

to achieve ablation. Although electroporation based therapies have proven to be safe and effective in the brain [9,37,43], they require the use of paralytic agents. H-FIRE obviates the need for paralytic agents and, in doing so, provides the possibility for performance of minimally invasive, outpatient intracranial surgery, conscious neurosurgical interventions, procedures in proximity to eloquent areas of the brain, and eliminates the inherent risk associated with general anesthesia. Finally, although not directly evaluated in this study, previous investigators have demonstrated that bipolar pulse delivery at 1 kHz is associated with less patient pain [45].

For frequencies well into the megahertz range, or individual pulse durations on the order of 10-100 nanoseconds, it is possible for a significant amount of current to bypass the plasma membrane through capacitive coupling. As a result, electroporation of both the plasma membrane and intracellular structures can occur for electric field strengths on the order of 10-100 kV/cm [46,47]. These nanosecond pulsed electric fields (nsPEFs) have shown great promise as a cancer therapy due to their ability to induce cell death through apoptotic mechanisms and reduce muscle contractions [48]. One challenge associated with nsPEFs that further distinguishes them from IRE is that the field strength required to induce electroporation of intracellular vesicles and organelles, such as the nucleus, is an order of magnitude greater (40 kV/cm) [49]. This is predominantly due to the small size of vesicles and organelles compared to the overall cell. In H-FIRE, by targeting the plasma membrane, which encompasses the entire cell, the field required to induce cell death is closer in amplitude to IRE protocols than nsPEFs protocols. From an electrical engineering perspective, this simplifies the pulse generation system, and allows for the utilization of silicon based components and commercially available high voltage switches.

Conclusion

This proof-of-concept study was performed to theoretically and experimentally investigate the potential of high-frequency, bipolar bursts to ablate tissue through IRE and eliminate the associated muscle contractions seen in traditional IRE treatments performed with unipolar pulses. In a rat model, high-frequency IRE (H-FIRE) performed with frequencies up to 500 kHz and voltage-to-distance ratios up to 4000 V/cm produced lesions in brain tissue characteristic of IRE outcomes without causing muscle contractions. Therefore, H-FIRE has the potential to be performed clinically without the administration of paralytic agents, which are used in IRE protocols to mitigate muscle contractions. While not explored explicitly in this study, H-FIRE also offers the benefits associated with charge balancing, including reduced electrolytic contamination. Additionally, high-frequency fields have the potential to overcome impedance barriers posed by low conductivity tissues, which could result in more homogenous and predictable treatment outcomes in heterogeneous systems. Future work should be directed towards further elucidating the relationship between different H-FIRE pulse parameters and ablation volumes, in order to successfully translate this technology for the treatment of tumors. Electroporation based therapies are gaining momentum as viable treatment options for cancer. H-FIRE has the potential to follow suit due to the added benefits that high-frequency, bipolar bursts provide.

Additional material

Additional file 1: Video of *in vivo* IRE and H-FIRE experiments.

Abbreviations

(IRE): Irreversible Electroporation; (H-FIRE): High-Frequency Irreversible Electroporation; (TMP): Transmembrane Potential; (nsPEF): nanosecond Pulsed Electric Field

Acknowledgements

This work was supported in part by the Coulter Foundation and the NSF under Awards CBET-0933335 and CAREER CBET-1055913. The authors thank Sara L. Matrangola for assisting with the analysis and interpretation of the accelerometer data and Robert E. Neal Jr. and Erica M. Davis for assisting with the data acquisition during *in vivo* treatments.

Author details

[1]Bioelectromechanical Systems Lab, Virginia Tech-Wake Forest University School of Biomedical Engineering and Sciences, 330 ICTAS Building (MC0298), Blacksburg, VA. 24061, USA. [2]Neurology and Neurosurgery, Virginia-Maryland Regional College of Veterinary Medicine, Small Animal Clinical Sciences Phase II (MC0442), Blacksburg, VA. 24061, USA. [3]Bioelectromechanical Systems Lab, Virginia Tech Bradley Department of Electrical and Computer Engineering, 330 ICTAS Building (MC0298), Blacksburg, VA. 24061, USA. [4]Tissue Engineering, Nanotechnology, and Cancer Research Lab, Virginia Tech-Wake Forest University School of Biomedical Engineering and Sciences, 335 ICTAS Building (MC0298), Blacksburg, VA. 24061, USA.

Authors' contributions

CBA, MBS, JHR, PAG, and RVD designed and performed the experiments and numerical modeling. JLC assisted with the design of the pulse generation system. MNR analyzed the experiments and numerical modeling. All authors read and approved the final manuscript.

Competing interests

The authors declare that they have no competing interests.

Received: 22 September 2011 Accepted: 21 November 2011 Published: 21 November 2011

References

1. Davalos RV, Mir LM, Rubinsky B: **Tissue ablation with irreversible electroporation.** *Ann Biomed Eng* 2005, **33(2)**:223-231.
2. Rubinsky B: **Irreversible electroporation in medicine.** *Technol Cancer Res Treat* 2007, **6(4)**:255-260.
3. Thomson KR, Cheung W, Ellis SJ, Park D, Kavnoudias H, Loader-Oliver D, Roberts S, Evans P, Ball C, Haydon A: **Investigation of the Safety of Irreversible Electroporation in Humans.** *J Vasc Interv Radiol* 2011, **22(5)**:611-621.
4. Edd JF, Horowitz L, Davalos RV, Mir LM, Rubinsky B: **In vivo results of a new focal tissue ablation technique: irreversible electroporation.** *IEEE Trans Biomed Eng* 2006, **53(7)**:1409-1415.
5. Maor E, Ivorra A, Leor J, Rubinsky B: **The effect of irreversible electroporation on blood vessels.** *Technol Cancer Res T* 2007, **6(4)**:307-312.
6. Maor E, Ivorra A, Rubinsky B: **Non Thermal Irreversible Electroporation: Novel Technology for Vascular Smooth Muscle Cells Ablation.** *Plos One* 2009, **4(3)**.
7. DeBruin KA, Krassowska W: **Modeling electroporation in a single cell. II. Effects of ionic concentrations.** *Biophysical Journal* 1999, **77(3)**:1225-1233.
8. Mir LM: **Therapeutic perspectives of in vivo cell electropermeabilization.** *Bioelectrochemistry* 2001, **53(1)**:1-10.
9. Gehl J, Agerholm-Larsen B, Iversen HK, Ibsen P, Moller JM, Mahmood F, Jensen KS: **Preclinical Validation of Electrochemotherapy as an Effective Treatment for Brain Tumors.** *Cancer Research* 2011, **71(11)**:3753-3762.
10. Daud AI, DeConti RC, Andrews S, Urbas P, Riker AI, Sondak VK, Munster PN, Sullivan DM, Ugen KE, Messina JL, *et al*: **Phase I Trial of Interleukin-12 Plasmid Electroporation in Patients With Metastatic Melanoma.** *Journal of Clinical Oncology* 2008, **26(36)**:5896-5903.
11. Al-Sakere B, Andre F, Bernat C, Connault E, Opolon P, Davalos RV, Rubinsky B, Mir LM: **Tumor ablation with irreversible electroporation.** *Plos One* 2007, **2(11)**:e1135.
12. Davalos RV, Rubinsky B: **Temperature considerations during irreversible electroporation.** *Int J Heat Mass Tran* 2008, **51(23-24)**:5617-5622.
13. Davalos RV, Rubinsky B, Mir LM: **Theoretical analysis of the thermal effects during in vivo tissue electroporation.** *Bioelectrochemistry* 2003, **61(1-2)**:99-107.
14. Rubinsky B: **Irreversible Electroporation in Medicine.** *Technology in Cancer Research and Treatement* 2007, **6(4)**:255-260.
15. Li W, Fan QY, Ji ZW, Qiu XC, Li Z: **The Effects of Irreversible Electroporation (IRE) on Nerves.** *Plos One* 2011, **6(4)**.
16. Ahmed M, Brace CL, Lee FT Jr, Goldberg SN: **Principles of and advances in percutaneous ablation.** *Radiology* 2011, **258(2)**:351-369.
17. Edd JF, Davalos RV: **Mathematical modeling of irreversible electroporation for treatment planning.** *Technol Cancer Res Treat* 2007, **6**:275-286.
18. Mir LM, Miklavcic D, Semrov D, Mekid H: **A validated model of in vivo electric field distribution in tissues for electrochemotherapy and for DNA electrotransfer for gene therapy.** *Bba-Gen Subjects* 2000, **1523(1)**:73-83.
19. Kuznetsov AV, Becker SM: **Thermal damage reduction associated with in vivo skin electroporation: A numerical investigation justifying aggressive pre-cooling.** *Int J Heat Mass Tran* 2007, **50(1-2)**:105-116.

20. Arena CB, Sano MB, Rylander MN, Davalos RV: **Theoretical considerations of tissue electroporation with high-frequency bipolar pulses.** *IEEE Trans Biomed Eng* 2011, **58(5)**:1474-1482.
21. Kotnik T, Miklavcic D, Mir LM: **Cell membrane electropermeabilization by symmetrical bipolar rectangular pulses. Part II. Reduced electrolytic contamination.** *Bioelectrochemistry* 2001, **54(1)**:91-95.
22. Kotnik T, Mir LM, Flisar K, Puc M, Miklavcic D: **Cell membrane electropermeabilization by symmetrical bipolar rectangular pulses. Part I. Increased efficiency of permeabilization.** *Bioelectrochemistry* 2001, **54(1)**:83-90.
23. Tekle E, Astumian RD, Chock PB: **Electroporation by Using Bipolar Oscillating Electric-Field - an Improved Method for DNA Transfection of Nih 3t3 Cells.** *Proceedings of the National Academy of Sciences of the United States of America* 1991, **88(10)**:4230-4234.
24. Ball C, Thomson KR, Kavnoudias H: **Irreversible Electroporation: A New Challenge in "Out of Operating Theater" Anesthesia.** *Anesth Analg* 2010, **110(5)**:1305-1309.
25. Reilly JP, Freeman VT, Larkin WD: **Sensory Effects of Transient Electrical-Stimulation - Evaluation with a Neuroelectric Model.** *IEEE Trans Biomed Eng* 1985, **32(12)**:1001-1011.
26. Kotnik T, Miklavcic D: **Theoretical evaluation of voltage inducement on internal membranes of biological cells exposed to electric fields.** *Biophysical Journal* 2006, **90(2)**:480-491.
27. Kotnik T, Pucihar G: **Induced Transmembrane Voltage - Theory, Modeling, and Experiments.** *Advanced Electroporation Techniques in Biology and Medicine* CRC Press; 2010, 51-70.
28. Yao CG, Mo DB, Li CX, Sun CX, Mi Y: **Study of transmembrane potentials of inner and outer membranes induced by pulsed-electric-field model and simulation.** *IEEE Trans Plasma Sci* 2007, **35(5)**:1541-1549.
29. Garcia PA, Rossmeisl JH, Neal RE, Ellis TL, Davalos RV: **A Parametric Study Delineating Irreversible Electroporation from Thermal Damage Based on a Minimally Invasive Intracranial Procedure.** *Biomed Eng Online* 2011, **10(1)**:34.
30. Gabriel C, Gabriel S: **Compilation of the Dielectric Properties of Body Tissues at RF and Microwave Frequencies.** Texas (USA): Brooks Air Force Base; 1996.
31. Chen MT, Jiang C, Vernier PT, Wu YH, Gundersen MA: **Two-dimensional nanosecond electric field mapping based on cell electropermeabilization.** *PMC Biophys* 2009, **2(1)**:9.
32. Yücel F, Ünal N, Erçakır M, Güven G: **Determination of age-related volume changes in rat brain by Cavalieri method.** *Erciyes Medical Journal* 2003, **25(4)**:170-185.
33. Floridi A, Gentile FP, Bruno T, Delpino A, Iacobini C, Paggi MG, Castiglione S, Benassi M: **Thermal-Behavior of a Human Glioma Cell-Line and Its Response to Combinations of Hyperthermia and Lonidamine.** *Oncol Res* 1993, **5(1)**:1-10.
34. Wright NT: **On a relationship between the Arrhenius parameters from thermal damage studies.** *Journal of Biomechanical Engineering-Transactions of the Asme* 2003, **125(2)**:300-304.
35. Sherar MD, Moriarty JA, Kolios MC, Chen JC, Peters RD, Ang LC, Hinks RS, Henkelman RM, Bronskill MJ, Kucharcyk W: **Comparison of thermal damage calculated using magnetic resonance thermometry, with magnetic resonance imaging post-treatment and histology, after interstitial microwave thermal therapy of rabbit brain.** *Physics in Medicine and Biology* 2000, **45(12)**:3563-3576.
36. Chang IA, Nguyen UD: **Thermal modeling of lesion growth with radiofrequency ablation devices.** *Biomed Eng Online* 2004, **3(1)**:27.
37. Ellis TL, Garcia PA, Rossmeisl JH, Henao-Guerrero N, Robertson J, Davalos RV: **Nonthermal irreversible electroporation for intracranial surgical applications Laboratory investigation.** *Journal of Neurosurgery* 2011, **114(3)**:681-688.
38. Weaver JC, Chizmadzhev YA: **Theory of electroporation: A review.** *Bioelectroch Bioener* 1996, **41(2)**:135-160.
39. Kotnik T, Pucihar G, Rebersek M, Miklavcic D, Mir LM: **Role of pulse shape in cell membrane electropermeabilization.** *Bba-Biomembranes* 2003, **1614(2)**:193-200.
40. Merkle EM, Shonk JR, Zheng L, Duerk JL, Lewin JS: **MR imaging-guided radiofrequency thermal ablation in the porcine brain at 0.2 T.** *Eur Radiol* 2001, **11(5)**:884-892.
41. Garcia PA, Rossmeisl JH, Neal RE, Ellis TL, Olson JD, Henao-Guerrero N, Robertson J, Davalos RV: **Intracranial Nonthermal Irreversible Electroporation: In Vivo Analysis.** *Journal of Membrane Biology* 2010, **236(1)**:127-136.
42. Morris DL, Gananadha S, Wulf S: **Safety and efficacy of radiofrequency ablation of brain: A potentially minimally invasive treatment for brain tumours.** *Minim Invas Neurosur* 2004, **47(6)**:325-328.
43. Garcia PA, Pancotto T, Rossmeisl JH, Henao-Guerrero N, Gustafson NR, Daniel GB, Robertson JL, Ellis TL, Davalos RV: **Non-Thermal Irreversible Electroporation (N-TIRE) and Adjuvant Fractionated Radiotherapeutic Multimodal Therapy for Intracranial Malignant Glioma in a Canine Patient.** *Technol Cancer Res T* 2011, **10(1)**:73-83.
44. Vandenhonert C, Mortimer JT: **Response of the Myelinated Nerve-Fiber to Short Duration Biphasic Stimulating Currents.** *Annals of Biomedical Engineering* 1979, **7(2)**:117-125.
45. Daskalov I, Mudrov N, Peycheva E: **Exploring new instrumentation parameters for electrochemotherapy - Attacking tumors with bursts of biphasic pulses instead of single pulses.** *IEEE Eng Med Biol Mag* 1999, **18(1)**:62-66.
46. Beebe SJ, White J, Blackmore PF, Deng YP, Somers K, Schoenbach KH: **Diverse effects of nanosecond pulsed electric fields on cells and tissues.** *DNA and Cell Biology* 2003, **22(12)**:785-796.
47. Pakhomov AG, Kolb JF, White JA, Joshi RP, Xiao S, Schoenbach KH: **Long-lasting plasma membrane permeabilization in mammalian cells by nanosecond pulsed electric field (nsPEF).** *Bioelectromagnetics* 2007, **28(8)**:655-663.
48. Long G, Shires PK, Plescia D, Beebe SJ, Kolb JF, Schoenbach KH: **Targeted Tissue Ablation With Nanosecond Pulses.** *IEEE Trans Biomed Eng* 2011, **58(8)**.
49. Nuccitelli R, Pliquett U, Chen XH, Ford W, Swanson RJ, Beebe SJ, Kolb JF, Schoenbach KH: **Nanosecond pulsed electric fields cause melanomas to self-destruct.** *Biochemical and Biophysical Research Communications* 2006, **343(2)**:351-360.
50. Sunderman FW: **Rapid measurement of serum total base and estimation of serum sodium; an improved conductivity assembly.** *Am J Clin Pathol* 1949, **19(7)**:659-664.
51. Gascoyne PRC, Pethig R, Burt JPH, Becker FF: **Membrane-Changes Accompanying the Induced-Differentiation of Friend Murine Erythroleukemia-Cells Studied by Dielectrophoresis.** *Biochimica Et Biophysica Acta* 1993, **1149(1)**:119-126.
52. Harris CM, Kell DB: **The Radio-Frequency Dielectric-Properties of Yeast-Cells Measured with a Rapid, Automated, Frequency-Domain Dielectric Spectrometer.** *Bioelectroch Bioener* 1983, **11(1)**:15-28.
53. Nortemann K, Hilland J, Kaatze U: **Dielectric properties of aqueous NaCl solutions at microwave frequencies.** *J Phys Chem A* 1997, **101(37)**:6864-6869.

54. Heizmann CW, Davey GE, Murmann P: **Intracellular Ca2+ and Zn2+ levels regulate the alternative cell density-dependent secretion of S100B in human glioblastoma cells.** *Journal of Biological Chemistry* 2001, **276(33)**:30819-30826.
55. McLaughlin S, Murray D: **Plasma membrane phosphoinositide organization by protein electrostatics.** *Nature* 2005, **438(7068)**:605-611.
56. Duck FA: **Physical Properties of Tissues: A Comprehensive Reference Book.** San Diego: Academic Press; 1990.

doi:10.1186/1475-925X-10-102
Cite this article as: Arena *et al.*: High-frequency irreversible electroporation (H-FIRE) for non-thermal ablation without muscle contraction. *BioMedical Engineering OnLine* 2011 **10**:102.

separation is on the order of microns.

Experimental Methods

Porcine kidneys were procured via surgical resection post mortem. Blood vessels from the kidney were identified and isolated from surrounding connective tissue. Luer lock syringe connectors were inserted into the renal artery and vein and secured using fine string and surgical knots. Perfusion electrodes were placed in line between the perfusion system and the organ. These electrodes provided an electrical connection to the conductive fluid being perfused through the vasculature. The organs were then flushed with Krebs solution, conductivity of 0.72 S/m, for 15 minutes to remove as many clots as possible. The resistance and capacitance of the vascular network was measured with an LCR meter to characterize the impedance of the vascular network. To establish a baseline for the electrical current delivered during treatment, a single 50 microsecond pulse was delivered through the vasculature at voltages of 100, 500, 750, 1000, 1500, and 2000 V_{peak} using an ECM 830 BTX pulse generator (Harvard Apparatus). The current delivered and the pulse decay time of the pulse was recorded. The organ was then subjected to 200 pulses at 1000 V, with a repetition rate of one pulse every second. TTC stain was administered via perfusion 15 minutes after pulsing was completed and the organ remained on

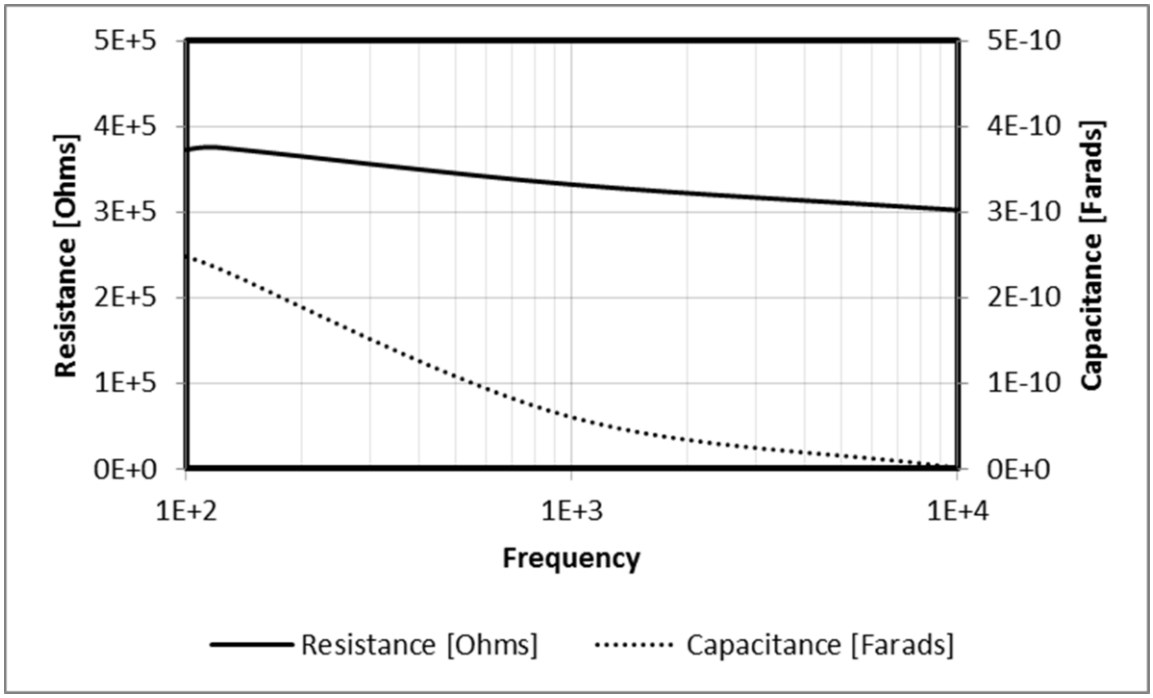

Figure 15-3: Impedance of the kidney as measured through the vasculature prior to IRE Treatment.

the perfusion system for another 30 minutes. The organ was then sectioned (Figure 15-5) and placed in formalin for fixation and histology.

Experimental Results and Discussion

Figure 2 shows the impedance and capacitance of the organ at frequencies between 100 Hz and 10 kHz. This shows that an organ being perfused with Krebs solution presents an impedance of less than 400 kΩ between the arterial and venous systems. It should be noted that the resistivity of Krebs solution and whole blood are nearly identical. At 100 Hz, the organ should have a theoretical RC time constant of 92.4 micro-seconds and a complete decay time (5*RC) of approximately 462 micro-seconds. When measured experimentally, the RC time constant and the complete decay time of the pulses indicate the impedance that the organ presents during the pulse. The impedance measured prior to pulsing (Figure 15-3) predicts a longer decay time than observed experimentally.

Figure 3 shows the current delivered for pulses with voltages between 100 and 2000 V. The current to voltage ratio decreases slightly at voltages of 750 V and above. For all of the applied

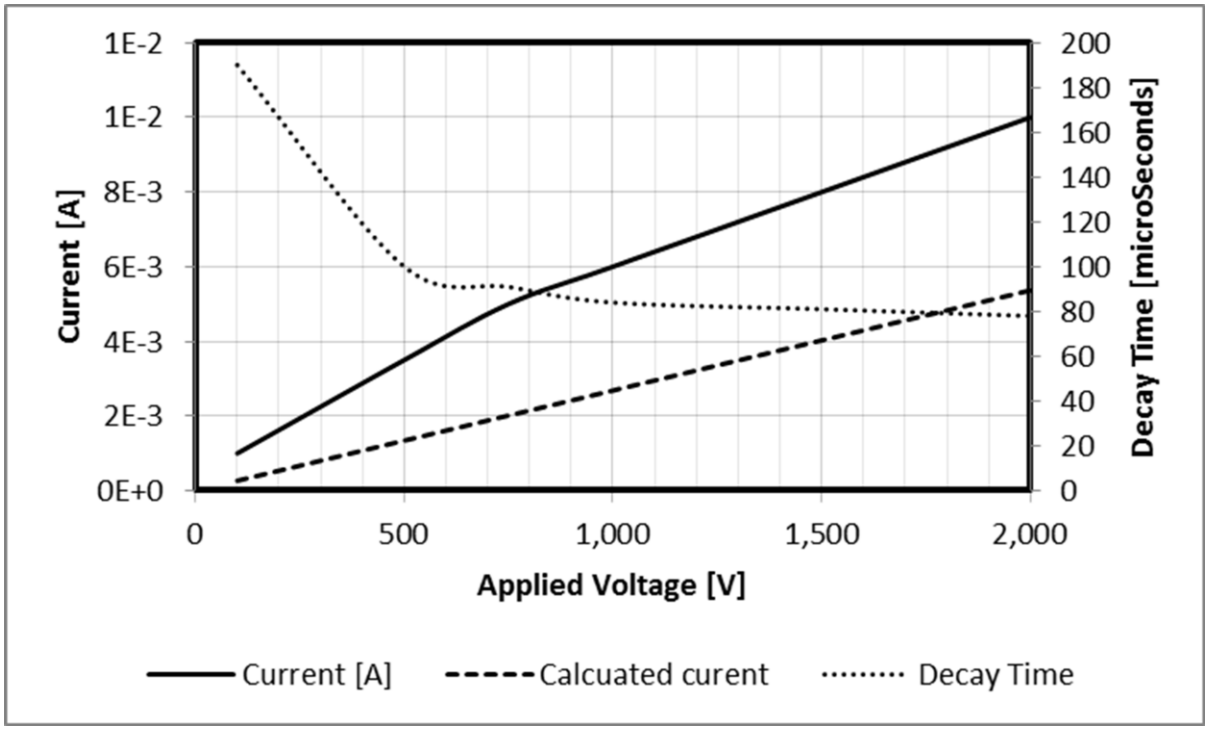

Figure 15-4: Maximum current delivered and decay time for pulses delivered with amplitudes between 100 and 2000 V.

voltages, the current delivered was greater than that calculated based on low voltage impedance measurements. This indicates that some level of electroporation is occurring even at the lowest voltages, resulting in a change in electrical properties of the tissue.

The decay times for the pulses at each voltage are shown in Figure 3. At 100 V, the pulse decays off over a relatively long 180 microseconds. At 500 V and above, this decay time has reduced to 100 microseconds or less. This change in decay time indicates that a more substantial change is occurring within the tissue, presumably IRE. Above 500 V, the slight decrease in decay time indicates an increase in the extent of electroporation occurring. Though further investigation is necessary, monitoring the decay time of pulses delivered through the vasculature may provide a method of real time detection and monitoring of electroporation.

The red regions in Figure 15-5 indicate regions of live tissue, while the white regions indicate necrotic electroporated tissue with intact ECM. A large volume of the kidney underwent IRE. It is anticipated that blood clots in the vasculature prevented the entire organ from undergoing electroporation. This issue can be resolved by flushing the vasculature of the organ immediately after surgical resection or by working with tissues *in-vivo* where clotting can be prevented.

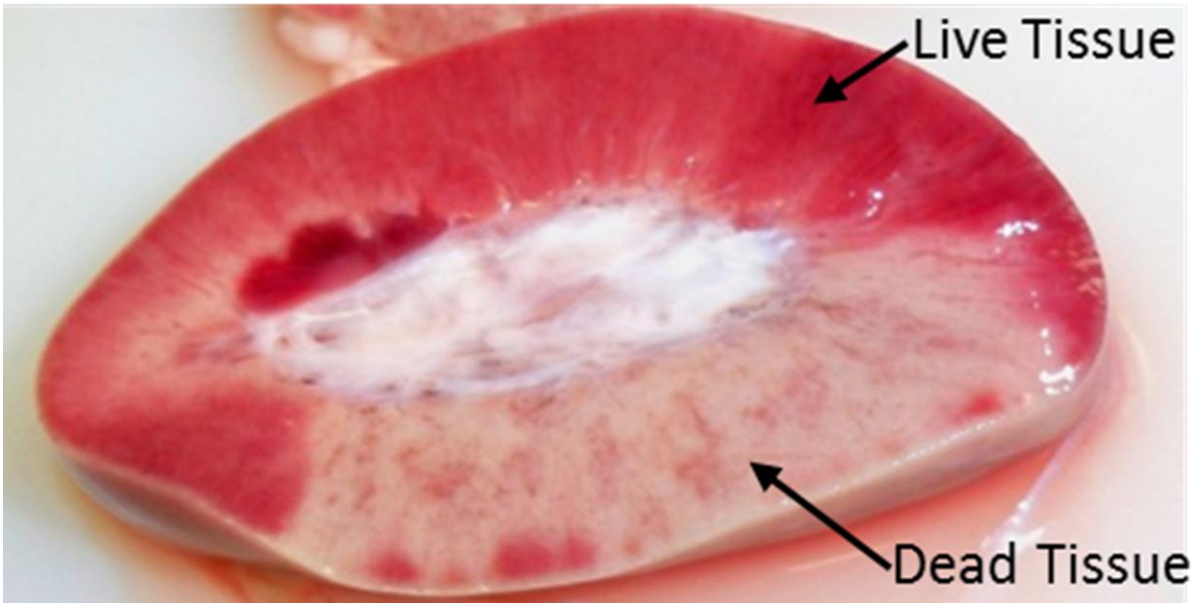

Figure 15-5: Kidney sections 30 minutes after pulsing. Dark red areas indicate live tissue and white areas indicate regions ablated by the IRE pulses.

Numerical Methods and Results

Though the experimental results presented in this chapter were conducted in kidney, we have also used this method to deliver pulses to whole livers. The results from those studies are pending; however, the liver contains a highly repetitive and organized structure which facilitates the modeling of this technique. Preliminary multiphysics modeling was conducted to establish the feasibility of using the vascular system as a pathway for electrical pulse delivery. The electric field distribution, which is the key factor for the development of pores (reversible or irreversible) in the cell membrane, was modeled using a finite element method. The Comsol Multiphysics was utilized to solve for the electric potential (ϕ) which obeys the Laplace Equation

$$\nabla \cdot (\sigma \nabla \phi) = 0$$

where σ is the electrical conductivity. Three liver tissue models were developed representing the liver structure with different levels of detail.

Element	Conductivity (S/m)
Liver	4.10E-01
Connective tissue	4.10E-02
Perfusate	1.40E+00
External Electrodes	5.998E+07

Table 15-1: Electrical conductivity values for elements used in all models.

Model 1: Initially, the liver was modeled as a 2 cm thick homogenous structure with 1 cm diameter plate electrodes on either side of the tissue. This model was used to correlate experimental lesions to electric field intensities. A single 10 microsecond 1500V/cm pulse was delivered to the top electrode while the bottom electrode was grounded.

Model 2: The liver is a complex organ populated by numerous sets of vasculature branches, lymph and bile ducts. Branches of the hepatic portal vein and hepatic artery deliver blood to basic functional units, lobules which are structurally functioned to filter blood, remove bacteria, and produce bile. Blood driven through the lobules eventually reach a large central venula which drain into the hepatic vein and return blood to the circulatory system. While under perfusion, a perfusate replaces blood as the fluid traveling through the vasculature, however, bile production has been observed to continue for up to 24 hours. A second model multi-scale was produced to understand how the complex vasculature effects the electric field distribution when two different

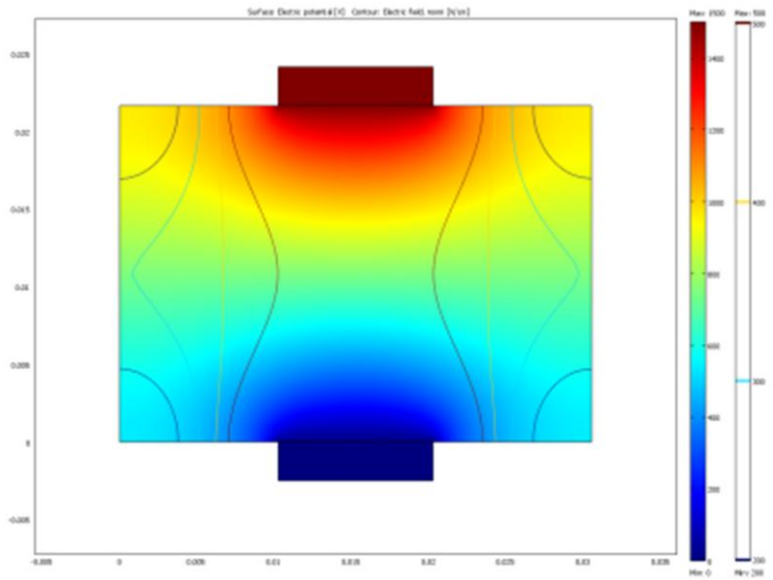

Figure 15-6: Electric potential and electric field contours developed in a numerical representation of previous experiments. These results show that an electric field intensity of approximately 400V/cm is experienced by simulated tissue in regions where experimental tissue developed lesions.

modalities of voltage application are used. The first modality used traditional electrodes placed outside of the tissue, while the second used the central venula as the voltage source and external electrodes as grounds. Each lobule was modeled as a hexagon with an equivalent radius of 1mm surrounded by a 5 micron connective tissue layer and a 200 micron diameter central venula which is consistent with swine histology. A single 10 microsecond 1500V/cm pulse was again simulated.

The electric field distribution within the tissue did not vary significantly with the additional inhomogeneity caused by the lobule epithelial layers when external electrodes are used. The most significant alterations occurred in proximity to the more highly conductive central venula. When the central venula of each lobule is charged to 1500V, a significantly different electric field distribution is formed. Regions of tissue which reach a high enough electric field to become irreversibly electroporated extend only approximately 0.5 cm into the tissue. *Though this modality of electric field application is not sufficient for total decellularization, it may be an effective means by which tumors close to the surface of highly vascularized organs may be treated.*

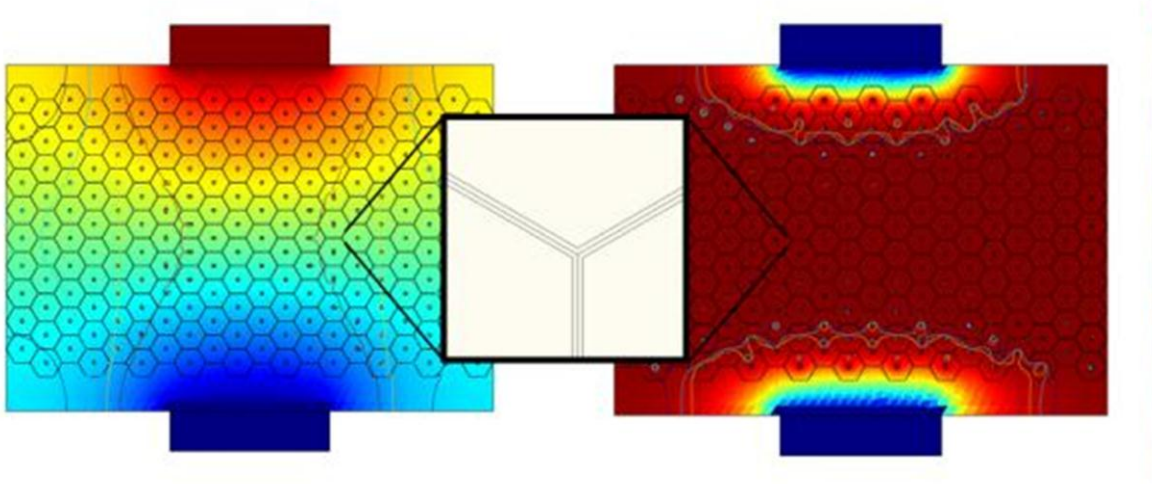

Figure 15-7: Numerical results of two different simulations with lobule level details (Model 2). (Left) External Electrodes are charged with either 1500V (top) or set to ground (bottom). The electric field distribution using this modality did not significantly change with the added inhomogeneity. (Right) Central venula of each lobule is charged to 1500V while external electrodes are grounded.

The models presented in Figure 15-7 are not completely physiologically exact as fluid readily flows from the portal arterioles and venules through the lobule into the central venula. Inclusion of these features in a tissue level model with near cellular resolution would be too computationally expensive for practical means so they were not included in the bulk model. Despite this, this model helps build a significant level of intuition as to how the vasculature of an organ can be used to deliver IRE treatments.

Model 3: Model 3 incorporates the portal arterioles, portal venules, and bile ducts at the vertices of a single lobule. The central vain is surrounded by bulk liver tissue. The magnitude of the applied 10 microsecond pulse was varied until an electric field distribution, in the range of that seen in bulk liver tissue, developed.

The results from this simulation show that the development of an IRE inducing electric field within a single lobule is feasible using the organ's vasculature. Additionally, it was found that a 50V pulse is significant enough to raise the electric field to IRE inducing levels. This is far below the 1500V pulse necessary to induce IRE when the electric field is applied across the entire tissue construct. It can be seen from Figure 15-8(right) and histological samples that there is a complex microvasculature network which connects the portal arterioles and venules from the central vein. Between the vasculature there are hepatocytes which secrete bile into the bile ducts.

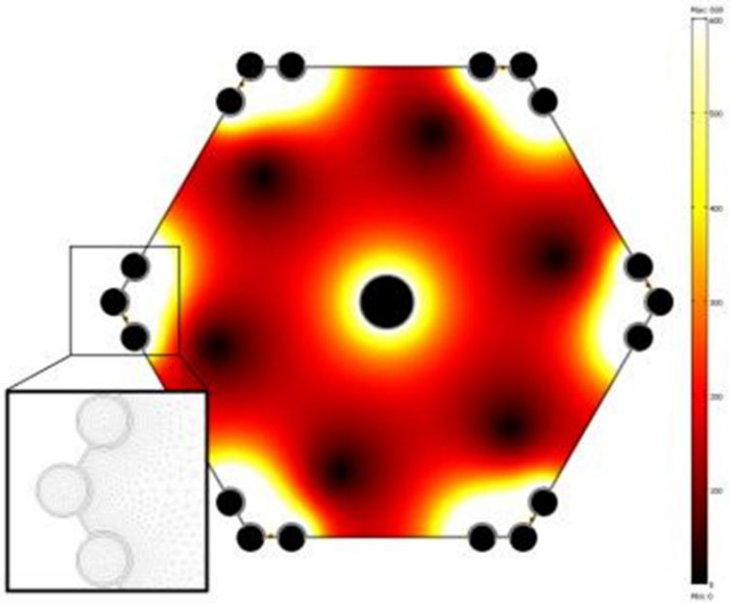

Figure 15-8: Simulated electric field distribution with a single lobule (left) when a 50V 100 microsecond pulse is administered to the bile duct and the central venule, portal venule and portal arteriole are grounded. Schematic representation of a liver lobule (right) shows the complex vascular network of these functional units.

Models 1 and 2 assume that these microvasculature networks present a significant resistance to the flow of current and the internal constituents of the lobule can be modeled as a heterogeneous tissue. This is a reasonable assumption to make where vascular occlusion may occur if erythrocytes (*in vivo*) or epithelial cells are damaged by the electric field.

Diameter (m)	Area (m^2)	Length (m)	Resistance (ohms)
1.0E-02	7.85E-05	1.0E-01	9.09E+02
1.0E-03	7.85E-07	1.0E-02	9.09E+03
1.0E-04	7.85E-09	1.0E-03	9.09E+04
1.0E-05	7.85E-11	1.0E-04	9.09E+05

Table 15-2: Resistance of vessels of decreasing diameter with a 10:1 length to diameter ratio and a fluid conductivity of 1.4S/m

An approximation of the resistance (R) of vasculature and microvasculature can be easily achieved if the fluid conductivity (ρ) is known by solving the constitutive relation

$$R = \frac{\rho L}{A}$$

where L and A are the length of the vessel and the vessel's cross sectional area respectively. The results presented in Table 15-2 show that the resistance of a 10μm diameter vessel 100μm long can be as high as 90kΩ when the vessel is filled with phosphate buffered solution. While

significant, this resistance is not high enough to prevent current flow through microvasculature. Additionally, the immense number of microvessels which are connected in parallel throughout the organ should drastically reduce the overall electrical resistance.

Conclusion

This work shows that large volumes of tissue can be ablated by using the vasculature as the conductive pathways to deliver pulses deep into an organ. These preliminary results show the potential of this technique, however, the minimum threshold and optimum pulse parameters to induce IRE in this modality remain to be established. Future work will focus on ablating the cells within an entire organ, isolating lobes and regions within an organ, and treating well vascularized tumors.

Chapter 16: Appendix

During the course of my academic career at Virginia Tech, I have had the opportunity to collaborate with a number of brilliant and hardworking investigators. This chapter contains the manuscripts that have been published as a result of those collaborations.

Contactless dielectrophoresis: a new technique for cell manipulation

This manuscript describes the original concept cDEP device. We first demonstrate that cells can be manipulated and trapped using a device containing insulating barriers that isolate fluid electrodes from a low conductivity sample channel. Additionally, we show that the DEP force and electro-rotational torque act differently on cells from distinct cell lines.

Selective concentration of human cancer cells using contactless dielectrophoresis

This manuscript was the first attempt to isolate live cells from different cell lines. We demonstrated that the voltage necessary to trap cells was different between breast cancer cell lines with different metastatic potential. This manuscript offers an extensive analysis of the Clausius-Mossotti factor for similar cells.

Dielectrophoretic differentiation of mouse ovarian surface epithelial cells, macrophages, and fibroblasts using contactless dielectrophoresis

This manuscript continues to explore the possibility of using cDEP to isolate rare cells. We evaluate the dielectrophoretic response of mouse ovarian surface epithelial (MOSE) cells as they transition from benign to highly metastatic. The work shows that the voltage necessary to trap early and late stage MOSE cells are significantly different and that there is a large difference in the dielectrophoretic response between the MOSE cells and normal cells. This work provides the foundation necessary to develop cDEP into an early cancer screening technology

Theoretical Considerations of Tissue Electroporation with High Frequency Bipolar Pulses

This manuscript is the basis for all of the HFIRE work presented in this dissertation. We demonstrate that high frequency pulses can short through fat and epithelial layers to increase the transmembrane potential of tumor cells located deep within tissue.

High-frequency irreversible electroporation (H-FIRE) for non-thermal ablation without muscle contraction

This manuscript presents the first experimental validation of HFIRE to ablate tissue and eliminate muscle contractions associated with traditional IRE therapies. This work forms the basis for all of our clinical work thus far.

References

1 Han, A., Yang, L. & Frazier, A. B. Quantification of the heterogeneity in breast cancer cell lines using whole-cell impedance spectroscopy. *Clin. Cancer. Res.* **13**, 139-143, doi:10.1158/1078-0432.ccr-06-1346 (2007).

2 Gimsa, J., Muller, T., Schnelle, T. & Fuhr, G. Dielectric spectroscopy of single human erythrocytes at physiological ionic strength: Dispersion of the cytoplasm. *BpJ* **71**, 495-506 (1996).

3 Pethig, R. & Kell, D. B. The passive electrical-properties of biological-systems - their significance in physiology, biophysics and biotechnology. *PMB* **32**, 933-970 (1987).

4 Yang, J. *et al.* Dielectric properties of human leukocyte subpopulations determined by electrorotation as a cell separation criterion. *BpJ* **76**, 3307-3314 (1999).

5 Sancho, M., Martinez, G., Munoz, S., Sebastian, J. L. & Pethig, R. Interaction between cells in dielectrophoresis and electrorotation experiments. *Biomicrofluidics* **4**, doi:10.1063/1.3454129 (2010).

6 Cruz, J. M. & Garcia-Diego, F. J. Dielectrophoretic motion of oblate spheroidal particles. Measurements of motion of red blood cells using the Stokes method. *Journal of Physics D-Applied Physics* **31**, 1745-1751 (1998).

7 Gossett, D. R. *et al.* Label-free cell separation and sorting in microfluidic systems. *Anal. Bioanal. Chem.* **397**, 3249-3267, doi:10.1007/s00216-010-3721-9 (2010).

8 Lapizco-Encinas, B. H., Simmons, B. A., Cummings, E. B. & Fintschenko, Y. Insulator-Based Dielectrophoresis for the Selective Concentration and Separation of Live Bacteria in Water. *Electrophoresis* **25**, 1695-1704 (2004).

9 Kumar, A. & Bhardwaj, A. Methods in cell separation for biomedical application: cryogels as a new tool. *Biomedical Materials* **3**, doi:034008
10.1088/1748-6041/3/3/034008 (2008).

10 Mohamed, H., Murray, M., Turner, J. N. & Caggana, M. Isolation of tumor cells using size and deformation. *J. Chromatogr.* **1216**, 8289-8295, doi:10.1016/j.chroma.2009.05.036 (2009).

11 Brody, J. P., Osborn, T. D., Forster, F. K. & Yager, P. A planar microfabricated fluid. *Sensors and Actuators a-Physical* **54**, 704-708 (1996).

12 Chen, X., Cui, D. F., Liu, C. C. & Li, H. Microfluidic chip for blood cell separation and collection based on crossflow filtration. *Sens. Actuator B-Chem.* **130**, 216-221, doi:10.1016/j.snb.2007.07.126 (2008).

13 VanDelinder, V. & Groisman, A. Separation of plasma from whole human blood in a continuous cross-flow in a molded microfluidic device. *AnaCh* **78**, 3765-3771, doi:10.1021/ac060042r (2006).

14 VanDelinder, V. & Groisman, A. Perfusion in microfluidic cross-flow: Separation of white blood cells from whole blood and exchange of medium in a continuous flow. *AnaCh* **79**, 2023-2030, doi:10.1021/ac061659b (2007).

15 Huang, L. R., Cox, E. C., Austin, R. H. & Sturm, J. C. Continuous particle separation through deterministic lateral displacement. *Sci* **304**, 987-990, doi:10.1126/science.1094567 (2004).

16 Davis, J. A. *et al.* Deterministic hydrodynamics: Taking blood apart. *Proc. Natl. Acad. Sci. U. S. A.* **103**, 14779-14784, doi:10.1073/pnas.0605967103 (2006).

17 Inglis, D. W., Lord, M. & Nordon, R. E. Scaling deterministic lateral displacement arrays for high throughput and dilution-free enrichment of leukocytes. *JMiMi* **21**, doi:054024
10.1088/0960-1317/21/5/054024 (2011).

18 Choi, S. & Park, J. K. Continuous hydrophoretic separation and sizing of microparticles using slanted obstacles in a microchannel. *LChip* **7**, 890-897, doi:10.1039/b701227f (2007).

19 Stroock, A. D., Dertinger, S. K., Whitesides, G. M. & Ajdari, A. Patterning flows using grooved surfaces. *AnaCh* **74**, 5306-5312, doi:10.1021/ac0257389 (2002).

20 Choi, S., Song, S., Choi, C. & Park, J.-K. Continuous blood cell separation by hydrophoretic filtration. *LChip* **7**, 1532-1538, doi:10.1039/b705203k (2007).

21 Choi, S., Song, S., Choi, C. & Park, J. K. Microfluidic Self-Sorting of Mammalian Cells to Achieve Cell Cycle Synchrony by Hydrophoresis. *AnaCh* **81**, 1964-1968, doi:10.1021/ac8024575 (2009).

22 Choi, S., Ku, T., Song, S., Choi, C. & Park, J.-K. Hydrophoretic high-throughput selection of platelets in physiological shear-stress range. *LChip* **11**, 413-418, doi:10.1039/c0lc00148a (2011).

23 Di Carlo, D. Inertial microfluidics. *LChip* **9**, 3038-3046, doi:10.1039/b912547g (2009).

24 Di Carlo, D., Edd, J. F., Humphry, K. J., Stone, H. A. & Toner, M. Particle Segregation and Dynamics in Confined Flows. *PhRvL* **102**, doi:094503
10.1103/PhysRevLett.102.094503 (2009).

25 Matas, J. P., Morris, J. F. & Guazzelli, E. Inertial migration of rigid spherical particles in Poiseuille flow. *JFM* **515**, 171-195, doi:10.1017/s0022112004000254 (2004).
26 Berger, S. A., Talbot, L. & Yao, L. S. FLOW IN CURVED PIPES. *AnRFM* **15**, 461-512, doi:10.1146/annurev.fl.15.010183.002333 (1983).
27 Gossett, D. R. & Di Carlo, D. Particle Focusing Mechanisms in Curving Confined Flows. *AnaCh* **81**, 8459-8465, doi:10.1021/ac901306y (2009).
28 Sudarsan, A. P. & Ugaz, V. M. Multivortex micromixing. *Proc. Natl. Acad. Sci. U. S. A.* **103**, 7228-7233, doi:10.1073/pnas.0507976103 (2006).
29 Lee, M. G., Choi, S. & Park, J.-K. Inertial separation in a contraction-expansion array microchannel. *J. Chromatogr.* **1218**, 4138-4143, doi:10.1016/j.chroma.2010.11.081 (2011).
30 Hur, S. C., Henderson-MacLennan, N. K., McCabe, E. R. B. & Di Carlo, D. Deformability-based cell classification and enrichment using inertial microfluidics. *LChip* **11**, 912-920, doi:10.1039/c0lc00595a (2011).
31 Yao, B. *et al.* A microfluidic device based on gravity and electric force driving for flow cytometry and fluorescence activated cell sorting. *LChip* **4**, 603-607, doi:10.1039/b408422e (2004).
32 Huh, D. *et al.* Gravity-driven microfluidic particle sorting device with hydrodynamic separation amplification. *AnaCh* **79**, 1369-1376, doi:10.1021/ac061542n (2007).
33 Warrick, J., Casavant, B., Frisk, M. & Beebe, D. A Microfluidic Cell Concentrator. *AnaCh* **82**, 8320-8326, doi:10.1021/ac101866p (2010).
34 Fuhr, G., Hagedorn, R., Muller, T., Wagner, B. & Benecke, W. in *Micro Electro Mechanical Systems, 1991, MEMS '91, Proceedings. An Investigation of Micro Structures, Sensors, Actuators, Machines and Robots. IEEE.* 259-264.
35 Fuhr, G., Glasser, H., Muller, T. & Schnelle, T. CELL MANIPULATION AND CULTIVATION UNDER AC ELECTRIC-FIELD INFLUENCE IN HIGHLY CONDUCTIVE CULTURE MEDIA. *Biochimica Et Biophysica Acta-General Subjects* **1201**, 353-360 (1994).
36 Gascoyne, P. R. C., Noshari, J., Anderson, T. J. & Becker, F. F. Isolation of rare cells from cell mixtures by dielectrophoresis. *Electrophoresis* **30**, 1388-1398, doi:10.1002/elps.200800373 (2009).
37 Asbury, C. L. & van den Engh, G. Trapping of DNA in nonuniform oscillating electric fields. *BpJ* **74**, 1024-1030 (1998).
38 Muller, T. *et al.* High frequency electric fields for trapping of viruses. *Biotechnol. Tech.* **10**, 221-226 (1996).
39 Archer, S., Li, T. T., Evans, A. T., Britland, S. T. & Morgan, H. Cell reactions to dielectrophoretic manipulation. *BBRC* **257**, 687-698 (1999).
40 Srivastava, S. K., Daggolu, P. R., Burgess, S. C. & Minerick, A. R. Dielectrophoretic characterization of erythrocytes: Positive ABO blood types. *Electrophoresis* **29**, 5033-5046, doi:10.1002/elps.200800166 (2008).
41 Hwang, H., Lee, D. H., Choi, W. J. & Park, J. K. Enhanced discrimination of normal oocytes using optically induced pulling-up dielectrophoretic force. *Biomicrofluidics* **3**, doi:014103
10.1063/1.3086600 (2009).
42 Iliescu, C., Tresset, G., Yu, L. M. & Xu, G. L. 3D Dielectrophoretic Chips: Trapping and Separation of Cell Populations. *Romanian Journal of Information Science and Technology* **13**, 49-64 (2010).
43 Cummings, E. B. & Singh, A. K. Dielectrophoresis in microchips containing arrays of insulating posts: Theoretical and experimental results. *AnaCh* **75**, 4724-4731, doi:10.1021/ac0340612 (2003).
44 Lapizco-Encinas, B. H., Davalos, R. V., Simmons, B. A., Cummings, E. B. & Fintschenko, Y. An insulator-based (electrodeless) dielectrophoretic concentrator for microbes in water. *J. Microbiol. Methods* **62**, 317-326 (2005).
45 Cummings, E. B. & Singh, A. K. in *Conference on Microfluidic Devices and Systems III.* (ed C. H. Becker H. Mastrangelo) 164-173.
46 Lapizco-Encinas, B. H., Ozuna-Chacon, S. & Rito-Palomares, M. Protein manipulation with insulator-based dielectrophoresis and direct current electric fields. *J. Chromatogr.* **1206**, 45-51, doi:10.1016/j.chroma.2008.05.077 (2008).
47 Gallo-Villanueva, R. C., Rodriguez-Lopez, C. E., Diaz-De-La-Garza, R. I., Reyes-Betanzo, C. & Lapizco-Encinas, B. H. DNA manipulation by means of insulator-based dielectrophoresis employing direct current electric fields. *Electrophoresis* **30**, 4195-4205, doi:10.1002/elps.200900355 (2009).

48 Moncada-Hernandez, H. & Lapizco-Encinas, B. H. Simultaneous concentration and separation of microorganisms: insulator-based dielectrophoretic approach. *Anal. Bioanal. Chem.* **396**, doi::10.1007/s00216-009-3422-4 (2010).
49 Davalos, R. V. *et al.* Performance impact of dynamic surface coatings on polymeric insulator-based dielectrophoretic particle separators. *Anal. Bioanal. Chem.* **390**, 847-855, doi:10.1007/s00216-007-1426-5 (2008).
50 Sabounchi, P. *et al.* Sample concentration and impedance detection on a microfluidic polymer chip. *BioMi* **10**, 661-670, doi:10.1007/s10544-008-9177-4 (2008).
51 Pysher, M. D. & Hayes, M. A. Electrophoretic and dielectrophoretic field gradient technique for separating bioparticles. *AnaCh* **79**, 4552-4557, doi:10.1021/ac070534j (2007).
52 Shafiee, H., Caldwell, J. L., Sano, M. B. & Davalos, R. V. Contactless dielectrophoresis: a new technique for cell manipulation. *BioMi* **11**, 997-1006, doi:10.1007/s10544-009-9317-5 (2009).
53 Shafiee, H., Sano, M. B., Henslee, E. A., Caldwell, J. L. & Davalos, R. V. Selective isolation of live/dead cells using contactless dielectrophoresis (cDEP). *LChip*, doi:10.1039/b920590j (2010).
54 Shafiee, H., Caldwell, J. L. & Davalos, R. V. A Microfluidic System for Biological Particle Enrichment Using Contactless Dielectrophoresis. *Jala* **15**, 224-232, doi:10.1016/j.jala.2010.02.003 (2010).
55 Sano, M. B., Caldwell, J. L. & Davalos, R. V. Modeling and Development of a Low Frequency Contactless Dielectrophoresis (cDEP) Platform to Sort Cancer Cells from Dilute Whole Blood Samples. *Biosens. Bioelectron.*, doi:10.1016/J.BIOS.2011.07.048 (2011).
56 Sano, M. B., Henslee, E. A., Schmelz, E. & Davalos, R. V. Contactless Dielectrophoretic Spectroscopy: Examination of the Dielectric Properties of Cells Found in Blood. *Electrophoresis* **DOI 10.1002/elps.2201100351** (2011).
57 Pohl, H. A. & Plymale, C. E. Continuous Separations of Suspensions by Nonuniform Electric Fields in Liquid Dielectrics. *JElS* **107**, 390-396 (1960).
58 Barz, D. P. J. & Ehrhard, P. Model and verification of electrokinetic flow and transport in a micro-electrophoresis device. *LChip* **5**, 949-958, doi:10.1039/b503696h (2005).
59 Tandon, V., Bhagavatula, S. K., Nelson, W. C. & Kirby, B. J. zeta potential and electroosmotic mobility in microfluidic devices fabricated from hydrophobic polymers: 1. The origins of charge. *Electrophoresis* **29**, 1092-1101, doi:10.1002/elps.200700734 (2008).
60 Kang, Y. J. & Li, D. Q. Electrokinetic motion of particles and cells in microchannels. *Microfluid. Nanofluid.* **6**, 431-460, doi:10.1007/s10404-009-0408-7 (2009).
61 Turcu, I. & Lucaciu, C. M. DIELECTROPHORESIS - A SPHERICAL-SHELL MODEL. *Journal of Physics a-Mathematical and General* **22**, 985-993, doi:10.1088/0305-4470/22/8/014 (1989).
62 Benguigui, L. & Lin, I. J. MORE ABOUT THE DIELECTROPHORETIC FORCE. *JAP* **53**, 1141-1143, doi:10.1063/1.329875 (1982).
63 Suehiro, J., Hamada, R., Noutomi, D., Shutou, M. & Hara, M. Selective detection of viable bacteria using dielectrophoretic impedance measurement method. *Journal of Electrostatics* **57**, 157-168 (2003).
64 Li, H. & Bashir, R. Dielectrophoretic separation and manipulation of live and heat-treated cells of Listeria on microfabricated devices with interdigitated electrodes. *Sensors and Actuators B-Chemical* **86**, 215-221 (2002).
65 Huang, Y., Holzel, R., Pethig, R. & Wang, X. B. Differences in the AC electrodynamics of viable and non-viable yeast cells determined through combined dielectrophoresis and electrorotation studies. *Phys Med Biol* **37**, 1499-1517 (1992).
66 Docoslis, A., Kalogerakis, N., Behie, L. A. & Kaler, K. V. A novel dielectrophoresis-based device for the selective retention of viable cells in cell culture media. *Biotechnol Bioeng* **54**, 239-250, doi:10.1002/(SICI)1097-0290(19970505)54:3<239::AID-BIT5>3.0.CO;2-G (1997).
67 Lapizco-Encinas, B. H., Simmons, B. A., Cummings, E. B. & Fintschenko, Y. Dielectrophoretic concentration and separation of live and dead bacteria in an array of insulators. *Anal Chem* **76**, 1571-1579, doi:10.1021/ac034804j (2004).
68 Blake A. Simmons, G. J. M., Rafael V.Davalos, Gregory J. Fiechtner, Yolanda Fintschenko, and Eric B. Cummings. The Development of Polymeric Devices as Dielectrophoretic Separators and Concentrators *MRS BULETIN* **31** (2006).
69 Sabounchi, P. *et al.* Sample concentration and impedance detection on a microfluidic polymer chip. *Biomed Microdevices* **10**, 661-670, doi:10.1007/s10544-008-9177-4 (2008).
70 Shafiee, H., Caldwell, J. L., Sano, M. B. & Davalos, R. V. Contactless dielectrophoresis: a new technique for cell manipulation. *Biomed Microdevices*, doi:10.1007/s10544-009-9317-5 (2009).

71 Borgatti, M. *et al.* Antibody-antigen interactions in dielectrophoresis buffers for cell manipulation on dielectrophoresis-based Lab-on-a-chip devices. *Minerva Biotechnol.* **19**, 71-74 (2007).
72 Del Bene, F. *et al.* A model-based approach to the in vitro evaluation of anticancer activity. *Cancer Chemotherapy and Pharmacology* **63**, 827-836, doi:10.1007/s00280-008-0798-3 (2009).
73 Ntouroupi, T. G. *et al.* Detection of circulating tumour cells in peripheral blood with an automated scanning fluorescence microscope. *Br. J. Cancer* **99**, 789-795, doi:10.1038/sj.bjc.6604545 (2008).
74 Sarantseva, S. V. & Schwarzman, A. L. Modern genetic approaches to searching for targets for medicinal preparations. *Russian Journal of Genetics* **45**, 761-770, doi:10.1134/s1022795409070011 (2009).
75 Tatosian, D. A. & Shuler, M. L. A Novel System for Evaluation of Drug Mixtures for Potential Efficacy in Treating Multidrug Resistant Cancers. *Biotechnology and Bioengineering* **103**, 187-198, doi:10.1002/bit.22219 (2009).
76 Leary, J. F., Reece, L. N., Szaniszlo, P., Prow, T. & Wang, N. in *Conference on Clinical Diagnostic Systems.* (ed G. E. Cohn) 16-27 (Spie-Int Soc Optical Engineering, 2001).
77 Flanagan, L. A. *et al.* Unique dielectric properties distinguish stem cells and their differentiated progeny. *Stem Cells* **26**, 656-665, doi:10.1634/stemcells.2007-0810 (2008).
78 Takagi, J., Yamada, M., Yasuda, M. & Seki, M. Continuous particle separation in a microchannel having asymmetrically arranged multiple branches. *LChip* **5**, 778-784, doi:10.1039/b501885d (2005).
79 Vona, G. *et al.* Isolation by size of epithelial tumor cells - A new method for the immunomorphological and molecular characterization of circulating tumor cells. *Am. J. Pathol.* **156**, 57-63 (2000).
80 Huang, R. *et al.* A microfluidics approach for the isolation of nucleated red blood cells (NRBCs) from the peripheral blood of pregnant women. *Prenatal Diagn.* **28**, 892-899, doi:10.1002/pd.2079 (2008).
81 Mach, A. J. & Di Carlo, D. Continuous Scalable Blood Filtration Device Using Inertial Microfluidics. *Biotechnol. Bioeng.* **107**, 302-311, doi:10.1002/bit.22833 (2010).
82 Martinez-Lopez, J. I. *et al.* Characterization of electrokinetic mobility of microparticles in order to improve dielectrophoretic concentration. *Anal. Bioanal. Chem.* **394**, 293-302, doi:10.1007/s00216-009-2626-y (2009).
83 Ros, A., Hellmich, W., Regtmeier, J., Duong, T. T. & Anselmetti, D. Bioanalysis in structured microfluidic systems. *Electrophoresis* **27**, 2651-2658, doi:10.1002/elps.200500923 (2006).
84 Yang, J., Huang, Y., Wang, X. B., Becker, F. F. & Gascoyne, P. R. C. Cell separation on microfabricated electrodes using dielectrophoretic/gravitational field flow fractionation. *AnaCh* **71**, 911-918 (1999).
85 Hawkins, B. G., Smith, A. E., Syed, Y. A. & Kirby, B. J. Continuous-flow particle separation by 3D insulative dielectrophoresis using coherently shaped, dc-biased, ac electric fields. *AnaCh* **79**, 7291-7300, doi:10.1021/ac0707277 (2007).
86 Chen, K. P., Pacheco, J. R., Hayes, M. A. & Staton, S. J. R. Insulator-based dielectrophoretic separation of small particles in a sawtooth channel. *Electrophoresis* **30**, 1441-1448, doi:10.1002/elps.200800833 (2009).
87 Staton, S. J. R., Chen, K. P., Taylor, T. J., Pacheco, J. R. & Hayes, M. A. Characterization of particle capture in a sawtooth patterned insulating electrokinetic microfluidic device. *Electrophoresis* **31**, 3634-3641, doi:10.1002/elps.201000438 (2010).
88 Hughes, M. P. Strategies for dielectrophoretic separation in laboratory-on-a-chip systems. *Electrophoresis* **23**, 2569-2582 (2002).
89 Holmes, D., Green, N. G. & Morgan, H. Microdevices for dielectrophoretic flow-through cell separation. *IEEE Eng. Med. Biol. Mag.* **22**, 85-90 (2003).
90 Bao, N., Le, T. T., Cheng, J.-X. & Lu, C. Microfluidic electroporation of tumor and blood cells: observation of nucleus expansion and implications on selective analysis and purging of circulating tumor cells. *Integrative Biology* **2**, 113-120, doi:10.1039/b919820b (2010).
91 Doyeux, V., Podgorski, T., Peponas, S., Ismail, M. & Coupier, G. Spheres in the vicinity of a bifurcation: elucidating the Zweifach-Fung effect. *JFM* **674**, 359-388, doi:10.1017/s0022112010006567 (2011).
92 Kawasaki, E. S. *et al.* DIAGNOSIS OF CHRONIC MYELOID AND ACUTE LYMPHOCYTIC LEUKEMIAS BY DETECTION OF LEUKEMIA-SPECIFIC MESSENGER-RNA SEQUENCES AMPLIFIED INVITRO. *Proc. Natl. Acad. Sci. U. S. A.* **85**, 5698-5702 (1988).
93 Mostert, B., Sleijfer, S., Foekens, J. A. & Gratama, J. W. Circulating tumor cells (CTCs): Detection methods and their clinical relevance in breast cancer. *Cancer Treat. Rev.* **35**, 463-474, doi:10.1016/j.ctrv.2009.03.004 (2009).
94 Hayes, D. F. *et al.* Circulating tumor cells at each follow-up time point during therapy of metastatic breast cancer patients predict progression-free and overall survival. *Clinical Cancer Research* **12**, 4218-4224 (2006).

95 Budd, G. T. *et al.* Circulating Tumor Cells versus Imaging--Predicting Overall Survival in Metastatic Breast Cancer. *Clinical Cancer Research* **12**, 6403-6409, doi:10.1158/1078-0432.ccr-05-1769 (2006).
96 Osman, I. *et al.* Detection of circulating cancer cells expressing uroplakins and epidermal growth factor receptor in bladder cancer patients. *International Journal of Cancer* **111**, 934-939, doi:10.1002/ijc.20366 (2004).
97 Galan, M. *et al.* Detection of occult breast cancer cells by amplification of CK19 mRNA by reverse transcriptase-polymerase chain reaction: Role of surgical manipulation. *Anticancer Research* **22**, 2877-2884 (2002).
98 Dingemans, A. M. C., Brakenhoff, R. H., Postmus, P. E. & Giaccone, G. Detection of cytokeratin-19 transcripts by reverse transcriptase-polymerase chain reaction in lung cancer cell lines and blood of lung cancer patients. *Laboratory Investigation* **77**, 213-220 (1997).
99 Berteau, P. *et al.* Molecular detection of circulating prostate cells in cancer II: Comparison of prostate epithelial cells isolation procedures. *Clinical Chemistry* **44**, 1750-1753 (1998).
100 Berteau, P. *et al.* Influence of blood storage and sample processing on molecular detection of circulating prostate cells in cancer. *Clinical Chemistry* **44**, 677-679 (1998).
101 Koike, E. *et al.* Endoscopic ultrasonography in patients with thyroid cancer: Its usefulness and limitations for evaluating esophagopharyngeal invasion. *Endoscopy* **34**, 457-460 (2002).
102 Schroder, C. P. *et al.* Detection of micrometastatic breast cancer by means of real time quantitative RT-PCR and immunostaining in perioperative blood samples and sentinel nodes. *International Journal of Cancer* **106**, 611-618, doi:10.1002/ijc.11295 (2003).
103 Traweek, S. T., Liu, J. & Battifora, H. KERATIN GENE-EXPRESSION IN NONEPITHELIAL TISSUES - DETECTION WITH POLYMERASE CHAIN-REACTION. *American Journal of Pathology* **142**, 1111-1118 (1993).
104 Pohl, H. A. The Motion and Precipitation of Suspensoids in Divergent Electric Fields. *JAP* **22**, 869-871 (1951).
105 Masuda, S., Itagaki, T. & Kosakada, M. DETECTION OF EXTREMELY SMALL PARTICLES IN THE NANOMETER AND IONIC SIZE RANGE. *ITIA* **24**, 740-744 (1988).
106 Becker, F. F. *et al.* The Removal of Human Leukemia-Cells from Blood Using Interdigitated Microelectrodes. *Journal of Physics D-Applied Physics* **27**, 2659-2662 (1994).
107 Shafiee, H., Caldwell, J. L., Sano, M. B. & Davalos, R. V. Contactless Dielectrophoresis: A New Technique For Cell Manipulation. *Biomedical Microdevices* (2009).
108 Shafiee, H., Sano, M. B., Henslee, E. A., Caldwell, J. L. & Davalos, R. V. Selective isolation of live/dead cells using contactless dielectrophoresis (cDEP). *LChip* **10**, 438-445, doi:10.1039/b920590j (2010).
109 Foster, K. R., Sauer, F. A. & Schwan, H. P. ELECTROROTATION AND LEVITATION OF CELLS AND COLLOIDAL PARTICLES. *BpJ* **63**, 180-190 (1992).
110 Docoslis, A., Kalogerakis, N., Behie, L. A. & Kaler, K. A novel dielectrophoresis-based device for the selective retention of viable cells in cell culture media. *Biotechnol. Bioeng.* **54**, 239-250 (1997).
111 Blythe, A. R. & Bloor, D. *Electrical properties of polymers*. 48 (Cambridge University Press, 2005).
112 Eddings, M. A., Johnson, M. A. & Gale, B. K. Determining the optimal PDMS-PDMS bonding technique for microfluidic devices. *JMiMi* **18**, doi:067001
10.1088/0960-1317/18/6/067001 (2008).
113 Whitesides, G. M. The origins and the future of microfluidics. *Nature* **442**, 368-373 (2006).
114 Ugaz, V. M. & Christensen, J. L. in *Microfluidic Technologies for Miniaturized Analysis Systems* (eds S. Hardt & F. Schonfeld) 393-438 (Springer, 2007).
115 Feng, J.-F. *et al.* Guided Migration of Neural Stem Cells Derived from Human Embryonic Stem Cells by an Electric Field. *Stem Cells* **30**, 349-355, doi:10.1002/stem.779 (2012).
116 Sun, Y.-S., Peng, S.-W., Lin, K.-H. & Cheng, J.-Y. Electrotaxis of lung cancer cells in ordered three-dimensional scaffolds. *Biomicrofluidics* **6**, 014102-014114 (2012).
117 Voyer, D., Frenea-Robin, M., Buret, F. & Nicolas, L. Improvements in the extraction of cell electric properties from their electrorotation spectrum. *Bioelectrochemistry* **79**, 25-30, doi:10.1016/j.bioelechem.2009.10.002 (2010).
118 Yang, L. & Bashir, R. Electrical/electrochemical impedance for rapid detection of foodborne pathogenic bacteria. *Biotechnol. Adv.* **26**, 135-150, doi:10.1016/j.biotechadv.2007.10.003 (2008).
119 Voldman, J. Electrical forces for microscale cell manipulation. *Annual Review of Biomedical Engineering* **8**, 425-454 (2006).

120 Bao, N., Wang, J. & Lu, C. Recent advances in electric analysis of cells in microfluidic systems. *Analytical and Bioanalytical Chemistry* **391**, 933-942 (2008).
121 Gagnon, Z. R. Cellular dielectrophoresis: Applications to the characterization, manipulation, separation and patterning of cells. *Electrophoresis* **32**, 2466-2487, doi:10.1002/elps.201100060 (2011).
122 Regtmeier, J., Eichhorn, R., Bogunovic, L., Ros, A. & Anselmetti, D. Dielectrophoretic Trapping and Polarizability of DNA: The Role of Spatial Conformation. *Analytical Chemistry* **82**, 7141-7149 (2010).
123 Ermolina, I., Milner, J. & Morgan, H. Dielectrophoretic investigation of plant virus particles: Cow Pea Mosaic Virus and Tobacco Mosaic Virus. *Electrophoresis* **27**, 3939-3948 (2006).
124 Hughes, M. P. & Hoettges, K. F. in *Principles of Bacterial Detection: Biosensors, Recognition Receptors and Microsystems* (eds Mohammed Zourob, Souna Elwary, & Anthony Turner) 895-907 (Springer New York, 2008).
125 Yang, F. *et al.* Dielectrophoretic separation of colorectal cancer cells. *Biomicrofluidics* **4**, 013204-013213 (2010).
126 Leonard, K. M. & Minerick, A. R. Explorations of ABO-Rh antigen expressions on erythrocyte dielectrophoresis: Changes in cross-over frequency. *Electrophoresis* **32**, 2512-2522, doi:10.1002/elps.201100077 (2011).
127 Martinez-Duarte, R., Gorkin-Iii, R. A., Abi-Samra, K. & Madou, M. J. The integration of 3D carbon-electrode dielectrophoresis on a CD-like centrifugal microfluidic platform. *Lab on a Chip* **10**, 1030-1043 (2010).
128 Jaramillo, M. d. C., Torrents, E., Martínez-Duarte, R., Madou, M. J. & Juárez, A. On-line separation of bacterial cells by carbon-electrode dielectrophoresis. *Electrophoresis* **31**, 2921-2928, doi:10.1002/elps.201000082 (2010).
129 Martinez-Duarte, R., Renaud, P. & Madou, M. J. A novel approach to dielectrophoresis using carbon electrodes. *Electrophoresis* **32**, 2385-2392, doi:10.1002/elps.201100059 (2011).
130 Baylon-Cardiel, J. L., Lapizco-Encinas, B. H., Reyes-Betanzo, C., Chávez-Santoscoy, A. V. & Martínez Chapa, S. O. Prediction of trapping zones in an Insulator-based dielectrophoretic device. *Lab on a Chip* **9**, 2896-2901 (2009).
131 Bhattacharya, S., Chao, T.-C. & Ros, A. Insulator-based dielectrophoretic single particle and single cancer cell trapping. *Electrophoresis* **32**, 2550-2558, doi:10.1002/elps.201100066 (2011).
132 Ivory, C. F. & Srivastava, S. K. Direct current dielectrophoretic simulation of proteins using an array of circular insulating posts. *Electrophoresis* **32**, 2323-2330, doi:10.1002/elps.201100115 (2011).
133 Gallo-Villanueva, R. C., Pérez-González, V. H., Davalos, R. V. & Lapizco-Encinas, B. H. Separation of mixtures of particles in a multipart microdevice employing insulator-based dielectrophoresis. *Electrophoresis* **32**, 2456-2465, doi:10.1002/elps.201100174 (2011).
134 Gallo-Villanueva, R., Jesús-Pérez, N., Martínez-López, J., Pacheco, A. & Lapizco-Encinas, B. Assessment of microalgae viability employing insulator-based dielectrophoresis. *Microfluidics and Nanofluidics* **10**, 1305-1315 (2011).
135 Srivastava, S. K., Artemiou, A. & Minerick, A. R. Direct current insulator-based dielectrophoretic characterization of erythrocytes: ABO-Rh human blood typing. *Electrophoresis* **32**, 2530-2540, doi:10.1002/elps.201100089 (2011).
136 Baylon-Cardiel, J. L., Jesús-Pérez, N. M., Chávez-Santoscoy, A. V. & Lapizco-Encinas, B. H. Controlled microparticle manipulation employing low frequency alternating electric fields in an array of insulators. *Lab on a Chip* **10**, 3235-3242 (2010).
137 Chávez-Santoscoy, A. V., Baylon-Cardiel, J. L., Moncada-Hernández, H. & Lapizco-Encinas, B. H. On the Selectivity of an Insulator-Based Dielectrophoretic Microdevice. *Separation Science and Technology* **46**, 384-394 (2011).
138 Lapizco-Encinas, B. H., Ozuna-Chacón, S. & Rito-Palomares, M. Protein Manipulation with Insulator-Based Dielectrophoresis and DC Electric Fields. *Journal of Chromatography A* **1206**, 45-51 (2008).
139 Moncada-Hernandez, H., Baylon-Cardiel, J. L., Pérez-González, V. H. & Lapizco-Encinas, B. H. Insulator-based dielectrophoresis of microorganisms: Theoretical and experimental results. *Electrophoresis* **32**, 2502-2511, doi:10.1002/elps.201100168 (2011).
140 Hawkins, B. G. & Kirby, B. J. Electrothermal flow effects in insulating (electrodeless) dielectrophoresis systems. *Electrophoresis* **31**, 3622-3633, doi:10.1002/elps.201000429 (2010).
141 Sridharan, S., Zhu, J., Hu, G. & Xuan, X. Joule heating effects on electroosmotic flow in insulator-based dielectrophoresis. *Electrophoresis* **32**, 2274-2281, doi:10.1002/elps.201100011 (2011).

142 Gencoglu, A. *et al.* Quantification of pH gradients and implications in insulator-based dielectrophoresis of biomolecules. *Electrophoresis* **32**, 2436-2447, doi:10.1002/elps.201100090 (2011).
143 Jones, P., Staton, S. & Hayes, M. Blood cell capture in a sawtooth dielectrophoretic microchannel. *Analytical and Bioanalytical Chemistry* **401**, 2103-2111, doi:10.1007/s00216-011-5284-9 (2011).
144 Sano, M. B., Henslee, E. A., Schmelz, E. & Davalos, R. V. Contactless dielectrophoretic spectroscopy: Examination of the dielectric properties of cells found in blood. *Electrophoresis* **32**, 3164-3171, doi:10.1002/elps.201100351 (2011).
145 Henslee, E. A., Sano, M. B., Rojas, A. D., Schmelz, E. M. & Davalos, R. V. Selective concentration of human cancer cells using contactless dielectrophoresis. *Electrophoresis* **32**, 2523-2529, doi:10.1002/elps.201100081 (2011).
146 Sano, M. B., Caldwell, J. L. & Davalos, R. V. Modeling and development of a low frequency contactless dielectrophoresis (cDEP) platform to sort cancer cells from dilute whole blood samples. *Biosens. Bioelectron.* **30**, 13-20, doi:10.1016/j.bios.2011.07.048 (2011).
147 Iverson, B. D. & Garimella, S. V. Recent advances in microscale pumping technologies: a review and evaluation. *Microfluid. Nanofluid.* **5**, 145-174, doi:10.1007/s10404-008-0266-8 (2008).
148 Machauf, A., Nemirovsky, Y. & Dinnar, U. A membrane micropump electrostatically actuated across the working fluid. *JMiMi* **15**, 2309-2316, doi:10.1088/0960-1317/15/12/013 (2005).
149 Lin, Q., Yang, B. Z., Xie, J. & Tai, Y. C. Dynamic simulation of a peristaltic micropump considering coupled fluid flow and structural motion. *JMiMi* **17**, 220-228, doi:10.1088/0960-1317/17/2/006 (2007).
150 Matteucci, M. *et al.* Compact micropumping system based on LIGA fabricated microparts. *MiEng* **83**, 1288-1290, doi:10.1016/j.mee.2006.01.259 (2006).
151 Felten, M., Geggier, P., Jager, M. & Duschl, C. Controlling electrohydrodynamic pumping in microchannels through defined temperature fields. *PhFl* **18**, doi:051707
10.1063/1.2209999 (2006).
152 Homsy, A., Linder, V., Lucklum, F. & de Rooij, N. F. Magnetohydrodynamic pumping in nuclear magnetic resonance environments. *Sens. Actuator B-Chem.* **123**, 636-646, doi:10.1016/j.snb.2006.09.026 (2007).
153 Srivastava, S. K., Gencoglu, A. & Minerick, A. R. DC insulator dielectrophoretic applications in microdevice technology: a review. *Analytical and Bioanalytical Chemistry* **399**, 301-321 (2011).
154 Weaver, J. C. Electroporation of biological membranes from multicellular to nano scales. *ITDEI* **10**, 754-768 (2003).
155 Garcia, P. *et al.* Intracranial nonthermal irreversible electroporation: in vivo analysis. *J. Membr. Biol.* **236**, 127-136 (2010).
156 Sel, D. *et al.* Sequential finite element model of tissue electropermeabilization. *IEEE Trans Biomed Eng* **52**, 816-827, doi:10.1109/TBME.2005.845212 (2005).
157 Lee, E. W. *et al.* Advanced Hepatic Ablation Technique for Creating Complete Cell Death : Irreversible Electroporation. *Radiology* **255**, 426-433, doi:10.1148/radiol.10090337 (2010).
158 Edd, J. F., Horowitz, L., Davalos, R. V., Mir, L. M. & Rubinsky, B. In vivo results of a new focal tissue ablation technique: irreversible electroporation. *IEEE Trans Biomed Eng* **53**, 1409-1415, doi:10.1109/TBME.2006.873745 (2006).
159 Davalos, R. V., Mir, L. M. & Rubinsky, B. Tissue ablation with irreversible electroporation. *Ann. Biomed. Eng.* **33**, 223-231, doi:10.1007/s10439-005-8981-8 (2005).
160 Maor, E., Ivorra, A., Leor, J. & Rubinsky, B. The effect of irreversible electroporation on blood vessels. *Technology in Cancer Research & Treatment* **6**, 307-312 (2007).
161 Loganathan, A. G. *et al.* IRREVERSIBLE ELECTROPORATION FOR INTRACRANIAL SURGERY: A PILOT STUDY IN A CANINE MODEL. *Neuro-Oncology* **11**, 588-588 (2009).
162 Phillips, M., Maor, E. & Rubinsky, B. Non-Thermal Irreversible Electroporation for Tissue Decellularization. *J. Biomech. Eng*, doi:10.1115/1.4001882 (2010).
163 Ott, H. C. *et al.* Perfusion-decellularized matrix: using nature's platform to engineer a bioartificial heart. *Nat. Med.* **14**, 213-221, doi:10.1038/nm1684 (2008).
164 Baptista, P. M. *et al.* The use of whole organ decellularization for the generation of a vascularized liver organoid. *Hepatology*, n/a-n/a, doi:10.1002/hep.24067 (2010).
165 Uygun, B. E. *et al.* Organ reengineering through development of a transplantable recellularized liver graft using decellularized liver matrix. *Nat. Med.* **16**, 814-U120, doi:10.1038/nm.2170 (2010).
166 Edd, J. F., Horowitz, L., Davalos, R. V., Mir, L. M. & Rubinsky, B. In vivo results of a new focal tissue ablation technique: Irreversible electroporation. *ITBE* **53**, 1409-1415, doi:10.1109/tmbe.2006.873745 (2006).

167 Sersa, G. *et al.* Vascular disrupting action of electroporation and electrochemotherapy with bleomycin in murine sarcoma. *Br. J. Cancer* **98**, 388-398, doi:10.1038/sj.bjc.6604168 (2008).
168 Nuccitelli, R. *et al.* A new pulsed electric field therapy for melanoma disrupts the tumor's blood supply and causes complete remission without recurrence. *Int. J. Cancer* **125**, 438-445, doi:10.1002/ijc.24345 (2009).
169 Gehl, J., Skovsgaard, T. & Mir, L. M. Vascular reactions to in vivo electroporation: characterization and consequences for drug and gene delivery. *Biochimica Et Biophysica Acta-General Subjects* **1569**, 51-58 (2002).
170 Kanthou, C. *et al.* The endothelial cytoskeleton as a target of electroporation-based therapies. *Mol. Cancer Ther.* **5**, 3145-3152, doi:10.1158/1535-7163.mct-06-0410 (2006).
171 Jarm, T., Cemazar, M., Miklavcic, D. & Sersa, G. Antivascular effects of electrochemotherapy: implications in treatment of bleeding metastases. *Expert Review of Anticancer Therapy* **10**, 729-746, doi:10.1586/era.10.43 (2010).
172 Sersa, G. *et al.* Reduced blood flow and oxygenation in SA-1 tumours after electrochemotherapy with cisplatin. *Br. J. Cancer* **87**, 1047-1054, doi:10.1038/sj.bjc.6600606 (2002).
173 Sersa, G., Cemazar, M., Miklavcic, D. & Chaplin, D. J. Tumor blood flow modifying effect of electrochemotherapy with bleomycin. *Anticancer Res.* **19**, 4017-4022 (1999).
174 Folkman, J. Self-Regulation of Growth In 3 Dimensions. *J. Exp. Med.* **338** (1973).
175 Kaufman, D. S., Hanson, E. T., Lewis, R. L., Auerbach, R. & Thomson, J. A. Hematopoietic colony-forming cells derived from human embryonic stem cells. *Proc. Natl. Acad. Sci. U. S. A.* **98**, 10716-10721 (2001).
176 Atala, A. Engineering organs. *Curr. Opin. Biotechnol.* **20**, 575-592, doi:10.1016/j.copbio.2009.10.003 (2009).
177 Kaufmann, P. M. *et al.* Long-term hepatocyte transplantation using three-dimensional matrices. *Transplant. Proc.* **31**, 1928-1929 (1999).
178 Mir, L. M. & Orlowski, S. Mechanisms of electrochemotherapy. *Adv Drug Deliv Rev* **35**, 107-118, doi:S0169-409X(98)00066-0 [pii] (1999).
179 Davalos, R. V., Mir, L. M. & Rubinsky, B. Tissue ablation with irreversible electroporation. *Ann Biomed Eng* **33**, 223-231 (2005).
180 Lamsa, T. *et al.* Biocompatibility of a new bioabsorbable radiopaque stent material (BaSO4 containing poly-L,D-lactide) in the rat pancreas. *Pancreatology* **6**, 301-305, doi:Doi 10.1159/000092772 (2006).